Durham E-Theses

On The evolution of phase separation in polymer blends

Henderson, Ian Charles

How to cite:

Henderson, Ian Charles (2005) *On The evolution of phase separation in polymer blends*, Durham theses, Durham University. Available at Durham E-Theses Online: http://etheses.dur.ac.uk/2730/

On The Evolution of Phase Separation in Polymer Blends

Ian Charles Henderson

PhD

University of Durham

Department of Chemistry

2005

0 5 MAY 2006

On The Evolution of Phase Separation in Polymer Blends

Ian Henderson

Abstract

An investigation is undertaken into the dynamics of phase separation in polymer blends in order to try to understand the morphologies produced via spinodal decomposition and to identify ways to target beneficial morphologies.

Cahn-Hilliard theory is used with the Flory-Huggins free energy to model phase separating systems undergoing spinodal decomposition for a number of different systems. Initially a simple two component blend is studied undergoing spinodal decomposition via a temperature quench from the one phase to the two phase region. The model is then used to study the process of secondary phase separation via a two-step quench process. A temperature quench from the one phase to the two phase region is undertaken and then the system is left to equilibrate for two different time periods before a quench further into the two phase region is carried out.

The model is then extended to focus on the technologically useful process of reaction induced phase separation. In this case a two component polydisperse blend is quenched from the one phase to the two phase region via polymerisation of one component of the blend. The phase separation process is followed for selected reaction rates and the consequences of changing the final degree of polymerisation are studied both with and without the formation of a network in the reacting component of the blend.

Finally a study of the effect of adding a surface into the blend is undertaken to show the development of a phase separated morphology at and near to the surface, we also present a method to overcome inconsistencies found in the Cahn-Hilliard model. The model is then used to target specific phase separated morphologies on a chemically patterned surface and to try and understand the processes involved in the phase separation of a three component, A-B-C, blend at a surface.

Acknowledgements

Statement of Copyright

Contents

Introduction

The blending of two or more polymers can yield materials with properties which are substantially greater than the sum of their parts and it is therefore important to understand the factors which affect these properties. A great proportion of polymer blends undergo the process of phase separation and it is known that the morphologies produced have a considerable effect on the properties of the materials formed. It is therefore of significant interest to attempt to understand the physical forces involved in the process of phase separation so that we can comprehend more fully the morphologies produced. With an understanding of the factors involved in the phase separation process we would like to be able to target specific morphologies and therefore give tuneable material properties. We use modelling to help us understand these systems and as it is straightforward to alter system variables we can probe a multitude of different situations to aid with the understanding of experimental results. We can also use modelling to test new ideas and make predictions about systems which are perhaps currently too difficult or expensive to investigate experimentally and therefore give an idea of whether the system would be worthwhile investing time and effort into developing an understanding of the physics and chemistry involved.

The use of these systems is widespread with applications in adhesives, coatings and in lightweight components for the automotive and aerospace industries. Recently the use of copolymers has been of great interest for photonic and electronic applications with block copolymers also receiving great interest. This is because the length-scale of the morphology is dictated by the size of the polymer blocks, which can be controlled by varying the ratio of the block lengths or architecture. However in, for example, photonic applications the creation of copolymers with chain lengths similar to that of the wavelength of light is currently a difficult and expensive task. Polymer blends however phase separate over a large range of wavelengths and therefore, with control, could be immensely useful materials in these and other similar applications.

In the following work we model the process of phase separation for a variety of different conditions all intended to try to further our understanding of the phase separation process; we also attempt to suggest ways in which this process can be controlled. Firstly an introduction to the principles used in the work is given

1

followed by a review of previous work undertaken in this area. This is followed by an introduction to the model and preliminary results used to test the model in the early stages. An investigation into multiple step quenches is then undertaken in order to attempt to create a highly ordered phase structure within a primary morphology. In chapter 5 we model blends which are polydisperse and include systems undergoing reaction induced phase separation, the model is then further extended to try to encapsulate the effects that a semi-interpenetrating polymer network would have upon the system. Chapter 6 shows the results found when a surface is used to try to order the morphology of the system at a hard wall surface; this is then followed by a study of phase separation on a surface which has been chemically patterned. Finally we extend the model to three component blends and once again try to model the effects which placing a surface in the system has upon the polymer morphology.

Parts of this work have been published, or have been submitted for publication, as follows:

Two-Step Phase Separation in Polymer Blends – Henderson I. C.; Clarke N., Macromolecules, **2004**, 37(5), 1953

Target Morphologies in Polymer Blends – Clarke N.; Henderson I., Mater. Res. Soc. Symp. Proc., **2005**, 856E, BB11.7.1

Reaction Induced Phase Separation of Pseudo-Interpenetrating Polymer Networks in Multi-Component Polymer Blends: A Simulation Study – Henderson I. C.; Clarke N., J. Chem. Phys., **2005**, 123(14), 144903

On Modelling Surface Directed Spinodal Decomposition– Henderson I. C.; Clarke N., Macromol. Theory Simul., **2005**, 14(7), 435

Surface Directed Spinodal Decomposition in Ternary Polymer Blends – Henderson I. C.; Clarke N., In Production

Chapter 1

Modelling the Dynamics of the Phase Separation Process

The modelling of polymer blends which are undergoing the process of phase separation is an area which has been developed over many years, hence the number of theories and studies which have been developed and undertaken is immense. Here an attempt is made to review both the most relevant work to the current project, including an in-depth review of the theoretical aspects of the work where it will be necessary in future chapters, and work which may not be directly relevant to the current study but which adds interest and understanding of the field.

Firstly, the main theories used in the study, Flory-Huggins theory and Cahn-Hilliard theory, are reviewed so we can describe how and why the phase separation process occurs in the systems studied.

1.1 Flory-Huggins Theory

1.1.1 The Flory-Huggins Free Energy

Flory-Huggins[1,2] theory was developed for polymer blends which comprise two linear monodisperse polymer chains each with N_A or N_B segments per polymer. Here a polymer chain is represented, as part of a mean field theory, as a random walk on a lattice[3]. Each lattice site is occupied by one of either type of chain monomer unit covalently bonded to an adjacent chain unit of the same polymer. The fraction of sites occupied by monomers is denoted ϕ_A (ϕ_B) and is related to concentration, c, (number of monomers per cm^3) by[4] $\phi = ca^3$ where a^3 is the volume of the unit cell in the cubic lattice. The blend is said to be incompressible such that $\phi_A + \phi_B = 1$. The free energy of the model is then described by the number of arrangements of chains which can exist on the lattice for a given ϕ, the entropic part of the free energy, and an energy term describing the interactions between adjacent molecules, the enthalpic part of the equation.

The mean field entropy, S, per lattice site is given by,

$$\frac{-S}{k_B} = \frac{\phi_A}{N_A}\ln\frac{\phi_A}{N_A} + \frac{\phi_B}{N_B}\ln\frac{\phi_B}{N_B} \qquad (1.1.1)$$

where k_B is the boltzmann constant.

It can be seen that as N_A (N_B) increases the entropy will consequently decrease, this is expected as with an increase in N_A, fewer configurations on the lattice will be available to the chain thereby decreasing the entropy of the system. The entropy of mixing is defined as the difference between the entropy given by equation 1.1.1 and the weighted average of the entropies of the pure polymer components. Instead of considering the entropy given in equation 1.1.1 we consider the entropy of mixing because it conveniently eliminates a number of trivial terms, such as all the contributions which are linear in, or independent of, ϕ_A. The entropy of mixing is given by,

$$S_{mix} = S - \phi_A S(\phi_A = 1) - \phi_B S(\phi_B = 1)$$
$$= -k_B\left(\frac{\phi_A}{N_A}\ln\phi_A + \frac{\phi_B}{N_B}\ln\phi_B\right) \qquad (1.1.2)$$

It has so far been assumed that no heat or energy change occurs on mixing, this is however an unlikely situation. By using regular solution theory it is possible to obtain an expression for the energy arising from three separate contact energies, those due to monomer A – monomer A, monomer A – monomer B and monomer B – monomer B interactions. This enthalpic energy can be expressed as,

$$U = k_B T\left(\frac{1}{2}\chi_{AA}\phi_A^2 + \frac{1}{2}\chi_{BB}\phi_B^2 + \chi_{AB}\phi_A\phi_B\right) \qquad (1.1.3)$$

where χ_{ij} are the contact interactions of components i and j. The internal energy of mixing therefore becomes[5],

$$U_{mix} = k_B T\phi_A\phi_B\left(\chi_{AB} - \frac{1}{2}\chi_{AA} - \frac{1}{2}\chi_{BB}\right) \equiv k_B T\phi_A\phi_B\chi \qquad (1.1.4)$$

4

where χ is known as the Flory interaction parameter. Having calculated both the entropy and enthalpy of mixing we can now combine the two contributions to give an expression for the free energy of mixing from, $\Delta G^{mix} = \Delta H^{mix} - T\Delta S^{mix}$,

$$\frac{F_{mix}}{k_B T} = \frac{\phi_A}{N_A}\ln\phi_A + \frac{\phi_B}{N_B}\ln\phi_B + \chi\phi_A\phi_B \qquad (1.1.5)$$

therefore the phase behaviour of a polymer blend is a result of the compromise between the first entropic part of equation 1.1.5, which always favours phase mixing, and the second enthalpic part, which usually favours phase separation.

The Flory interaction parameter is a widely used quantity which characterises a variety of polymer – solvent, polymer – polymer interactions. While originally χ was proposed as a dimensionless concentration independent parameter, many systems exhibit increases of χ with polymer concentration. This is because χ is in fact a free energy component which compromises both an entropic, χ_S, and enthalpic, χ_H, contribution. The Flory interaction parameter is however assumed to be a constant, concentration independent parameter in all our calculations. It is assumed that the correlation between monomers in the system is due to excluded volume effects, two monomer units cannot reside in the same lattice square, so the internal energy is independent of temperature and therefore $\chi \propto 1/T$.

1.1.2 The Coexistence Curve

By plotting equation 1.1.5 vs. ϕ for a number of different values of χ, as shown in figure 1.1, it is possible to determine the main features of the polymer blend phase diagram.

5
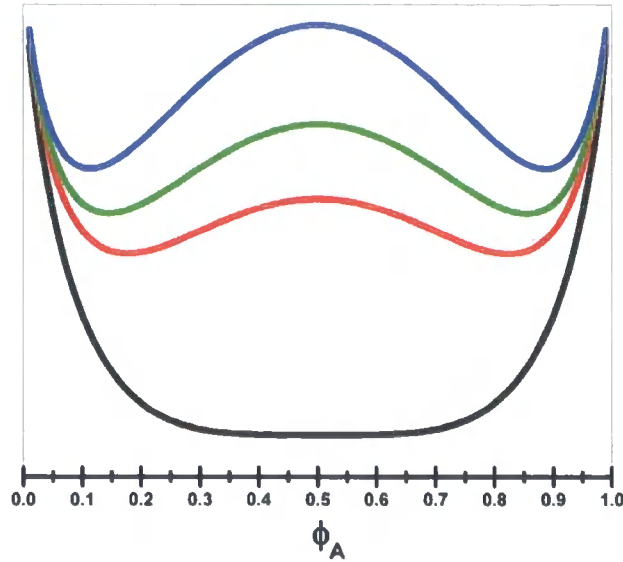
Figure 1.1

The free energy of a polymer blend for $\chi = 0.0133$ (—), $\chi = 0.0119$ (—), $\chi = 0.0110$ (—) and $\chi = 0.01$ (—) corresponding to equation 1.1.5, with $N_A = N_B = 200$.

We see from figure 1.1 that the free energy curve when χ is less than a critical value, χ_c, has a single potential well, a single free energy minimum, indicating a phase mixed system is present. Upon increasing χ a double potential well form of the resultant free energy curve is present and the system forms two phases of volume fraction $\phi_A{}'$ and $\phi_A{}''$; as illustrated in figure 1.2. Constructing the tangent to the curve, as shown in figure 1.2, for a number of free energy curves allows us to plot the positions of these minima on a temperature-concentration axis, thus forming the coexistence curve. The tangent between the two points is used as this defines the lowest possible free energy of the phase separated composition, i.e. it is the condition which must be satisfied for two or more phases of different compositions to coexist in that the chemical potentials within each phase must be equal, these two limits therefore define the composition within which a single phase is not present.
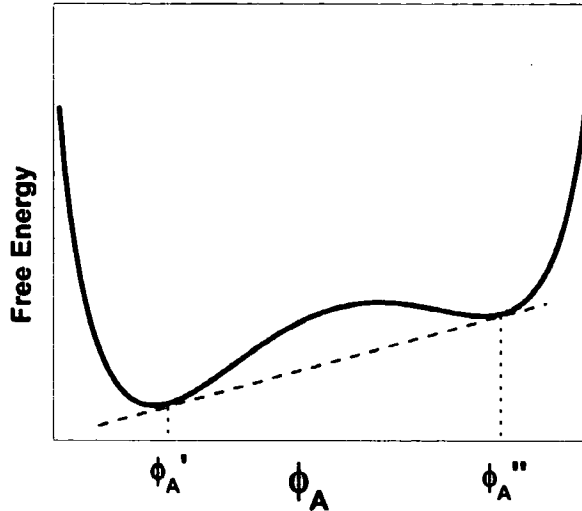
Figure 1.2

The tangent to the free energy curve for a phase separated system showing the volume fraction of the two phases, ϕ_A' and ϕ_A''.

As stated above, when the two minimum points are plotted on a temperature-concentration axis the coexistence curve, also known as the cloud point curve or the binodal curve is formed. The calculation of this curve is not straightforward as it is necessary to find the solution to two simultaneous equations. The chemical potential, μ, is defined by $\mu_A = \partial F / \partial n_A$, where n_A is the number of particles of species A, such that a change of $\phi \rightarrow \phi + d\phi$ represents an increase in the number of A monomers (equal to $d\phi$) but with an equivalent decrease of B monomers[4] ($-d\phi$), is used to calculate the coexistence curve[6].

$$\mu_A = F_{mix} - \phi_B \frac{\partial F_{mix}}{\partial \phi_B} + (1 - \phi_A)\frac{\partial F_{mix}}{\partial \phi_A}, \qquad (1.1.6)$$

A similar expression for μ_B can also be written, substituting in equation 1.1.5, the Flory-Huggins free energy, and setting $\mu_A' = \mu_A''; \mu_B' = \mu_B''$ allows us to determine the conditions for phase equilibrium, and therefore coexistence,

7

$$\frac{1}{N_A}\ln(\phi_A'/\phi_A'') - (\phi_A' - \phi_A'')\left[\frac{1}{N_A} - \frac{1}{N_B}\right] + \chi\left[(1-\phi_A')^2 - (1-\phi_A'')^2\right] = 0,$$

(1.1.7)

and,

$$\frac{1}{N_B}\ln((1-\phi_A')/(1-\phi_A'')) - (\phi_A' - \phi_A'')\left[\frac{1}{N_A} - \frac{1}{N_B}\right] + \chi\left[\phi_A'^2 - 1 - \phi_A''^2\right] = 0,$$

(1.1.8)

As stated above the coexistence curve is formed from these conditions as χ is varied, however it can be seen that a numerical solution to two simultaneous equations is necessary to find the curve. When $N_A = N_B = N$ however the situation is greatly simplified as the free energy diagram becomes symmetric around[4] $\phi = \frac{1}{2}$, as in figure 1.1, so that $\phi_A' = 1-\phi_A''$. Upon substituting this condition into equations 1.1.7 and 1.1.8 we find,

$$\frac{1}{N}\ln\left[\frac{\phi}{1-\phi}\right] + \chi(1-2\phi) = 0,$$

(1.1.9)

which we can rearrange to give,

$$\chi = \frac{1}{N}\frac{1}{(1-2\phi)}\ln\left[(1-\phi)/\phi\right],$$

(1.1.10)

The phase diagram for a symmetric blend, $N_A = N_B = N$, is shown in figure 1.3.
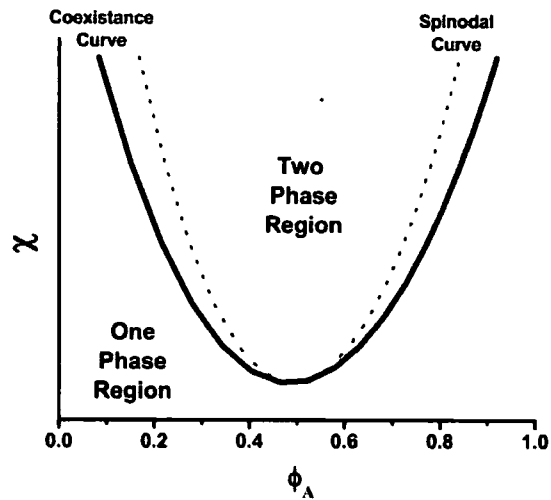
Figure 1.3

Phase diagram for a symmetric polymer blend.

1.1.3 The Spinodal Curve

Figure 1.3 also indicates the presence of a spinodal curve on the phase diagram, this curve represents the boundary between a state of instability with respect to the two phase region, i.e. where the system undergoes spontaneous phase separation via spinodal decomposition, and a metastable state, where the system undergoes phase separation via the thermally activated process of nucleation and growth. Figure 1.4 shows the magnification of the free energy curve just inside the coexistence area[7].
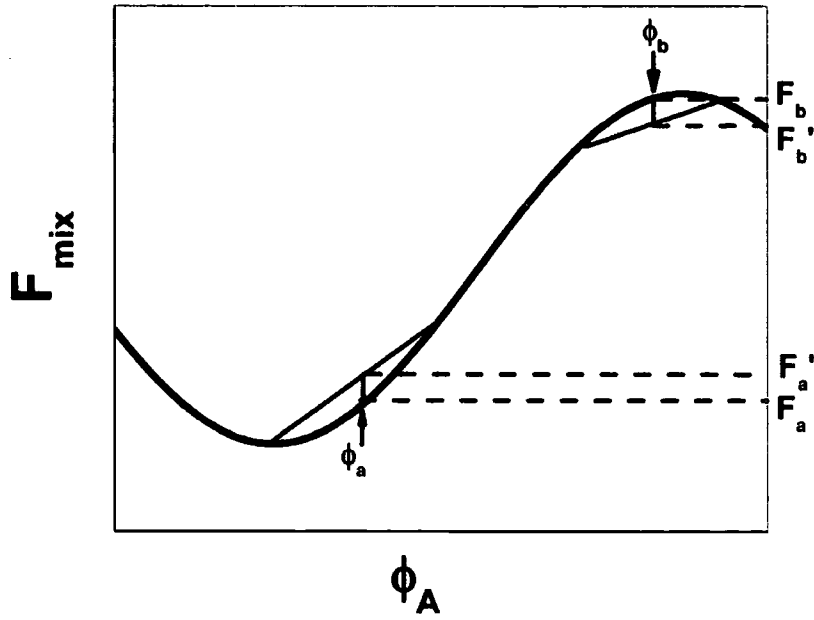
Figure 1.4

Magnification of the free energy curve just inside the co-existence area.

From figure 1.4 we see that at composition ϕ_b, small phase fluctuations created by phase separation result in the lowering of the overall free energy from F_b to F_b'. At this composition the system is susceptible to equilibrium thermal fluctuations in composition which will lead to spontaneous phase separation occurring. However at composition ϕ_a these thermal phase fluctuations lead to an increase in the overall free energy from F_a to F_a' indicating that the system is locally stable and therefore an activation energy barrier has to be overcome for phase separation to occur. The system is said to be globally unstable but locally stable to the process of phase separation. The spinodal curve is given by the condition that the second derivative of the free energy with respect to ϕ is zero, $d^2F/d\phi^2 = 0$, and is the point of inflection between the two above cases. By taking the second derivative of equation 1.1.5 we find that the spinodal is given by,

$$\chi_s = \frac{1}{2}\left(\frac{1}{N_A\phi_A} + \frac{1}{N_B\phi_B}\right),$$

(1.1.11)

The critical value, above which phase separation occurs, corresponds to the point at which the coexistence and spinodal curves meet, known as the critical point. It can be seen that this critical point, in a binary mixture, is,

$$\frac{\partial^3 F_{mix}}{\partial \phi^3} = 0,$$

(1.1.12)

and is given by,

$$\phi_{crit} = \frac{N_B^{1/2}}{N_A^{1/2} + N_B^{1/2}},$$

(1.1.13)

and,

$$\chi_{crit} = \frac{\left(N_A^{1/2} + N_B^{1/2}\right)^2}{2N_A N_B},$$

(1.1.14)

In the symmetric case where $N_A = N_B = N$ it can be seen that the critical value is given more simply by $\chi_{crit} = 2/N$ indicating that miscibility, mixing, becomes increasingly difficult as N increases, due to the corresponding decrease in entropy.

1.1.4 Limitations to Flory-Huggins theory

Although widely used it has long been recognised that limitations to Flory-Huggins theory exist from the comparison of the theory with experimental results. The first of these is that in Flory-Huggins theory it is assumed that the long range chain statistics of the polymer chains are defined by ideal random walks. In reality however this is not the case as a polymer chain in, for example, a solvent would collapse as solvent conditions are changed, this can induce phase separation between the solvent and the polymer. We would expect a similar situation within a polymer mixture upon approaching the phase separation conditions. Secondly the Flory interaction parameter is assumed to be independent of concentration when this is often not the case. This is because χ is derived solely from the entropy of combinatorial contributions to the mixing term seen in equation 1.1.2 and no account is taken for entropic non-combinatorial contributions which occur on mixing. An example would be the change in the vibrational frequency of a monomer when it comes into contact with a monomer of a different polymer, which acts against the

11

mixing process. We can allow for this by recognising that χ is a free energy parameter which is comprised of both an entropic, χ_S, and an enthalpic, χ_H, contribution such that $\chi = \chi_H + \chi_S$ and,

$$\chi = a + \frac{b}{T},$$
(1.1.15)

Flory-Huggins theory also assumes that no change of volume is seen when two, or more, polymers are mixed together, i.e. no extra free space is created when the polymers are mixed together. If however two polymers have a strongly unfavourable interaction parameter then it becomes energetically favourable for the system to slightly lower its density, this reduces the number of unfavourable contacts between monomer units and allows extra translational entropy to be gained by forming vacancies. Finally the structure of each monomer may cause packing issues that will reduce the possible number of configurations which it is possible for the chains to adopt. This in turn affects the entropy of mixing and is most likely to be important in polymers with large side groups or polymers with very different chain stiffness.

The limitations to Flory-Huggins theory are well known, however the theory is still used as a universal framework for polymer blend problems as it manages to capture the underlying principles of the behaviour in a simple and mathematically straightforward way.

1.1.5 Temperature Dependence of χ

We expect polymer blend systems to phase separate upon cooling as with higher temperatures greater thermal motion is available to decrease the attractive force between like molecules and to encourage less favourable contacts. This leads to a phase diagram as shown in figure 1.5, where the critical temperature occurs at the maximum point of the coexistence curve; this situation is often referred to as the *upper critical solution temperature* (UCST).
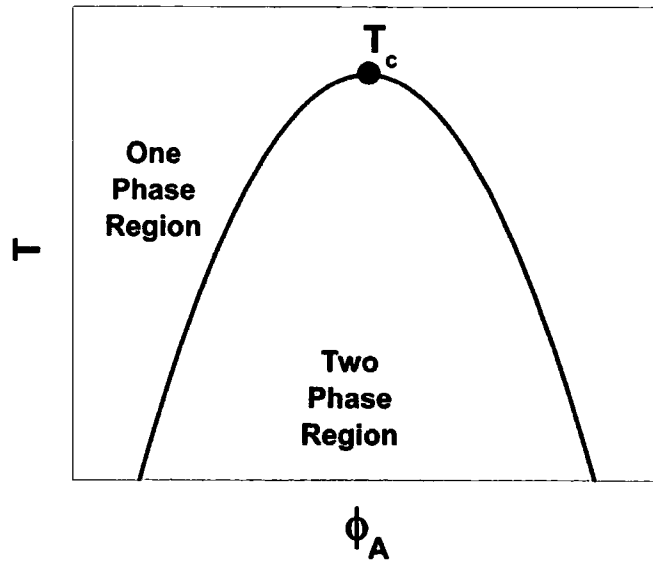
Figure 1.5

An example of the phase diagram characterised by an upper critical solution temperature.

Many blends however are known to phase separate upon heating and the phase diagram is inverted when compared to that shown in figure 1.5, these systems are known to have a critical temperature at the minimum point of the coexistence curve; known as a *lower critical solution temperature* (LCST) curve and an example is shown in figure 1.6.

13
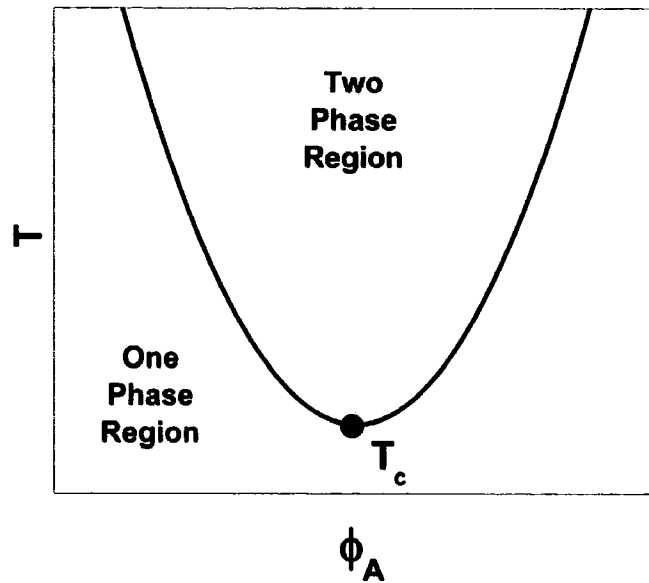
Figure 1.6

An example of the phase diagram characterised by a lower critical solution

temperature.

In this case we find that although the entropy of the system increases with T, it is not sufficient to balance the increase in the magnitude of the enthalpy. Therefore as T increases the free energy becomes more dependant on the enthalpic part of equation 1.1.5 and therefore phase separation occurs. The LCST is usually at a higher temperature than the UCST and it is possible to see both sets of behaviour in some blends.

1.2   The Random Phase Approximation

It can be shown that the Flory-Huggins free energy for polymer blends can be derived using a method termed the random phase approximation, without using the lattice model[7-10]. The method is based on how the local composition responds when the local chemical potentials are changed. In an ideal polymer blend, when $\chi = 0$, the chemical potential of component A can be written as,

$$\mu_A = \frac{kT}{N_A} \ln \phi_A + C,$$ (1.2.1)

so that,

$$\frac{\partial \phi_A}{\partial \mu_A} = \phi_A \frac{N_A}{kT},$$ (1.2.2)

and similarly for component B, here the blend is assumed to be incompressible such that $\phi_A + \phi_B = 1$. One chain is then chosen such that the density of monomers belonging to that chain at distance **r** is known as the correlation function, g(**r**), or when Fourier transformed the chain structure factor, S(**q**). Equation 1.2.2 can be generalised to arbitrary wave-vectors, **q**[9,10],

$$\frac{\partial \phi_A(\mathbf{q})}{\partial \mu_A(\mathbf{q})} = \frac{\phi_A S_A(\mathbf{q})}{kT},$$ (1.2.3)

again a similar equation can be written for component B. It is now possible to define the exchange chemical potential, Δμ, which is the energy change seen when a monomer unit of component A is replaced by a monomer unit of component B. Therefore by using 1.2.3 we find,

$$\delta(\Delta\mu(\mathbf{q})) = \delta\mu_A(\mathbf{q}) - \delta\mu_B(\mathbf{q}) = kT\left[\frac{\delta\phi_A}{\phi_A S_A(\mathbf{q})} - \frac{\delta\phi_B}{\phi_B S_B(\mathbf{q})}\right],$$ (1.2.4)

as the blend is assumed to be incompressible we can rearrange 1.2.4 to give,

$$\frac{\partial \phi(\mathbf{q})}{\partial(\Delta\mu(\mathbf{q}))} = \frac{1}{kT}\left(\frac{1}{\phi S_A(\mathbf{q})} + \frac{1}{(1-\phi)S_B(\mathbf{q})}\right)^{-1},$$ (1.2.5)

where $\phi = \phi_A$ and $(1 - \phi) = \phi_B$. The structure factor for the ideal mixture is therefore[10],

$$S_{ideal}(\mathbf{q}) = \left(\frac{1}{\phi S_A(\mathbf{q})} + \frac{1}{(1-\phi)S_B(\mathbf{q})}\right)^{-1},$$ (1.2.6)

15

This function describes both the response to an external perturbation and the equilibrium concentration fluctuations of a mixture of polymers that have no thermodynamic interaction between them. There is however a strong interaction which acts on all segments equally; these are the molecular forces of cohesion which act to maintain a constant density mixture[7]. The treatment is extended later and used for non-ideal systems to describe both the domain size during the phase separation process and also to quantify the volume fraction changes during the process of phase separation. The analogue of equation 1.2.5, derived from Flory-Huggins theory for a system in which χ is non zero is,

$$\frac{\partial \phi}{\partial (\Delta \mu)} = \frac{1}{kT} \left(\frac{1}{\phi N_A} + \frac{1}{(1-\phi)N_B} - 2\chi \right)^{-1},$$

(1.2.7)

which suggests that equation 1.2.6 can be modified to take account of non-zero χ by simply writing,

$$\frac{1}{S(\mathbf{q})} = \frac{1}{S_{ideal}(\mathbf{q})} - V(\mathbf{q}),$$

(1.2.8)

where the latter part of equation 1.2.8 is the Fourier Transform of the net thermodynamic interaction between chemically different monomers at small $\mathbf{q}$, given by $V(\mathbf{q}) = 2\chi(1 - \frac{1}{6}\mathbf{q}^2 r_0^2)$, and r_0 is a measure of the intersegment distances. In the ideal random walk case $S_A(\mathbf{q})$, and $S_B(\mathbf{q})$, is given by the Debye function, $f_D(x)$, such that,

$$S_A(\mathbf{q}) = N_A f_D(x),$$

(1.2.9)

where

$$f_D(x) = \frac{2}{x} \left[1 - \left(\frac{1-e^{-x}}{x} \right) \right] : x = \frac{1}{6} N_A b^2 \mathbf{q}^2,$$

and b is the Kuhn length in polymer A (B).

By combining equations 1.2.6, 1.2.8 and 1.2.9 for the Debye function at small q it is found that,

$$\frac{1}{S(\mathbf{q})} = \frac{1}{\phi N_A} + \frac{1}{(1-\phi)N_B} - 2\chi + \frac{b^2 \mathbf{q}^2}{18\phi(1-\phi)} + \frac{\mathbf{q}^2 r_0^2 \chi}{3}, \qquad (1.2.10)$$

where we have used $f(x) \cong 1 - (x/3)$ at small x.

It is noted that the RPA is used as a basis for determining χ via neutron scattering, however this leads to problems with the assumptions made here. Firstly the polymer mixture is assumed to be incompressible, however as shown above this is not likely to be the case. Secondly the model assumes that the conformations in the blend are ideal which is again highly unlikely in any real system. These assumptions can cause the RPA to break down, especially at higher $\mathbf{q}$.

1.3   Cahn-Hilliard Theory

As shown above, Flory-Huggins theory is used extensively to understand the reasons for phase separation in polymer blends. In the work presented a study of phase separation via spinodal decomposition is undertaken. Here the system moves from the one phase region, below χ_c, to the two phase region, above χ_c, for a system which is considered to have a UCST. To understand the dynamics of this phase separation process we turn to a model originally developed by Cahn and Hilliard[11] for binary metal alloys. The theory developed was then extended in combination with the above Flory-Huggins theory by de Gennes[12], Pincus[13] and Binder[14].

1.3.1   The Cahn-Hilliard-Cook Model

The starting point for this model is a continuity equation for each component of the blend. This continuity equation expresses the conservation of mass in the system and relates the time and spatial dependencies of the concentration, $\phi_i(\mathbf{r},t)$, of species i to the mass current $\mathbf{j}_i(\mathbf{r},t)$, where the mass current is the total polymer flux at position $\mathbf{r}$ at time t. In other words, the net flow of polymer i out of the volume at position $\mathbf{r}$ instigates a decrease in the concentration at $\mathbf{r}$. We therefore have an equation of motion for each species of the form,

17

$$\frac{\partial \phi_i(\mathbf{r},t)}{\partial t} = -\nabla \cdot \mathbf{j}_i(\mathbf{r},t), \qquad (1.3.1)$$

The mass current and the free energy functional are related through the chemical potential, the mass current is related to the chemical potential, μ_i, through[15],

$$\mathbf{j}_i(\mathbf{r},t) = -\sum_j^{n+1} M_{ij} \nabla \mu_{ij} + \mathbf{j}_T(\mathbf{r},t), \qquad (1.3.2)$$

where M_{ij} is the mobility of species i due to j and $\mathbf{j}_T(\mathbf{r},t)$ is the mass current arising from thermal noise. The chemical potential is related to the free energy thermodynamically by,

$$\mu_j = \frac{\partial F}{\partial n_j}, \qquad (1.3.3)$$

Cook[16] added a thermal noise term, $\eta(\mathbf{r},t)$ to the diffusion equation for spinodal decomposition to allow for the solute flux from thermal fluctuations (Brownian motion). Cook found that discrepancies between theory and experimental work during the very early stages of spinodal decomposition could be accounted for by adding this term as the thermal driving force initiated these stages. The Cook term satisfies the conditions,

$$\langle \eta(\mathbf{r},t) \rangle = 0, \qquad (1.3.4)$$

which states that the noise added over the entire lattice is zero, and,

$$\langle \eta(\mathbf{r},t)\eta'(\mathbf{r}',t') \rangle = -2Mk_BT\nabla^2\delta(\mathbf{r}-\mathbf{r}')\delta(t-t'), \qquad (1.3.5)$$

The resultant Cahn-Hilliard-Cook nonlinear diffusion equation is,

$$\frac{\partial \phi(\mathbf{r},t)}{\partial t} = M\nabla^2 \frac{\delta\Delta F\{\phi(\mathbf{r},t)\}}{\delta\phi(\mathbf{r},t)} + \eta(\mathbf{r},t), \qquad (1.3.6)$$

18

The free energy, ΔF, in equation 1.3.6 is taken from Flory-Huggins theory as described above. However it was suggested by de Gennes[12] that by combining Flory-Huggins theory with an additional gradient term, derived from the RPA, it is possible to account for the slow spatial variations in concentration due to fluctuations, such that,

$$\frac{F\{\phi(\mathbf{r})\}}{kT} = \int d\mathbf{r} \left[\frac{f[\phi(\mathbf{r})]}{kT} + \kappa[\phi(\mathbf{r})] |\nabla \phi(r)|^2 \right], \qquad (1.3.7)$$

where the free energy, $f[\phi(\mathbf{r})]$, is given by equation 1.1.5 and κ is given by,

$$\kappa(\phi) = \frac{b^2}{36\phi(1-\phi)} + \chi\lambda^2, \qquad (1.3.8)$$

for an incompressible blend, and λ is the effective distance between monomers, $\lambda^2 = r_0^2/6$.

De-Gennes argued that in this way the chain connectivity within the polymer molecules, which manifests itself as an explicit entropic contribution, can be accounted for. He then further argued that since χ is typically quite small in most blends the entropic contribution to κ will dominate over the enthalpic contribution to the free energy. This method has also found applications in theories for simple liquids as the addition of this square gradient contribution reflects the unfavourable contribution to the free energy caused by the formation of interface between two domains. Preliminary studies showed that the composition independent term in (1.3.8) has a negligible effect on structure development and hence all calculations presented are performed with $\lambda = 0$.

1.3.2 Solving the Cahn-Hilliard-Cook Model

The functional derivative of equation 1.3.7 is given by,

$$\frac{\delta F}{\delta \phi} = \left[\frac{1}{N_A} \ln\phi - \frac{1}{N_B} \ln(1-\phi) \right] - 2\chi\phi + \frac{(2\phi-1)}{36\phi^2(1-\phi)^2}(\nabla\phi)^2 - \frac{1}{18\phi(1-\phi)}\nabla^2\phi,$$

$$(1.3.9)$$

which when combined with equation 1.3.6 gives,

$$\frac{\partial \phi_i(\mathbf{x}, \tau)}{\partial \tau} = \frac{1}{2} \nabla^2 \left[\frac{1}{N_A(\chi_f - \chi)} \ln \phi - \frac{1}{N_B(\chi_f - \chi)} \ln(1 - \phi) - \frac{2\chi}{\chi_f - \chi} \phi \right.$$
$$\left. + \frac{(2\phi - 1)}{36\phi^2(1 - \phi^2)} (\nabla \phi)^2 - \frac{1}{18\phi(1 - \phi)} \nabla^2 \phi \right],$$

$$(1.3.10)$$

where $\mathbf{x}$ and τ are rescaled spatial and temporal variables respectively given by

$\mathbf{x} = \sqrt{|\chi_f - \chi|} \mathbf{r} / b$ and $\tau = ND(\chi_f - \chi)^2 t / b^2$. The noise term from equation 1.3.6 has

been neglected. Clearly the scaling is determined by χ_f, which for a single step

quench is most conveniently chosen to be equal to χ, the value of the Flory-Huggins

parameter at the final quench depth.

Equation 1.3.10 can then be solved using a simple finite difference scheme

and once mesh size, time step and system parameters have been set it is possible to

integrate the resulting equation of motion. This gives a finite difference scheme of

the form,

$$\phi_{ij}^{m+1} = \phi_{ij}^m + \frac{\Delta \tau}{2(\Delta x)^2} \sum_{nn} \left[\frac{1}{N_A(\chi_f - \chi)} \ln \phi_{ij}^m - \frac{1}{N_B(\chi_f - \chi)} \ln(1 - \phi_{ij}^m) - \frac{2\chi}{\chi_f - \chi} \phi \right.$$
$$\left. + \frac{(2\phi_{ij}^m - 1)}{36(\phi_{ij}^m)^2(1 - \phi_{ij}^m)^2(2\Delta x)^2} \prod_{nn} \phi_{ij}^m - \frac{1}{(\Delta x)^2} \left(\frac{1}{18\phi_{ij}^m(1 - \phi_{ij}^m)} \right) \sum_{nn} \phi_{ij}^m \right],$$

$$(1.3.11)$$

where for notational convenience,

$$\prod_{nn} f_{ij} \equiv f^2_{i+1,j} + f^2_{i-1,j} + f^2_{i,j+1} + f^2_{i,j+1} - 2(f_{i+1,j} f_{i-1,j} + f_{i,j+1} f_{i,j-1}),$$

$$(1.3.12)$$

and

$$\sum_{nn} f_{ij} \equiv f_{i+1,j} + f_{i-1,j} + f_{i,j+1} + f_{i,j-1} - 4f_{ij}, \qquad (1.3.13)$$

20

In order to speed up computation it is best to choose a large mesh size and a large time step but in order to stop such problems as "pinning", as discussed later, it is important to choose a mesh size which is smaller than the smallest important length scale and a time step which is too large can generate instabilities and spurious results.

The evolution of the phase separated morphology needs to be followed throughout and can be quantified by the time dependent structure factor. The time dependent structure factor is employed as it can also be found in experimental studies from light scattering, where it is used to probe the size of polymer domains, for this reason experimental and theoretical results can be directly compared. The time dependent structure factor is found from,

$$S(\mathbf{q},\tau) = \left\langle \frac{1}{L^d} \sum_x \sum_{x'} e^{i\mathbf{q}\cdot\mathbf{x}} \left[\phi(\mathbf{x}+\mathbf{x}',\tau)\phi(\mathbf{x}',\tau) - \langle\phi\rangle^2 \right] \right\rangle, \qquad (1.3.14)$$

where L^d is the total number of lattice sites. The wave vectors are defined as $\mathbf{q} = (2\pi/L\Delta x)\mathbf{n}$, where $\mathbf{n} = 1,2,...,L/2$ and $<...>$ denotes an averaging over all possible configurations. When the structure factor is found it can be plotted against $\mathbf{q}$ and the peak in its graph gives an indication of the size of the polymer domains corresponding to a single wavelength in the Fourier transform becoming dominant.

Chapter 2

Extensions to Cahn-Hilliard Theory

In the following chapter a review of the areas of interest in the current work will be performed, including extensions to the theories shown in the previous chapter. This includes reviews of areas encompassing;

- Multi-step quenches into the two phase region;

- Reaction induced phase separation;

- Polydisperse systems;

- Crosslinking and semi-interpenetrating polymer networks;

- Multi-component blends;

- The addition of hard wall surfaces;

- Phase separation on a chemically patterned surface;

- Block co-polymers

2.1   Spinodal Decomposition
2.1.1   Domain Growth

Cahn-Hilliard theory, as described in the previous chapter, has been extensively used over the past few decades to study the process of spinodal decomposition in blends of two, or more, polymers[17]. The spinodal decomposition process is usually split into three distinct time regimes, these are: (i) the growth at early times immediately following a quench into the two phase region; (ii) the medium to late regime and (iii) the very late stage of the phase separation process when hydrodynamic interactions dominate the coarsening of the polymer domains. It has been shown that initially fluctuations above a critical correlation length grow exponentially with a particular length-scale dominating; as is shown in figure 2.1. Eventually coarsening of the domains occurs to reduce the interfacial area[18-20].
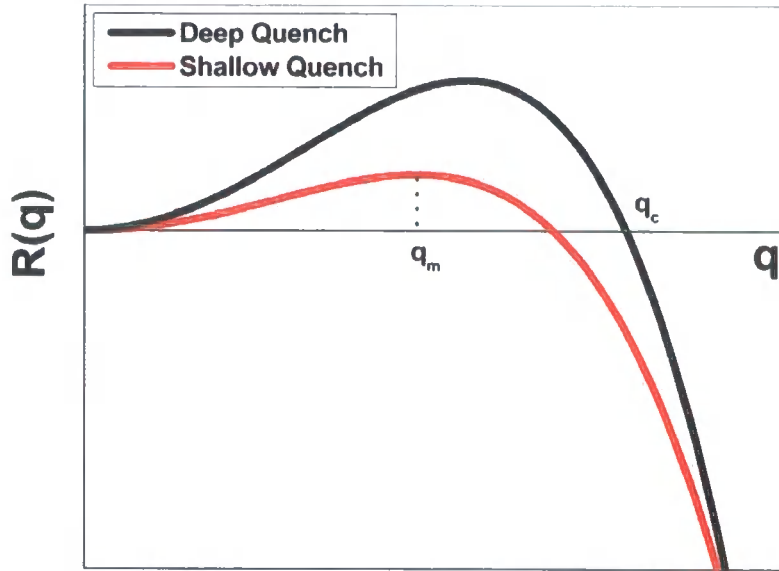
Figure 2.1

Rate of growth, $R(\mathbf{q})$ vs. wavevector, $\mathbf{q}$, for both a deep and shallow quench.

Figure 2.1 shows a plot of growth function vs. the wavevector found from Cahn's linear theory[11,21], as described later, where $\mathbf{q}_m = \left(1/\sqrt{2}\right)\mathbf{q}_c$. Here we see that wavevectors larger than the critical wavevector, $\mathbf{q}_c$, decay whereas wavevectors which are smaller than $\mathbf{q}_c$ grow, with the wavevector $\mathbf{q}_m$ dominating. Therefore during the phase separation process the length-scale which dominates is proportional to $\mathbf{q}_m$, known as the fastest growing wavevector. The difference between a deep and shallow quench can also be seen in figure 2.1. Here it can be seen that the position of $\mathbf{q}_m$ is found at larger $\mathbf{q}$ in the case of a deep quench. Since $\lambda \propto 1/\mathbf{q}$, where λ is the wavelength of the phase separated domains, deeper quenches imply smaller characteristic lengthscales of the phase separated domains during the "early stages".

Initially the growth rate of the late stage dynamics, without hydrodynamic effects, were thought to scale either with time[22,23] as $\tau^{1/4}$ or as $\tau^{1/3}$. After a number of studies[18,19,24-26] it was confirmed that in the absence of hydrodynamic effects the growth of the domains in the medium to late stages of the spinodal decomposition process do indeed scale with time as $\tau^{1/3}$. It is also found that during the late stages the growth law is independent of thermal noise[24] whilst pioneering analytical studies of the intermediate and late stages have also been carried out by Langer[27] and Akcasu and Klein[28].

23

Figure 1.3 shows the phase diagram of a critical system, where $N_A = N_B$, this produces a curve that is symmetric about the critical point χ_c. When phase separation then occurs at χ_c, equal concentrations of species A and species B are found giving continuous domain morphology. If a system is studied where $N_A \neq N_B$, an asymmetric phase diagram is produced, as shown in figure 2.2,
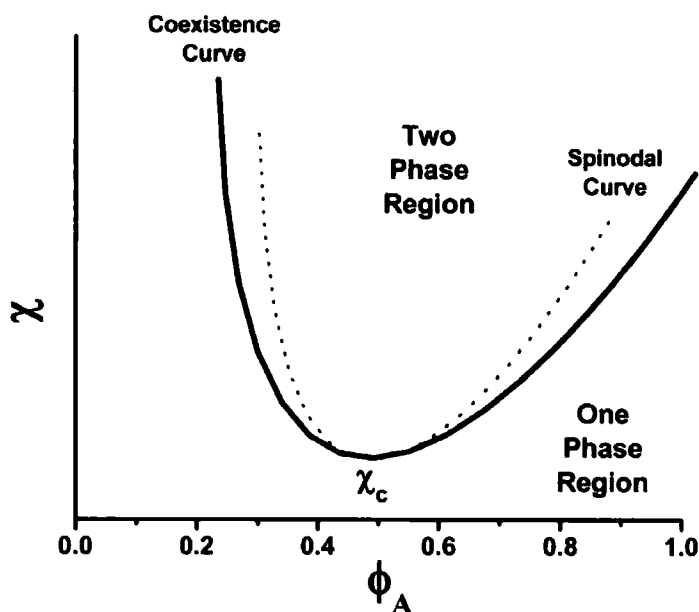
Figure 2.2

The phase diagram for a blend where $N_A \neq N_B$

From figure 2.2 it can be seen that the phase curve is no longer symmetric about χ_c. If a quench is undertaken into the two phase region with a 50:50 binary blend it is possible to see that the co-continuous structure we would observe in the symmetric case will give way to droplet type morphology[29,30]. It is also possible to see that in either case if a non-critical blend, one that is not equivalent to the volume fraction at χ_c, is used a droplet morphology will again form[29]. For example if in figure 1.3 we undertook a quench into the two phase region using a 70:30 blend, the final values of φ' and φ'' will be equivalent to those seen in a 50:50 blend but in the 70:30 case greater overall volume of one component than the other is present. In all cases the system moves to reduce the amount of high energy interface present between each polymer component in order to lower the overall free energy. In the case of the 50:50 blend a co-continuous structure is therefore seen as this is the best

24

way to reduce the amount of interface present. For the 70:30 blend the system creates a droplet structure as the circular, or in three dimensions spherical, structure again gives the minimum amount of interface between the two components. A comparison of the two types of morphology is shown in figure 2.3.

(a) **(b)**
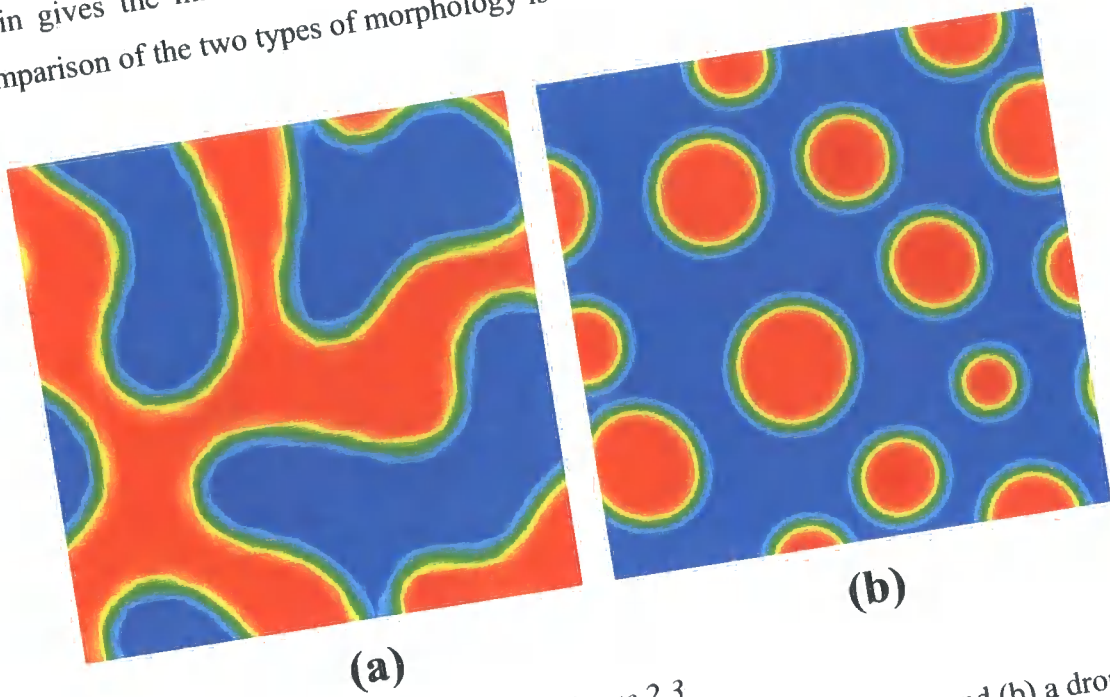
Figure 2.3

Example morphologies produced for (a) a continuous morphology and (b) a droplet morphology.

The lever rule can be used to find the theoretical area occupied by each component of the blend using,

$$v\overline{\phi_A} = v'\phi_A' + v''\phi_A'',$$ (2.1.1)

where the total area of the domain is v, and v' and v'' are the areas of the phases with compositions ϕ_A' and ϕ_A'' respectively, determined from the coexistence curve. Since $v = v' + v''$,

$$v' = v\left[\frac{\langle\phi_A\rangle - \phi_A''}{\phi_A' - \phi_A''}\right],$$ (2.1.2)

and,

$$v'' = v\left[\frac{\langle\phi_A\rangle - \phi_A'}{\phi_A'' - \phi_A'}\right],$$ (2.1.3)

2.1.2 Pinning

As stated previously it is important to choose a mesh size which is smaller than the smallest important length scale in order to stop the phenomena of "pinning" occurring within the simulations. It was originally suggested[30] that there was a regime in the phase diagram of an off-critical symmetric polymer blend where domain growth is suppressed even though the system is thermodynamically unstable and that this area could be seen using Cahn-Hilliard theory. It was found that the morphology was observed to "freeze" after some time and after this point very little phase separation was seen; the authors therefore concluded that this model contained all the information necessary to explain pinning. Experimentally this phenomena has also been seen[31,32] however the physical reasoning for this is less well understood. It is found that domain growth stops soon after the break-up of domains into the droplet morphology shown in figure 2.3(b) but the mechanism which then prevents further coarsening is still unknown. It was then found, theoretically, that with the addition of the noise term into the free energy functional pinning was not observed[20]. It was suggested that the reason for this is that the noise term does not allow the system to become trapped in a local minima of the free energy. Castellano and Glotzer[33] however showed that the pinning phenomena seen in the simulations using Cahn-Hilliard theory was simply an artefact of the discretisation scheme. They found that the mesh size must always be smaller than the smallest propagating length scale in the problem and that this had not been obeyed in previous work[30]. It was therefore shown that the Cahn-Hilliard model does not contain all the information necessary to explain the process of pinning and additional physical parameters would be needed to properly model such a system. Further studies into the dependence of the evolution of the morphology due to the mesh size have also been undertaken[34,35] to try to understand this artefact of the discretisation.

2.1.3 Noise

The effect of the addition of thermal noise to the system, and its subsequent effect on the dynamics of the phase separation process, has also received attention in the academic literature[36,37]. It is found that the magnitude of the external noise term can have a great effect on the phase separation process in that it can enhance, or even induce, the process of phase separation. A large noise term has also been found to

decrease the sharp interface between components making it less well defined. In the systems presented here noise is either added once before phase separation occurs or continuously throughout the simulation, the amount and frequency of the noise changes depending on which model is used and is decided upon through test simulations to observe the effect on the final morphology. The addition of noise is a computationally inefficient process so the aim is to add minimal noise without effecting computational results.

2.1.4 Hydrodynamics

The late stage dynamics of polymer blends can be strongly affected by hydrodynamic interactions[38-40]. Here a moving monomer generates a flow field around itself as it diffuses through the polymer matrix. The flow field then starts to propagate at a much greater rate than the monomer that generated it, i.e. momentum transport instead of particle transport occurs. Other monomers then feel this field in such a way that their dynamics become strongly correlated, leading to an increase in the rate of phase separation especially at the late stages of the phase separation process. As seen above, normally the late stages of phase separation scale with time as $\tau^{1/3}$, but when hydrodynamic effects are taken into account this rate can increase into the region of $\tau^{1/2}$. In the following work hydrodynamics are not included as the area of interest is the early stages of the phase separation process where control is needed to target the final morphology and where hydrodynamics have little or no effect.

2.2 Multi-Step Quenches into the Two Phase Region

There have been many experimental reports of phase separation in a mixture of polymeric species quenched from the single phase to a temperature inside the spinodal region. More recently two-step temperature jumps have been studied experimentally[41-44] using light scattering techniques. In these systems a quench is undertaken from the one phase region into the two phase region, from χ_0 to χ_1 in figure 2.4, where the system is allowed to reach coexistence and a primary domain structure is allowed to develop. A second quench is then undertaken further into the two phase region to χ_2, again as shown in figure 2.4.
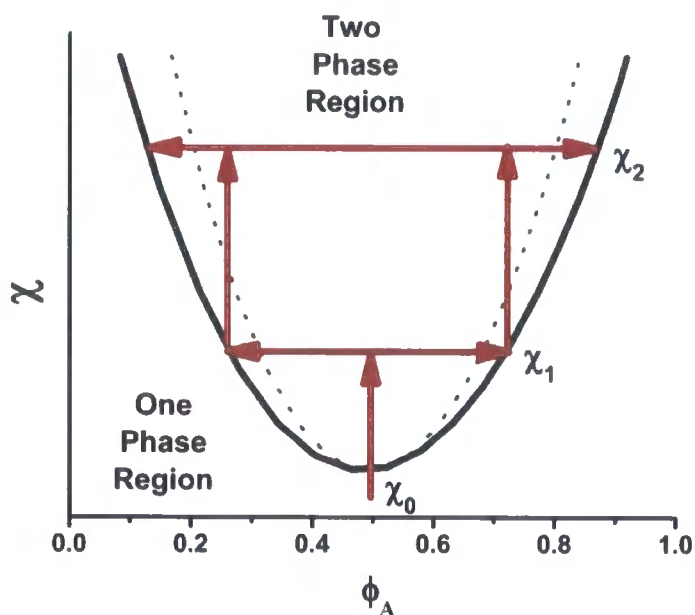
Figure 2.4

Phase diagram illustrating the two-step quench phase separation process in a symmetric binary polymer blend.

Using a binary blend of deuterated polybutadiene and protonated polyisoprene at the critical composition Hashimoto et al.[43] found that large primary domains grew after the first quench from χ_0 to χ_1. Using small angle light scattering it was then possible to follow the growth of the secondary domains after a quench from χ_1 to χ_2. It was found that small secondary domains grew within the larger primary domains. The scattering peak for both the primary and secondary domains next shifted towards small **q**, indicating that both domains grew in size. It was then found that although the primary domain continued to grow in size the peak for the secondary domain tended to shift to larger **q** and reduce in magnitude. This indicates that the secondary domains were reducing in size and annihilating. It was suggested that this decrease in the secondary domains was due to them being absorbed into the primary domains to reduce the interfacial energy in the system. The same group then characterised the time evolution of the structure factor[42,44] and the early-stages of the second step, which they found to be well characterised by linearised theory. It was also noted that, after the second temperature jump, the structure grew according to the scaling laws that are relevant to a single-step spinodal decomposition experiment[23]. Theoretical studies in this area are limited, Fialkowski and Holyst[45,46] have recently studied the relaxation of structures during quenches into the two phase

28

region followed by a jump back into the single phase region both experimentally and theoretically. It is suggested that this method is useful for the determination of both the spinodal and binodal, coexistence, temperatures for a polymer blend. Clarke[47] has investigated target morphologies using a novel method. In this work a droplet of polymer A is placed in a matrix of polymer B, the droplet is then allowed to dissolve into the matrix. Before complete dissolution of polymer A the blend is quenched into the two phase region and phase separation takes place, creating domains of polymer B within the droplets of polymer A. Tanaka[48,49] has studied the process of secondary phase separation and found that the secondary phase separation could be separated into three regimes. It was found that in the first two time regimes, where the secondary structure first develops, the secondary system can be considered to be isolated from the primary domain morphology. In the late time regime however, when the secondary structure is incorporated into the primary structure, it was found that the secondary system can no longer be considered to be isolated from the primary as the two strongly interact. It is also noted that secondary structure is also possible in a single quench system, where the diffusion cannot keep up with fast hydrodynamic coarsening[50].

2.3   Reaction Induced Phase Separation

As we have seen, a common way to induce phase separation is via a temperature jump or quench into the two-phase region of the phase diagram, this is known as thermally induced phase separation (TIPS), however a common technological approach is the process of reaction induced phase separation (RIPS)[51] or polymerisation induced phase separation (PIPS). Here phase separation and polymerisation occur simultaneously. Phase separation occurs because the boundary between the one phase (stable) and the two-phase (unstable) region moves as the reaction proceeds, so that at a fixed temperature the blend moves from the one phase region into the two phase region, as schematically illustrated in figure 2.5.
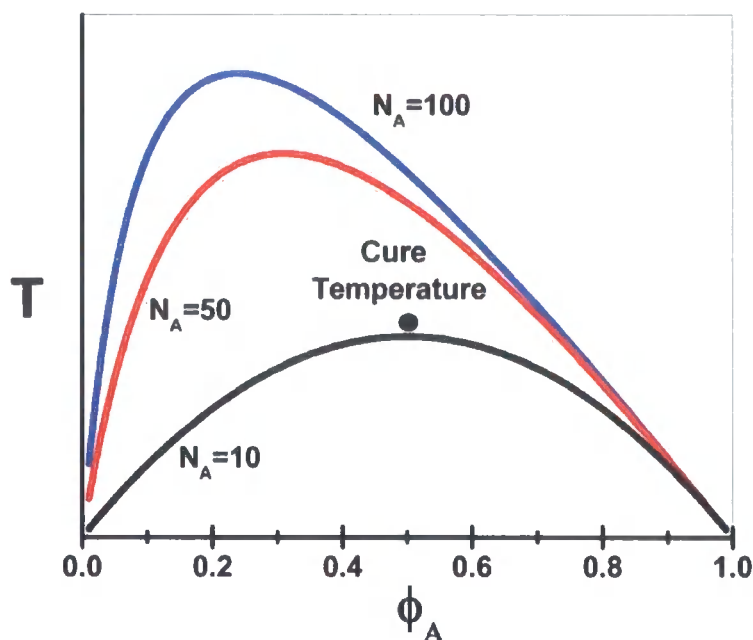
Figure 2.5

Temperature (T)/Volume Fraction (ϕ_A) phase diagram as polymerisation of component A proceeds. N_A = 10, 50 and 100 and N_B = 10. In the above example the blend phase separates when $N_A \geq 10$

This technique to induce phase separation is used as a common technological method to produce materials with phase separated morphologies. This is because it is not necessary to start the process with two polymers but instead monomers can be used. This leads to greater mixing in the one phase region. Either one or both components of the blend can then be polymerised in situ leading to a phase separated structure. It has long been known[52] in the area of rubber toughened plastics that this method leads to improved properties over a TIPS system as the greater mixing in the initial stages leads to final morphologies with greater structure.

Previous studies on such a process have been undertaken by Glotzer et al[53] who considered a simple two component system with a mixture of molecules, A and B. The system then undergoes a reaction, where A and B react to form C, which has temperature dependant forward and backward rates. Using this method the initial long-wavelength instability, which is characteristic of spinodal decomposition, was suppressed by the chemical reaction and this restricted the domain growth to intermediate length scales even in the late stages of spinodal decomposition. However the reversibility of the reaction results in the model being inappropriate for

most RIPS processes. Chan and Rey[54,55] modelled RIPS in a binary trifunctional monomer-small molecule system in order to investigate the formation of polymer dispersed liquid crystals (PDLC's) and found that the polymerisation had no effect on the morphology formed during phase separation, as a similar periodic phase separated structure developed to that which occurs during TIPS. Using two-dimensional simulations it was found that a droplet-type structure was formed which is consistent with experimental results. It was also found that the droplet size depends on both the quench depth and the molecular weight; this means the droplet size can be controlled, giving rise to target morphologies and therefore controllable properties of the phase separated blend. We however note that the only feature of RIPS incorporated into this model is the increase in molecular weight with time for one of the components. Polydispersity and elasticity of a growing network have both been neglected. Ishii et al[56] and Clarke[57] developed a thermodynamic model in which RIPS occurs for polydisperse systems and used it to give quantitative predictions of the phase diagram of a curing polyphenylene ether/epoxy/amine bend. Morphology control has also been attempted in experimental systems undergoing reaction induced phase separation[58]. Here the morphology is controlled by either changing the reaction temperature or by adding extra components to the blend in the initial stages of phase separation. The blend used in this case was poly(ethyl acrylate) (PEA) and poly(methyl methacrylate) (PMMA) with a ratio of 79:21 respectively. It was found that by changing these reaction conditions the miscibility between components can be affected but no real control over the structure of the morphology is seen. A computational study of PIPS under a temperature gradient has been undertaken by Oh and Rey[59]. Here it is found that the evolution of the phase separation process followed the propagation front of the temperature gradient, as would be expected. It was however found that droplet morphologies were formed in the hotter regions of the temperature gradient with a lamella morphology formed in the cooler regions.

2.4   Polydisperse Systems

Flory-Huggins theory assumes that all the polymers in the system are monodisperse, in reality however most polymers, especially those used in technological applications, are polydisperse with a wide range of molecular weights. Two averages are normally used to characterise the polydispersity of polymers, these

are the number, n, average molecular weight and the weight, w, average molecular weight, given by[60],

$$\overline{N_n} = \frac{\sum_i \phi_i}{\sum_i \phi_i / N_i},$$

(2.4.1)

and,

$$\overline{N_w} = \frac{\sum_i \phi_i N_i}{\sum_i \phi_i},$$

(2.4.2)

Flory-Huggins theory was therefore extended to polydisperse solution systems by Scott and Magat[61] as,

$$\frac{F_{mix}}{k_B T} = \phi_0 \ln \phi_0 + \sum_i \frac{\phi_i}{N_i} \ln \phi_i + \chi \phi_0 (1 - \phi_0),$$

(2.4.3)

Such that $\sum_i \phi_i = 1 - \phi_0$ where ϕ_0 is the volume fraction of a solvent and the subscript i refers to the components of the polydisperse polymer. Equation 2.4.3 can be extended for a binary polymer blend where component A is polydisperse and component B is monodisperse as by modification with equation 2.4.2[60],

$$\frac{F_{mix}}{k_B T} = \int_V dr \left[\sum_i \frac{\phi_{Ai}(\mathbf{r})}{N_{Ai}} \ln \phi_{Ai}(\mathbf{r}) + \frac{\phi_B(\mathbf{r})}{N_B} \ln \phi_B(\mathbf{r}) + \chi \sum_i \phi_{Ai}(\mathbf{r}) \phi_B(\mathbf{r}) + \sum_{n,m} \kappa_{nm} \nabla \phi_n(\mathbf{r}) \nabla \phi_m(\mathbf{r}) \right],$$

(2.4.4)

where n and m refer to any component of the blend, V is the volume of the system and κ is now given by,

$$\kappa_{ij} = \frac{q^2 b^2}{36} \left[\frac{\delta_{ij}}{\phi_{Ai}} + \frac{1}{\phi_B} \right],$$

(2.4.5)

32

where δ_{ij} is the Kronica delta such that if $i = j$ then $\delta_{ij} = 1$ but if $i \neq j$ then $\delta_{ij} = 0$. The RPA is again used, as in chapter 1.2, to derive this expression. In this case the spinodal is now given by,

$$\chi_s = \frac{1}{2}\left[\frac{1}{\overline{N}_{wAi}\phi_{Ai}} + \frac{1}{N_B\phi_B}\right], \qquad (2.4.6)$$

A key feature of reaction induced phase separation is the polydispersity of the reacting component, recently there has been significant progress made on studying polydisperse[60,62-67] polymer blends. The early stages of phase separation in such blends have been studied by Schichtel and Binder[66] who made the assumption that the equation of motion for each component of the blend was only coupled to that of the other components through the presence of vacancies. Using this method a limited analytical solution to the equations of motion was developed. Takenaka and Hashimoto[67] investigated whether Cahn's[21] linearised theory could be used to approximate the early stages of spinodal decomposition in a polymer blend in which one component was polydisperse. It was found that the early stages of spinodal decomposition in the polydisperse blend were still well described by linearised theory. Warren[68,69] developed a method to study the thermodynamics of the early stages of the phase separation process. He replaced an infinite number of differential equations with equations of motion for the first and second moments of the distribution function, making it possible to model the later stages of the phase separation process. Clarke[60] further developed Cahn-Hilliard[11] (CH) theory to study the early stages of phase separation in a mixture of a polydisperse polymer and a monodisperse polymer. An arbitrarily large number of discrete components were used to model polymers with continuous polydispersity. It was found that as the number of components increased, and the computational demand increased, the behaviour converged when a computationally reasonable number of components were used. The shape of the growth rate curve was found to be independent of the number of components in the polymer blend and was also indistinguishable from that of the original Cahn-Hilliard theory. For a polydisperse blend the magnitude of the growth rate has a more complex dependence on the quench depth than that predicted for monodisperse blends, for example the effect of polydispersity at small quench depths is to slow down the phase separation process. Pagonabarraga and Cates[62]

supplemented the phenomenological equations of Clarke with explicit calculations of the dynamical coefficients from a model based on tube theory. Finally Yashin and Balazs[70] developed a system to model the interdiffusion in binary polymer blends which exhibit polydispersity in length, this system can be used to study polymer systems in which the degree of polymerisation changes due to interfacial or bulk reactions.

When modelling polydispersity we consider the effect which polymer interdiffusion has on the system. Interdiffusion considers the dynamics of concentration fluctuations throughout the system. A distinction between interdiffusion and the self diffusion coefficient is made as the latter describes the motion of single chains. A model for mutual diffusion was first proposed by Brochard[71,72], and has found wide spread use as it can be applied to incompressible systems. In this theory it is assumed that there exists a local flow field, common to all polymers, that has a velocity, $v(r)$. It is then assumed that the total flux of each component is the sum of the flux that would occur in a fixed background and the flux due to the flow field, such that equation 1.3.2 can be re-written as,

$$J_m = \lambda_m \nabla \mu_m + \phi_m v_m,$$

(2.4.7)

where λ_m is the mobility of component m. By incompressibly constraining the system such that the total flux is zero, $J_B + \sum_i J_{Am} = 0$, it is possible to show that,

$$J_m = \lambda_m \nabla \mu_m - \phi_i \sum_n \lambda_n \nabla \mu_n$$

(2.4.8)

where λ_n is the mobility of component n.

Equation 2.4.8 can then be re-written in terms of the differences between the chemical potential of each component of the polydisperse polymer and that of polymer B,

$$J_i = \sum_j \Lambda_{ij} \nabla (\mu_j - \mu_B),$$

(2.4.9)

where Λ_{ij} are the Onsager coefficients shown below.

The Gibbs-Duhem equation, $\sum_n \phi_n \mu_n = 0$, allows the flux to be written as,

$$J_i = \sum_j \left(\delta_{ij}\lambda_i - \phi_i\lambda_j + g_i\phi_j\right)\nabla\mu_j - \left(\phi_i\lambda_B - g_i\phi_B\right)\nabla\mu_B, \qquad (2.4.10)$$

Equating equations 2.4.9 and 2.4.10 gives, $g_i = -\lambda_i + \phi_i\sum_m \lambda_m$, such that the Onsager coefficients are,

$$\Lambda_{ij} = \left(\delta_{ij} - \phi_i\right)\lambda_j - \phi_j\lambda_i + \phi_i\phi_j\sum_{m=1}^{s}\lambda_m, \qquad (2.4.11)$$

when s components are present and $\Lambda_{ij} = \Lambda_{ji}$. This methodology allows the mutual diffusion in the system to be described, and will be used extensively later to describe the mutual diffusion in both polydisperse and multi-component, greater than two, polymer blends.

2.5   Crosslinking and Semi-Interpenetrating Polymer Networks

Polymer networks are important soft solid materials; examples include adhesives such as epoxy resins and vehicle tyres, which undergo the well known process of vulcanisation. During crosslinking polymer chains are linked together to form a three dimensional network, this network will then resist deformation, improving the dimensional stability and other material properties such as the ability to resist solvents, reduce creep rate and make the material less prone to heat distortion as the glass transition temperature is raised. The glass transition, T_g, is the temperature at which a material passes from the glassy, hard rigid solid, state into a state where it softens and becomes rubberlike. It is an important temperature in polymer physics as it is the point at which material property changes occur, i.e. the material may become more ductile or more easily deformed above the T_g. The glass transition is seen in amorphous polymers, where the chains are arranged in a random fashion, however in a perfectly crystalline polymer, one where the chains are incorporated in areas of three dimensional order, the polymer passes through a point known as the melting temperature, T_m, where it melts and turns to a viscous liquid. In practise perfectly crystalline polymers are rarely seen and instead semi-crystalline

polymers are found containing areas of both ordered and disordered polymer. In this case both T_g and T_m are observed corresponding to the proportions of ordered and disordered polymer present. As a polymer is glassy below T_g clearly crosslinking has very little effect on the properties of the material other than to increase T_g, however above T_g creep, or polymer flow, can have a serious effect on the uses of polymeric materials. Use of crosslinking in these cases can reduce, or in certain cases eliminate, creep as its response depends mainly on the temperature of the polymer and its crosslink density, hence an increase in crosslink density can lead to a decrease in creep.

Phase separation in cross-linked polymer blends has been of great interest due to the possible technological uses of such systems. Phase separation has been predicted in systems in which two polymers are first cross-linked and then brought into the two phase region[73]. Here two linear polymers are crosslinked in the one phase region of the phase diagram before being quenched into the two phase region. A competition between the process of phase separation and the elasticity of the network that resists the phase separation was then seen. In this case strongly crosslinked systems were considered and good agreement between experiment and theory was observed, however this approach assumed an ideal network with all the linear chains crosslinked. A further study by Bettachy et al.[74] then considered a weakly cross-linked system in which not all the linear polymer chains become crosslinked and phase separation was again seen. Experimentally the structure of blends which have been photo-crosslinked during spinodal decomposition has also been studied[75]. Here 40:60 blends of polystyrene/poly(2-chlorostyrene) were studied and a freezing of the phase separated morphology was seen upon photo-crosslinking with a XeF excimer laser. It was also seen that control over the morphology could be displayed by allowing a greater amount of time before photo-crosslinking; this led to larger morphologies as the spinodal decomposition process was allowed to occur for longer times. The phase behaviour of crosslinked polymers with liquid crystals has also been of interest[76]. The phase diagrams for these systems exhibit a wider variety of properties than that seen in analogous systems containing only linear polymers. It was found that this was reflected in the larger number of parameters describing the thermodynamics and elasticity of the crosslinked network. Clearly as a liquid crystal is present the phase diagram is different to that seen for a linear polymer blend as a

nematic – isotropic region is seen at higher temperatures and liquid crystal volume fractions.

Binder and Frisch[77,78] proposed a method of simulating Interpenetrating Polymer Networks (IPN's) in a weakly cross-linked network. An IPN is composed of two or more chemically distinct cross-linked polymer networks which are prevented from macroscopically phase separating by permanent crosslinks which are produced when each network is cured. As with any polymer blend the formation of an IPN has the potential for combining the properties of the two types of cross-linked polymer networks, however an IPN differs from a homo-polymer blend because either one polymer is cross-linked in the presence of another cross-linked polymer or both polymers are simultaneously cross-linked. This leads to a situation where one network interpenetrates the other and constrains processes such as phase separation. Models were also proposed for a pseudo-IPN or semi-IPN; here one species is a cross-linked network which is swollen by linear polymer chains of a second component. This means that we have a network component with low diffusion and which resists deformation and a linear component which has diffusion properties like those seen in normal linear polymer blends. It is possible to study the effect crosslinking has on systems such as these, using the free energy of an elastically deformed network, given by,

$$\frac{F_{net}}{k_B T} = \frac{\nu(\phi_0)}{2}\left(\lambda_x^2 + \lambda_y^2 + \lambda_z^2 - 3\right) - B\nu(\phi_0)\ln\lambda_x\lambda_y\lambda_z, \qquad (2.5.1)$$

where λ_x, λ_y and λ_z are deformation ratios defined with respect to a reference state in which the chain dimensions are such that there do not exist any elastic forces on the crosslinks. The value of the coefficient B is not well known, with it being absent in certain cases. Flory[3] calculated B to be $2/f$ where f is the functionality of the crosslinks whilst Kuhn[79] wrote B = 1. By considering a uniform deformation such that $\lambda = \lambda_x = \lambda_y = \lambda_z$ which is brought about by changing the volume fraction from ϕ to another value, ϕ_0, we can write,

$$\lambda^2 = \langle r^2 \rangle / \langle r^2 \rangle_\bullet = (\phi/\phi_\bullet)^{-\frac{2}{3}}, \qquad (2.5.2)$$

where $\langle r^2 \rangle$ are the linear dimensions in state ϕ and $\phi_\bullet$ is the hypothetical volume fraction which is chosen, after crosslinking, to eliminate the elastic forces of the crosslinks, where $\phi_\bullet = \phi_\bullet(\phi_0)$. Rewriting equation 2.5.1 with 2.5.2 for a Flory-Huggins lattice the free energy of the network per site is therefore given by,

$$F_{el} = \frac{\phi_i}{N_i}\left[\left(\frac{3}{2}\left(\frac{\phi_i}{\phi_0}\right)^{-\frac{2}{3}} - 1\right) + B\ln\left(\frac{\phi_i}{\phi_0}\right)\right], \qquad (2.5.3)$$

where i is the network component of the polymer blend and N_i is its degree of polymerisation.

Schulz, Binder and Frisch[80,81] investigated phase separation in simultaneously formed interpenetrating polymer networks, here the monomers, cross-linkers, initiators and catalysts for both species are mixed together. The reactions, leading to two simultaneously formed networks, are followed by a quench into the two phase region. A well developed phase transition from the disordered to the ordered phase was observed. Schulz and Frisch[82] also undertook a study into the microphase separation transition (MST), i.e. in gels. We note that in all cases, phase separation and cross-linking reactions were not occurring simultaneously as is the case for RIPS. There have been a large number of experimental studies using RIPS[56,58,83-87], for example morphological control of a semi-IPN undergoing RIPS has been attempted by Kim and An[58]. Linear poly(ethyl acrylate) (PEA) and crosslinked poly(methyl methacrylate) (PMMA) were used and the effect of temperature of polymerisation and the addition of linear PMMA to the initial mixture were studied. Reducing the temperature of polymerisation means that the mobility of the polymer chains is reduced which reduces the rate of phase separation. It was also found that the addition of linear PMMA to the initial mixture helped phase separation to occur during the IPN formation, as the onset of phase separation was shifted towards lower conversion.

2.6 Multi-Component Blends

It is clear that the phase separation of binary polymer blends has been widely studied but fewer studies have been undertaken into phase separation in ternary mixtures. A number of studies have investigated di-block copolymers in the presence of two different homopolymers both experimentally[88-90] and theoretically[91-

[94] where it is found that the block copolymer resides at the interface between the two homopolymers when the system is quenched under the tri-critical point. Investigations have also been undertaken to try and understand the internal wetting in a three component system[95,96]. In multi-component systems Flory-Huggins theory is extended to take account of the interactions between each component[97], giving for a three component A-B-C blend,

$$\frac{f_{FH}(\phi)}{k_B T} = \frac{\phi_A}{N_A}\ln\phi_A + \frac{\phi_B}{N_B}\ln\phi_B + \frac{\phi_C}{N_C}\ln\phi_C + \chi_{AB}\phi_A\phi_B + \chi_{AC}\phi_A\phi_C + \chi_{BC}\phi_B\phi_C,$$

(2.6.1)

where N_i is the degree of polymerisation of component i, when i = A, B or C and ϕ_i is the local composition volume fraction of component i. For these systems the spinodal is given by,

$$\begin{vmatrix} \dfrac{\partial^2 F}{\partial\phi_A^2} & \dfrac{\partial^2 F}{\partial\phi_A\partial\phi_B} \\[3mm] \dfrac{\partial^2 F}{\partial\phi_B\partial\phi_A} & \dfrac{\partial^2 F}{\partial\phi_B^2} \end{vmatrix} = 0,$$

(2.6.2)

where it can be seen that differentiation of 2.6.1 gives,

$$\frac{\partial^2 F}{\partial\phi_A^2} = \frac{1}{N_A\phi_A} + \frac{1}{N_C\phi_C} - 2\chi_{AC},$$

(2.6.3)

$$\frac{\partial^2 F}{\partial\phi_A\partial\phi_B} = \frac{\partial^2 F}{\partial\phi_B\partial\phi_A} = \frac{1}{N_C\phi_C} + \chi_{AB} - \chi_{AC} - \chi_{BC},$$

(2.6.4)

$$\frac{\partial^2 F}{\partial\phi_B^2} = \frac{1}{N_B\phi_B} + \frac{1}{N_C\phi_C} - 2\chi_{BC},$$

(2.6.5)

when ϕ_C = 1 - ϕ_A - ϕ_B due to incompressibility. Numerically solving the determinant of 2.6.2, given by 2.6.6, for various values of ϕ_A and ϕ_B therefore allows a plot of the three component phase diagram to be produced.

$$\left(\frac{\partial^2 F}{\partial \phi_A^2}\right)\left(\frac{\partial^2 F}{\partial \phi_B^2}\right) - \left(\frac{\partial^2 F}{\partial \phi_A \partial \phi_B}\right)^2 = 0, \qquad (2.6.6)$$

This method has been used by Huang et al.[97] in a study of the process of phase separation in a symmetric ternary mixture. During this study it was found that in a ternary system with majority components A and B present the minority component, C, would form at the interface between components A and B. If however component C is the majority component then components A and B form "caterpillar" type structures in a matrix of component C. In the former case however upon domain coarsening the minority phase is seen not to coarsen and can be considered to be purely increasing the interfacial thickness. The growth law of $R \approx \tau^{1/3}$ is however maintained in both the two and three component phase separation processes. The interfacial properties of a three component system have been further studied by Yeung et al.[95] who investigated how the presence of the third phase affected the interface between two other components. It was found that by forming the minority phase at the interface between majority phases the interfacial tension was significantly reduced. This effect was also seen by Liang[93], who used a Monte Carlo simulation, to confirm that a linear decrease of the interfacial tension is indeed seen with copolymer volume fraction. Clearly this effect is important for the production of materials as the properties depend greatly on the strength of the interface between components. By using compatibilisers in the interface between components, like the block co-polymers below, it is possible to tune the properties of the materials. The dynamics of the early stages of the spinodal decomposition process in a system which has an A-B block copolymer in the presence of a linear A and linear B polymers have also been studied[91,98]. Here a Cahn-Hilliard simulation was undertaken to describe the early phase separation stages. The growth rates were again found to be equal to $\tau^{1/3}$ when the hydrodynamic interactions are ignored because the random A-B copolymer acts as a solvent for both linear polymers and therefore does not effect the interdiffusion between them. Finally the interfacial layering in a three component system has been studied[99]. Here a system is set up in which two polymers, A and B, are indifferent to each other, i.e. $\chi_{AB} \approx 0$, but with a third which is strongly attracted to A and repulsed by B. Layered structures were observed at the interface which could clearly lead to interesting material properties,

for example multi-layered films formed purely by diffusional processing. Example morphologies seen when the blend composition in a three component (A-B-C) is altered are shown in figure 2.6,
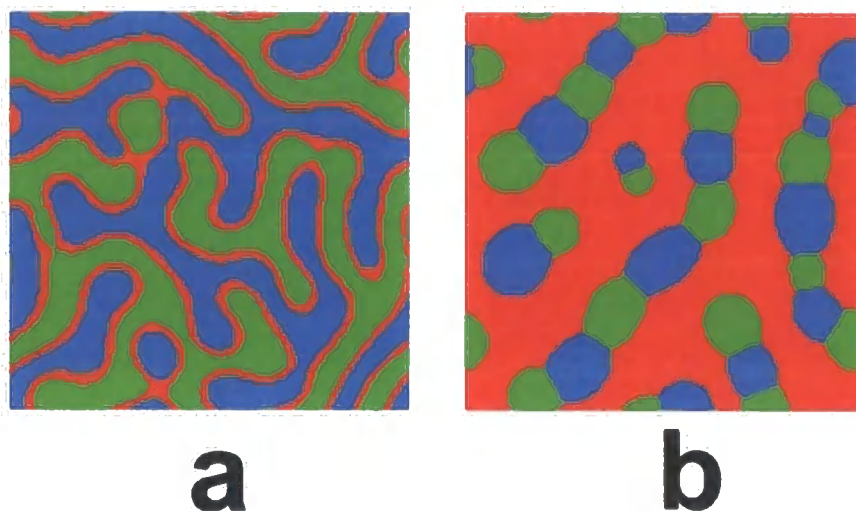

Figure 2.6

Example morphologies when $\chi_{AB} = \chi_{AC} = \chi_{BC} = 0.015$ at $\tau = 1250$ for a three component system where ■ represents component A, ■ represents component B and ■ represents component C with blend composition (a) 40:40:20, and (b) 25:25:50.

In figure 2.6 each value of χ is set to be equal so no two components preferentially "dislike" each other to a greater extent than any other two components do. In figure 2.6(a) we see that component C is the minority component and is therefore seen to form a continuous phase at the interface between components A and B. By increasing the amount of component C within the blend composition it is possible to create a matrix of component C as in figure 2.6(b), here we see small droplets of components A and B forming an alternating "caterpillar" structure in order to reduce the amount of interface with component C.

41

2.7 Polymers at Surfaces

2.7.1 Uniform Hard Wall Surfaces

The affect of a surface on a polymer blend has been extensively studied experimentally[100-103]. This is because in substances such as adhesives and coatings, surface composition plays a highly important role. Jones et al.[101] showed that by using a blend of poly(ethylenepropylene) (PEP) and perdeuterated poly(ethylenepropylene) (d-PEP) which was quenched into the two-phase spinodal region on a silicone wafer it is possible to attain preferential phase segregation of one of the two components of the blend to the surface, in this case the d-PEP, i.e. the surface preferentially attracts one of the components of the polymer blend. The phase rich area at the surface inevitably leads to a phase poor depletion layer just below and a damped oscillating wave with a wavevector normal to the surface dominates the structure development at the surface, therefore the surface wetting behaviour affects the phase separation dynamics at and near to the surface. Ion-beam experiments using ^{3}He nuclear-reaction analysis have been extensively used to depth profile such systems[100,103,104] perpendicular to the surface where the oscillating morphology is seen. Using this method the growth rate of this surface layer has been seen to grow at a rate of $\tau^{1/3}$.

The dynamics of a phase separated polymer blend at or near a surface have also been widely studied theoretically using a method proposed by Jones et al.[105], here a comparison with experimental results from forward recoil spectrometry was made. Using a model proposed by Binder and Frisch[106,107], which is similar to that of Jones, based on the Kawasaki spin-exchange model it is possible to derive the Cahn-Hilliard equation in the bulk with two special boundary conditions which account for the presence of the surface. Numerous theoretical studies[108-112] have been carried out on the process of surface directed spinodal composition. Brown and Chakrabarti[109] found good agreement between their results and those found by experiment[101] as they observed the formation of a damped oscillating wave from the surface into the bulk. The thickness of the surface layer varies as $\tau^{1/3}$ however it has been noted that hydrodynamic effects[110] play a major role in the growth of a surface and can lead to faster growth of the surface layer in the late stages of spinodal decomposition.

Surface segregation has also been proposed[113] for a miscible polymer blend, i.e. a blend in the single-phase region. Here the component with the lower surface free energy will tend to segregate to the surface to lower the overall free energy of

the system. The surface free energy (F_s) and the bulk free energy (F_b) are thought of as two distinct components of the overall free energy, however it has been shown that there is a coupling between F_s and F_b[113]. This coupling accounts for a slower increase in surface excess than expected as χ, the Flory interaction parameter, increases. In experimental studies, a blend of dueterated polystyrene (dPS) and a statistical copolymer poly(styrene-co-4-bromostyrene) (PBrS) is often used[113] as the Flory interaction parameter, χ, can easily be tuned by varying the amount of BrS in the copolymer. The advantage of this blend is that due to the 'tune ability' of the χ parameter it is a good representation of a model blend. PBrS has a higher surface energy than dPS which leads the dPS to segregate preferentially at the surface. The driving force for surface segregation depends not only on the surface parameter but also on the bulk properties of the blend such as χ and χ_c, the Flory interaction parameter at the critical point. The surface excess increases rapidly as χ tends towards χ_c.

The morphology of polymer blends in thin film systems has been of great interest from both the fundamental and technological viewpoints. In, for example, adhesives such as epoxy resins a thin film may occur between two surfaces, here the morphology of the thin film can play an important role in the properties of the adhesive and therefore control of this morphology can be very important. Puri and Binder[112] studied a thin film in which a polymer blend undergoes phase separation between two adjacent surfaces which both preferentially attract the same component. It was found that for a small distance between the two surfaces it is possible to create a system in which layers are formed perpendicular to the surface throughout the system. As the distance between the walls was increased however this structure gave way to the random co-continuous morphology away from the surfaces.

It is noted that the amount of noise (thermal fluctuations) applied during the phase separation simulation will also affect the final morphology of the polymer blend. Using a cell dynamics simulation Marko[114] found that as the noise strength was reduced the surface segregation waves formed out to greater depths in the bulk of the polymer blend and longer times were required for the layered structure to be replaced with disordered spinodal decomposition patterns. The effects of thermal noise on the structure of a phase separated polymer blend have also been studied[24]. It is found that increasing the strength of the noise leads to domains with broader, more diffuse interfaces.

To study the influence of a surface on a polymer blend the model which has been extensively developed by Puri, Binder and Frisch[107,108,112,115-118] is commonly used. The Cahn-Hilliard equation is used to describe the evolution of the concentration in the bulk, but a term representing the surface effect is added, represented by the boundary condition,

$$\frac{\partial \phi(\mathbf{R},\mathbf{0},\tau)}{\partial \tau} = -h_1 - g\phi(\mathbf{R},\mathbf{0},\tau) + \gamma \frac{\partial \phi(\mathbf{R},\mathbf{x},\tau)}{\partial \mathbf{x}}\bigg|_{\mathbf{x}=0} \qquad (2.7.1)$$

where $\mathbf{R}$ and $\mathbf{x}$ are rescaled coordinates parallel and perpendicular to the surface and h_1, g and γ characterise the static surface phase diagram such that at the surface,

$$\phi_{surface} = -\frac{h_1}{g}, \qquad (2.7.2)$$

and γ is related to the correlation length.

The competition between the surface field and the energy cost associated with a gradient in the order parameter creates an equilibrium value of the order parameter at the surface and the above boundary condition is used to pin the surface value to this equilibrium value. A second boundary condition, $\Delta J|_{\mathbf{x}=0} = 0$, where J is the polymer flux, is used to ensure that the flux of the polymer components though the surface boundary is zero, which enforces conservation of the order parameter, where $J \propto \nabla \delta F / \partial \phi$. Typically the first boundary condition, equation 2.7.1, is applied to one surface, at $\mathbf{x} = 0$, and the second boundary condition is applied to two parallel surfaces at $\mathbf{x} = 0$ and $\mathbf{x} = \mathbf{x}'$. All the above variables are rescaled into dimensionless units. For two dimensional simulations, periodic boundary conditions are applied at the $\mathbf{y} = 0$ and $\mathbf{y} = \mathbf{y}'$ surfaces.

Jones[7] developed a method to calculate h_1 and g from experimental variables, in this case the surface tension γ. The surface free energy can be described by[105] starting with a "bare" surface free energy term,

$$f_s^{(b)}(\phi) = -h_1\phi - \frac{1}{2}g\phi^2, \qquad (2.7.3)$$

If the energy of contact between two monomers of A is ε_{AA}, that between two monomers of B is ε_{BB} and therefore the contact energy between a monomer of A and a monomer of B is ε_{AB}. The coordination number of the lattice is said to be z and z' bonds are cut when a new surface is made, this means that the surface energy term can now be written as,

$$\frac{f_s^{(b)}}{k_B T} = \frac{z'}{2k_B T}\left[\phi^2 \varepsilon_{AA} + (1-\phi)^2 \varepsilon_{BB} - 2\phi(1-\phi)\varepsilon_{AB}\right], \qquad (2.7.4)$$

$$\Rightarrow \frac{f_s^{(b)}}{k_B T} = \frac{z'}{2k_B T}\left[\varepsilon_{BB} + \phi(2\varepsilon_{AB} - 2\varepsilon_{BB}) + \phi^2\left(\varepsilon_{AA} + \varepsilon_{BB} - 2\varepsilon_{AB}\right)\right], \qquad (2.7.5)$$

If equation 2.7.5 is compared to equation 2.7.3 we can define,

$$h_1 = \frac{z'}{2k_B T}\left(2\varepsilon_{BB} - \varepsilon_{AB}\right), \qquad (2.7.6)$$

$$g = \frac{z'}{k_B T}\left(2\varepsilon_{AB} - \varepsilon_{AA} - \varepsilon_{BB}\right), \qquad (2.7.7)$$

where surface energies are given by,

$$\gamma_A = \frac{z'}{2}\frac{\varepsilon_{AA}}{b^2}, \qquad (2.7.8)$$

$$\gamma_B = \frac{z'}{2}\frac{\varepsilon_{BB}}{b^2}, \qquad (2.7.9)$$

and b^2 is the surface area of the Flory-Huggins lattice cell. Rearranging equations 2.7.8 and 2.7.9 in terms of ε_{AA} and ε_{BB} and writing ε_{AB} in terms of the Flory interaction parameter,

$$\varepsilon_{AB} = \frac{1}{2}\left(\frac{k_B T \chi}{z} + \varepsilon_{AA} + \varepsilon_{BB}\right), \qquad (2.7.10)$$

gives the coefficients h_1 and g in terms of χ and the surface energy when substituted into equations 2.7.6 and 2.7.7.

45

$$h_1 = \frac{-\chi z'}{2z} - \frac{\Delta\gamma b^2}{k_B T},$$

(2.7.11)

$$g = \frac{z'\chi}{z},$$

(2.7.12)

where $\Delta\gamma$, is the difference in surface energies between the two blend components, given by,

$$\Delta\gamma = \frac{k_B T}{b^3}\left(h_1 + \frac{g}{2}\right),$$

(2.7.13)

This argument however neglects any entropic factors arising from changes of correlations near the surface and from local packing effects so is therefore clearly an approximation.

2.7.2 Pore Confinement

As shown above studies have been undertaken into phase separation in thin films of a polymer at a surface, another interesting area is phase separation in pores or tubes. Here the diameter of the tube can be approximately equal to, or smaller than, the wavelength of the fastest growing wave-vector, q_m in figure 2.1, in the spinodal decomposition process. If this is the case then phase separation cannot occur in the direction perpendicular to the surface and instead only occurs in the direction parallel to the surface, meaning that "plugs" within a tube can form, as schematically shown in figure 2.7.
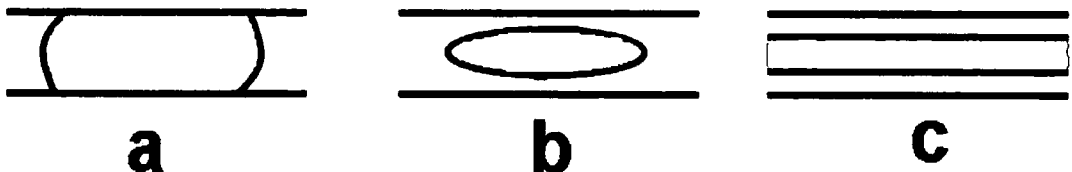

Figure 2.7

Examples of the possible morphologies formed in a pore (a) a plug, (b) a capsule and (c) a tube.

Lui et al.[119-121] first proposed the above possible structures for binary mixtures in a cylindrical pore. In these studies a plug system was first formed in each case and it was found that by changing the attraction strength of the surface for one of the blend components it was possible to move between the plug, capsule and tube morphologies. It was also shown that these effects can be seen in more cases than just a tube with an example of a plug at the point where three tubes meet. Clearly if the change from the plug morphology to the tube morphology could be controlled then this system can be used to create valves within a cylindrical pore. The dynamics of the wetting process were then studied[122-124] with particular attention focused on the role of hydrodynamic interactions within the system. Here it was found that the formation of the wetting layer, the uniform layer formed at the surface shown in figure 2.7(c), depended strongly on the spatial dimensionality of the geometric constraint. A growth exponent of $\tau^{1/3}$ was seen when the pore was very narrow and hydrodynamic effects were suppressed, however upon increasing the pore size it was found that the wetting dynamics were vastly increased as hydrodynamic effects increased the rate of the phase separation process. It is assumed that when the pore size is too narrow the enhanced diffusion seen from hydrodynamic effects cannot occur due to the confinement. Lately the morphologies of block copolymers within a cylindrical pore have been of considerable interest. By confining block copolymers in this way it was found that a number of novel self assembled layered structures[125,126] could be formed which in turn could be controlled by changing the surface attraction. It has been noted however that a change in the block lengths did in itself not change the morphologies seen; however when surface alignment, strong surface interactions, was observed the kinetic rate of the phase separation was increased.

2.7.3 Patterned Surfaces

If the above ideas can be used on a surface which is patterned so that different areas of a substrate are attractive to different components of a polymer blend then many technologically useful materials could be produced. The patterns may also be able to direct chemical transformations, detect molecular recognition events or carry signals which could be useful in biological and medical applications. Another possible use of these systems could be in the area of Polymer Dispersersed Liquid

47

Crystals (PDLC's), here a liquid crystal is dispersed within a polymer matrix. In these systems it is important to create well defined liquid crystal domains which are highly phase separated. Recently the use of chemical patterning to grow polymer brushes on a surface, therefore changing the polymer properties, has become an interesting area of research[127-129]. Here thiols can be used to pattern coated wafers which are then used to grow polymer brushes at the surface changing the surface properties of the wafer. Stamps are used to "print" the chemical onto the wafers, which have been formed using AFM techniques, however focused ion beams have also been used to create these stamps in an attempt to reduce the pattern size[130], here a beam of high energy ions is used to etch lines in a PDMS stamp. It has been suggested that if one component of the blend is a liquid crystal then the brushes grown on the surface should be liquid crystalline polymer brushes[131] and it has been shown that this is possible giving lines which are around 5μm wide. This method has been used to pattern a substrate and then phase separation has been allowed to occur in a blend above this patterned area[132]. A circle pattern was used with a blend of poly(9,9-dioctylfluorene) PFO and poly(9,9-dioctylfluorene-*alt*-benzothiadiazole) F8BT and it was found that by patterning the substrate it was possible to control the phase separated morphology to a high degree[133]. Theoretically these systems have been studied and growth exponents have been explored[133-136]. Once again a growth exponent of $\tau^{1/3}$ is present but if an alternating pattern is used then, due to the phase oscillations perpendicular to the blend, a checkerboard type morphology can form which propagates into the blend to the point at which phase separation becomes dominant.

2.7.4 Dispersed Surfaces

Finally particles can be dispersed in a polymer blend matrix and then phase separation can be allowed to occur around the particles. Immobile spherical nanoparticles[137,138] and rods[139] have been used and domain growth has been seen to be promoted due to the surface effects giving morphology control if the particles are correctly placed. It is clear that a system such as this can be used to promote a rich diversity of new morphologies and therefore potentially new materials.

2.8   Block Copolymer

No review of current research into polymer blends would be complete without an introduction to the work being carried out in the area of block copolymers, the amount of research undertaken on this matter is vast and therefore it is impossible to describe it all here. Pioneering work in the area of block copolymer morphologies was carried out by Bates[140] who first described the morphologies seen in block copolymer blends in the well known diagram shown below:
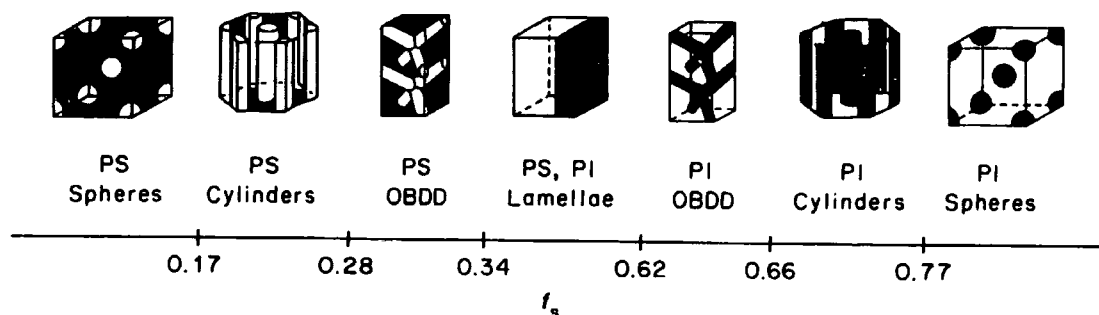
PS	PS	PS	PS, PI	PI	PI	PI
Spheres	Cylinders	OBDD	Lamellae	OBDD	Cylinders	Spheres

0.17   0.28   0.34   0.62   0.66   0.77

f_s

Figure 2.8[140]

Effect of varying composition on the morphology in a polystyrene-polyisoprene (PS-PI) diblock copolymer where f_s refers to the volume fraction of PS.

Figure 2.8 shows the various morphologies present in a diblock copolymer blend as the volume fraction of the polystyrene increases. The morphology moves from a spherical structure at low PS volume fraction to a cylindrical structure then a gyroid (OBDD) structure and then finally to a lamellae structure. By further increasing the volume fraction we see that the "matrix" now becomes the lesser component and the sequence is reversed. The phase diagram for such a system is shown below.

Spheres (BCC)   Cylinders (HEX)   Gyroid (GYR)   Lamellar (LAM)
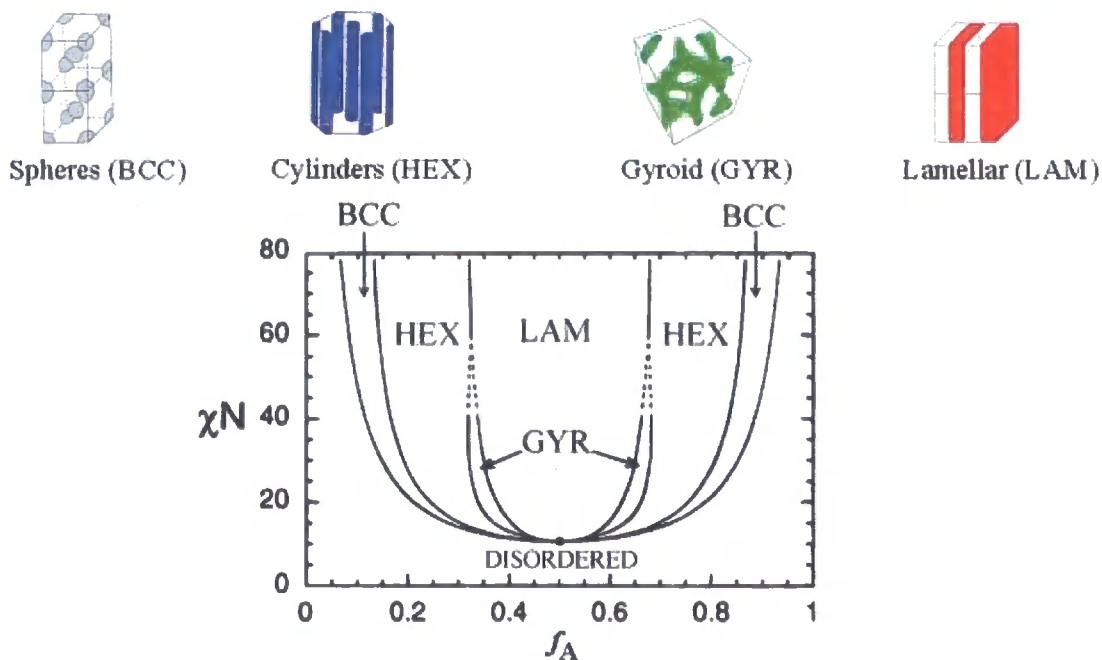
Figure 2.9

Phase diagram for a diblock copolymer blend.

Figure 2.9 shows the areas of the phase diagram which lead to each morphology, it can be seen that the area for the gyroid structure is very small with the lamellar and cylinder structures being the most easily seen. The interesting structures shown above have led to a great interest in to research in the area of block copolymers as these highly order structures can lead to interesting applications.

The first studies into block copolymers were focused on examining the effects of adding a small amount of block copolymer into a binary blend, here the block copolymer is expected to reside at the interface and compatibilise the system. Hashimoto[88,89] studied the kinetics in such a system and found that the interfacial tension between the two polymeric components was affected by the addition of small amounts of copolymer however it was noted that on changing the amount of copolymer the kinetics remained constant throughout the system. It can be seen that this sort of compatibilisation can be used to improve properties by increasing the strength of polymer blend interfaces. Recently however there has been considerable interest in blending nanoparticles with diblock copolymers, here hard walled particles are placed in a polymer blend, as in 2.7.4, but here the blend is formed using diblock copolymers[141,142]. The reason for making use of block copolymers in these systems is that, as seen above, more structures can be formed which can be better controlled and which self assemble into useful morphologies. These materials

can then be used as templates for organic and inorganic devices such as photonic band gap devices. The thermodynamic behaviour of these polymer systems has been studied[143] and elegant new morphologies have been seen. When the particle size was comparable to the radius of gyration of the minority block the particles preferentially attracted this block and three layer micelles are seen with a particle-rich inner layer with an A-block layer followed by a B-block outer layer. Other two and three dimensional morphologies have been proposed[144] which depend on the size of the particles used and can form sheets, wires and dots. These systems therefore clearly have possible applications in polymer wires, circuit boards and photonic devices as a very ordered array structure is seen. By varying the size of the particles the morphology of the system can be changed[145] and therefore the mechanical properties of the material are effected. It has been shown[145] that smaller particle sizes lead to greater clustering of the particles and can lead to, for example, increased stiffness throughout the material.

Chapter 3

The Phase Separation Process

In the following chapter a description of the basic model used in the simulations, and examples of the different morphologies produced, are shown. Also an introduction is made to the one of the main methods used to study the dynamic growth of phase separation in polymer blends, the structure factor. For clarity intended for the reader from this point onwards ϕ_A is referred to as ϕ and ϕ_B is referred to as $1-\phi$.

3.1 The One Dimensional Model

The first step when creating a model to understand the properties of the phase separation process is to create a one dimensional system, this is then used as a starting point for all the following work as it is conceptually the easiest to understand. In this initial model a one dimensional array is created of length x. Values corresponding to the volume fraction of one of the components, ϕ, are then assigned to each position of the array at the start of the simulation, as shown in figure 3.1.

0.5	0.5	0.5	0.5	0.5	0.5	0.5	0.5	0.5	0.5	0.5	0.5	0.5	0.5	0.5	0.5	0.5

Figure 3.1

Example of an initial array used for a one dimensional phase separation simulation.

Noise is first added to the system to account for the Cook[16] term and then the finite difference scheme shown in equation 1.3.11 is solved for each array element in turn. The noise is calculated to obey,

$$\langle \varepsilon(\mathbf{r},\tau), \varepsilon(\mathbf{r}',\tau') \rangle = -\nabla^2 \delta(r-r')\delta(\tau-\tau'), \qquad (3.1.1)$$

By using equation 3.1.1 a more random spread of numbers is found than when just using the random number generator, in this case, taken from Numerical Recipes in Fortran 90[146], on its own. This linear congruency generator uses a mathematical algorithm to move from one random number to the next and a random

seed is stored at the end of each simulation to ensure that the random number generator starts its calculation from a different point each time. To satisfy equation 3.1.1 it is necessary to generate two random numbers for each array position and then use equation 3.1.2 to generate a third number, therefore improving the statistical distribution of the random numbers, for example in the two dimensional case[24],

$$noise = (v_1(i+1, j) - v_1(i, j) + v_2(i, j+1) - v_2(i, j)), \qquad (3.1.2)$$

where v_1 and v_2 are random numbers, between -1 and 1, for each array position, addressed by i and j. This noise value is then multiplied by a noise magnitude, i.e. 0.001, to give a final noise value in the range ±0.001.

Periodic boundary conditions are used to model an array of infinite size, here the array is allowed to 'wrap' itself around from element $x = 1$ to element $x = x$. The system is then allowed to evolve in the two phase region. This involves setting χ in equation 1.3.11 to be equal to χ_s, the value of χ on the spinodal, and χ_f is the point to which the system is quenched. This method mimics a system which undergoes a temperature quench from a point on the spinodal line to a point inside the two phase region, defined by χ. An example of this system is shown below, here the system has an array size of 128 array elements, although not all are shown to increase clarity, with initially $\phi = 0.5$. A symmetric blend is used with $N_A = N_B = 200$ with $\Delta\tau$ and Δx from equation 1.3.11 set to be 0.01 and 0.5 respectively. In this case initially $\chi = 0.01$ and the system is quenched to $\chi = 0.0119$.
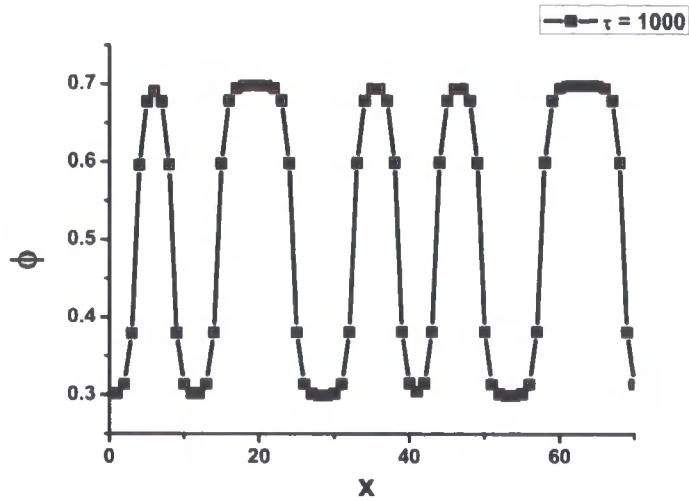
Figure 3.2

Morphology found in a 1D simulation at $\tau = 1000$.

Figure 3.2 shows an example morphology for component A at $\tau = 1000$, where τ = number of computational steps * $\Delta\tau$, and in figure 3.2 x is the array size. We see a periodic structure has formed with coexistence values of $\phi' = 0.3$ and $\phi'' = 0.7$. It is possible to follow the growth of this structure with time,
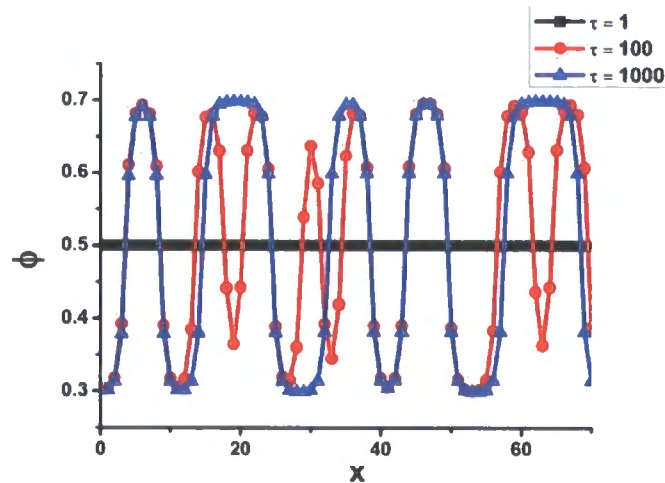

Figure 3.3

Growth of the morphology with time for three values of τ.

In figure 3.3 we see very little structure at $\tau = 1$ but after greater phase separation we see an oscillating structure formed which then broadens with time at $\tau = 1000$. This process can be characterised by using the structure factor, given by

54

equation 1.3.14; this is the Fourier Transform of the array with time and is shown in figure 3.4.
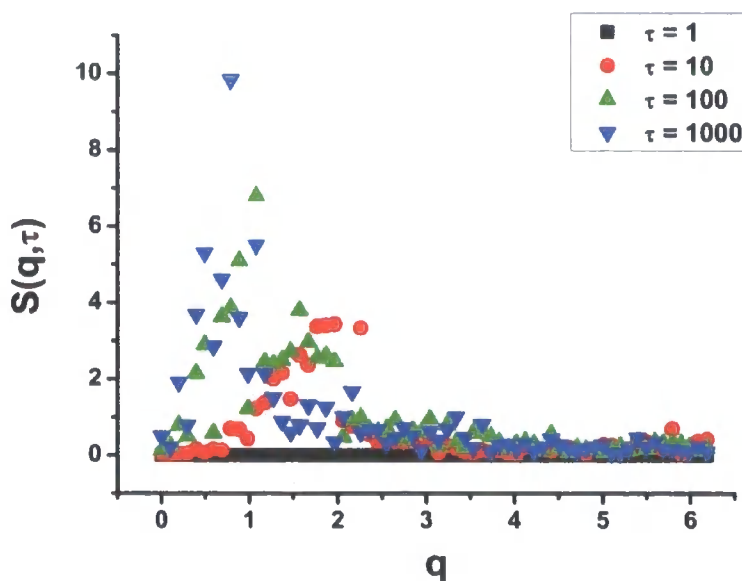
Figure 3.4

Growth of the structure factor with time

where **q** is a dimensionless variable which corresponds to the experimental quantity,

$$\mathbf{q} = \frac{\overline{q}\sqrt{(\chi_f - \chi)}}{b}, \qquad (3.1.3)$$

and $\overline{q} = \dfrac{2\pi}{b\Delta\mathbf{x}}$.

In figure 3.4 the peak in the structure factor grows and shifts to lower **q** with time. As stated above $\mathbf{q} \propto 1/\lambda$ so the shift of the peak to the left in figure 3.4 indicates a broadening of the phase separated morphology.

3.2   The Two Dimensional Model

Although the one dimensional model can be used effectively to study the process of phase separation it is useful to extend the model to the two dimensional case. The method used for the one dimensional model is followed with the addition of periodic boundary conditions on the **y** axis.

55

3.2.1 Radial Averaging

When a two dimensional simulation is undertaken the structure factor is calculated using a two dimensional Fast Fourier Transform (FFT) and can be compared to the scattering pattern found from Small Angle Light Scattering (SALS). A comparison of a SALS scattering pattern and the two dimensional Fast Fourier Transform is shown below,

(a)   **(b)**
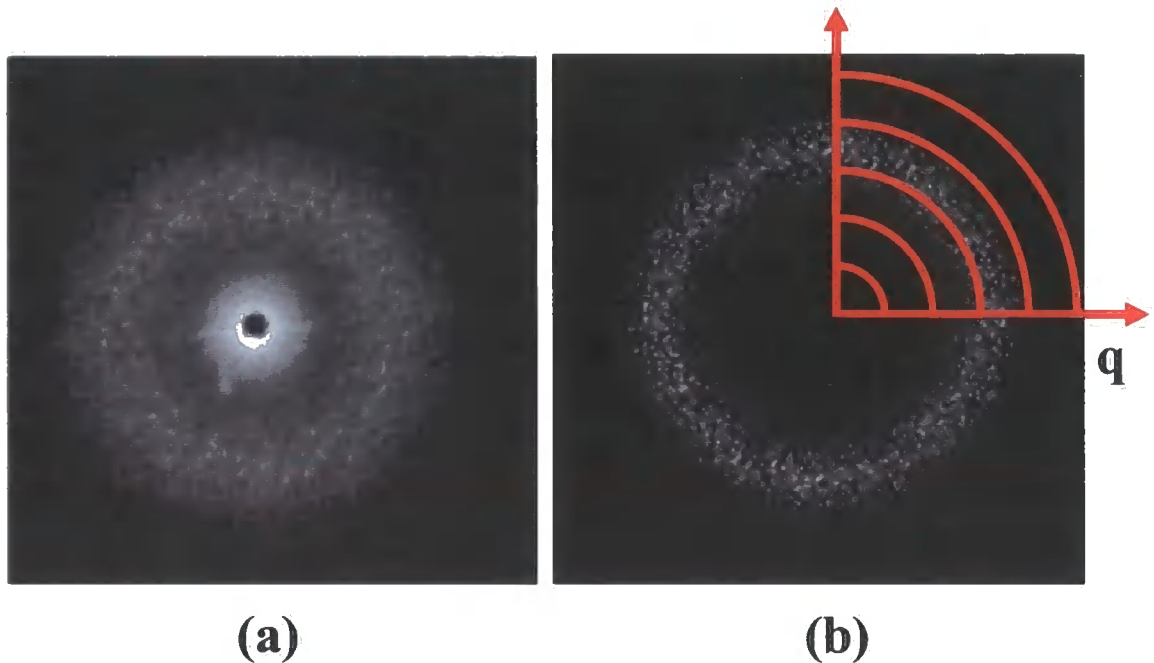
Figure 3.5

Comparison of scattering patterns from (a) a SALS experiment[147] and (b) a two dimensional Fast Fourier Transform, also shown is the radial averaging array.

A comparison of figures 3.5(a) and 3.5(b) shows similar scattering patterns in each case, however the two dimensional scattering patterns needs to be converted into the one dimensional structure factor, this is done by radial averaging which is the method used both experimentally and theoretically. Radial averaging may be performed since the structure factor depends only on the magnitude of **q**, this is a consequence of the phase separation being isotropic. The process of radial averaging has been graphically described in figure 3.5(b), here 5 'radial bins' can be seen along the **q** axis, within each bin the magnitude of each point is considered and is added to the total bin value. This 'binning' method gives a number of bins with values corresponding to the sum of the magnitude of each point within the bin, therefore

giving a one dimensional representation of the frequency of each bin along the **q** axis.

3.2.2 Examples of Quenches into the Two Phase Region

Firstly an example of the morphology formed when a 50:50 symmetric ($N_A = N_B$) blend, as shown in figure 1.3, is quenched from a point on the spinodal, $\chi = 0.01$, to a point in the two phase region, $\chi = 0.0133$, is shown. The simulation is carried out on a 128^2 array with $\Delta\tau = 0.0001$ and $\Delta x = 0.25$ with a noise value of ± 0.001 added once at the start of the simulation.
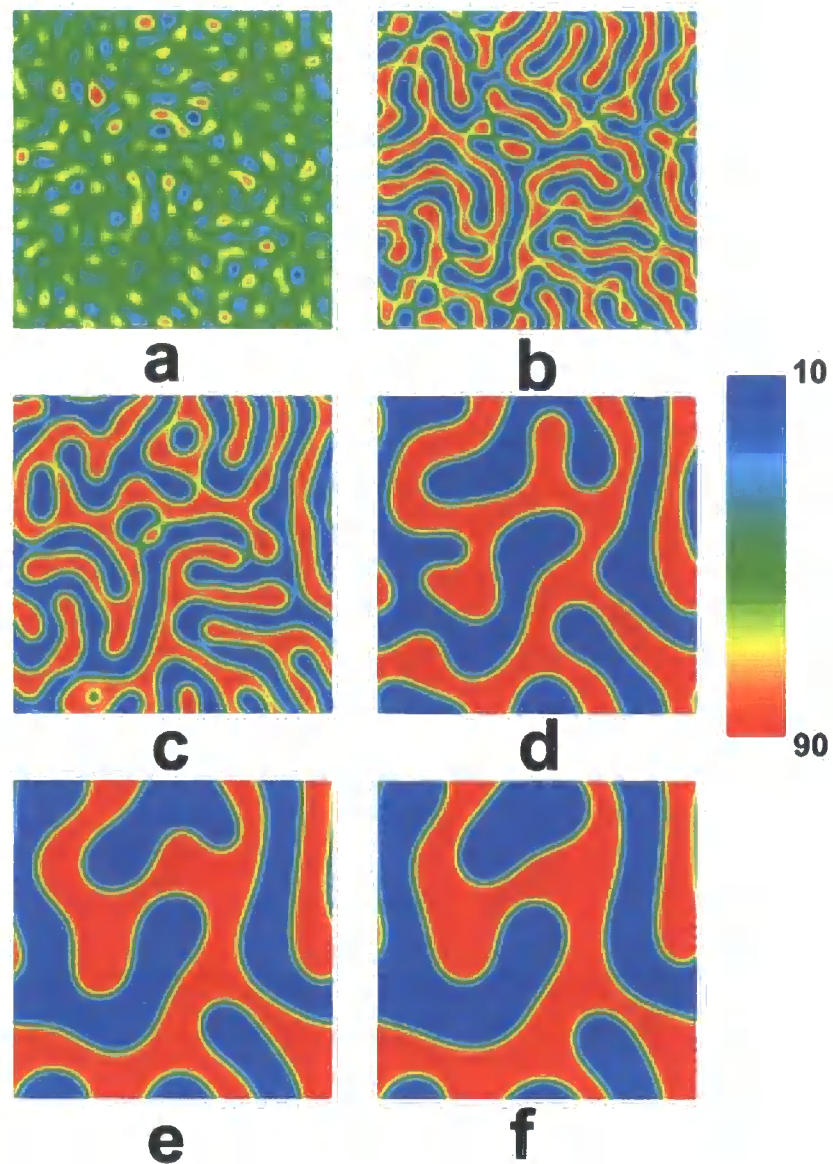
Figure 3.6

Spinodal decomposition in a 50:50 symmetric blend at (a) $\tau = 1$, (b) $\tau = 5$, (c) $\tau = 10$, (d) $\tau = 50$, (e) $\tau = 100$ and (f) $\tau = 150$. Extra colours have been added to improve picture contrast with the maximum and minimum phase concentration shown in the legend.

From figure 3.6 we see that at small τ, phase separation results in domains with coexistence volume fractions of $\phi' = 0.1$ and $\phi'' = 0.9$, as shown in the legend. As the simulation progresses however it can be seen that the small co-continuous domains aggregate together and domain broadening occurs, this reduces the overall free energy of the system and is therefore a favourable process. The phase separation

and domain growth process is followed using the structure factor, found as described above and shown in figure 3.7.
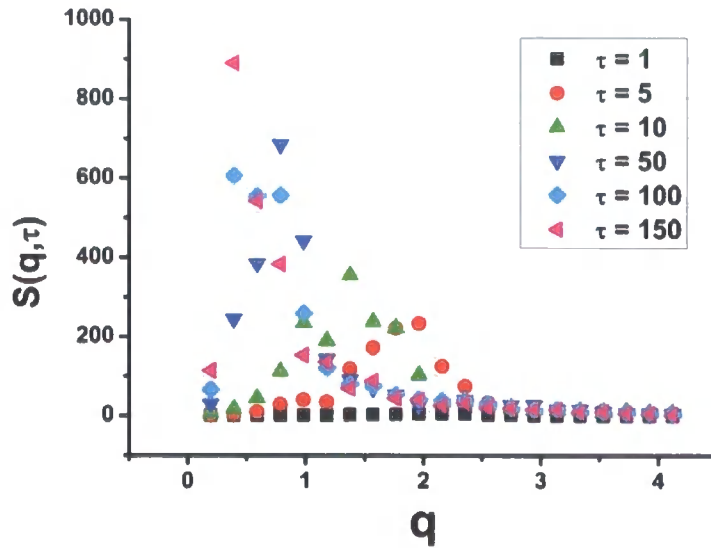
Figure 3.7

Growth of the structure factor at various times as shown in the legend and corresponding to the morphologies in figure 3.6.

The main structure factor peak can be seen to increase in magnitude and shift to smaller q with time, the shifting to lower q of $S(q,\tau)_{max}$, the maximum of the structure factor peak, indicates domain broadening is occurring. The change in the value of $S(q,\tau)$ is a consequence of the phase separation process. To further illustrate the process of domain broadening a comparison of typical morphologies taken from the same simulation, at two different times, after a quench is also shown in figure 3.8.
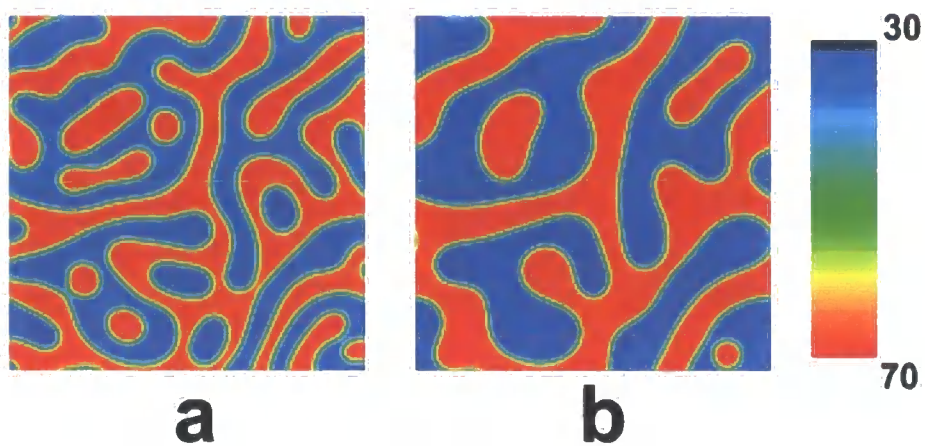
Figure 3.8

Comparison of domain size at (a) $\tau = 2500$ and $\tau = 7500$ on a 256^2 array.

In the above simulation a co-continuous structure is formed as equal amounts of each component are present, however figure 3.8(b) has had a greater amount of time to undergo domain broadening to reduce the overall free energy and therefore larger domains of each component are present when compared to figure 3.8(a). If however a 70:30 blend is used, so we have a greater volume fraction of one component than the other, then a droplet morphology is seen in figure 3.9.
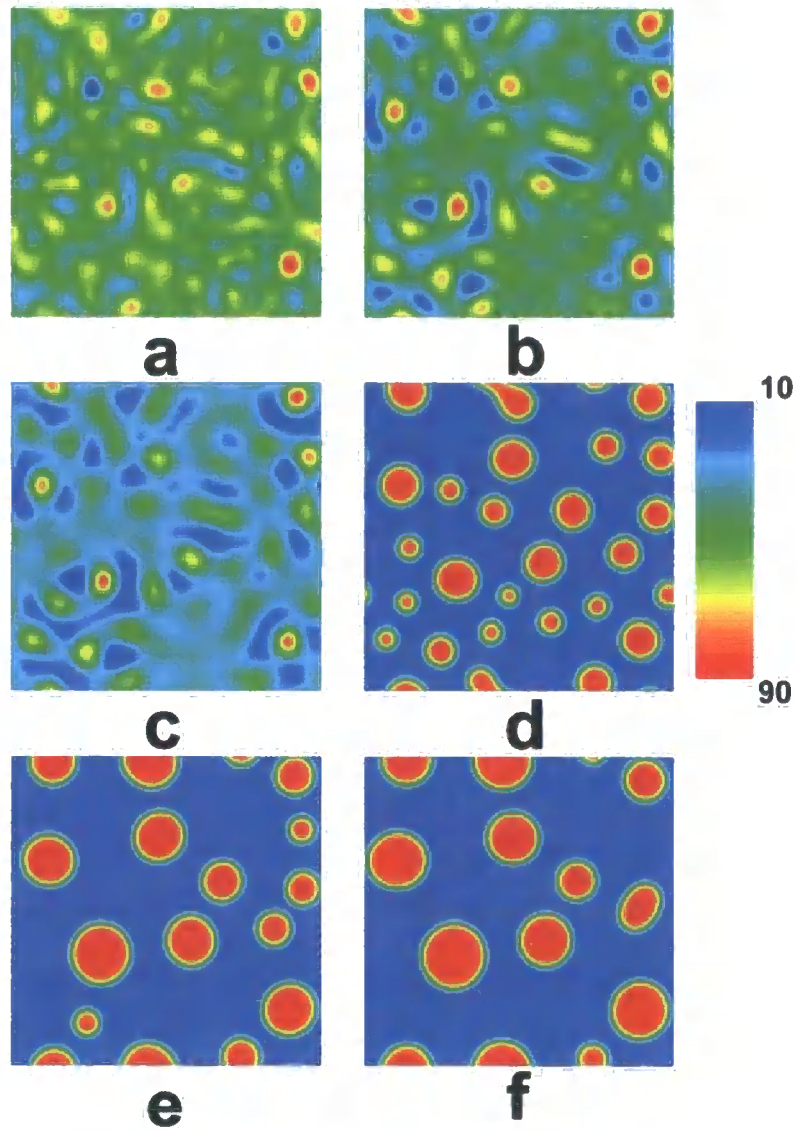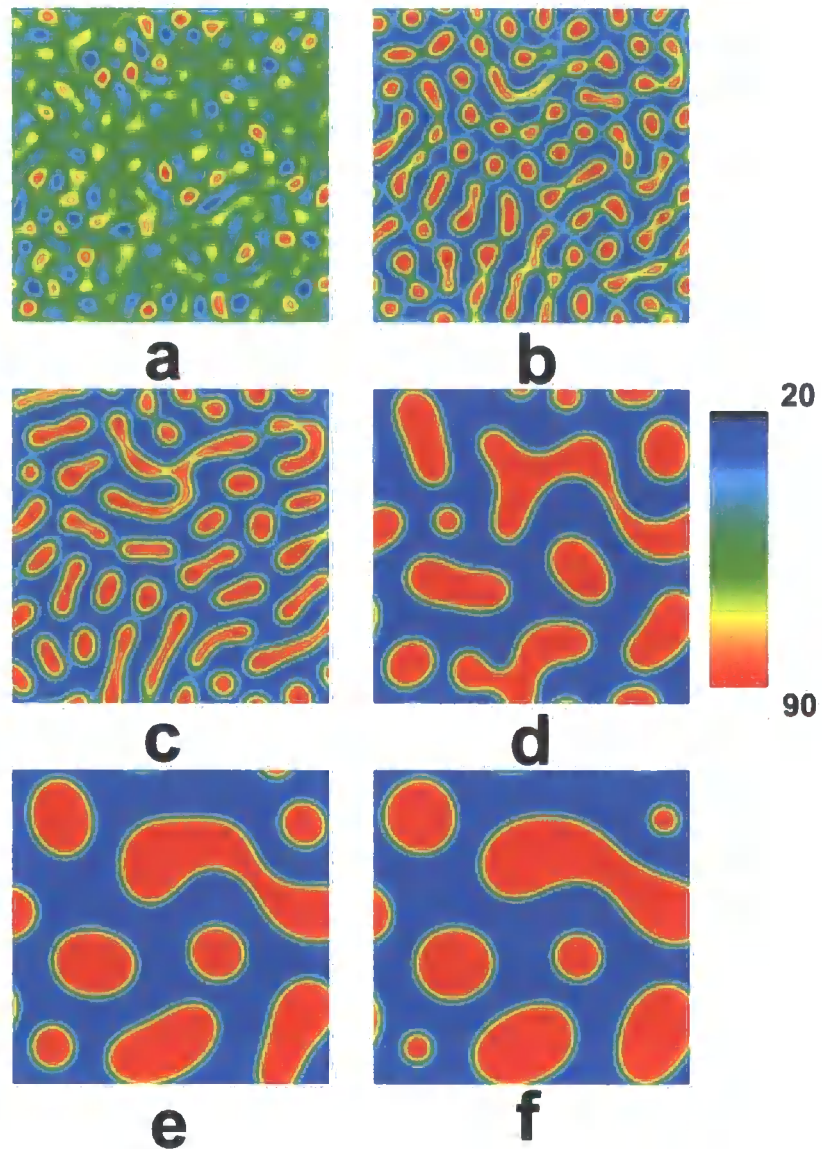
Figure 3.9

Spinodal decomposition in a 70:30 symmetric blend at (a) $\tau = 1$, (b) $\tau = 5$, (c) $\tau = 10$, (d) $\tau = 50$, (e) $\tau = 100$ and (f) $\tau = 150$.

In this system $N_A = N_B = 200$ and the blend is again quenched from the spinodal, $\chi = 0.0119$, to $\chi = 0.0133$ such that $\phi' = 0.1$ and $\phi'' = 0.9$ with $\Delta\tau = 0.0025$, $\Delta x = 0.5$ and a noise value of ± 0.001. Here we again observe domain broadening; however droplets are formed as this structure creates the smallest amount of A-B interface. Again the structure factor can be plotted for a number of different times and its maximum is again seen to grow and shift to lower $\mathbf{q}$ with time indicating phase separation and domain broadening. Note that although the structure is droplet

like the underlying length-scale from spinodal decomposition is retained as highlighted by the existence of the peak in the structure factor in figure 3.10.
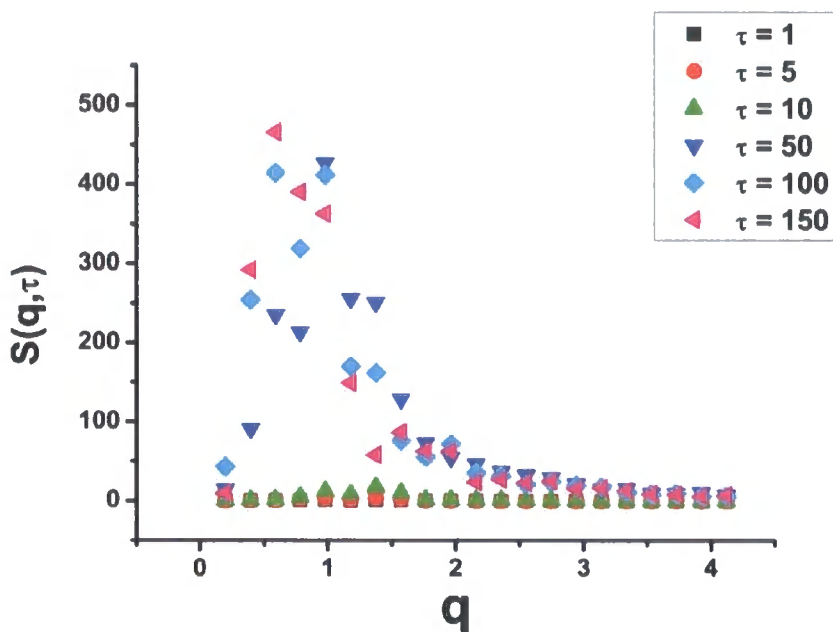
Figure 3.10

Growth of the structure factor at various times as shown in the legend and corresponding to the morphologies shown in figure 3.9.

An example of a quench in an asymmetric system is also shown, here $N_A \neq N_B$ so a phase diagram such as that seen in figure 2.2 is present and for easy comparison with the results for a symmetric blend a 50:50 composition is again used. Here $N_A = 200$ and $N_B = 400$ and a quench from the spinodal, $\chi = 0.00625$, to $\chi = 0.0108$ is undertaken. Once again $\Delta\tau = 0.0025$ and $\Delta x = 0.5$ with a noise value of ± 0.001 is added at the start of the simulation and the results are shown in figure 3.11.

Figure 3.11

Spinodal decomposition in a 50:50 asymmetric blend at (a) $\tau = 1$, (b) $\tau = 5$, (c) $\tau = 10$, (d) $\tau = 50$, (e) $\tau = 100$ and (f) $\tau = 150$.

The equilibrium compositions in this case depend on the binodal curve and as stated in equations 1.1.7 and 1.1.8 in a system such as this, where $N_A \neq N_B$, the curve is found by equating the chemical potentials in each phase, i.e. $\mu_A' = \mu_A''$ and $\mu_B' = \mu_B''$. By comparison with figure 3.6 it can however be seen that the co-continuous structure present in that example is not apparent in the current case. Here phase separation occurs to $\phi' = 0.2$ and $\phi'' = 0.9$ with the volume in each case being given by the lever rule, equation 2.1.1. This means a droplet type structure once again forms as the volume fraction of each phase is not equal, however a comparison of

figures 3.9 and 3.11 shows that the structures are very different as we do not have a simple case of differing volume fractions. Once again domain broadening is observed as the system attempts to reach its minimum energy state and the structure factor can be plotted, as shown in figure 3.12.
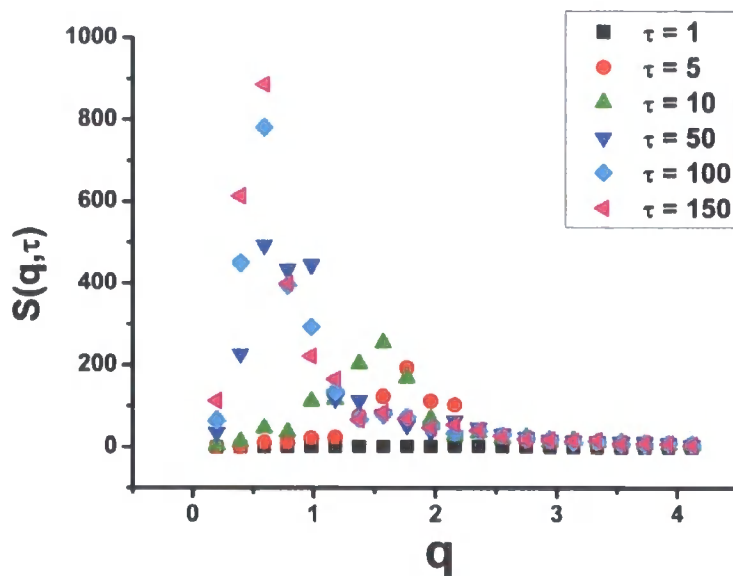

Figure 3.12

Growth of the structure factor at various times as shown in the legend and corresponding to the morphologies shown in figure 3.11.

In this case the maximum in the structure factor is again seen to grow and shift to lower **q** as an indication of the phase separation and domain broadening processes.

Chapter 4

Multi-Step Quenches into the Two Phase Region

The phase separation process shown in chapter 3 has been extensively studied in great detail for many years and is therefore not investigated further here. The model in chapter 3 is now used as a basis for all the following work. As described in chapter 2.2 theoretical work on a multi-step quench process, such as that shown in figure 2.4, is very limited and will therefore be considered in greater detail in the following study.

4.1   Two-Step Quench Process

Firstly the elegant and ordered morphologies formed in a two step quench system are studied. In this system we define three values of χ, initially that on the spinodal, T_0 in figure 2.4, is defined as χ_0. We then quench to the point T_1, defined as χ_1 in this system. The simulation is then allowed to equilibrate for two different lengths of time before being thrust further into the two phase region to the point χ_2, as shown in figure 2.4. To keep the length scaling of the system consistent throughout the simulation equation 1.3.11 is re-written as,

$$\phi_{ij}^{m+1} = \phi_{ij}^{m} + \frac{\Delta\tau}{2(\Delta x)^2} \sum_{nn} \left[\frac{1}{N_A(\chi_f - \chi_0)} \ln\phi_{ij}^m - \frac{1}{N_B(\chi_f - \chi_0)} \ln(1-\phi_{ij}^m) - \frac{2\chi}{\chi_f - \chi_0}\phi \right.$$
$$\left. + \frac{(2\phi_{ij}^m - 1)}{36(\phi_{ij}^m)^2(1-\phi_{ij}^m)^2(2\Delta x)^2} \prod_{nn}\phi_{ij}^m - \frac{1}{(\Delta x)^2}\left(\frac{1}{18\phi_{ij}^m(1-\phi_{ij}^m)}\right)\sum_{nn}\phi_{ij}^m \right],$$

$$(4.1.1)$$

such that χ (appearing in the third term in the summation on the right hand side of equation 4.1.1) is either χ_1 or χ_2 depending on the quench being undertaken.

4.1.1   The Initial Quench into the Two-Phase Region

The first quench was undertaken from $\chi_0 = 0.01$ to $\chi_1 = 0.0104$, with structural evolution being allowed until two different quench times, $\tau_1 = 2500$ and 7500. In each case a well defined initial structure develops, and then a second

quench was applied to three different χ_2 values of 0.0133, 0.0125 and 0.0119. To determine structure factors, each result was averaged over 10 runs and the only case studied was the symmetric case ($N_A = N_B$). These values of the interaction parameters were chosen to allow an exploration of a similar region of the phase diagram to that studied by Hashimoto et al.[43]. Whilst the values of their interaction parameters ($\chi_s = 0.00145$, $\chi_1 = 0.00151$ and $\chi_2 = 0.00175$) differ from the values here, these parameters were chosen for computational convenience and to achieve similar values of the equilibrium coexistence compositions at the first and second quench depths. The work was carried out on a 256^2 two dimensional lattice using periodic boundary conditions, the initial concentration of the matrix was set as $\phi = 0.5$ with an initial random noise of ± 0.01 applied at the start of each quench. The $\Delta\tau$ (time step) value used during the temporal discretisation was 0.0025 and the spatial discretisation was $\Delta x = 0.5$. To keep the length scaling of the system consistent χ_f was fixed throughout the simulation, such that $\chi_f = \chi_2$, as seen in equation 4.1.1. This choice of scaling ensures that the lattice size is fine enough to capture the relevant phase separation length scales during both the first and second quenches and also avoids the phenomenon of pinning, as described previously. The degree of polymerisation was chosen such that $\chi_c = 0.01$ for all simulations during both the primary and secondary quenches.
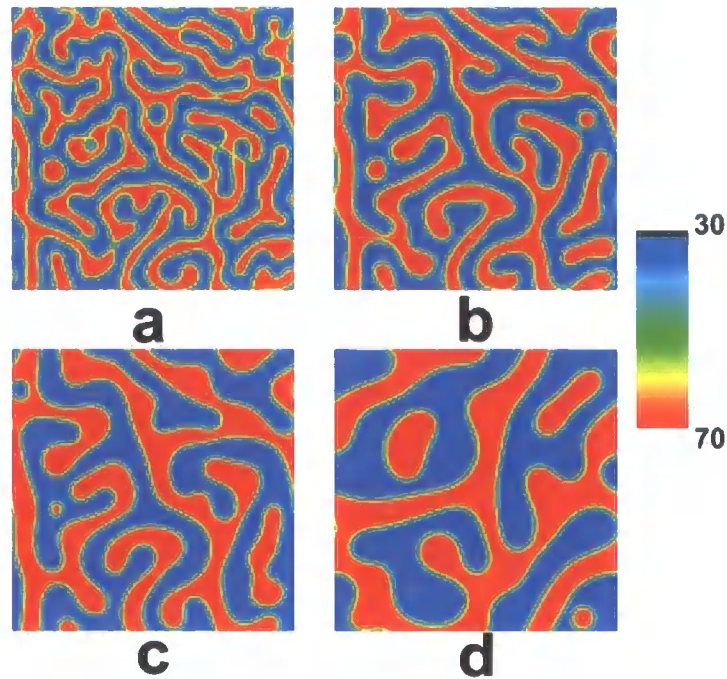
Figure 4.1

Development of the morphology following a quench into the two phase region with $\chi_1 = 0.0104$. Quench times after the quench are (a) $\tau_1 = 625$, (b) $\tau_1 = 1250$, (c) $\tau_1 = 2500$ and (d) $\tau_1 = 7500$. The initial conditions (random noise) were different for (c) and (d); hence, the structure in (d) is not simply a coarsened version of the structure in (c).

In figure 4.1(a) - (c) a series of snapshots can be seen which show the growth and broadening of two domains from the single-phase polymeric mixture into a two-phase system. Due to symmetry the structures exhibit the characteristic co-continuous morphology.

The quench depth corresponds to an equilibrium morphology with $\phi' = 0.33$ in the B-rich phases, and due to symmetry, $\phi'' = 0.67$, in the A-rich phases. Figures 4.1(c) and 4.1(d) show a comparison of the typical morphologies for the two different times at which the second quench was applied. The equilibrium composition within each phase has been reached by $\tau_1 = 625$.

As already noted, the growth process can be quantified by determining the evolution of the structure factor with quench time, as shown in figure 4.2,
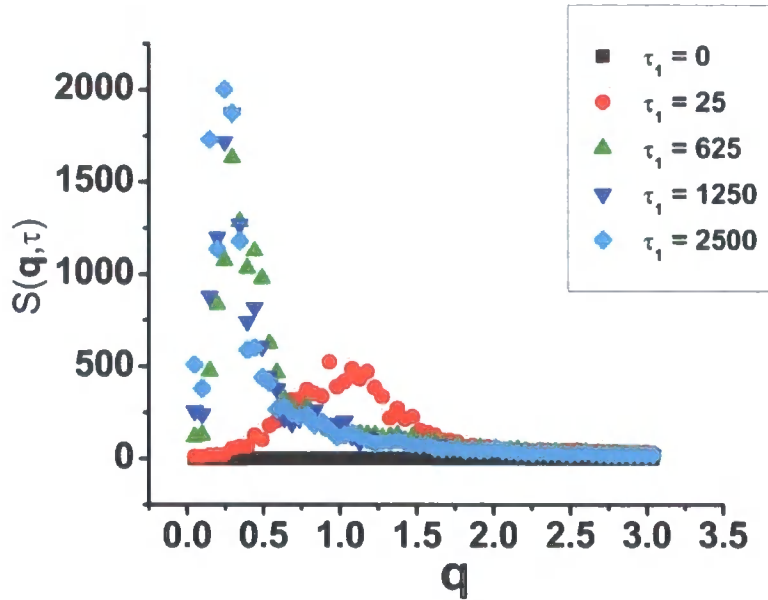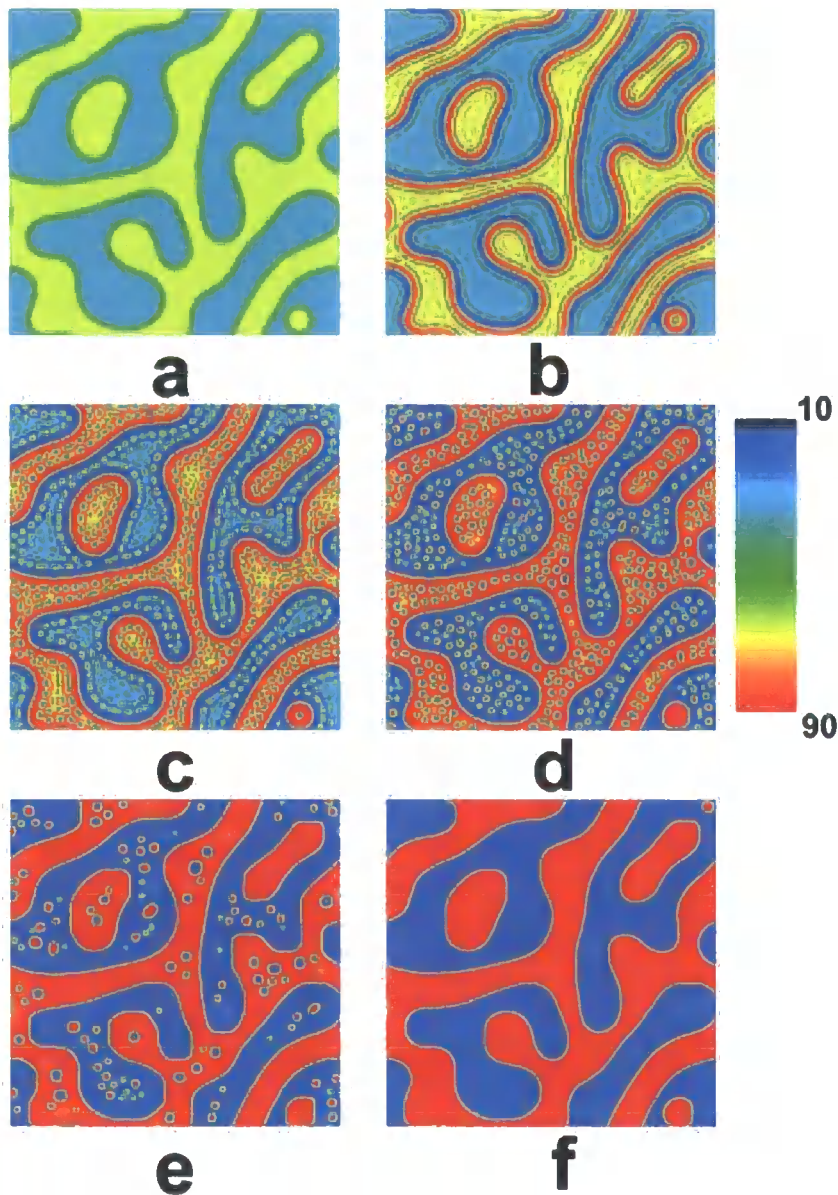
Figure 4.2

The radially averaged structure factor, $S(q,\tau)$ vs. q for several values of τ_1 and $\chi_1 = 0.0104$.

From figure 4.2 we see that at $\tau_1 = 0$ negligible structure is present since the system is still homogeneous, but as the morphology develops and broadens with quench time, the structure factor increases in intensity with a particular wave vector dominating (q_{max}), and as expected the position of q_{max} decreases with quench time. The results thus far have previously been considered in detail by a number of authors[15] and in the previous chapter; hence the single quench case will not be discussed further.

4.1.2 Second Quench into the Two-Phase Region

The second step was carried out to three different quench depths, $\chi_2 = 0.0133$, 0.0125 and 0.0119, and was again averaged over 10 runs in order to determine the structure factor. An example of the domain growth can be seen in figure 4.3.
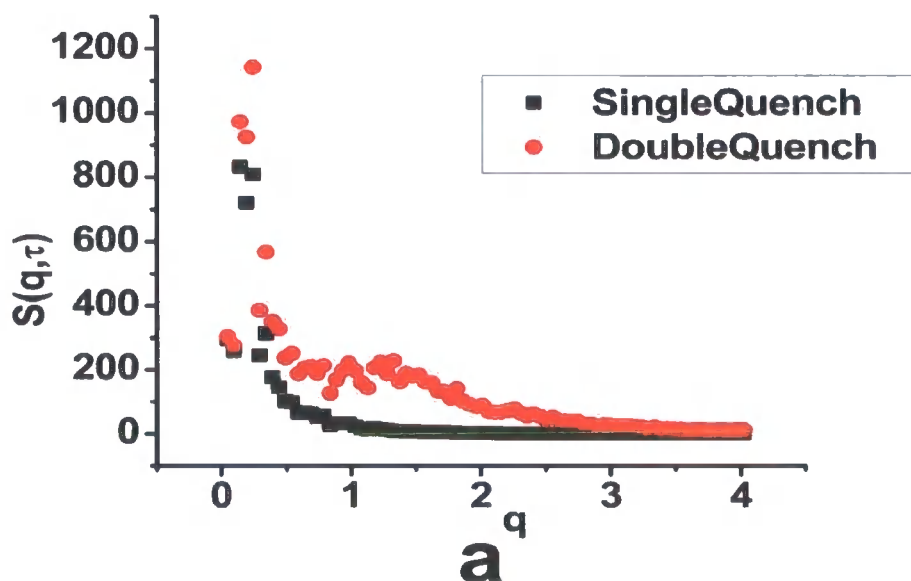
Figure 4.3

Development of the polymer morphology following a second quench into the two phase region with $\chi_2 = 0.0133$. Quench times after the second quench correspond to (a) $\tau_2 = 0$, (b) $\tau_2 = 3.75$, (c) $\tau_2 = 6.25$, (d) $\tau_2 = 12.5$ (e) $\tau_2 = 50$ and (f) 375.

Note that although experimentally the mobility is temperature and hence quench depth dependent, it is not necessary to explicitly account for this since the time steps are scaled by the mobility. Hence the difference between mobility during the first and second quench can be reflected in a different scaling factor from

numerical time to real time for each of the two stages. Importantly, the structural growth is not affected by this assumption.

As the simulation proceeds, small secondary domains of each polymer appear in the larger primary domains. This is a consequence of the initially favoured lengthscale (the fastest growing fluctuation), as determined from linearised theory, being smaller than the primary structural scale. Although these secondary domains are initially dynamically favourable, they 'dissolve' into the surrounding phases since they create large interfacial areas and a large increase in free energy. The structure in figure 4.3(c) is particularly noteworthy: not only are the secondary domains strongly phase separated, the droplets are apparently regularly spaced (as revealed quantitatively by the scattering maximum from the interference of the scattering from secondary domains). This highlights the possibility of using such quench sequences to develop regular morphologies that may have unusual physical properties. Eventually, the original morphology is returned but with concentrations of $\phi' = 0.1$ and $\phi'' = 0.9$. This is clearly seen by comparing figures 4.3(a) and 4.3(f); the structures are very similar but the contrast between phases has increased. The point at which the second quench step is started to the point at which the original morphology (i.e. no secondary structure) is returned depends on quench depth. The deeper the depth of the quench the longer it takes to return the morphology to its original state. If the primary morphology is broader then more time is needed to return to this original morphology.
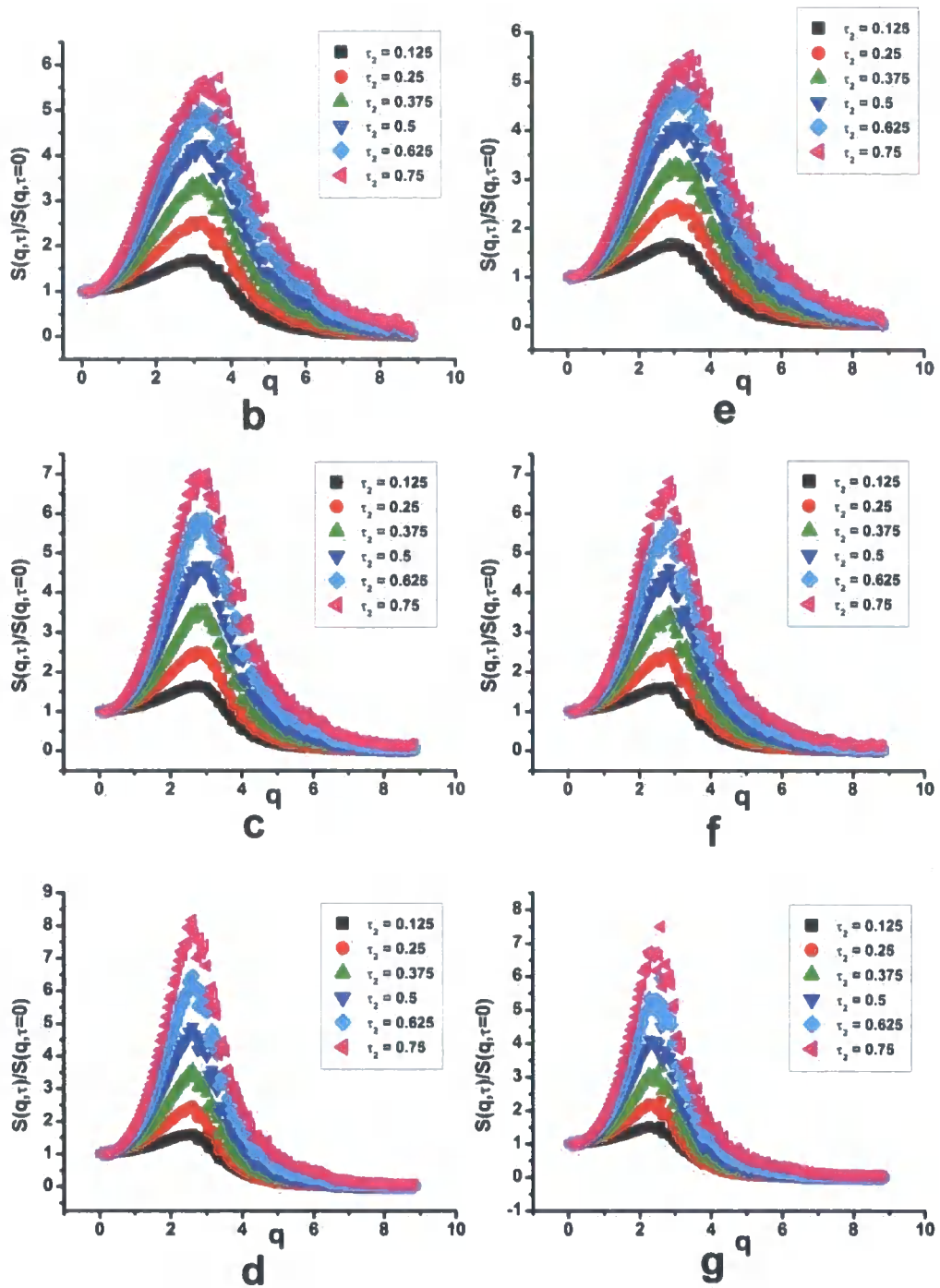

a

Figure 4.4

Development on the structure factor: (a) a comparison of $S(\mathbf{q})$ immediately prior to the second quench at $\tau_2 = 0$ and at $\tau_2 = 12.5$, for $\chi_2 = 0.0133$ and $\tau_1 = 7500$, (b-g) for various values of τ_2 as shown in the legend, after a primary quench of $\tau_1 = 2500$ for (b) $\chi_2 = 0.0119$, (c) $\chi_2 = 0.0125$, (d) $\chi_2 = 0.0133$, and $\tau_1 = 7500$ for (e) $\chi_2 = 0.0119$, (f) $\chi_2 = 0.0125$, (g) $\chi_2 = 0.0133$. In (b-g), $S(\mathbf{q})$ at each time step has been divided by the values of $S(\mathbf{q})$ when the second quench was initiated.

Figure 4.4(a) shows the structure factor at the start of the second quench and after $\tau_2 = 12.5$. The development of the secondary structure manifests itself as a weak but distinct shoulder. From equation 4.1.1 growth of the form,

$$S(\mathbf{q},\tau_2)/S(\mathbf{q},\tau_2 = 0) = \exp\{R(\mathbf{q})\tau_2\}, \qquad (4.1.2)$$

where R(**q**) is the growth rate of fluctuations with wavevector **q**, is predicted for a quench from a homogeneous state with only very weak fluctuations. However, the presence of the secondary structure is a consequence of the behaviour of such fluctuations superimposed on an inhomogeneous background; hence, it seems reasonable to factor out the structure factor at the start of the second quench. Note that we also considered the effect of subtracting $S(\mathbf{q},\tau_2 = 0)$; however this resulted in less well defined secondary structure factors that did not show exponential growth. The factorisation may not however necessarily be legitimate in the later stages of the second step phase separation in which non-linear effects in the time evolution process become increasingly important. Figures 4.4(b) – 4.4(g) show the growth of this secondary peak.

As τ_2 increases, the magnitude of the secondary peak also increases. Eventually the peak stops increasing in magnitude and decays as the secondary structure disappears, as can be seen in figure 4.5.
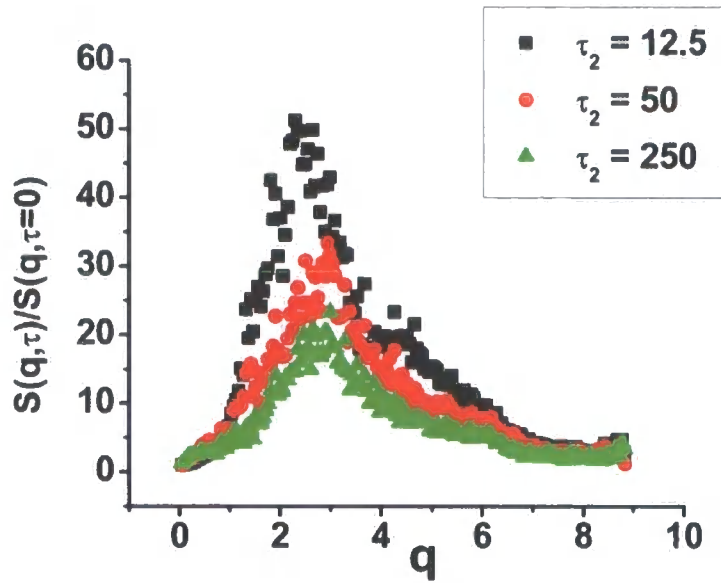
Figure 4.5

Decrease in magnitude of secondary structure factor for three values of τ_2, with $\chi_2 =$ 0.0133 and $\tau_1 = 7500$.

4.1.3 The Structural Growth with Time

During the early stages of growth it was found that the structure factor initially increased exponentially with time as shown in figure 4.6.
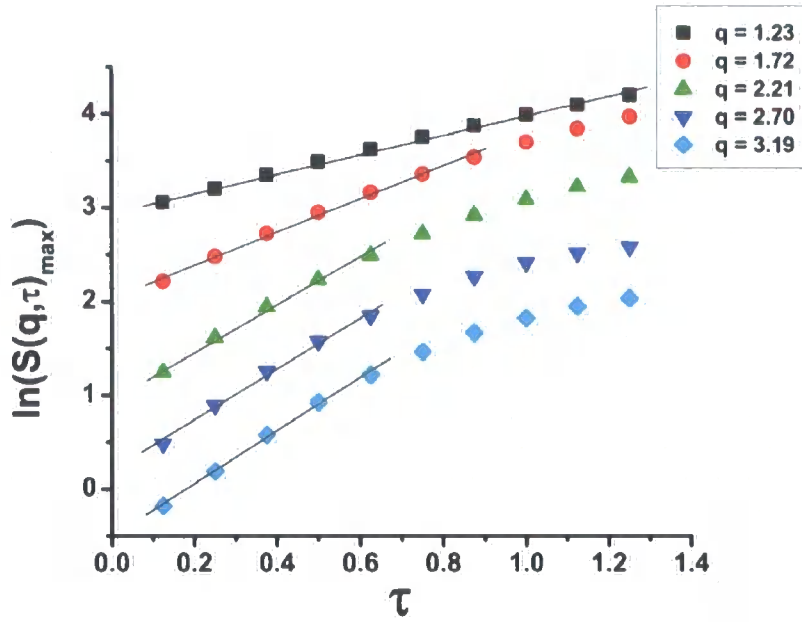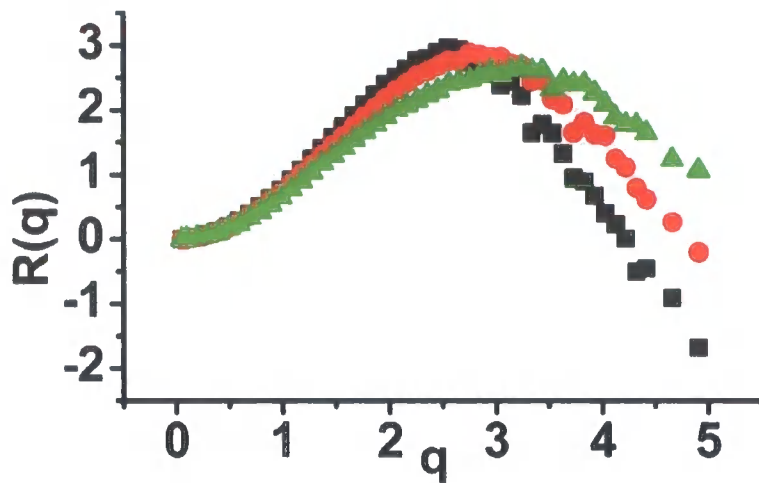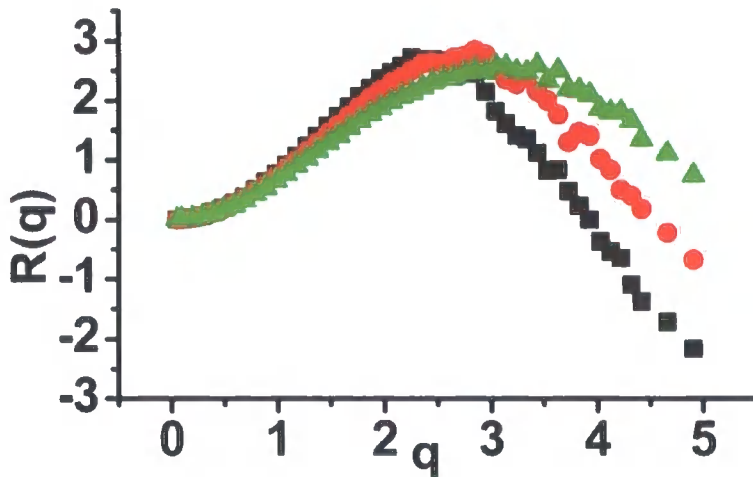
Figure 4.6

Growth of the structure factor, S($\mathbf{q}$,τ), with time, τ_2, for various wavevectors, $\mathbf{q}$, as indicated in the legend, after $\tau_1 = 2500$ and with $\chi_2 = 0.0119$. The lines show the fitting used to determine the growth rates during the early stages.

By fitting the numerical results to equation 4.1.2, the growth rates R($\mathbf{q}$) have been determined in figure 4.7.

Figure 4.7

Early stage growth and decay of secondary structure analysed using linearised theory for (a) $\tau_1 = 2500$ and (b) $\tau_1 = 7500$ and three quench depths of $\chi_2 = 0.0119$ (■), $\chi_2 = 0.0125$ (●) and $\chi_2 = 0.0133$ (▲).

Using linearised theory it is possible to predict the growth rate during the early stages of the second quench in a two step process, if equation 1.3.10 is linearised with $N_A = N_B = N$ this gives,

$$\frac{\partial \delta\phi}{\partial t} = \frac{1}{2}\nabla^2 \left[\frac{1}{N(\chi_f - \chi_0)}\left[\frac{1}{\phi} + \frac{1}{1-\phi}\right] - \frac{2\chi}{(\chi_f - \chi_0)} - \frac{1}{18\phi(1-\phi)}\nabla^2 \right]\delta\phi,$$

$$(4.1.3)$$

where χ_2 is the final χ value and χ_0 is the initial χ value. By carrying out a Fourier Transform the equation becomes,

$$\frac{\partial \delta\phi}{\partial t} = -\frac{1}{2}\mathbf{q}^2 \left[\frac{1}{N(\chi_f - \chi_0)}\left[\frac{1}{\phi(1-\phi)}\right] - \frac{2\chi}{(\chi_f - \chi_0)} + \frac{1}{18\phi(1-\phi)}\mathbf{q}^2 \right]\delta\phi,$$

$$= R(\mathbf{q})\delta\phi$$

$$(4.1.4)$$

therefore

$$R(\mathbf{q}) = -\frac{1}{2}\left[\frac{1}{N(\chi_f - \chi_0)\phi(1-\phi)} - \frac{2\chi}{\chi_f - \chi_0} \right]\mathbf{q}^2 - \frac{1}{18\phi(1-\phi)}\mathbf{q}^4,$$

$$(4.1.5)$$

It is known that the fastest growing wave vector occurs at $\mathbf{q}^2_{max}$ which corresponds to,

$$\mathbf{q}^2_{max} = -\frac{A}{2B},$$

$$(4.1.6)$$

where,

$$A = \frac{1}{N(\chi_f - \chi_0)\phi(1-\phi)} - \frac{2\chi}{\chi_f - \chi_0},$$

$$(4.1.7)$$

and,

$$B = -\frac{1}{18\phi(1-\phi)},$$

$$(4.1.8)$$

and as in the second quench $\chi = \chi_2$,

$$\mathbf{q}^2_{max} = -\frac{18}{\chi_f - \chi_0}\left[\frac{1}{2N} - \chi_2\phi^{(2)}{}_0(1-\phi^{(2)}{}_0) \right],$$

$$(4.1.9)$$

76

by taking χ_0 as shown in equation 1.1.11 and by using,

$$\frac{1}{2N} = \chi_0 \phi^{(1)}{}_0 (1 - \phi^{(1)}{}_0), \qquad (4.1.10)$$

it is found that,

$$\mathbf{q}^2{}_{max} = -\frac{18}{\chi_f - \chi_0}\left[\chi_2 \phi^{(2)}{}_0 (1 - \phi^{(2)}{}_0) - \chi_0 \phi^{(1)}{}_0 (1 - \phi^{(1)}{}_0)\right], \qquad (4.1.11)$$

where $\phi^{(1)}{}_0$ is the volume fraction ($\phi^{(1)}{}_0 = \frac{1}{2}$ for all the calculations) at the start of the first quench, and $\phi^{(2)}{}_0$ is the volume fraction within one of the two phases at the start of the second quench. Table 1 shows the predicted positions of the fastest growing wavevector, based on $\phi^{(2)}{}_0 = 0.33$, the composition on the coexistence curve for $\chi_1 = 0.0104$.

χ	q_{max}		
	Predicted	$\tau_1 = 2500$	$\tau_1 = 7500$
0.0119	1.1	2.5	2.3
0.0125	1.6	2.8	2.8
0.0133	2.1	3.2	3.4

Table 4.1

Comparison of the predicted and observed fastest growing wavevectors as a function of secondary quench depth.

The predicted quench depth dependence of q_{max} follows the same trend to that seen in the simulations, however the values do not seem commensurate with those predicted using Cahn's linearised theory, and this suggests that it is not possible to capture the true early stages of secondary domain growth, particularly for larger $\mathbf{q}$. It is noted that the above calculations assume an infinite system, whereas the secondary phase separation is effectively occurring within restricted domains. The disparity between the early stage theory and the results for larger q is highlighted in figure 4.8 where $R(q)/q^2$ is plotted against q^2. From equation 4.1.5 it is clear that such a plot should be linear.
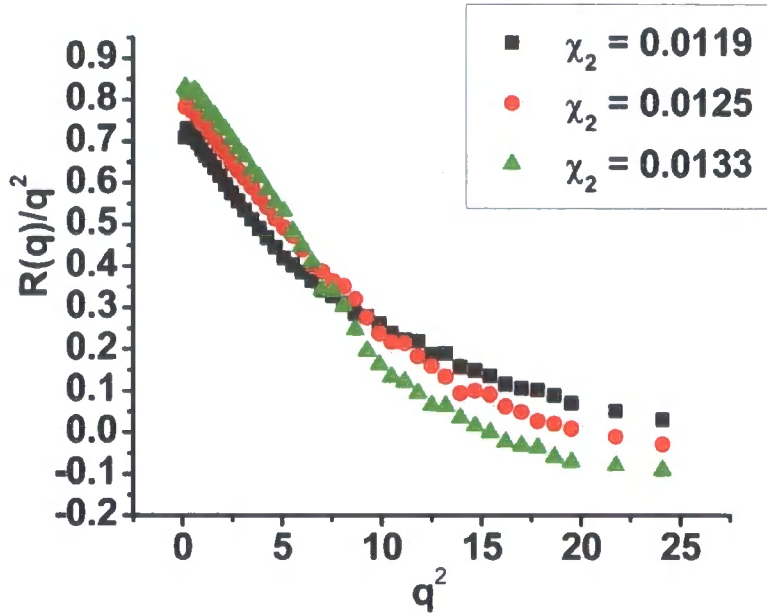
Figure 4.8

Plot of R($\mathbf{q}$)/$\mathbf{q}^2$ vs. $\mathbf{q}^2$, showing that linearity is observed only for smaller values of $\mathbf{q}$.

Figure 4.8 shows however that the results are not linear throughout and are only linear at low $\mathbf{q}$. The behaviour at lower values of $\mathbf{q}$ is however well characterised by linearised theory.

From equation 4.1.5 it is possible to calculate the theoretical gradient and intercept for a set of data when R($\mathbf{q}$)/$\mathbf{q}^2$ vs. $\mathbf{q}^2$ is plotted.

$$Gradient = -\frac{1}{36\phi^{(2)}{}_0(1-\phi^{(2)}{}_0)}, \qquad (4.1.12)$$

$$Intercept = -\frac{1}{2}\left[\frac{1}{N(\chi_f-\chi_0)\phi^{(2)}{}_0(1-\phi^{(2)}{}_0)} - \frac{2\chi}{(\chi_f-\chi_0)}\right], \quad (4.1.13)$$

The results during the early stages for each simulation are summarised in table 4.2,

1st step τ	χ	Results		Calculated	
		Gradient	Intercept	Gradient	Intercept
2500	0.0133	-0.0627	0.856	-0.116	0.8735
2500	0.0125	-0.0575	0.795	-0.116	0.835
2500	0.0119	-0.0617	0.736	-0.116	0.785
7500	0.0133	-0.0717	0.877	-0.116	0.8735
7500	0.0125	-0.0567	0.794	-0.116	0.835
7500	0.0119	-0.0633	0.738	-0.116	0.785

Table 4.2

Summary of simulation results for two different initial steps (τ_1 = 2500 and 7500) quenched to χ_1 = 0.0104 and then quenched to χ_2 = 0.0133, 0.0125 and 0.0119

The results shown in this table are very sensitive to changes in $\phi^{(2)}_0$ and the results again show that it is not possible to capture the very early stages of secondary domain growth.

4.1.4 Variation of the Secondary Quench Depth

The results shown thus far have been for quenches where χ_2 is identical to χ_f, hence the scaling for each simulation is different. It is therefore difficult to make quantitative comparisons of the secondary structure between the three different secondary quenches, particularly with regards to the degree of secondary phase separation. Hence we also conducted simulations in which the scaling ($\chi_f - \chi_0$) was fixed (χ_f = 0.0133, χ_0 = 0.01) but χ_2 i.e., the secondary quench depth, was varied. The first quench depth (χ_1 = 0.0104) was identical in each case. Clearly it is not to be expected that all quenches will result in a secondary structure; not only does the secondary quench depth have to be large enough that each domain becomes unstable i.e.,

$$\chi_2 \geq \frac{1}{2N\phi^{(2)}_0(1-\phi^{(2)}_0)},$$ (4.1.14)

but also the favoured secondary structure must be smaller than the length-scale of the larger domain. This is illustrated in figure 4.9, in which the maximum value of the structure factor with time for various secondary quench depths is shown in figure 4.9.
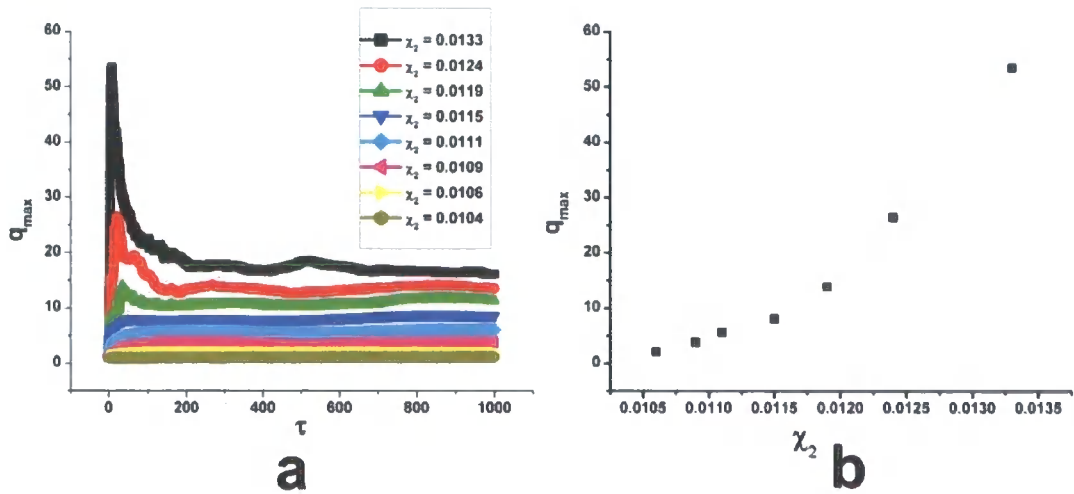
Figure 4.9

Plot showing (a) the change in the maximum value of the secondary structure factor with time for various values of χ_2 and (b) the peak value of the secondary structure factor for varying values of χ_2.

It can be seen from figure 4.9 that the deeper the quench the greater the change of the structure factor with time. When the secondary quench depth is only slightly deeper than the primary quench no secondary structure is observed, and only a slight growth in the structure factor is seen due to continued domain broadening. In figure 4.10, the morphology at a time corresponding to the peak in the secondary structure factor is shown for various quench depths. Clearly, as would be expected, the greater the quench depth, the greater the degree of secondary phase separation and the finer the secondary morphology.
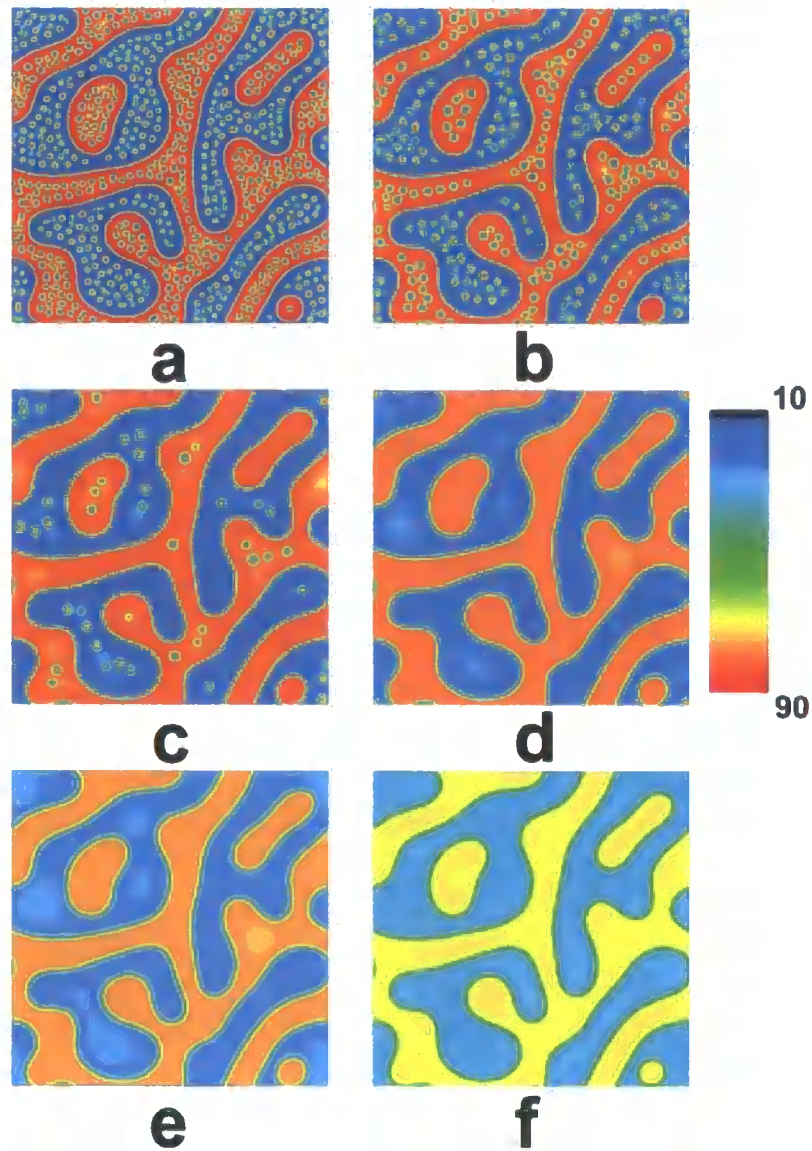
Figure 4.10

Secondary structure: (a) $\chi_2 = 0.0133$, $\tau_2 = 9$; (b) $\chi_2 = 0.0124$, $\tau_2 = 21$; (c) $\chi_2 = 0.01119$, $\tau_2 = 33$; (d) $\chi_2 = 0.01115$, $\tau_2 = 65$; (e) $\chi_2 = 0.01111$, $\tau_2 = 112$; (f) $\chi_2 = 0.01106$, $\tau_2 = 166$ corresponding to the time of the maximum structure factor (figure 4.9).

To quantify the secondary process further, we isolated domains in which $\phi > \frac{1}{2}$ at the start of the second quench, and probed the dynamics by considering the time dependence of the variance defined by,

$$\text{variance} = \frac{1}{N_T} \sum_{\substack{i,j \\ \phi_{i,j}(\tau_2=0)>1/2}} \left[\phi_{i,j}(\tau_2) - \bar{\phi}(\tau_2) \right]^2, \qquad (4.1.15)$$

The average $\bar{\phi}(\tau_2)$ was also only determined for lattice sites in which $\phi(\tau = 0) > \frac{1}{2}$, and N_T corresponds to the number of such lattice sites. The advantage of equation 4.1.15, which can also be easily measured experimentally with image analysis techniques, is that we remove factors due to the primary structure. In particular, when no secondary phase separation occurs, the variance only varies slightly from zero due to the random fluctuations.
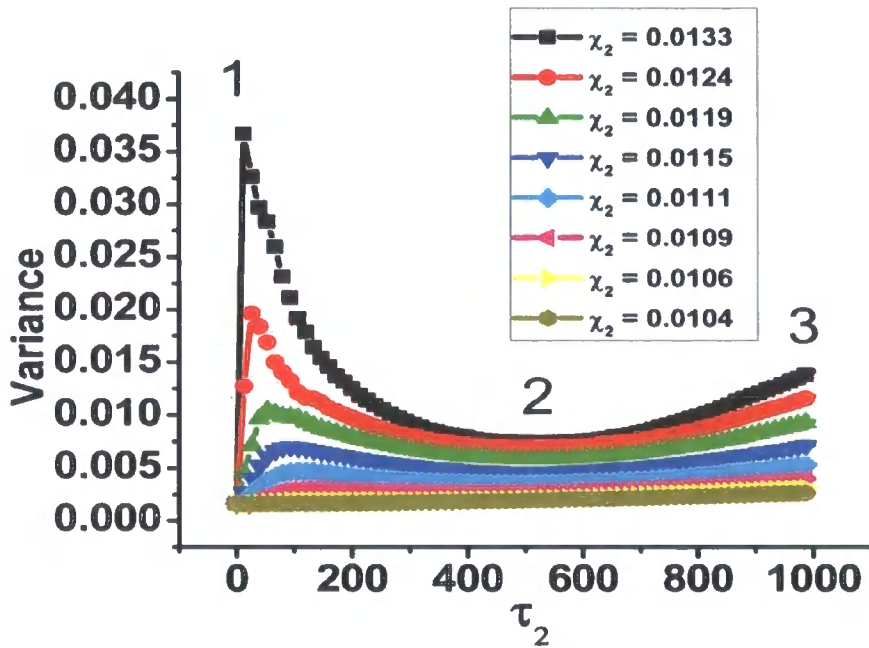
Figure 4.11

Variance of ϕ for various different second quench depths as indicated by the numbers in the inset. The numbers 1, 2 and 3 refer to the three stages of the second quench, as discussed in the text.

As can be seen in figure 4.11, as τ_2 increases the variance goes through three distinct stages. At stage 1 the maximum degree of secondary phase separation occurs, after this the secondary phase disappears; hence the subsequent reduction in the variance. By stage 2, the secondary phase separation has been "absorbed" back into the larger phases and the original morphology has been returned. Between stages 2 and 3 the domains continue to broaden so the variance again increases with

τ_2 since the originally isolated regions with $\phi > \frac{1}{2}$ no longer correspond to the primary morphology. It can be seen that the deeper the quench the greater the changes in variance. When no secondary phase separation occurs the variance still increases due to the domain broadening effects, but there is no peak.
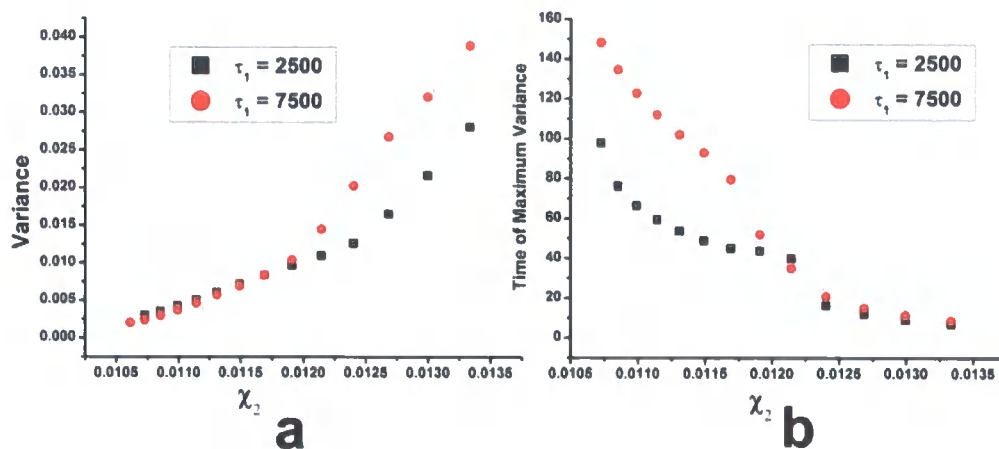

Figure 4.12

Comparison of (a) the maximum variance and (b) the time of the maximum variance with secondary quench depth χ_2 for a first quench of $\tau_1 = 2500$ and 7500.

The increased degree of secondary phase separation, as measured by the variance, is illustrated clearly in figure 4.12(a); as χ_2 increases so does the maximum value of the variance. Similar trends can be seen for both $\tau_1 = 2500$ and $\tau_1 = 7500$, although the degree of secondary phase separation is greater for the latter case when $\chi_2 > 0.0120$. We also show in figure 4.12(b) that the time at which the greatest secondary structure occurs decreases as the quench depth increases. It is interesting to note that there appears to be an abrupt change in behaviour at $\chi_2 \approx 0.0120$ for $\tau_1 = 7500$, and $\chi_2 \approx 0.01225$ for $\tau_1 = 2500$ but the reasons for this are unclear.

The absolute value of the variance as illustrated in figure 4.12, is clearly a useful tool for qualitative comparisons between quench depths, however, it is possible to further quantify the process since we can determine the maximum theoretical variance. We reasonably assume that the maximum degree of secondary phase separation corresponds to the two secondary phases attaining the coexistence compositions, ϕ' and ϕ'', associated with the secondary quench depth as determined

by the binodal curve. First we need to determine the theoretical area that would be occupied by each of the two secondary phases using the Lever rule, $v'\phi' + v''\phi'' = v\overline{\phi}$, where, as shown previously, the total area of the domain is v, and v' and v'' are the areas of the phases with compositions ϕ' and ϕ'' respectively. Since $v = v' + v''$, $v' = v\left[\left(\overline{\phi} - \phi''\right)/\left(\phi' - \phi''\right)\right]$ and $v'' = v\left[\left(\overline{\phi} - \phi\right)/\left(\phi'' - \phi'\right)\right]$

Hence, if we further assume sharp interfaces, the maximum theoretical variance corresponds to,

$$\text{variance}_{max} = \frac{1}{v}\left[v'\left(\phi' - \overline{\phi}\right)^2 + v''\left(\phi'' - \overline{\phi}\right)^2\right], \qquad (4.1.16)$$

The minimum and maximum polymer concentrations (ϕ' and ϕ'') are determined from equation 1.1.10.
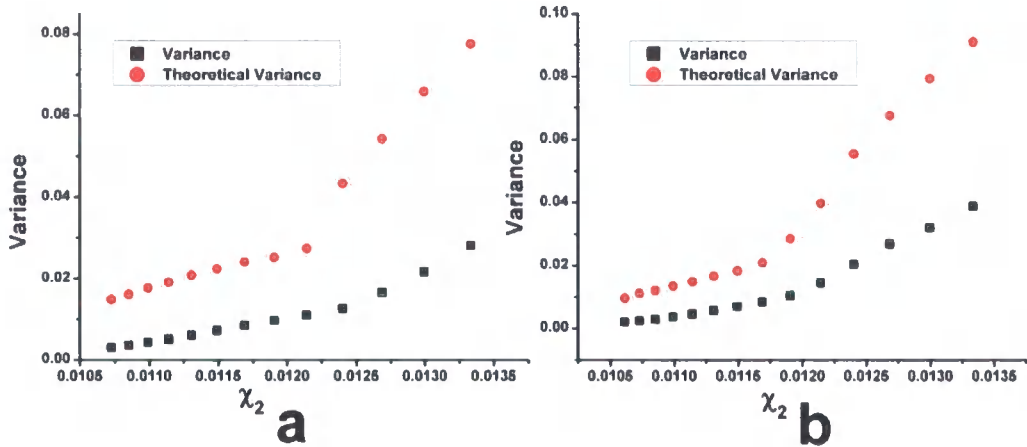
Figure 4.13

Comparison of the maximum theoretical variance and the maximum variance found by simulation for (a) first quench of $\tau_1 = 2500$ and (b) $\tau_1 = 7500$.

Whilst the theoretical variance and the variance determined from the simulation follow the same trend, as shown in figure 4.13, the secondary phase separation is unable to reach 'completion' before penalties due to interfacial energy become too costly, and diffusion enables larger scale rearrangement. It is also clear from figure 4.13, that the larger the initial structure the smaller the difference

between the theoretical variance and the actual variance, in agreement with the observations of Hayashi et al.[42]. This is due to the secondary phases being able to develop further before 'interaction' with the primary structure becomes significant. Again there appears to be an abrupt change in behaviour at $\chi_2 \approx 0.0120$ for $\tau_1 = 7500$, and $\chi_2 \approx 0.01225$ for $\tau_1 = 2500$.

4.2   Continuously Quenched Phase Separation

The next step in the evolution of the modelling of spinodal decomposition is to investigate a continuously quenched system[86]. During this process χ is constantly increased with time and the noise term, removed from equation 1.3.10, is replaced. The phase behaviour expected for this process is shown in figure 4.14.
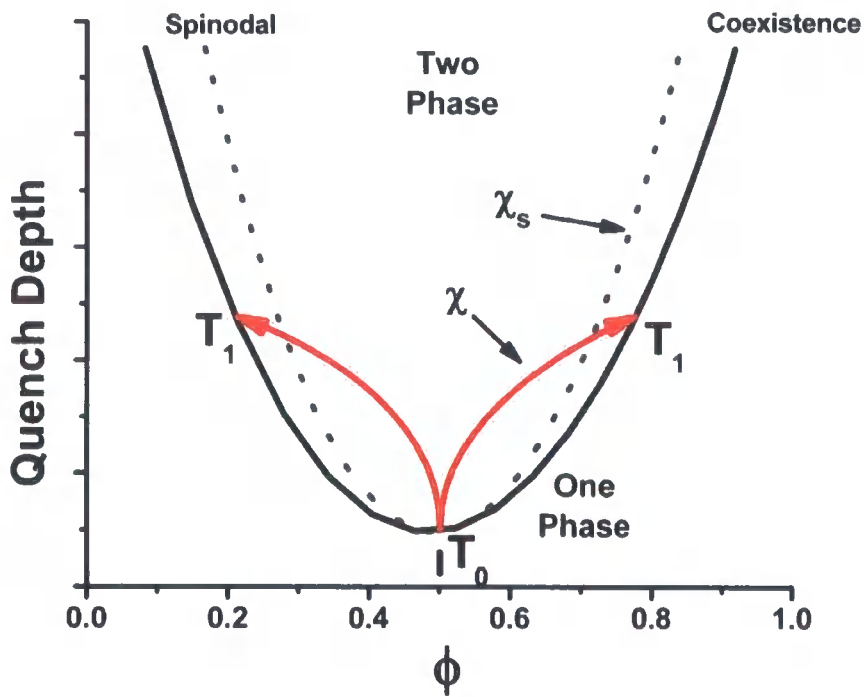
Figure 4.14

Phase diagram of a symmetric monodisperse polymer blend undergoing a continuous quench from the single phase region into the two phase region.

The dynamics and array set-up does not change from that seen previously, however in the current case with each time step χ is recalculated to correspond to an increase in χ on the phase diagram and random noise is added every 100 time steps.

Figure 4.14 shows a quench starting at T_0, corresponding to χ_0, and which ends at T_1, corresponding to χ_f. We assume a simple linear variation of χ with time,

$$\chi(\tau) = \chi_0 + \alpha\tau\chi_f,\qquad\qquad (4.2.1)$$

So that at the start of the simulation ($\tau = 0$), $\chi = \chi_0$ but as the simulation proceeds χ tends (with each time step) to $\chi = \chi_f$. In equation 4.2.1 α is a constant term which determines the rate of quenching

The value of χ is then re-calculated for each time step undertaken. The simulations are carried out on a 256^2 array using a symmetric blend. Random noise (± 0.001) is added every 100 steps, these values are chosen from trials to asses the effect of noise on the morphological growth within the system. It is found that the effect of adding noise every time step is negligibly different to the effect of adding noise every 100 steps, however the simulation is slowed considerably the more often noise is added, it is therefore more efficient to add noise as little as possible as long as the results are not affected. The value of $\Delta\tau$ used was 0.0025, with $\Delta x = 0.5$ and $\phi = 0.5$.

The structure factor is again studied using radial averaging to understand the domain growth of the polymer blend. The simulation is quenched to $\chi_f = 0.0133$ from $\chi_0 = 0.01$ continuously.
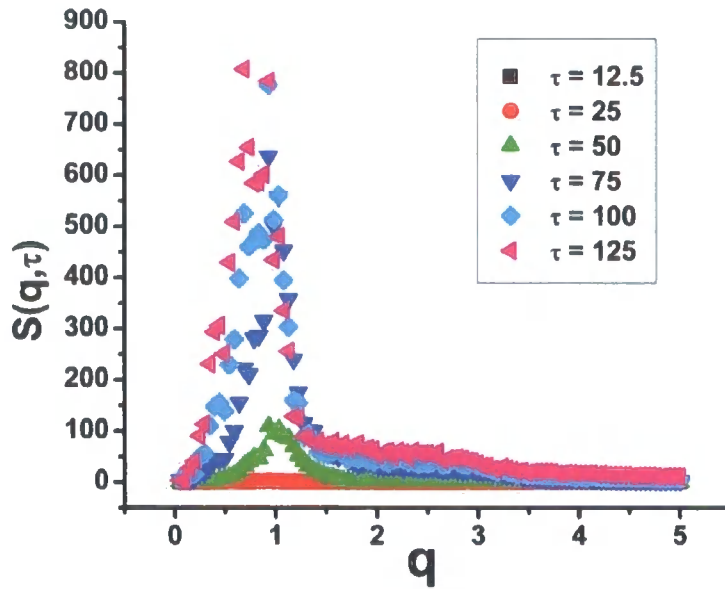
Figure 4.15

Growth of the structure factor for a continuous quench for various values of τ as shown in the legend.

The graph of the growth of the structure factor, figure 4.15, again shows the maximum of the peak increasing as one wave vector becomes dominant. The peak shifts to lower **q**, however this shift seems to be less apparent than in the single quench system and the peak appears to have a narrower distribution. This could be because the peak does not arise until a greater time has passed in this system and because fewer growing wavelengths are present when compared to the single quench system.
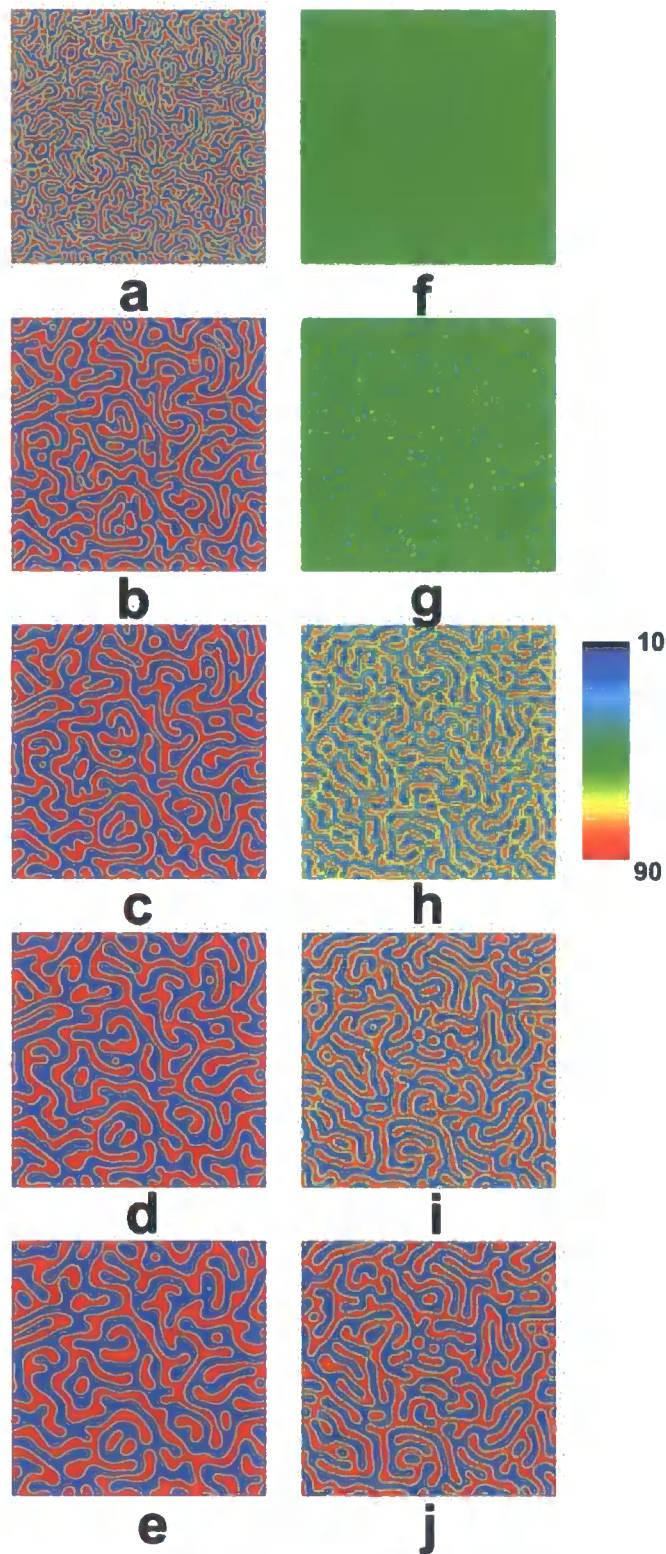
Figure 4.16

Comparison of the growth of a single quench process (a)-(e) with a continuous quench (f)-(j). (a) and (f) $\tau = 12.5$, (b) and (g) $\tau = 50$, (c) and (h) $\tau = 75$, (d) and (i) $\tau = 100$ and (e) and (j) $\tau = 125$ when $\chi_f = 0.0133$

Figure 4.16 clearly shows the difference in the early stages of growth between the single and continuous quench process. In the continuous quench no phase separated morphology is seen until $\tau = 50$, however in the single quench phase separation is seen almost immediately, by $\tau = 12.5$. At the end of the simulation the domain morphology of both systems becomes comparable as χ_f is the same in each case. If the simulation is undertaken to larger τ the domain morphologies broaden to similar sizes, as seen in figure 4.17.
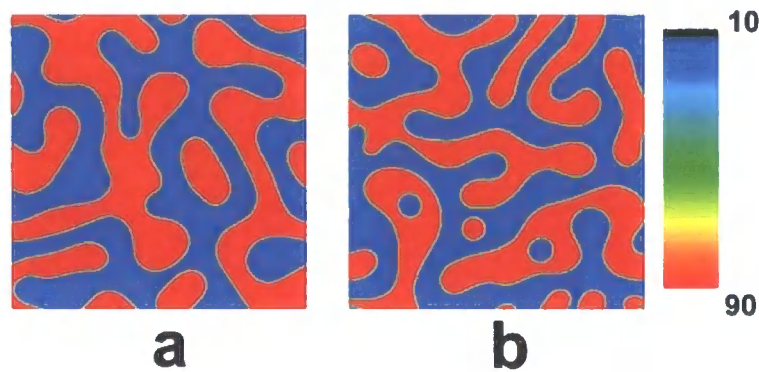
Figure 4.17

Comparison of final morphologies for (a) a single step quench and (b) a continuous quench at $\tau = 2500$ and where $\chi_f = 0.0133$

The continuous quench process has a greater magnitude of phase separation when the simulation is undertaken to larger τ. To explain the difference in compositions between short and long simulation run times it is useful to understand how the quench depth is changing compared to the χ value of the quench depth and the χ_s value of the spinodal curve. For this reason we define three values of χ, the first is χ_s given by equation 1.1.11, the second is χ_a which is again found using equation 1.1.11, however the value of ϕ used is taken as the maximum of the composition in the phase separated structure. Finally we define χ as the value taken from equation 4.2.1 at each time, χ and χ_s are shown diagrammatically in figure 4.14. In simpler terms, χ_s is the spinodal line, χ is the quench set in the system and χ_a is the true phase position of the system.

Simulations were carried out for long shallow ($\tau = 2500$, $\chi_f = 0.0101$) quenches, for long deep ($\tau = 2500$, $\chi_f = 0.0133$) quenches, for short shallow ($\tau = 125$, $\chi_f = 0.0101$) quenches and for short deep ($\tau = 125$, $\chi_f = 0.0133$) quenches, the results are summarised in figure 4.18.
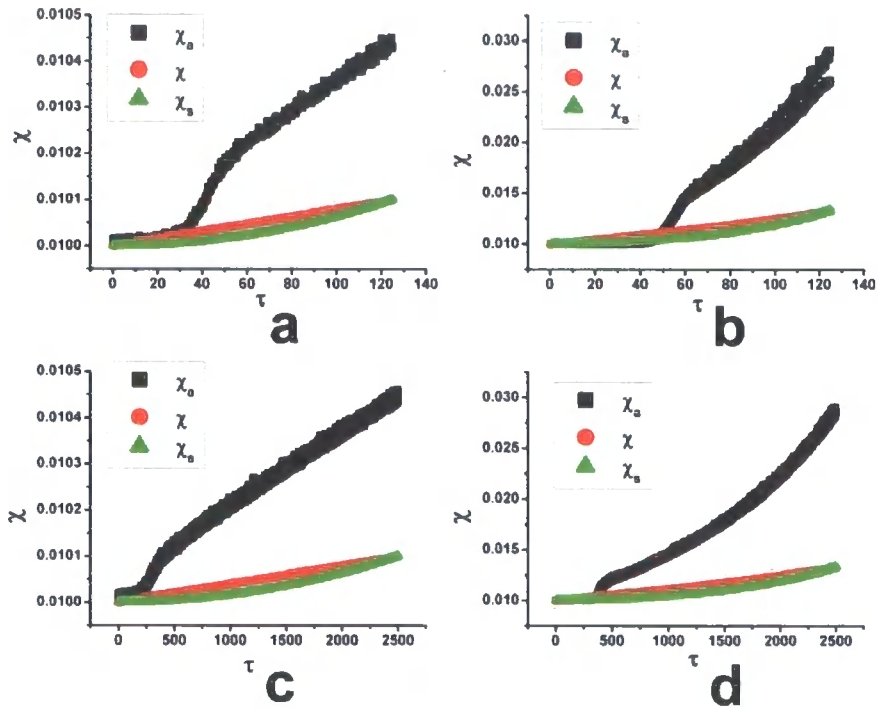

Figure 4.18

Comparison of χ_a (■), χ (●) and χ_s (▲) for (a) $\tau = 125$, $\chi_f = 0.0101$, (b) $\tau = 125$, $\chi_f = 0.0133$, (c) $\tau = 2500$, $\chi_f = 0.0101$ and (d) $\tau = 2500$, $\chi_f = 0.0133$.

Figure 4.18 can now be used to explain the results found in figure 4.16, here we find that when the simulation is undertaken to low τ, χ_a does not pass far enough into the spinodal region to see phase separation until τ is around 50. This is why no morphology is present at the start of the simulation, χ_a then increases rapidly and at this point domains start to appear in the blend. It can be seen that limited time is available for domain broadening in this case, which is why the domains in the single step system have larger domain morphologies. When large τ is used however χ_a passes into the spinodal region at relatively low τ so much more time is available for domain broadening and simultaneous phase separation.

Secondary phase separation in a continuously quenched process is seen experimentally, and is theoretically possible in this continuous model given the

correct conditions. The continuously quenched model is used to attempt to create a secondary phase within a larger primary one; however secondary phase separation has not yet been seen, figure 4.18 can be used to illustrate the reasons why. To obtain secondary phase separation, a quench that jumps inside the spinodal region is needed; this quench then needs to reside on the coexistence curve where domain broadening can occur. The quench then needs to jump back inside the spinodal region so that the secondary structure can be formed. This type of behaviour is not seen in any of the diagrams in figure 4.18 as once a jump into the spinodal region has occurred χ_a never drops back out of the spinodal region and into the binodal region. To overcome this a quench depth dependent diffusion term, D, can be included in the dynamics equations which has the form,

$$D = \exp[-\beta(\chi(\tau) - \chi(\tau = 0)], \qquad (4.2.2)$$

where β is a constant term which is calculated relative to the quench depth and the total number of time steps undertaken by the simulation. The diffusion term is set such that at low τ, D is high (≈ 1) and at high τ, D is low (≈ 0). This means that at the start of the simulation the dynamics continue as normal with the simulation passing into the spinodal region. As the simulation continues however the diffusion term dominates and the dynamics of the phase separation should slow down, dropping the simulation below the spinodal line. As more time then passes χ increases so the simulation should be forced back into the spinodal region and secondary structure should be seen. This is very similar to experimentally having a blend which becomes more viscous as phase separation occurs.

Unfortunately the correct conditions have yet to be found to cause secondary structure, as currently it is not possible to drop below the spinodal line for a great enough time to allow the primary structure to develop adequately to allow secondary phase separation to occur when the simulation moves back into the spinodal region. This is probably because the difference in size between the favoured length scale and the primary structural scale is not large enough.

4.3 Conclusions

We have explored the early stages of secondary phase separation following a two-step quench process, using a finite difference scheme for a spatially and

temporally discretised version of the Cahn-Hilliard equation. The morphology development was probed by determining the structure factor. These results showed a secondary shoulder, associated with secondary phase separation, appearing immediately after the second quench, which shares features in common with the initial time dependence expected from the linearised Cahn-Hilliard theory. Differences arise due to the numerical difficulty of capturing the 'true' early stages. In all cases the secondary structure reaches a maximum before the morphology relaxes back to the initial structure, but with a greater difference in composition between the two phases. As in experiments[42-44], we find that the secondary structure is absorbed back into the primary structure whilst the primary structure coarsens. However we do not observe significant coarsening of the secondary structures, this is probably due to the initial primary structure not having a significantly greater lengthscale than the secondary, although another possibility is the neglect of hydrodynamic effects. Achieving such a wide range of lengthscales with the resultant increase in timescales is beyond the scope of this study.

From the point of view of applications, we have quantified the degree of secondary phase separation as a function of time and quench depth by determining the variation of the variance within one of the primary domains. The time at which the maximum variance occurs corresponds to the optimally secondary phase separated structure. We have found that the secondary structure does not attain the theoretical maximum secondary structure, which would correspond to secondary domains possessing the equilibrium compositions expected from the coexistence curves. These predictions suggest further experiments that will enable theory to be quantifiably tested.

A study has also been undertaken to attempt to model phase separation in a continuously quenched process, one where the temperature is constantly changing. In this case we find that the formation of the phase separated morphology is restricted in the very early stages, when compared to a single quench system. At later stages however the morphology becomes comparable to that of a single quench system as χ_f is the same in each case. Attempts have been made to model the process of secondary phase separation, however, even with the addition of diffusion limiting terms; it has not as yet been possible to see this phenomena.

Chapter 5

Reaction Induced Phase Separation of Pseudo-Interpenetration Polymer Networks in Polydisperse Polymer Blends

The model is now developed to incorporate the process of reaction induced phase separation in a polydisperse polymer blend. During the reaction one component undergoes a polymerisation reaction, leading to phase separation via spinodal decomposition. The effect that changing the final degree of polymerisation has on the phase separation process is also studied. Finally an elastic energy term is included mimicking the cross linking process and the generation of a semi-interpenetrating polymer network. The effect of changing the final degree of polymerisation is again studied and a comparison of the results is made. Finally the scaling of the dominant lengthscale with time is shown to vary according to the reaction conditions.

5.1 Modelling RIPS in a Polydisperse System with Crosslinking

As seen in chapter 2.4 the spinodal of a polydisperse system can be written in terms of the weight average degree of polymerisation. By combining equations 2.4.4 and 2.4.5 with equation 1.3.7 and once again rescaling into the dimensionless form we arrive at a dynamic equation for a polydisperse polymer blend,

$$\frac{\partial \phi_i(\mathbf{x}, \tau)}{\partial \tau} = \sum_{j=1}^{s-1} \Lambda_{ij} \nabla^2 \left[\left(\frac{1}{N_j(\chi - \chi_s)} \ln \phi_j - \frac{1}{N_B(\chi - \chi_s)} \ln \phi_B + \frac{\chi(2\phi_B)}{(\chi - \chi_s)} \right) \right. $$
$$\left. + \frac{1}{36} \sum_{k=1}^{s-1} \left(\frac{1}{\phi_B^2} - \frac{\delta_{jk}}{\phi_k^2} \right)(\nabla \phi_k)^2 - \frac{1}{18} \sum_{k=1}^{s-1} \left(\frac{1}{\phi_B} + \frac{\delta_{jk}}{\phi_k} \right) \nabla^2 \phi_k \right],$$

(5.1.1)

where Λ_{ij} is determined by equation 2.4.11 and $\lambda_i = 1/N_i$.

In this chapter we explore how equation 5.1.1 can now be used to model the process of reaction induced phase separation via polymerisation.

5.1.1 Modelling the RIPS Process

During the RIPS process, temperature, and hence χ, is fixed initially below the spinodal so that $\chi < \chi_s$. The simplest model is one where monomers/polymers with degree of polymerisation N_{A1} and initial volume fraction ϕ_{A1} react to form polymers with a higher degree of polymerisation N_{A2}, and volume fraction ϕ_{A2}, as seen in figure 5.1, such that ϕ_{A1} decreases and ϕ_{A2} increases.
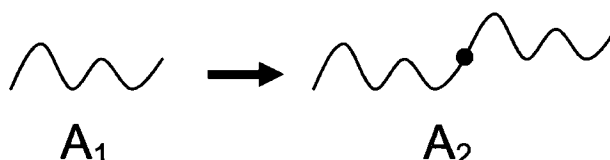
$$A_1 \longrightarrow A_2$$

Figure 5.1

Polymerisation of component A_1 to component A_2.

The consequence of this is that the entropy and hence χ_s, the value of χ on the spinodal, decreases. For RIPS to occur, at some point the condition $\chi > \chi_s$ needs to be fulfilled.

During most RIPS processes, cross-linking also occurs; this prevents macroscopic phase separation from taking place, and slows down the structural growth significantly. In addition, vitrification often occurs, freezing the morphology; however this effect is not investigated here. Cross-linking is incorporated into the model by adapting the method described by Binder and Frisch[78]. In our case the network is both continually evolving and locally dependant on the polymerisation/cross-linking history. During the process component A_2 reacts to form a network A_3 with volume fraction ϕ_{A3}. This network fraction of the A component contributes an additional elastic term to the free energy as described by equation 2.5.4. In the original theory, ϕ_0 is the bulk volume fraction of the network, however during RIPS the network is continually evolving so this parameter needs to be carefully redefined. It is assumed that ϕ_0 is a spatially dependant variable representing the total amount of network generated by chemical reaction on any given lattice site since the initiation of the process an ϕ_0 does not include information about the diffusion of the network between lattice sites. The justification for such a definition is that ϕ_0 represents the local equilibrium volume fraction of network in the absence of interactions other than those giving rise to the elastic energy. In this

system the "equilibrium" depends on the evolution of the system, for example if phase separation occurs well before network formation, regions rich in component B will have essentially no elastic energy throughout the simulation. By allowing ϕ_0 to be dependant on the history of the system, we incorporate this essential physics into the model. When the volume fraction of the component in question differs from the value of ϕ_0, mimicking an expansion or contraction of the network, a high energy state ensues and the system moves to reduce this energy by bringing the network back to its lowest energy configuration. Of course this occurs in competition with other contributions to the free energy. Equation 2.5.3 can be re-written as,

$$\frac{\partial F_{el}}{\partial \phi_{Ai}} = \frac{1}{N_{Ai}}\left[\left(\frac{1}{2}\phi_{Ai}^{-2/3}\phi_0^{2/3} - 1\right) + B\left(1 + \ln\phi_{Ai} - \ln\phi_{A0}\right)\right], \qquad (5.1.2)$$

A range of values for B have been used, we use B = ½ since this minimises the elastic energy when $\phi_{Ai} = \phi_0$,

During the simulations in which network formation is included, we define component A_3 as the semi-IPN and therefore the evolution of ϕ_{A3} is found by substituting equation 5.1.3 into 5.1.1 to give,

$$\frac{\partial \phi_3(\mathbf{x},\tau)}{\partial \tau} = \sum_{j=1}^{s-1} \Lambda_{ij}\nabla^2\left[\left(\frac{1}{N_{A3}(\chi-\chi_s)}\left[\left(\frac{1}{2}\phi_{A3}^{-2/3}\phi_0^{2/3} - 1\right) + B\left(1 + \ln\phi_{Ai} - \ln\phi_{A0}\right)\right] - \frac{1}{N_B(\chi-\chi_s)}\ln\phi_B\right)\right.$$
$$\left. + \frac{\chi(2\phi_B)}{(\chi-\chi_s)} + \frac{1}{36}\sum_{k=1}^{s-1}\left(\frac{1}{\phi_B^2} - \frac{\delta_{jk}}{\phi_k^2}\right)(\nabla\phi_k)^2 - \frac{1}{18}\sum_{k=1}^{s-1}\left(\frac{1}{\phi_B} + \frac{\delta_{jk}}{\phi_k}\right)\nabla^2\phi_k\right]$$

$$(5.1.3)$$

An additional characteristic of structural growth is given by the reaction pathway, determined by the conversion of each component, $P_i = \phi_i/(\phi_i + \phi_j)$. Whilst it is easy to calculate an average value for the blend it is also useful to distinguish between the maximum, minimum and average values of ϕ against time to monitor how the reaction is progressing for each component of the blend in each of the phase separated regions. This is a consequence of the fact that although we use a simple scheme for the reaction kinetics,

95

$$\frac{-\partial[\phi_{Ai}]}{\partial\tau} = k[\phi_{Ai}]^2 , \qquad (5.1.4)$$

the phase separation might be expected to result in non-homogeneous reaction pathways.

5.1.2 The Reaction Rate

During the simulations a study of three different rate constant values, k, is undertaken corresponding to a "fast" reaction, a "medium" rate reaction and a "slow" reaction. The rate of the medium reaction is set so that the kinetic rate, k, is equal to the phase separation rate, $R(\mathbf{q}_m)$, the rate of growth of the fastest growing wavevector. For simplicity, we use the same rate constant for the conversion of both A_1 to A_2 and A_2 to A_3. By linearisation of equation 1.3.10 we find that for small fluctuations, $R(\mathbf{q}_m) = 9\phi(1-\phi)$ [60]. Linearisation of 1.3.10 gives,

$$\frac{\partial\delta\phi}{\partial\tau} = \frac{1}{2}\mathbf{q}^2 \left[\frac{1}{\chi_f - \chi_s} \left[\frac{1}{N_A\phi_A} + \frac{1}{N_B\phi_B} \right] - \frac{2\chi_f}{\chi_f - \chi_s} + \frac{\mathbf{q}^2}{18\phi(1-\phi)} \right] \delta\phi, \quad (5.1.5)$$

where from rearranging equation 1.1.11 $2\chi_s = (1/N_A\phi) + (1/N_B(1-\phi))$, such that 5.1.5 becomes,

$$\frac{\partial\phi}{\partial\tau} = \frac{1}{2}\mathbf{q}^2 \left[\frac{2\chi_s}{\chi_f - \chi_s} - \frac{2\chi_f}{\chi_f - \chi_s} + \frac{\mathbf{q}^2}{18\phi(1-\phi)} \right] \delta\phi, \qquad (5.1.6)$$

The critical wavevector, $\mathbf{q}_c$, below which fluctuations grow and above which they decay can be found by equating the part of equation 5.1.6 in brackets to zero such that,

$$\frac{2\chi_s}{\chi_f - \chi_s} - \frac{2\chi_f}{\chi_f - \chi_s} + \frac{\mathbf{q}_c^2}{18\phi(1-\phi)} = 0, \qquad (5.1.7)$$

hence,

$$\mathbf{q}_c^2 = 18\phi(1-\phi)\left[\frac{2(\chi_f - \chi_s)}{\chi_f - \chi_s} \right], \qquad (5.1.8)$$

96

The fastest growing wavevector, q_m, is given by $q_m = q_c/\sqrt{2}$, so that,

$$q_m^2 = 18\phi(1-\phi),\qquad\qquad(5.1.9)$$

Substituting 5.1.9 into 5.1.6 gives,

$$R(q_m) = 9\phi(1-\phi),\qquad\qquad(5.1.10)$$

In the simulation of fast reaction kinetics $k = 10R(q_m)$ and conversely for slow reaction kinetics we set $k = R(q_m)/10$.

5.2 The Ternary System

Firstly a simple ternary RIPS system without network formation where component A_1 undergoes a second order reaction to create component A_2, e.g. $A_1 \rightarrow A_2$, is investigated.

5.2.1 Ternary Phase Separation

Initially $\chi = \chi_s$, so that the blend lies on the spinodal line, therefore as the reaction proceeds the blend moves immediately into the two-phase region of the phase diagram. This is so that no computational effort is wasted on simulating a homogeneous system for which the kinetics can be modelled analytically. We choose $N_{A1} = 500$, $N_{A2} = 2000$ and $N_B = 750$ with $\phi_{A1} = 0.495$, $\phi_{A2} = 0.005$ and $\phi_B = 0.5$, i.e. a 50:50 blend, so that $\chi_s = 0.00328$. For 100% conversion (i.e. $\phi_{A2} = 0.5$), $\chi_s = 0.00183$ showing that the fully reacted system is located in the two-phase region of the phase diagram as shown in figure 5.2.
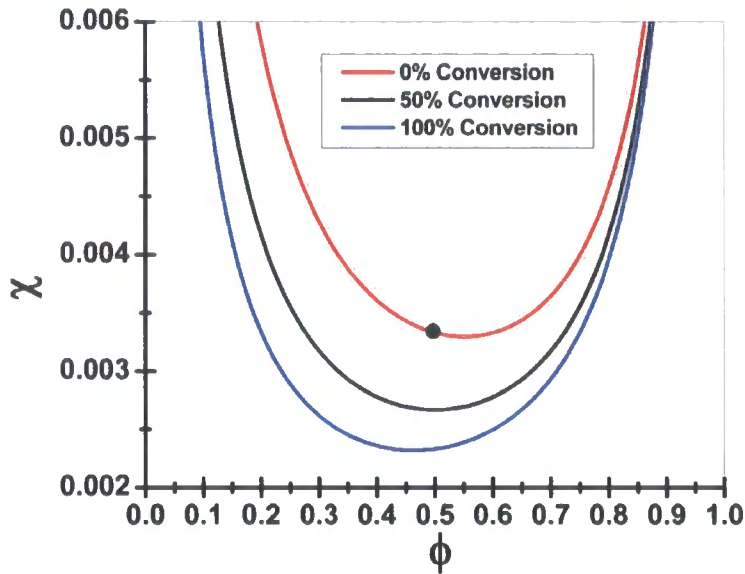
Figure 5.2

Spinodal curves of a three component polymer blend with $N_{A1} = 500$, $N_{A2} = 2000$ and $N_B = 750$, for 0% conversion (100% N_{A1}), 50% conversion (50% N_{A1} and 50% N_{A2}) and 100% conversion (100% N_{A2}). The reaction point for our simulation is indicated by •. Above the respective curves, the blend is unstable and will phase separate via spinodal decomposition.

All the results are averaged over 5 runs with noise of magnitude ±0.0001 added every 100 time steps to mimic the fluctuations found in real systems. The simulations are carried out on a two-dimensional 128^2 array with $\Delta\tau = 0.00001$ and $\Delta x = 0.5$.

5.2.2   Phase Separation in the 50:50 Blend

During phase separation the domains form continually changing compositions in order to reach the evolving coexistence values as described by figure 5.3.
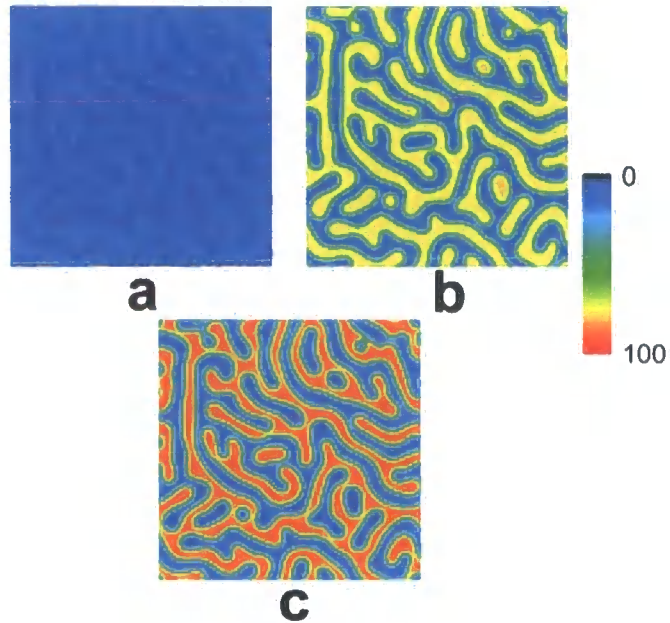
Figure 5.3

Morphology of blend at $\tau = 60$ for (a) component A_1, (b) component A_2 and (c) component B for a slow ($k = R(q_m)/10$) conversion rate.

The morphology for components A_1 and A_2 are identical but obviously the volume fraction is different in each case, as shown by the contrast in the colours in figure 5.3. The corresponding structure factor for each component is shown in figure 5.4.
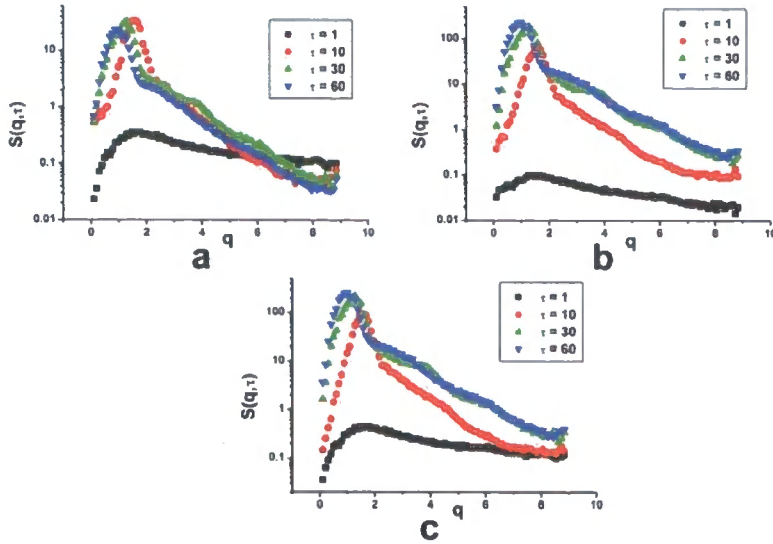
Figure 5.4

Growth of the structure factor with time for (a) component A_1, (b) component A_2 and (c) component B for the slow ($k = R(q_m)/10$) conversion rate.

It can be seen that the peak height increases with time and the position of the maximum peak shifts to lower **q** as phase separation occurs and the domains broaden with time. For component A_1 it can be seen that the maximum value of the structure factor decreases at larger τ values. This is because as conversion increases the average volume fraction of component A_1 rapidly decreases therefore reducing the maximum of the structure factor.

For analysis of the structure factor the method proposed by Glotzer[148] is followed, here we define the function $<q_1>$ as being,

$$< q_1 >= \frac{\sum_i \mathbf{q}_i S(\mathbf{q}_i, \tau)}{\sum_i S(\mathbf{q}_i, \tau)}, \qquad (5.2.1)$$

By following the maximum value of the structure factor, $S(\mathbf{q},\tau)_{max}$, and $<q_1>$ at each time interval we are able to monitor the length-scale of the morphology and also to give an indication of the extent of phase separation, this process is undertaken in figure 5.5.

100
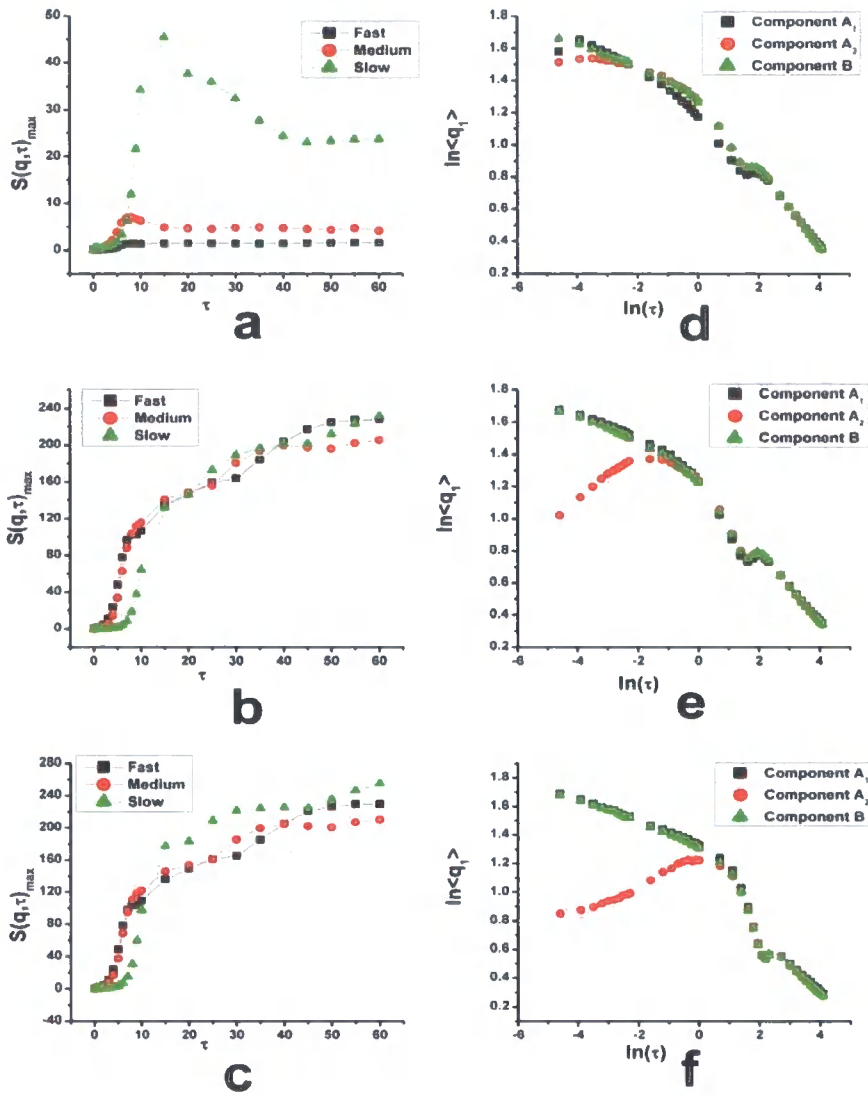
Figure 5.5

$S(\mathbf{q},\tau)_{max}$ vs. τ for (a) component A_1, (b) component A_2 and (c) component B. $<q_l>$ vs. τ for (d) the "fast" reaction, (e) the "medium" reaction and (f) the "slow" reaction for a 50:50 blend.

From figure 5.5 we see that for the fast reaction the value of $S(\mathbf{q},\tau)_{max}$ for component A_1 actually decreases with time in the very early and later stages. This is because in the early stages very little phase separation is occurring but the average value of A_1 is rapidly decreasing, giving a reduction in $S(\mathbf{q},\tau)_{max}$. In the late stages the maximum amount of phase separation has occurred but $<\phi_{A1}>$, the mean value of component A_1, is still decreasing. In figures 5.5(e) and 5.5(f) we see that $<q_l>$ for component A_2 is initially at a much lower value than that of components A_1 and B, this is because very little of component A_2 is initially present in the blend. It can be

seen that the behaviour in the later stages may be described by a power law, i.e. $<q_1>$ $\propto \tau^{-\alpha}$; fits to these regimes for each of the three rates are shown in figure 5.6.
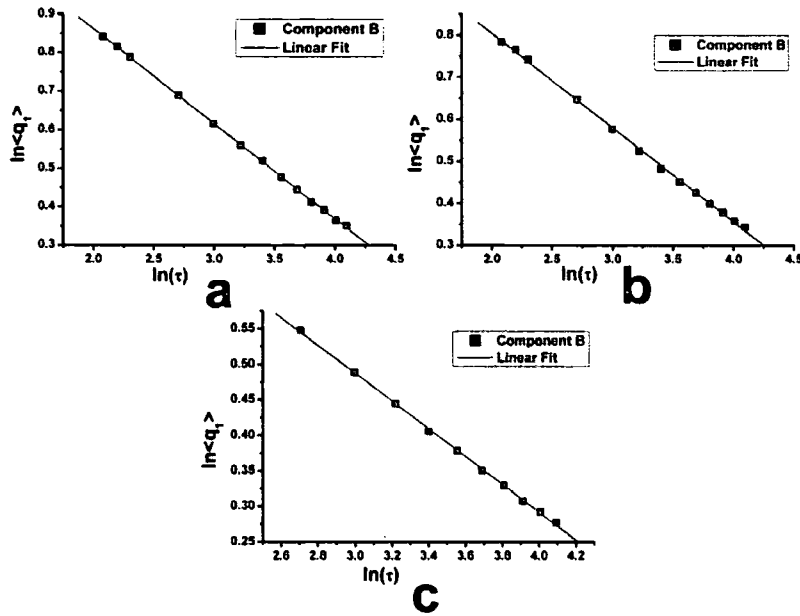
Figure 5.6

$\ln<q_1>$ vs. $\ln(\tau)$ for component B in a 50:50 blend undergoing (a) a "fast" reaction with growth exponent of $\alpha = \frac{1}{4}$, (b) a "medium" reaction with a growth exponent of $\alpha = \frac{2}{9}$ and (c) a "slow" reaction with a growth exponent of $\alpha = \frac{1}{5}$.

The growth exponent above shows we do not see the more universally recognised $\tau^{-1/3}$ relationship, which is due to the different dynamics involved in our simulations when compared to a simple 2 component blend undergoing a rapid temperature quench. We do however see a trend to a lower growth exponent when moving to slower reaction rates, as the faster the reaction the earlier we move into the two phase region.

5.2.3 The Reaction Pathway

It is possible to monitor the "reaction pathway" by following the mean volume fraction of each component with time, $\bar{\phi}_n = \langle \phi_n \rangle$. Since the extent of reaction varies with composition, as phase separation occurs the two phases will have different reaction kinetics. Hence we also follow the mean of the volume fraction

102

above $\overline{\phi}_n$, i.e. $\overline{\phi}_{n\max} = \langle \phi_n > \overline{\phi}_n \rangle$ and the mean of the volume fraction below $\overline{\phi}_n$, i.e.

$\overline{\phi}_{n\min} = \langle \phi_n < \overline{\phi}_n \rangle$, this is shown in figure 5.7.
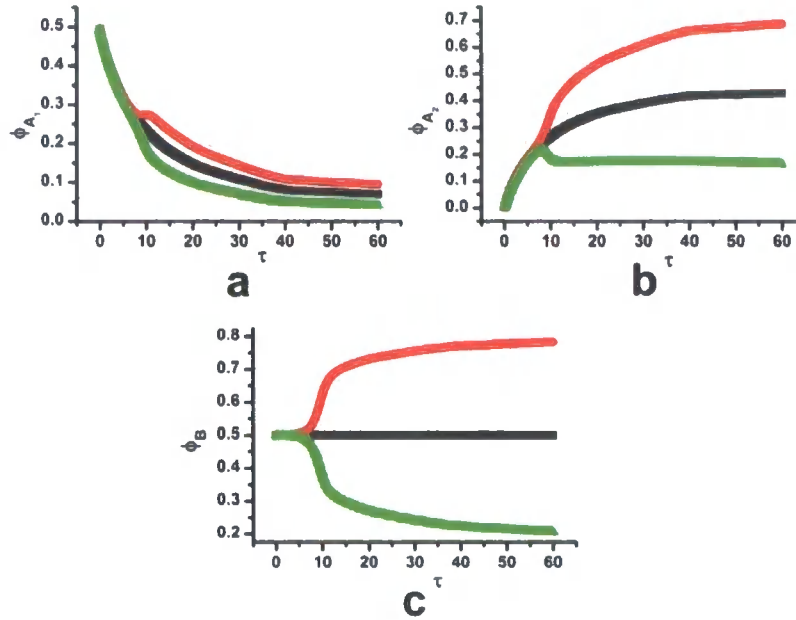
Figure 5.7

Reaction pathway for (a) component A_1, (b) component A_2 and (c) component B for a slow ($k = R(\mathbf{q}_m)/10$) conversion rate. $\overline{\phi}_n$ is represented by ■, $\overline{\phi}_{n\max}$ is represented by ● and $\overline{\phi}_{n\min}$ is represented by ▲.

Figure 5.7 shows that as the reaction proceeds, the average volume fraction of component A_1 decreases at the same rate as the average volume fraction of component A_2 increases, with the average volume fraction of component B remaining constant throughout. The point at which phase separation occurs for the system can clearly be seen as the values of $\overline{\phi}_{n\max}$ and $\overline{\phi}_{n\min}$ rapidly deviate from $\overline{\phi}_n$. Phase separation does not rapidly occur at the start of the simulation because the system is only slowly moving into the two-phase region of the phase diagram and the phase separation process is limited by the mobility of each component, determined by the Onsagar coefficient Λ_{ij}. The critical length-scale is also very large for shallow quenches requiring diffusion over large distances.

As stated above three values of k, the rate constant, are used in the simulation and the reaction pathway can be used to show the effect of different rates of reaction, as illustrated in figure 5.8.
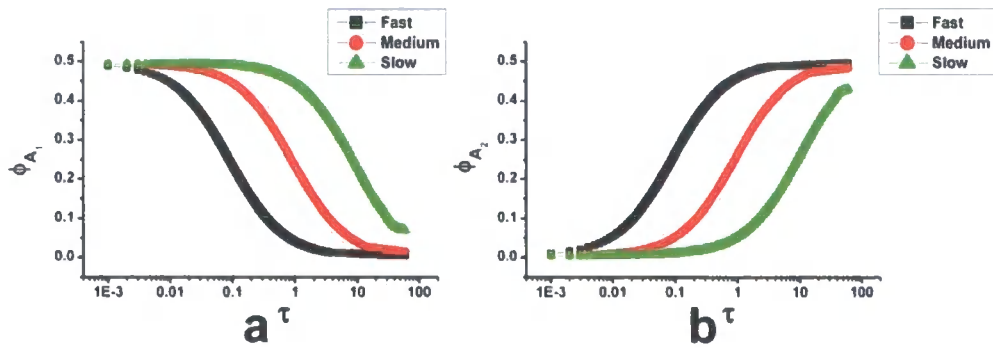

Figure 5.8

Reaction pathway for (a) $\bar{\phi}_{A1}$ and (b) $\bar{\phi}_{A2}$ for the three different reaction rates.

By following $\bar{\phi}_n$ for each component it can be seen that an increase in rate constant leads to an increase in the rate of reaction and therefore the rate of conversion. It can also be seen that for ϕ_{A1} as conversion increases phase separation in component A_1 is constrained because $\bar{\phi}_n$ approaches zero. For the slow conversion rate we see that $\bar{\phi}_n$ seems to become almost constant at $\phi_{A1} = 0.1$ and $\phi_{A2} = 0.4$, this is not however seen in the fast and medium reactions which both reach $\phi_{A1} = 0.0$ and $\phi_{A2} = 0.5$ within the time scale of the simulation. If however the simulation was allowed to continue to much greater τ the slow reaction would also reach 100% conversion, not seen here because the change has become infinitesimally small and to run the simulation for such a great length of time is computationally expensive. The results shown in figure 5.8 are again shown in figure 5.9 but here we have scaled the τ axis by k for each rate of reaction.

104
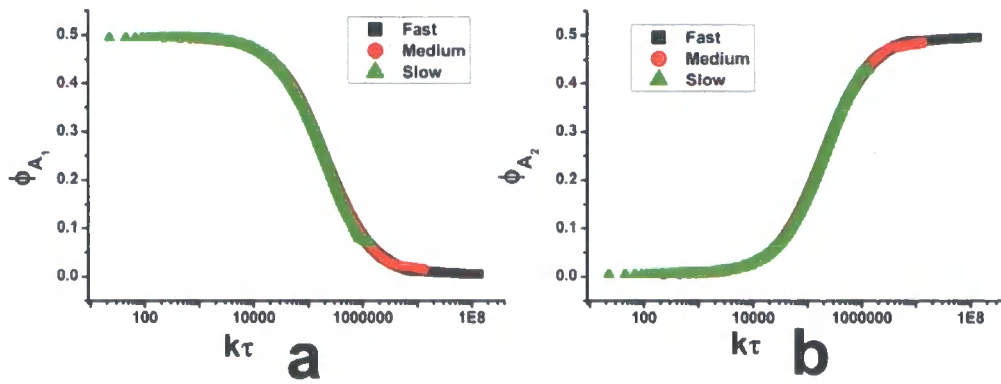
Figure 5.9

Reaction pathway for (a) $\bar{\phi}_1$ and (b) $\bar{\phi}_2$ for the three different reaction rates where the τ axis is scaled by k for each reaction rate.

Figure 5.9 shows that for each reaction rate the curves collapse onto a master curve, suggesting that the overall reaction is unaffected by the phase separation process and the resultant heterogeneous chemical kinetics. The same process is also undertaken for $\bar{\phi}_{n\max}$ and $\bar{\phi}_{n\min}$ for components A_1 and A_2 in figure 5.10.
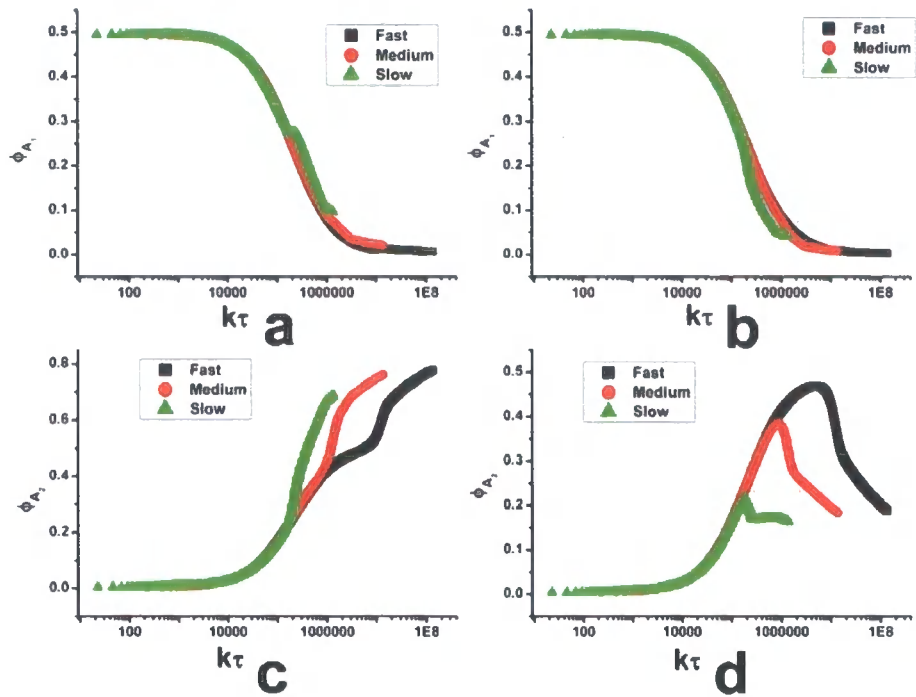
Figure 5.10

Reaction pathway for (a) $\bar{\phi}_{A_1 \max}$, (b) $\bar{\phi}_{A_1 \min}$, (c) $\bar{\phi}_{A_2 \max}$ and (d) $\bar{\phi}_{A_2 \min}$ for the three different reaction rates where the τ axis is scaled by k for each reaction rate.

In figure 5.10 we see that the curves are equivalent at small τ, however at higher τ we find that the curves for each reaction rate start to deviate from one another. This indicates that the reaction rate in each phase is affected by the process of phase separation because in the phase separated regions the rate of reaction increases or decreases as more or less of each component is available for polymerisation. The deviation is greatest for the slow reaction as a greater extent of phase separation occurs at lower conversion, as described below.

5.2.4 Conversion
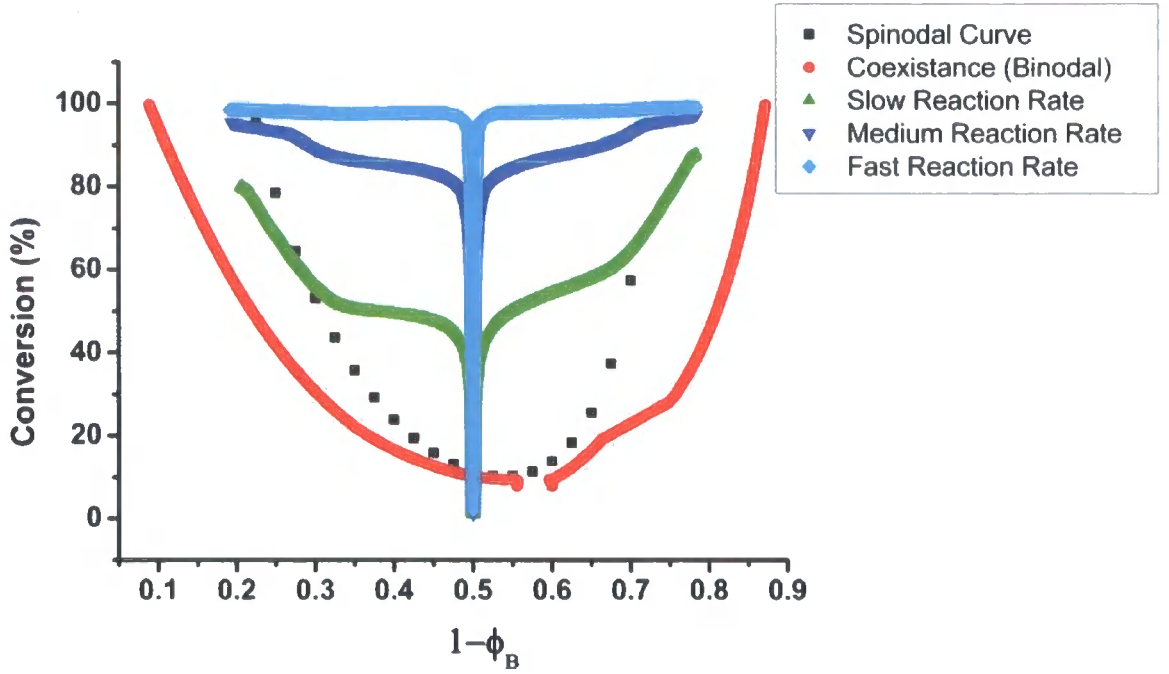
Figure 5.11

Conversion vs. 1-ϕ_B for three rates of reaction.

The coexistence curve for this system, as shown in figure 5.11, was found by equating the chemical potential of each blend component. The chemical potential in a polydisperse system is related to the free energy by[60],

$$\mu_m = f_{FH} + \sum_n (\delta_{nm} - \phi_n) \frac{\partial f_{FH}}{\partial \phi_n}, \qquad (5.2.2)$$

where n and m refer to any component of the blend and f_{FH} is defined by,

$$\frac{f_{FH}}{k_B T} = \sum_i \frac{\phi_i}{N_i} \ln \phi_i + \frac{\phi_B}{N_B} \ln \phi_B + \chi \left(\sum_i \phi_i \right) \phi_B, \qquad (5.2.3)$$

Substitution of equation 5.2.3 into equation 5.2.2 gives,

$$\mu_{A1} = \frac{1}{N_{A1}}[1 + \ln \phi_{A1}] - \frac{\phi_{A1}}{N_{A1}} - \frac{\phi_{A2}}{N_{A2}} - \frac{\phi_B}{N_B} + \chi \phi_B^2, \qquad (5.2.4)$$

$$\mu_{A2} = \frac{1}{N_{A2}}[1 + \ln \phi_{A2}] - \frac{\phi_{A1}}{N_{A1}} - \frac{\phi_{A2}}{N_{A2}} - \frac{\phi_B}{N_B} + \chi \phi_B^2, \qquad (5.2.5)$$

$$\mu_B = \frac{1}{N_B}[1 + \ln \phi_B] - \frac{\phi_{A1}}{N_{A1}} - \frac{\phi_{A2}}{N_{A2}} - \frac{\phi_B}{N_B} + \chi(1 - \phi_B)^2, \qquad (5.2.6)$$

On the coexistence curve, $\mu_{A1}' = \mu_{A1}''$, $\mu_{A2}' = \mu_{A2}''$ and $\mu_B' = \mu_B''$ where $'$ and $''$ denote the two coexisting phases. By setting $\mu_{A1}' - \mu_{A1}'' = 0$, $\mu_{A2}' - \mu_{A2}'' = 0$ and $\mu_B' - \mu_B'' = 0$ and by solving the three resulting simultaneous equations we can find values for ϕ_{A1}', ϕ_{A1}'', ϕ_{A2}', ϕ_{A2}'' as a function of conversion. Note that the condition of materials balance reduces the four unknowns to three.

The spinodal curve, given by equation 1.1.11, is shown with conversion data for the three reaction rates. These values are found using equations 5.2.7 and 5.2.8 for each reaction rate and are plotted against $1 - \overline{\phi}_{B\max}$ and $1 - \overline{\phi}_{B\min}$ respectively.

$$P_{\max} = \frac{\phi_{A2\max}}{\phi_{A1\max} + \phi_{A2\max}}, \qquad (5.2.7)$$

$$P_{\min} = \frac{\phi_{A2\min}}{\phi_{A1\min} + \phi_{A2\min}}, \qquad (5.2.8)$$

where P is conversion.

The phase separated composition, at each rate shown, tends towards an equivalent value of ϕ. For the fast reaction it can be seen that nearly 100% conversion is achieved prior to any significant phase separation but for the slow reaction only ~40% conversion is achieved prior to phase separation with the remainder of the conversion occurring during the phase separation process. For the medium reaction rate, where the reaction rate is of the order of the phase separation rate, it can be seen that the maximum extent of phase separation in terms of the difference between the compositions of the phases occurs at the same time as 100% conversion is approached.

5.2.5   Phase Separation in the 65:35 Blend

A polymer blend wherein N_{A1}, N_{A2} and N_B are as above but with (different) initial compositions, $\phi_1 = 0.645$, $\phi_2 = 0.005$ and $\phi_B = 0.35$, i.e. a 65:35 blend, is also studied.   Here the interaction parameter χ is again equal to χ_s which for 0% conversion for the 65:35 blend is 0.00341.   After 100% conversion $\chi = 0.00229$ so that the blend again moves immediately into the two phase region with increasing conversion.

Figure 5.12 shows the reaction pathway for the three reaction rates, fast, medium and slow as above, when a blend with a 65:35 composition is used.   The results shown are analogous to those shown in figure 5.8.   Figure 5.13 shows a plot of conversion vs. $1-\phi_B$ for these three reactions with the 65:35 blend composition.
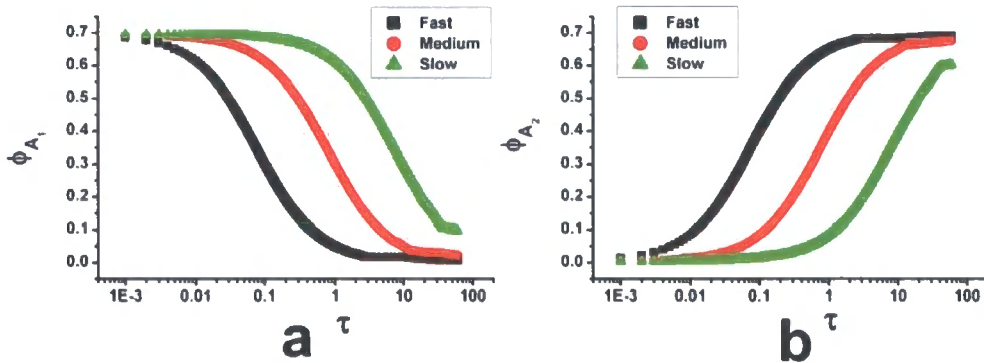
Figure 5.12

Reaction pathway for (a) component A_1 and (b) component A_2 for three reaction rates.
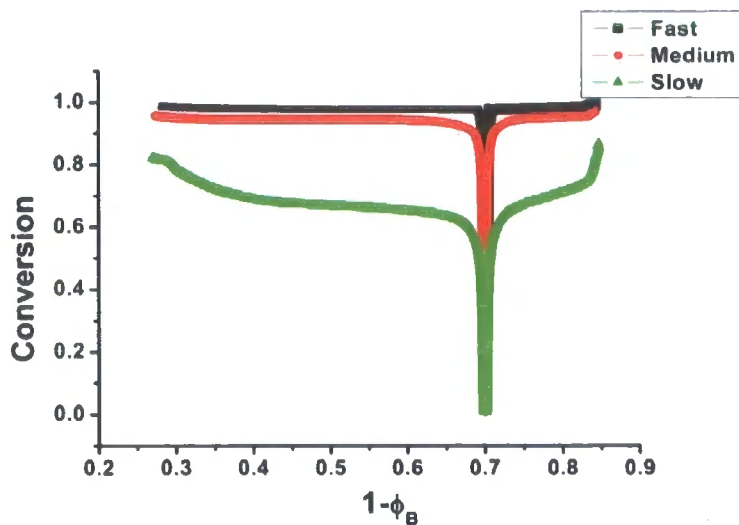
Figure 5.13

Conversion vs. 1-ϕ_B for three rates of reaction.

To quantify the effect of reaction rates we determine the value of conversion at which 10% phase separation has occurred for various rates for the 50:50 blend and also for the 65:35 blend. Whilst this choice is purely arbitrary it does allow insight into the relative behaviour of the blends and the results are shown in figure 5.14.
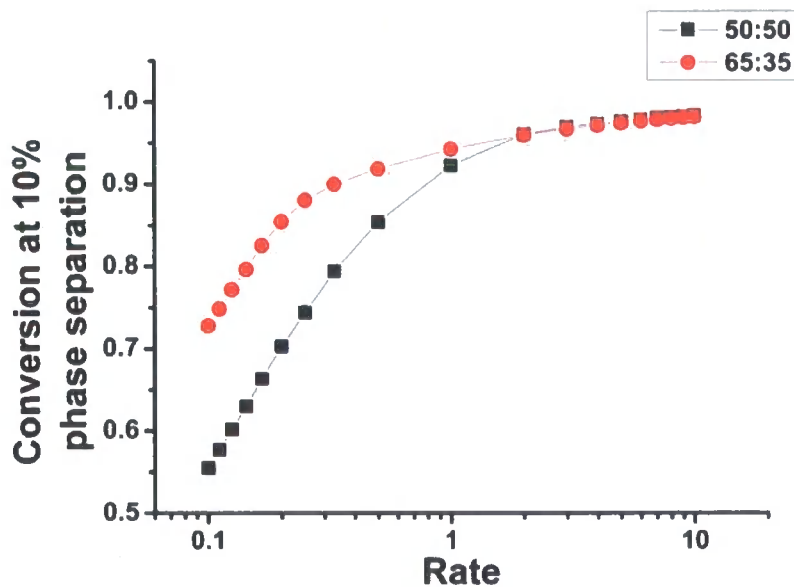
Figure 5.14

Conversion at which 10% phase separation has occurred vs. rate for a 50:50 blend and a 65:35 blend.

From figure 5.14 it can be seen that for the 65:35 blend a greater extent of reaction is necessary for the blend to develop significant phase separation. It is also clear that as the rate increases the conversion also increases, as would be expected.

5.3   The Quaternary Model

The model is now extended to include a further reaction, i.e. $A_1 \rightarrow A_2 \rightarrow A_3$, where the initial system is set such that $\chi = \chi_s$. A "slow" reaction rate is used in each case with $N_{A1} = 500$, $N_{A2} = 2000$, $N_B = 750$ and N_{A3} is varied between 500 and 4000. A "slow" reaction rate is chosen in preference to a "fast" reaction rate as for "fast" reactions any difference in the results are not obvious as conversion has essentially reached 100% before phase separation occurs. The values of N_{A3} have been chosen to give a broad range of results and so that they can be directly compared to the quaternary case below where we include the formation of a semi-IPN. For computational convenience a ternary blend is used until $\overline{\phi}_{A2} = 0.1$, then the data is transferred into a quaternary model where initially $\phi_{A3} = 0.0$. The reason for undertaking such a process is that in the models that include network formation, to be described in the next section, the network is only allowed to form once a particular value of ϕ_{A2} (in this case $\overline{\phi}_{A2} = 0.1$) has been reached. We wish to directly compare the two cases when network formation occurs and when it does not, so the same methodology is used in each case.

Once again all the results are averaged over 5 runs with noise of magnitude ± 0.0001 added every 100 time steps to mimic the thermal fluctuations found in real systems. The simulations are carried out on a two-dimensional 128^2 array with $\Delta\tau = 0.00001$ and $\Delta x = 0.5$. The value of χ is determined only by the values of N_{A1}, N_{A2} and N_B so that the scaling of equation 5.1.1 is the same for each case when N_{A3} is varied. The final value of χ_s is found by assuming all of component A_1 is converted to component A_2 and by not considering the conversion to component A_3, thus the quench depth is the same for each simulation and a direct comparison of the effect of varying N_{A3} is possible. In the simulation $\chi = \chi_s$ at 0% percent conversion, $\chi_s = 0.00328$ for the 50:50 blend. The final value of χ_s at 100% conversion is 0.00183 showing that the system has moved into the two phase region.

5.3.1 Morphology Growth in the 50:50 Blend

The growth of the morphology as the simulation proceeds is shown in figure 5.15 and we can compare the morphology of each component of the blend at different times, as in figure 5.16.
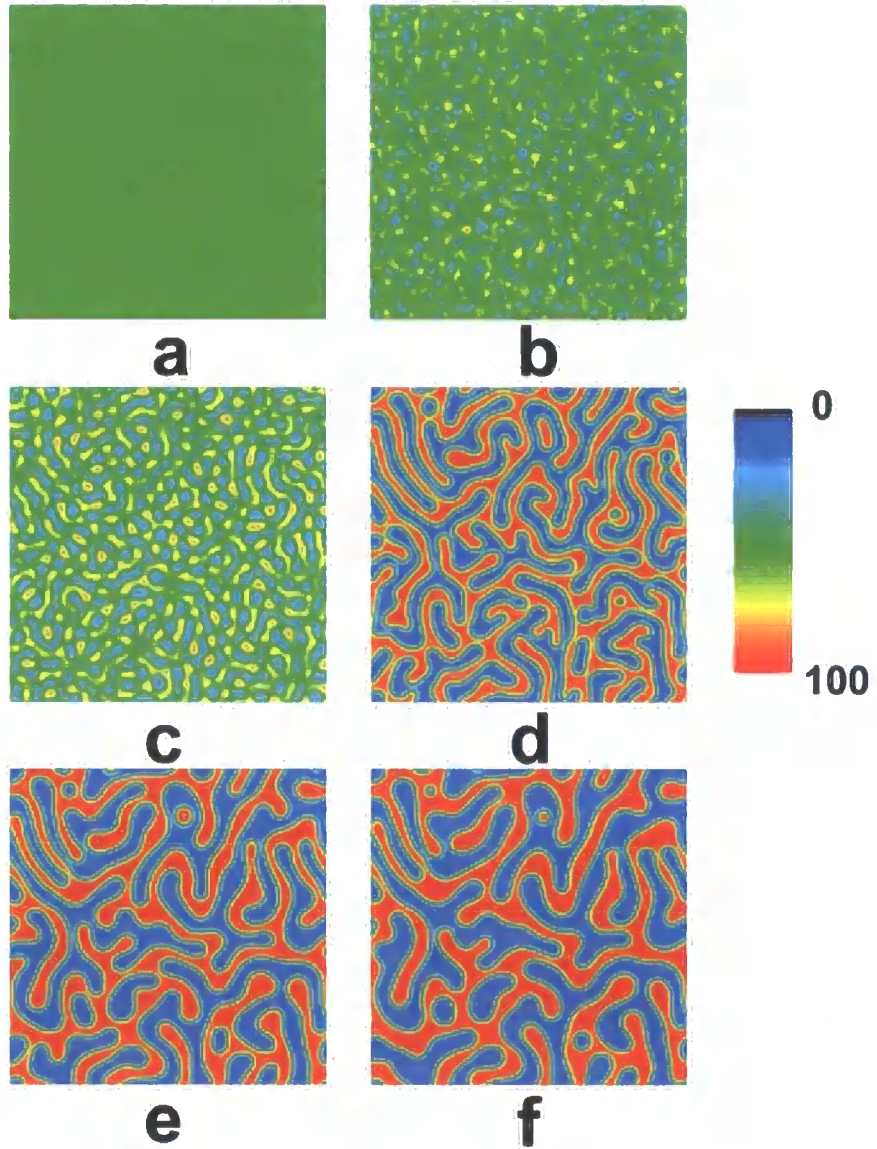

Figure 5.15

Morphology of component B at (a) $\tau = 0.1$, (b) $\tau = 1$, (c) $\tau = 10$, (d) $\tau = 40$, (e) $\tau = 80$ and (f) $\tau = 120$ for a blend in which $N_{A1} = 500$, $N_{A2} = 2000$, $N_{A3} = 4000$ and $N_B = 750$.
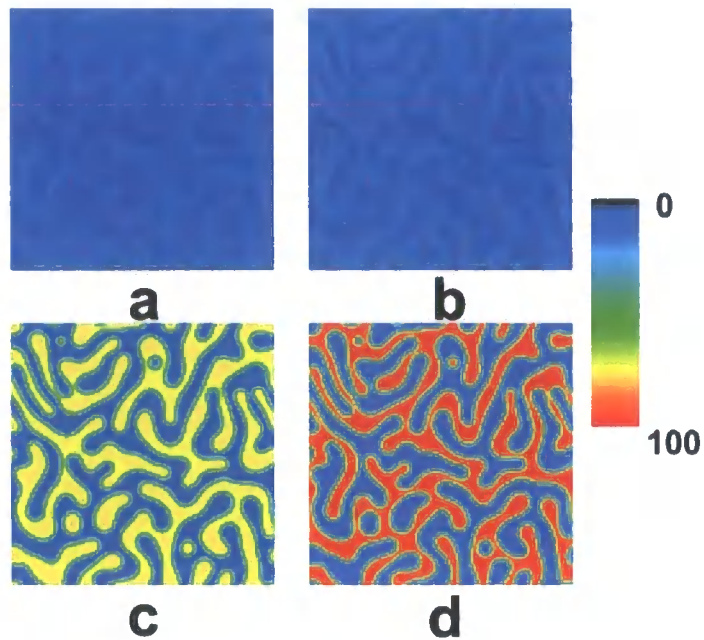
Figure 5.16

Morphology of blend at $\tau = 120$ for (a) component A_1, (b) component A_2, (c) component A_3 and (d) component B for a slow ($k = R(q_m)/10$) conversion rate where $N_{A1} = 500$, $N_{A2} = 2000$, $N_{A3} = 4000$ and $N_B = 750$.

Figure 5.16 shows that very little of components A_1 and A_2 remain at the end of the simulation.

5.3.2 The Reaction Pathway

We can once again follow the reaction pathway for the blend to quantify this situation, as shown in figure 5.17.
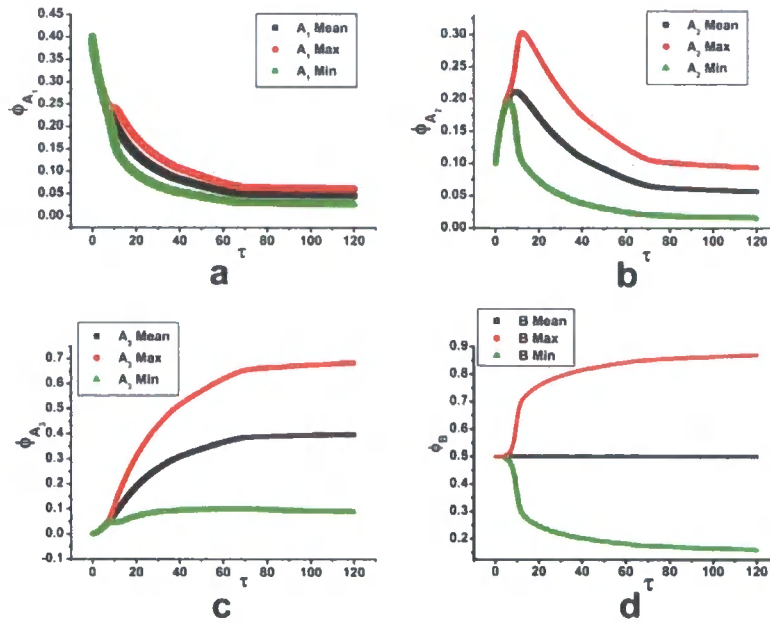
Figure 5.17

Reaction pathway for (a) component A_1, (b) component A_2, (c) component A_3 and (d) component B for a slow ($k = R(\mathbf{q}_m)/10$) conversion rate where $N_{A1} = 500$, $N_{A2} = 2000$, $N_{A3} = 4000$ and $N_B = 750$. $\overline{\phi}_n$ is represented by ■, $\overline{\phi}_{n\max}$ is represented by ●

and $\overline{\phi}_{n\min}$ is represented by ▲.

From figure 5.17 we can again see a decrease in the amount of component A_1 with time as it undergoes a reaction to component A_2. The amount of component A_2 increases initially but after $\tau = 10$ this values decreases due to the conversion to component A_3. From the reaction pathway the point of phase separation can again clearly be seen at around $\tau = 10$ as the values of $\overline{\phi}_{n\max}$ and $\overline{\phi}_{n\min}$ rapidly deviate from $\overline{\phi}_n$ at this point.

5.3.3 The Structural Growth Rate

The structure factor is shown in figure 5.18 for the case where $N_{A3} = 4000$.
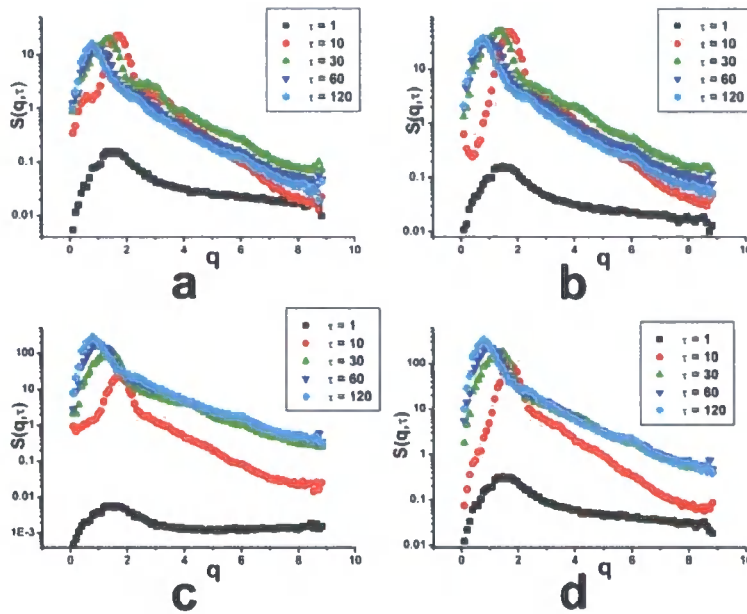
Figure 5.18

Growth of structure factor with time for (a) component A_1, (b) component A_2, (c) component A_3 and (d) component B for slow ($k = R(\mathbf{q}_m)/10$) conversion rate when $N_{A1} = 500$, $N_{A2} = 2000$, $N_{A3} = 4000$ and $N_B = 750$.

Figure 5.18 shows the peak in the structure factor shifting to the left in each case, indicating domain broadening. At late times the magnitude of the peak also decreases in figures 5.18(a) and 5.18(b), this could be due to reduction in the volume fraction of components A_1 and A_2. The maximum value of the structure factor $S(\mathbf{q},\tau)_{max}$ and $<q_1>$ are shown in figure 5.19.
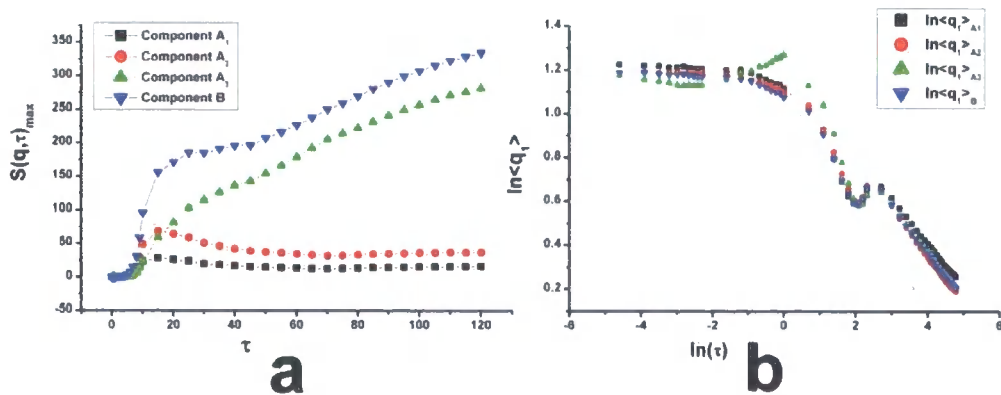
Figure 5.19

$S(q,\tau)_{max}$ vs. τ and (b) $ln<q_1>$ vs. ln (τ) for each component of the polymer blend when $N_{A1} = 500$, $N_{A2} = 2000$, $N_{A3} = 4000$ and $N_B = 750$.

By examining figure 5.19 it can be seen that at the start of the reaction very little phase separation occurs in each component of the polymer blend. As τ increases, the value of $S(\mathbf{q},\tau)_{max}$ also increases, however because components A_1 and A_2 are being converted by the reaction to create components A_2 and A_3 respectively, the value of $S(\mathbf{q},\tau)_{max}$ in each case reaches a maximum value before decreasing and then becoming constant. The values of $S(\mathbf{q},\tau)_{max}$ for components A_3 and B increase as the domains in the morphology increase their compositional purity. The graph of $ln<q_1>$ vs. $ln(\tau)$ shows that the domain growth is minimal to start with, as little phase separation has occurred, but then as we move deeper into the two phase region the domain growth rapidly increases. The two time regions around $ln(\tau) = 0.5$-2.0 and $ln(\tau) = 2.5$-4.5 have been isolated and the growth rates in each case for component B have been found in figure 5.20.
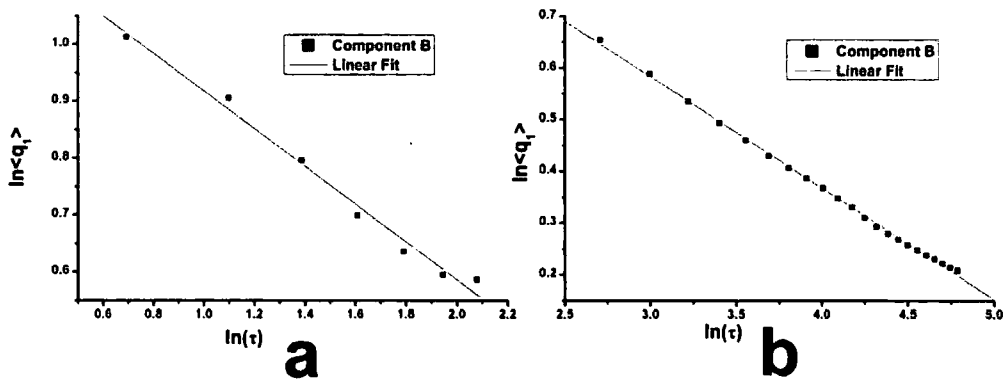
116

Figure 5.20

$\ln<q_1>$ vs. $\ln(\tau)$ for component B in the range (a) $\ln(\tau) = 0.5$-2.0 and (b) $\ln(\tau) = 2.5$-4.5. The fitted lines have a growth exponent of (a) $\alpha = \frac{1}{3}$ and (b) $\alpha = \frac{1}{5}$.

Figure 5.20(a) shows phase separation with a growth rate of $\alpha = \frac{1}{3}$ as expected for late stage growth in a system with a conserved order parameter, however at $\ln(\tau) \approx 3$ the growth rate undergoes a change, firstly increasing corresponding to a decrease in the domain growth and then decreasing again with a slower growth rate of $\alpha = \frac{1}{5}$. The time at which this change occurs is around $\tau = 70$ which we can see from figure 5.17 corresponds to the point at which the reaction becomes infinitesimal.

5.3.4 Conversion

A graph of conversion vs. 1-ϕ_B is plotted in figure 5.21 for five different values of N_{A3}.

117
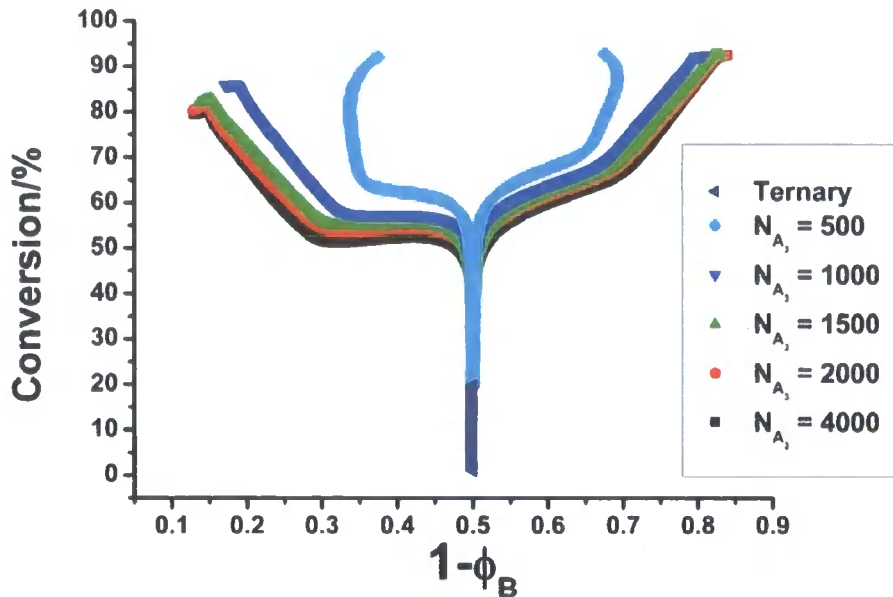
Figure 5.21

Conversion vs. 1-ϕ_B for five different N_{A3} values.

The ternary simulation is shown in figure 5.21, here the simulation is allowed to run from 0% conversion to the point at which $\overline{\phi}_{A2} = 0.1$, after this point component A_3 is formed in the quaternary simulation. We see that an increase in N_{A3} leads to a quicker phase separation process; this is expected because an increase in N_{A3} creates a greater driving force for phase separation to occur. The greater driving force is due to the fact that with a larger N_{A3} value we have longer polymer chains interacting with the other polymeric components, these chains have lower mobility so they diffuse at a reduced rate but the driving force for phase separation becomes the dominating effect, leading to a more rapid phase separation process. For interest, figure 5.21 also shows the situation when $N_{A3} = 500$, as component A_3 is formed the phase separation process reverses and the system starts to phase mix again. This is because the value of N_{A3} is now less than that of N_{A2}, simplistically representing chain scission for example. However the main reason for including the scenario is that during the crosslinking process it is possible for the degree of polymerisation between crosslinks to be less than the degree of polymerisation of the precursor polymers if there are multiple crosslinking sites per chain. The spinodal curves for the system when 100% of component A_3 is formed are shown in figure 5.22, from this it is clear that the driving force for phase separation increases with increasing N_{A3}, and why phase re-mixing occurs when $N_{A3} = 500$.
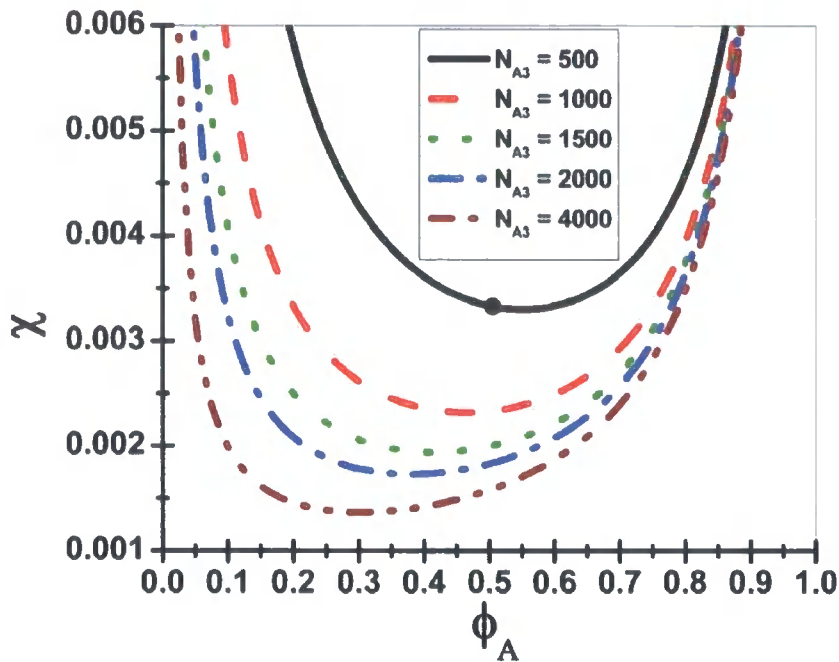
Figure 5.22

Spinodal curves for systems with 100% component A_3 formed for five different
values of N_{A3}. The value of χ for our simulations is represented by •.

It is worth noting that the values attained for the maximum amount of phase
separation in each phase of the blend refer to the coexistence (binodal) curve (not
calculated for the quaternary blend) in each case, not the spinodal curve shown in
figure 5.22, it is also noted that 100% conversion is never reached in these
simulations.

5.3.5   Morphology Growth in the 65:35 Blend

As with the results for the ternary blend we again model an off critical
(65:35) blend undergoing phase separation via the same mechanism as that shown
above. Here $N_{A1} = 500$, $N_{A2} = 2000$, $N_B = 750$ and N_{A3} is varied as before, $\chi =$
$0.00362 = \chi_s$ of the un-reacted blend and at 100% reaction of component A_2 $\chi_s =$
0.00279. The results are averaged over 5 runs with noise of magnitude ± 0.0001
added every 100 time steps to mimic the thermal fluctuations found in real systems.
The simulations are carried out on a two-dimensional 128^2 array with $\Delta \tau = 0.00001$

and $\Delta x = 0.5$. The "reaction pathway" of the system is shown in figure 5.23 and the results mirror those of the 50:50 blend.
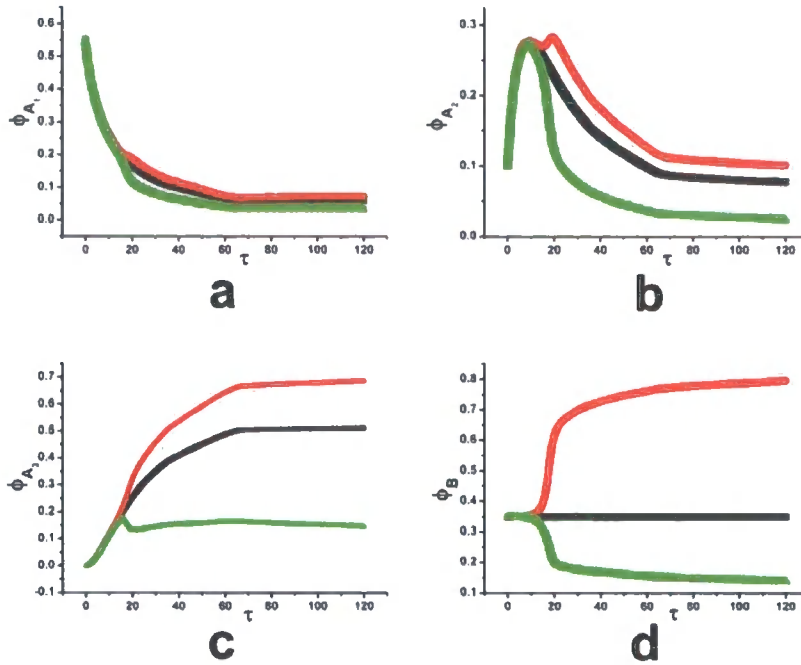

Figure 5.23

Reaction pathway for (a) component A_1, (b) component A_2, (c) component A_3 and (d) component B for a 65:35 blend with a slow ($k = R(q_m)/10$) conversion rate where $N_{A1} = 500$, $N_{A2} = 2000$, $N_{A3} = 4000$ and $N_B = 750$. $\bar{\phi}_n$ is represented by ■, $\bar{\phi}_{n\,max}$ is represented by • and $\bar{\phi}_{n\,min}$ is represented by ▲.

The point of phase separation can clearly be seen, but appears to occur at greater τ than in the 50:50 blend, around $\tau = 20$ in this case, this is due to the change in the values of χ used when changing from a 50:50 blend to a 65:35 blend and agrees with the result shown in figure 5.14.

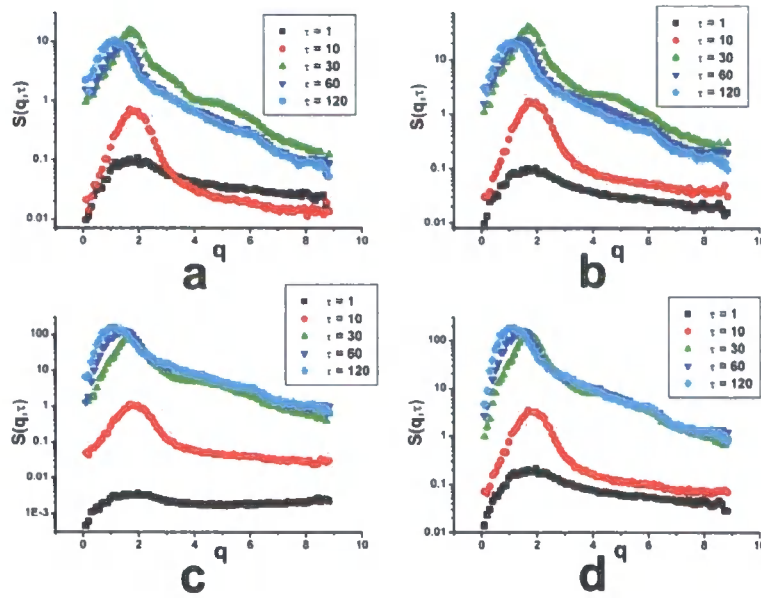The corresponding structure factors are shown in figure 5.24.

Figure 5.24

Growth of structure factor with time for (a) component A_1, (b) component A_2, (c) component A_3 and (d) component B for a 65:35 blend using a slow ($k = R(\mathbf{q}_m)/10$) conversion rate when $N_{A1} = 500$, $N_{A2} = 2000$, $N_{A3} = 4000$ and $N_B = 750$.

When the results in figure 5.24 are compared to those in figure 5.18 we see that $S(\mathbf{q},\tau)$ for $\tau = 10$ in this case seems to have a lesser value than in the case of the 50:50 blend, this again leads us to the conclusion that the formation of the morphology in the 65:35 blend takes a greater amount of time. The maximum value of the structure factor and $<q_1>$ are shown in figure 5.25.
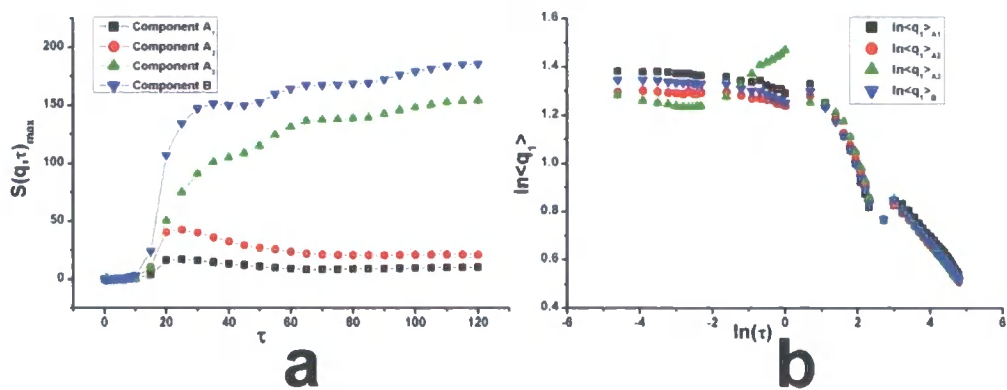
Figure 5.25

(a) S($\mathbf{q}$,τ) vs. τ for each component of the polymer blend and (b) ln<q_1> vs. ln(τ) for component B of a 65:35 polymer blend when N_{A1} = 500, N_{A2} = 2000, N_{A3} = 4000 and N_B = 750.

The results shown here are comparable to those shown in figure 5.19, two regions around ln(τ) = 1.0-3.0 and ln(τ) = 3.0-4.5 are again isolated and the growth rates in each case for component B are found. The growth exponents found are α = $\frac{1}{3}$ and α = $\frac{1}{6}$ respectively and are shown in figure 5.26.
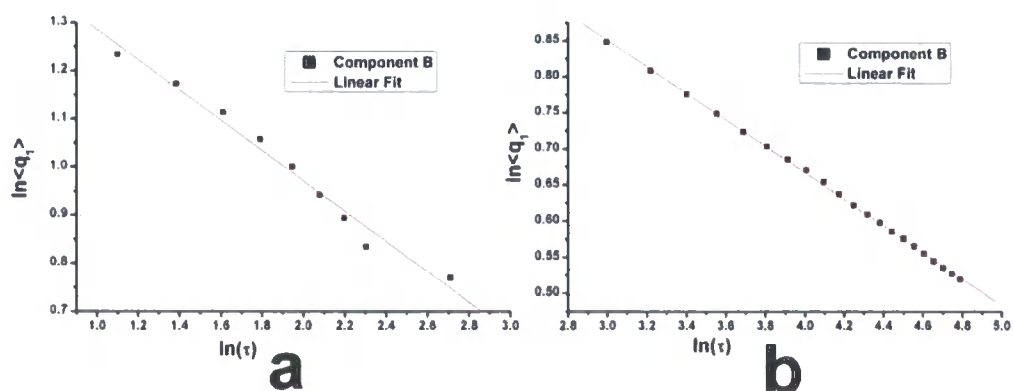
Figure 5.26

ln<q_1> vs. ln(τ) for component B in the range (a) ln(τ) = 1.0-3.0 and (b) ln(τ) = 3.0-4.5. The fitted lines have a growth exponent of (a) α = $\frac{1}{3}$ and (b) α = $\frac{1}{6}$.

Finally a plot of conversion vs. composition of the two phases is shown in figure 5.27.
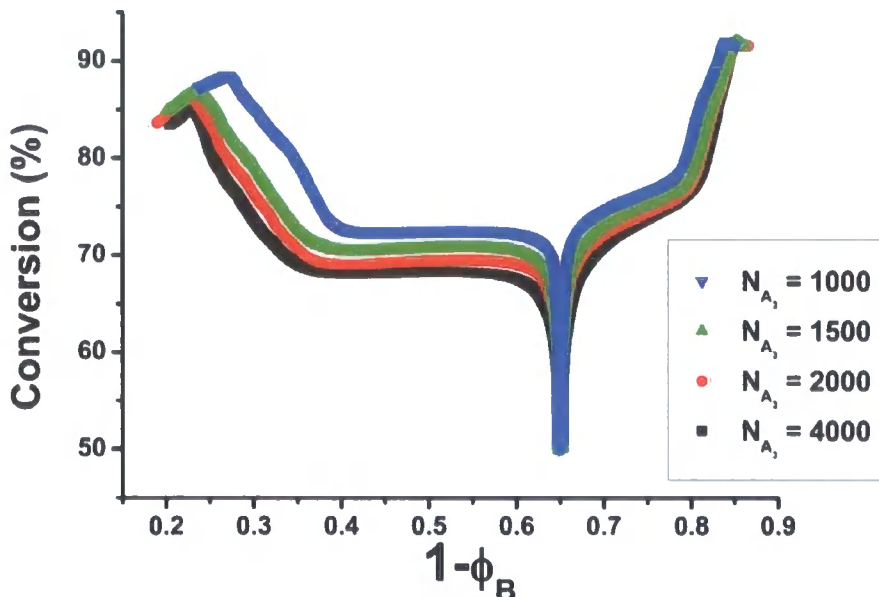

Figure 5.27

Conversion vs. $1-\phi_B$ for four different N_{A3} values in a 65:35 polymer blend.

It can be seen from figure 5.27 that the trend observed for the 50:50 blend is again present, i.e. as N_{A3} is increased the driving force for phase separation is increased and phase separation occurs at a lower conversion. It seems from the graph that the conversion decreases at high phase separation, this result seems to arise as a consequence of preferred segregation of the high molecular weight component into the A-rich phase.

5.4 The Quaternary Model Including Semi-IPN Interactions in Component A_3

Finally simulations in which component A_3 includes the elastic free energy and entropy associated with a cross-linked polymer network are undertaken. This is believed to be a minimal model for most technologically relevant RIPS processes. As we have one cross-linked polymer network formed in the presence of a linear polymer, B, we create a semi interpenetrating polymer network. The methodology used for the quaternary blend above is again used here with a ternary simulation

undertaken until $\overline{\phi}_{A2} = 0.1$, at which time a network is allowed to start forming. The simulation is carried out on a 128^2 array with $\Delta x = 0.5$ and $\Delta \tau = 0.00001$ with noise of ± 0.0001 added every 100 time steps. The mobility, λ, of the network component in equation 2.4.11, is set to be zero as the network is considered to be infinitely large and diffusion is not possible. Equation 5.1.3 is used in place of equation 5.1.1 when the dynamics of component A_3 are modelled. As a reminder, N_{A3} represents the degree of polymerisation between crosslink's.

5.4.1 Morphology Growth in the 50:50 Blend

The growth of the morphology can be seen in figure 5.28 and the final morphologies of each component in figure 5.29.
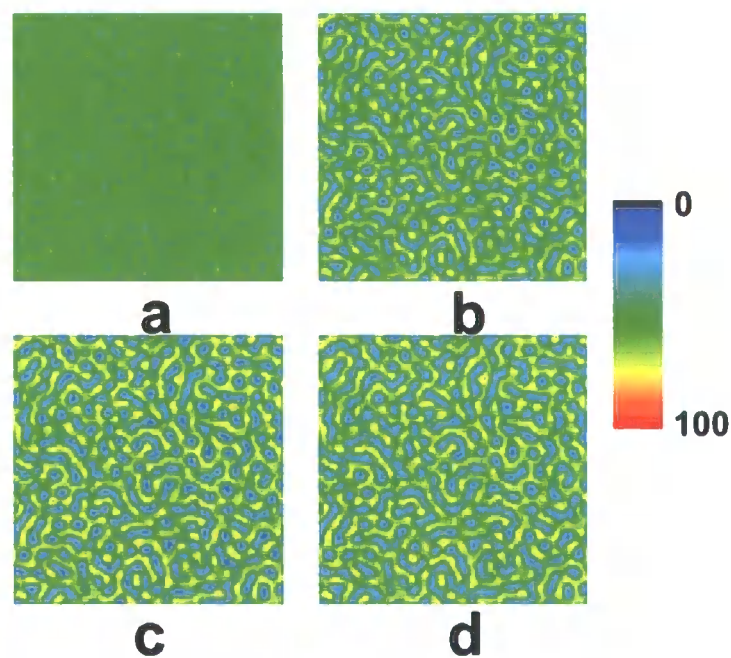

Figure 5.28

Morphology of component B at (a) $\tau = 10$, (b) $\tau = 40$, (c) $\tau = 80$ and (d) $\tau = 120$ for a blend in which $N_{A1} = 500$, $N_{A2} = 2000$, $N_{A3} = 4000$ and $N_B = 750$.
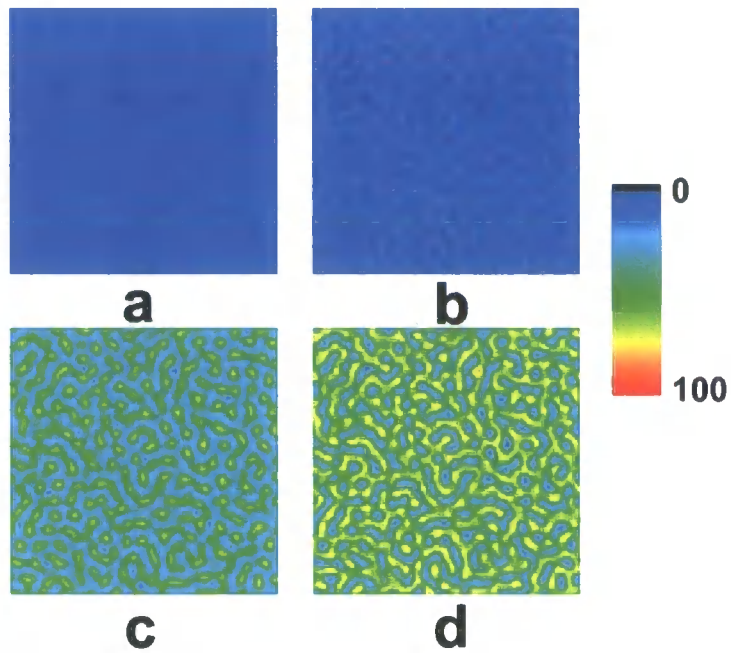
Figure 5.29

Morphology of blend at $\tau = 120$ for (a) component A_1, (b) component A_2, (c) component A_3 and (d) component B where $N_{A1} = 500$, $N_{A2} = 2000$, $N_{A3} = 4000$ and $N_B = 750$.

Figures 5.28 and 5.29 can be compared to figures 5.15 and 5.16 as all the variables are equal; it can be seen that the morphology of the network simulation is significantly less developed when compared to the morphology when no network is present, this suggests that the formation of a network is, as expected, constraining the process of phase separation.

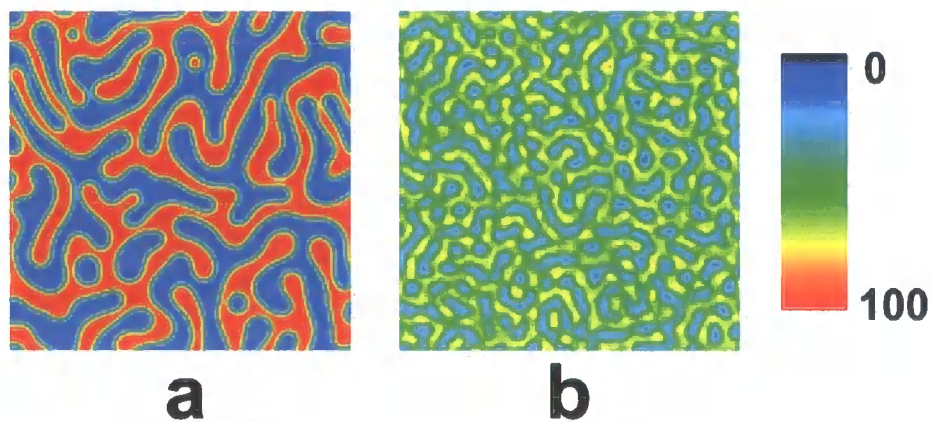A comparison of the final morphology for the two cases is shown in figure 5.30.

Figure 5.30

Comparison of the morphology of component B for a 50:50 blend when (a) no network is present and (b) a network is present in component A$_3$. N$_{A1}$ = 500, N$_{A2}$ = 2000, N$_{A3}$ = 4000 and N$_B$ = 750.

The comparison above shows that not only has the size of the domains been constrained because the mobility of the network is zero but also the amount of phase separation is reduced when a network is present because phase separation would mean the formation of a high energy state in component A$_3$. Also seen is disruption of the co-continuous nature of the morphology by network formation, with the B-rich phase breaking up into discrete but elongated droplets.

5.4.2 Interface Count

We have determined the amount of interface present throughout the simulation as this gives a direct measure of domain size within the system and is shown in figure 5.31.
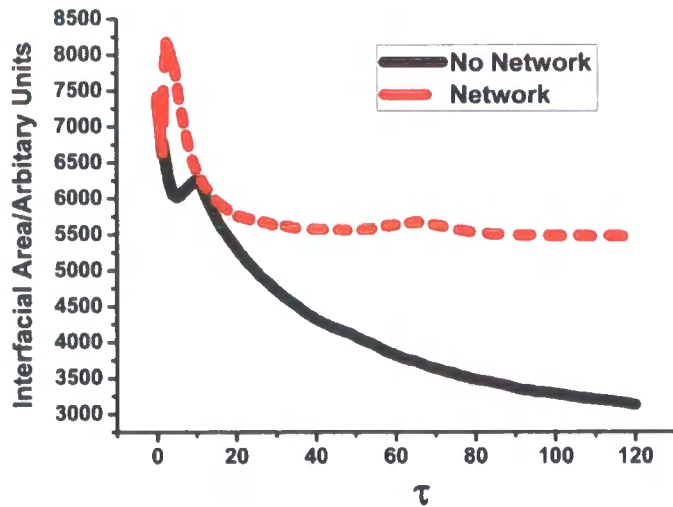
Figure 5.31

Interface count for a blend where no network formation (solid line) occurs and a blend where network formation (dashed line) does occur.

The difference in the amount of interface generated in each case can clearly be seen in figure 5.31, when no network is present the amount of interface continually reduces as the domains broaden with time. When network formation does occur we see much less reduction in the amount of interface present as the domains cannot broaden due to the elastic energy contribution to the free energy. To determine the interface count each array point is examined and if it is found to lie between two points which are either side of the array average then this point is counted as interface.

5.4.3 Conversion in the Presence of a Network

A graph of conversion vs. composition of the two phases for a blend undergoing network formation is shown in figure 5.32.
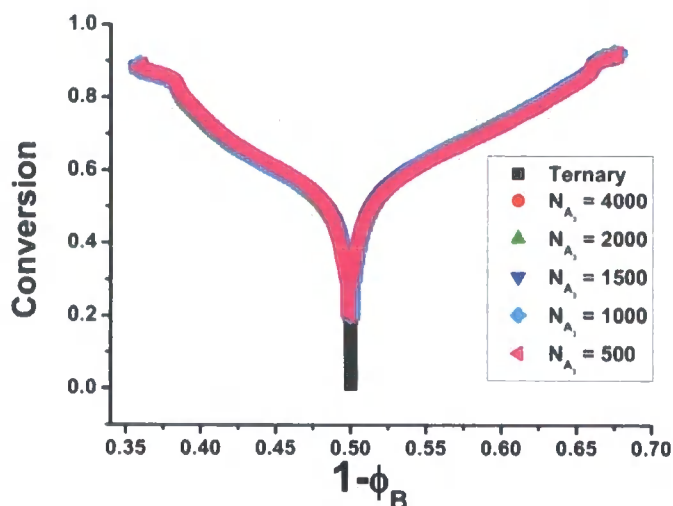
Figure 5.32

Conversion vs. 1-ϕ_B for five different N_{A3} values in a 50:50 polymer blend which forms a semi-IPN.

A comparison of the phase separation which occurs with conversion shows the same results for varying N_{A3} values, we believe this is because the phase separation shown in figure 5.32 results from the growth of the N_{A2} component and is therefore the same within random noise considerations. As component A_3 grows the phase separation is constrained by the network and therefore the phase separation process can no longer occur. We show a comparison of a system which does not form a network and one that does in figure 5.33.
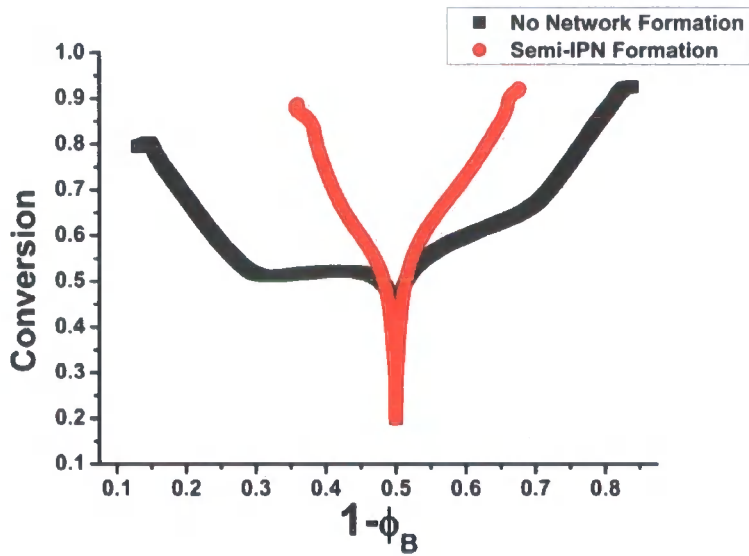
Figure 5.33

Comparison of conversion vs. $1-\phi_B$ for a system in which a network is formed and one where no network is formed when $N_{A3} = 4000$ in each case.

The amount of phase separation can be seen to be much greater in the case where no network is present; this result is comparable with the morphologies shown in figure 5.30.

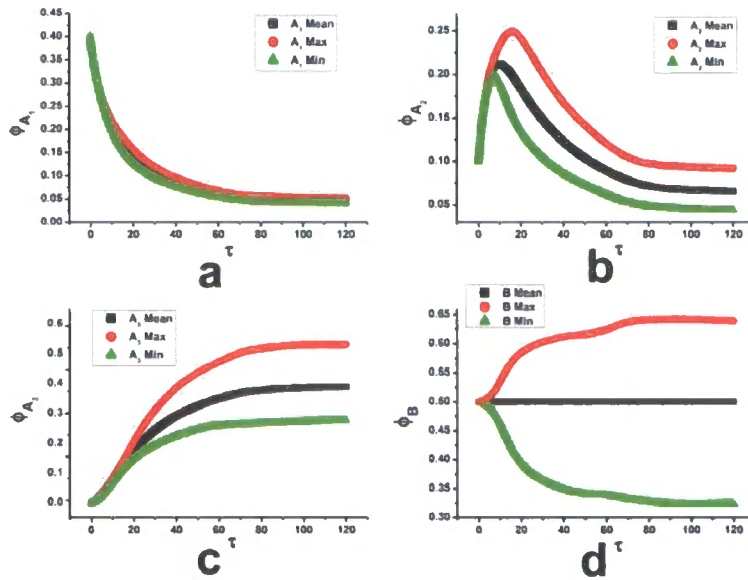The reaction pathway of the system is shown in figure 5.34.

Figure 5.34

Reaction pathway for (a) component A_1, (b) component A_2, (c) component A_3 and (d) component B for a slow ($k = R(q_m)/10$) conversion rate where $N_{A1} = 500$, $N_{A2} = 2000$, $N_{A3} = 4000$ and $N_B = 750$.

The trend shown above is analogous with that shown in figure 5.17 but the extent of phase separation in each phase is shown to be greatly reduced due to the formation of the network, i.e. phase separation to $\phi_B' = 0.9$ and $\phi_B'' = 0.1$ in the case of no network and phase separation to $\phi_B' = 0.65$ and $\phi_B'' = 0.35$ in the case where a network is present. The corresponding structure factors are shown in figure 5.35.
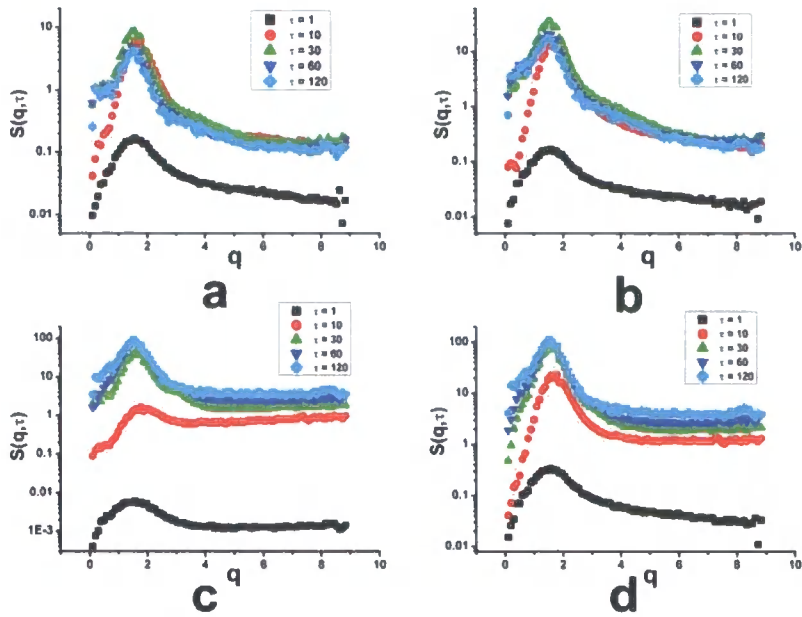
Figure 5.35

Growth of structure factor with time for (a) component A_1, (b) component A_2, (c) component A_3 and (d) component B for slow ($k = R(\mathbf{q_m})/10$) conversion rate when $N_{A1} = 500$, $N_{A2} = 2000$, $N_{A3} = 4000$ and $N_B = 750$.

It can be seen that the position of the peak does not seem to move to lower $\mathbf{q}$, this is because domain growth does not occur, as seen in figure 5.25. The maximum value of the structure factor and $\langle q_l \rangle$ are shown in figure 5.36.
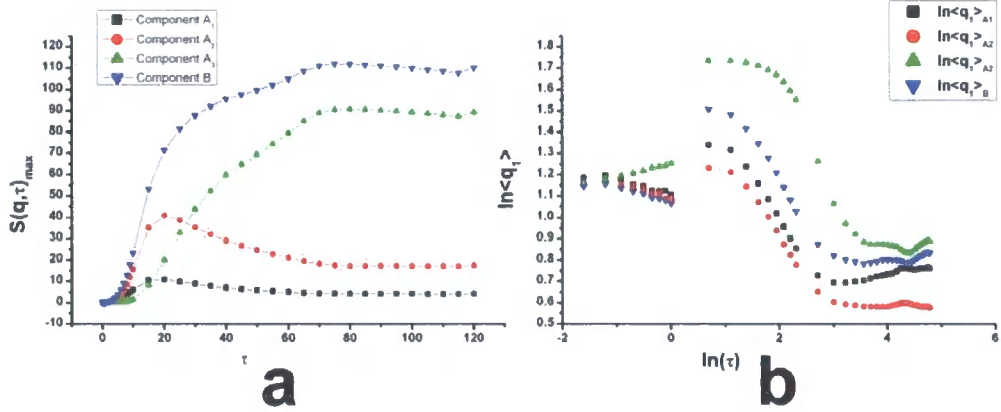
Figure 5.36

(a) $S(\mathbf{q},\tau)_{max}$ vs. τ for each component of the polymer blend and (b) $\ln{<}q_1{>}$ vs. $\ln(\tau)$ for each component of a 50:50 polymer blend when $N_{A1} = 500$, $N_{A2} = 2000$, $N_{A3} = 4000$ and $N_B = 750$.

If we compare figure 5.19(a) to figure 5.36(a) we find that the trend appears to be the same in each case but due to the reduced amount of phase separation in the latter case we find that the value of $S(\mathbf{q},\tau)_{max}$ is significantly smaller for components A_3 and B. The maximum value also starts to drop slightly in figure 5.36(a), this suggests that the system is starting to phase mix due to the elastic energy in the network becoming the key factor in the system. A comparison of figures 5.19(b) and 5.36(b) shows that a very different process is occurring, the point of rapid phase separation can be seen at $\ln(\tau) = 1$ but at very late times we see an upward trend in the results, indicating domain narrowing. We follow the growth rate for two areas of figure 5.36(b) corresponding to $\ln(\tau) = 1.5$-2.5 and $\ln(\tau) = 4.0$-5.0 in figure 5.37.
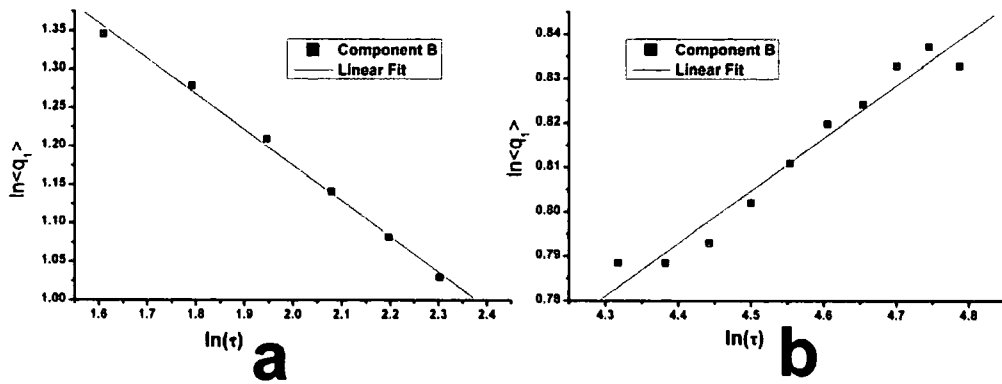
Figure 5.37

ln<q_1> vs. ln(τ) for component B in the range (a) ln(τ) = 1.5-2.5 and (b) ln(τ) = 4.0-5.0 The fitted lines have a growth exponent of (a) α = 0.46 and (b) α = -0.12.

Figure 5.37(a) shows a broadening of the domains with time; however the behaviour shown in figure 5.37(b) indicates a reduction in the domain morphology size due to the formation of the network system.

5.4.4   The 65:35 Blend

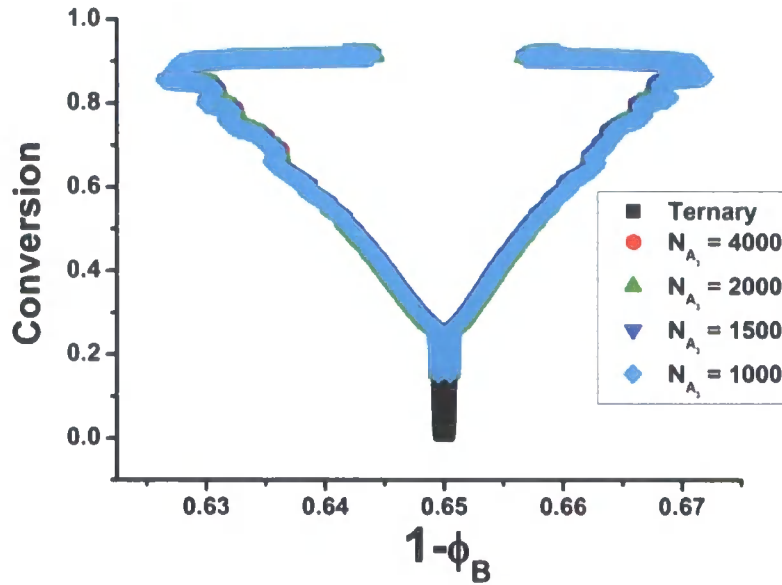The results of conversion in a 65:35 blend are presented in figure 5.38.

Figure 5.38

Conversion vs. $1-\phi_B$ for five different N_{A3} values in a 65:35 polymer blend which forms a semi-IPN. Note the scales on the composition axis.

We see a marked difference in the formation of the blend in this case; figure 5.38 shows us that as conversion increases very little phase separation takes place compared to previous systems. The phase separation would again be due to the formation of component A_2 but in this system we have more of the network component formed than in the previous case, therefore as the network forms the elastic energy becomes dominant in the system. The elastic energy therefore forces the system into its lowest energy state which in this case means undertaking phase mixing to reach a less phase separated equilibrium state. A comparison of the system with and without the network interactions is shown in figure 5.39, it can be seen that minimal phase separation takes place before the system moves to reduce the elastic energy by phase mixing.
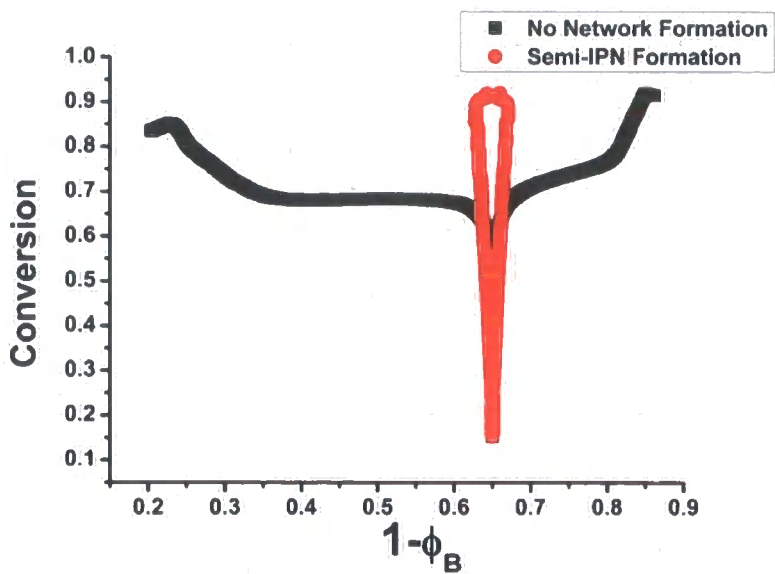
Figure 5.39

Comparison of conversion vs. 1-ϕ_B for a system in which a network is formed and one where no network is formed when $N_{A3} = 4000$ in each case.

By following the reaction pathway the amount of phase separation with time can be monitored.
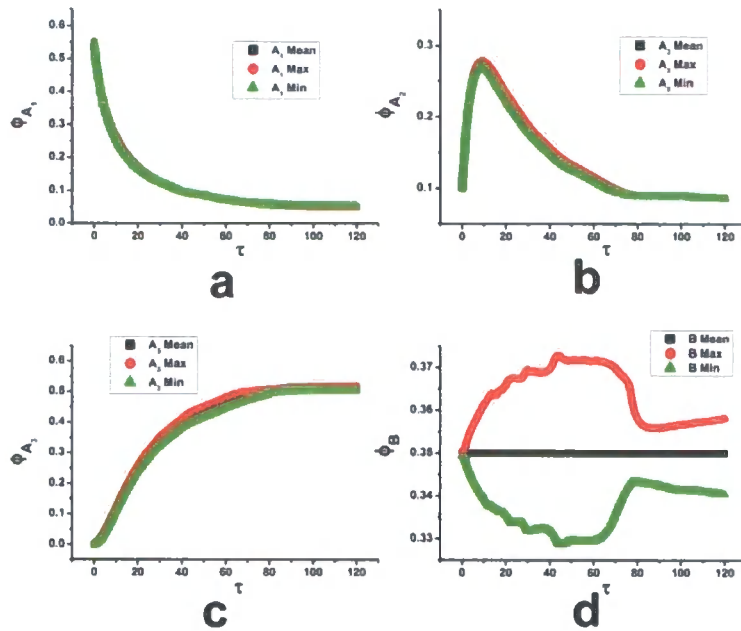
Figure 5.40

Reaction pathway for (a) component A_1, (b) component A_2, (c) component A3 and (d) component B for a slow ($k = R(q_m)/10$) conversion rate where $N_{A1} = 500$, $N_{A2} = 2000$, $N_{A3} = 4000$ and $N_B = 750$. $\bar{\phi}_n$ is represented by ■, $\bar{\phi}_{n\,max}$ is represented by ● and $\bar{\phi}_{n\,min}$ is represented by ▲.

Figure 5.40(d) shows phase separation occurring in component B, at around τ = 60 the elastic energy in component A_3 becomes dominant and the amount of phase separation rapidly decreases in component B to a minimum value before equilibration due to a compromise between the driving force for phase separation and the elastic energy term in the free energy of the blend. We also see that very little phase separation is able to occur in any component of the blend due to the network formation.
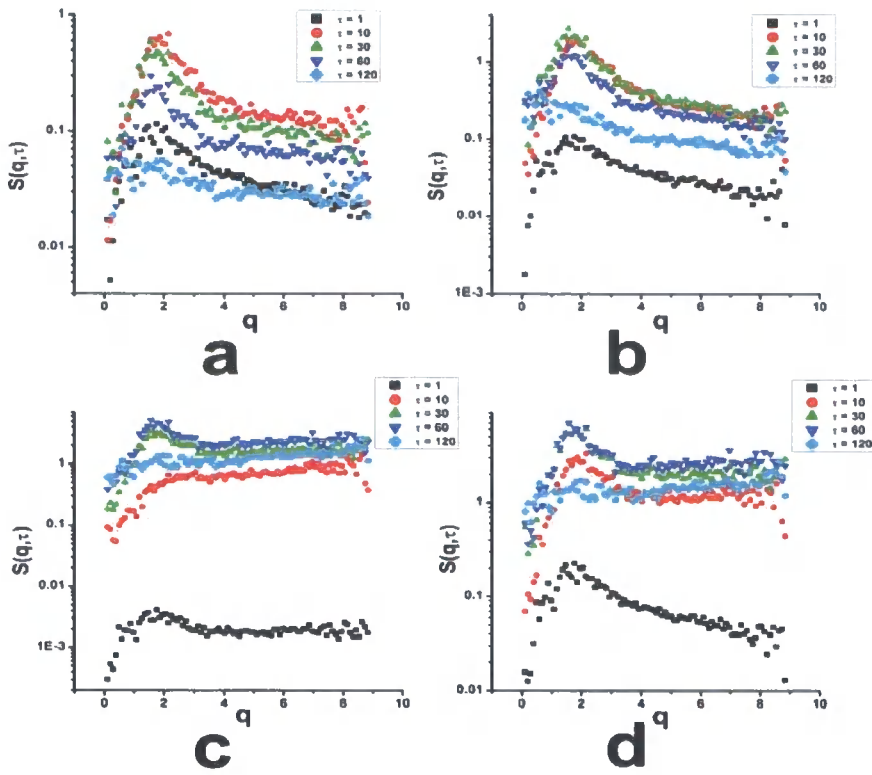
Figure 5.41

Growth of structure factor with time for (a) component A_1, (b) component A_2, (c) component A_3 and (d) component B for slow ($k = R(q_m)/10$) conversion rate when $N_{A1} = 500$, $N_{A2} = 2000$, $N_{A3} = 4000$ and $N_B = 750$.

The peak of the structure factor in figure 5.41 again does not shift to smaller wave-vectors indicating little domain growth in the system but the maximum value does increase as phase separation takes place. When compared to figure 5.17 it can be seen that the value of $S(q,\tau)_{max}$ is greatly reduced and the plots show greater amounts of noise, this is due to the minimal phase separation taking place as seen in figure 5.35. At $\tau = 60$ the structure factor decreases considerably in each case, notably in figure 5.41(a) $S(q,\tau)$ at $\tau = 120$ is below that of $\tau = 1$ indicating the phase mixing we see elsewhere.
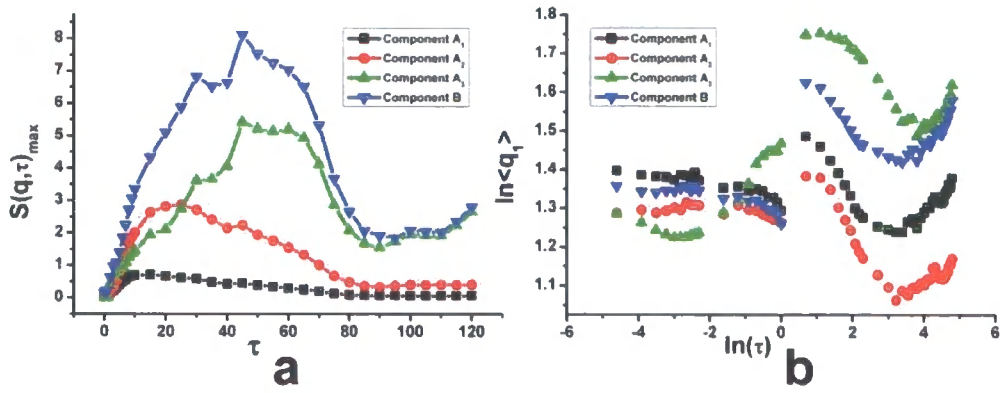
Figure 5.42

(a) $S(\mathbf{q},\tau)_{max}$ vs. τ for each component of the polymer blend and (b) $\ln\langle q_1 \rangle$ vs. $\ln(\tau)$ for each component of a 65:35 polymer blend when $N_{A1} = 500$, $N_{A2} = 2000$, $N_{A3} = 4000$ and $N_B = 750$.

Figure 5.42 shows that the maximum value of $S(\mathbf{q},\tau)$ once again rapidly decreases at around $\tau = 60$ but the value of $S(\mathbf{q},\tau)_{max}$ is significantly smaller than the corresponding values in figure 5.25. Unlike in previous systems the value of $S(\mathbf{q},\tau)_{max}$ for component A_1 also decreases with time to a value which is around the same as its start value. The results shown in figure 5.42(b) are comparable to those shown in figure 5.36, however they seem more pronounced in this case. Here we again see an indication of phase mixing in the later stages of the simulation, characterised in figure 5.43.
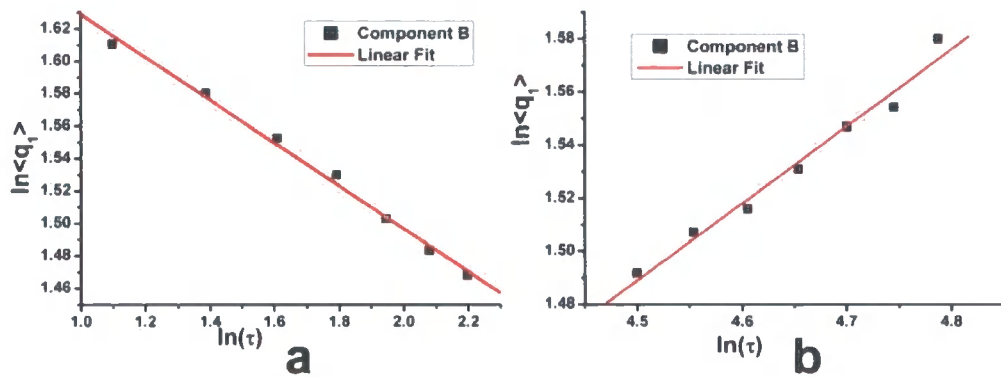
Figure 5.43

$\ln<q_1>$ vs. $\ln(\tau)$ for component B in the range (a) $\ln(\tau) = 1.0$-2.3 and (b) $\ln(\tau) = 4.5$-4.8. The fitted lines have a growth exponent of (a) $\alpha = 0.13$ and (b) $\alpha = -0.29$.

The growth exponent from figure 5.43(b) indicates phase mixing at a greater rate than that seen in figure 5.37, this result is in agreement with the other results presented here and adds further proof to our conclusion that the elastic energy interactions associated with the network formation constrain, and oppose, the phase separation process.
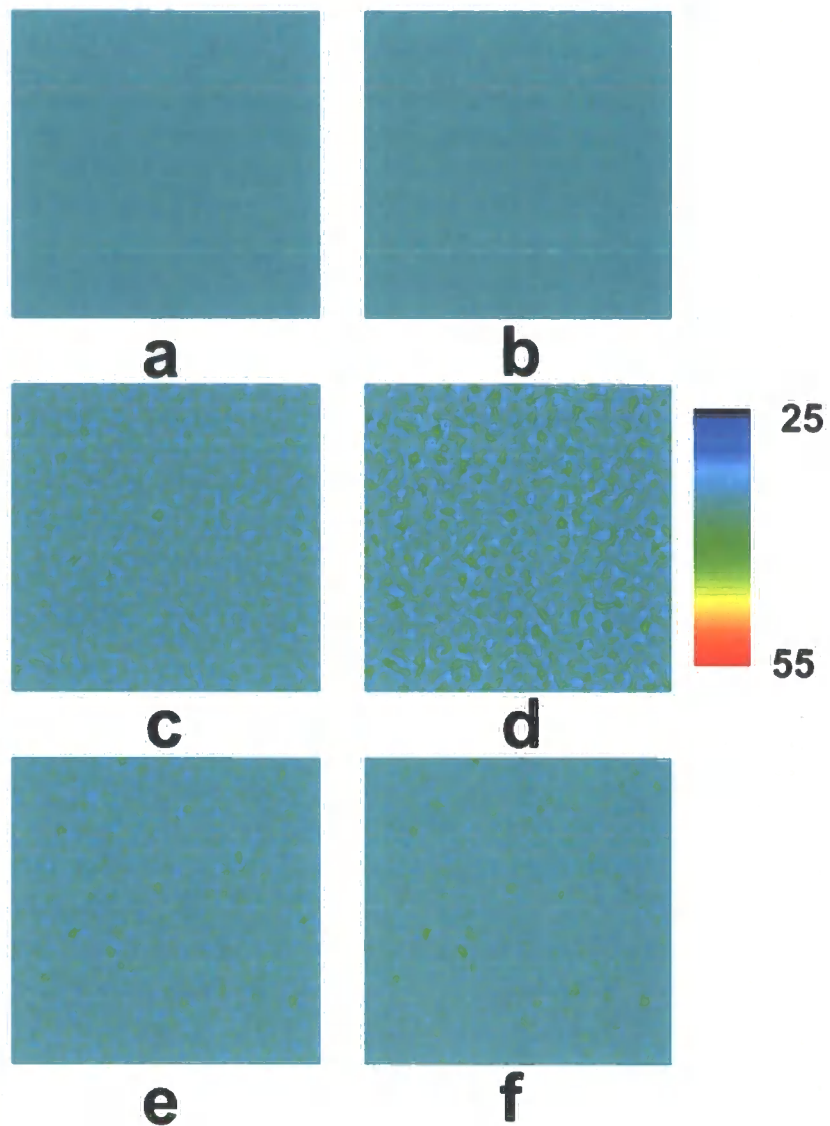
Figure 5.44

Morphology of component B at (a) $\tau = 0.1$, (b) $\tau = 1$, (c) $\tau = 10$, (d) $\tau = 40$, (e) $\tau = 80$ and (f) $\tau = 120$ for a blend in which $N_{A1} = 500$, $N_{A2} = 2000$, $N_{A3} = 4000$ and $N_B = 750$.

In figure 5.44 we see small domains have developed by $\tau = 80$ but the system then starts to phase mix and at $\tau = 120$ the domains, although still present, have decreased in size and phase purity.

5.5   Conclusions

We have developed a model to understand blends undergoing reaction induced phase separation, using theories developed for polydisperse polymer blends

to follow the reaction of a component, A, undergoing a series of changes in degree of polymerisation. This model can be used to study both ternary and quaternary blends undergoing phase separation and is extended to consider the effect of one of the components forming a network, creating a semi-interpenetrating polymer network with component B.

Whilst we present here what we believe to be a minimalist model that captures the underlying physical mechanisms involved in RIPS, we recognise that a number of features are missing. For example, in many processes grafting or copolymerisation between the A and B components occur; the viscosity increases can be several orders of magnitude; morphology growth is frozen by vitrification. The first of these could be dealt with within the framework of our model using an appropriate free energy and kinetic equation for the reaction. The second requires a different choice of the mobility coefficients, and the last effect could also be incorporated.

For the ternary polymer blend without network formation, we find that although the rate of the reaction affects the time at which phase separation occurs the system always tends to the same values of phase purity irrespective of when phase separation becomes significant. For a quaternary system, by changing the degree of polymerisation of component A_3 the extent of phase separation is affected, as the larger the degree of polymerisation, the greater the driving force for the phase separation process. The model has been extended to include the elastic energy associated with the formation of a polymer network, this energy is at a minimum when no deformation of the network is present, and therefore phase separation becomes a high energy process and is resisted by the network. We find that the degree of polymerisation of the network component has no effect on the phase separation process, because the network resists the phase separation process equally in each case. The system seeks an equilibrium free energy which is a compromise between the driving force for phase separation and the need for the system to resist deformation, by increasing the amount of network present the elastic energy term becomes more important so the system can phase mix after phase separation has occurred. The effect on the morphology is shown to be significant.

Chapter 6

Modelling Surface Directed Spinodal Decomposition

An important area of research into polymer blends concerns the formation of morphologies at or near to a surface. As stated previously polymer blends find wide ranging uses in adhesives, for example epoxies, and it is therefore important to know how the morphology evolves at the surface as this can affect the qualities of the adhesive. Firstly the model developed by following the method shown in chapter 2.7.1 is used to investigate the morphological formation at a uniform hard wall surface. Discrepancies are found within this model and a method is therefore proposed to physically remove them.

6.1   Modelling Surfaces in Polymer Blends

To simulate the effects of a surface on the polymer morphology the model needs to be set up in a manner which is slightly different to that seen in the previous chapters. As stated in chapter 2.7.1 two new, opposing, boundary conditions are used in the model, one which is given by equation 2.7.1, to dictate the competition between the surface attraction and the process of phase separation, on this wall and on the opposing wall a boundary condition given by $\Delta J|_{x=0} = 0$ is also used. Typically these conditions are used for the two parallel surfaces given by $x = 0$ and $x = x'$, periodic boundary conditions are applied at the $y = 0$ and $y = y'$ surfaces.

6.1.1   The Surface Model

To set the flux through the boundary to zero it is useful to understand in more detail how the dynamics of the simulation are calculated. An example of the array used in the simulation at a surface is shown in figure 6.1 and is used to illustrate how the $\Delta J|_{x=0} = 0$ equation is implemented.
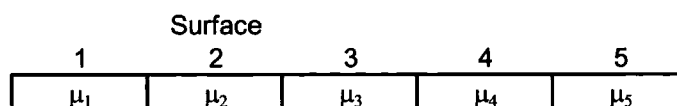
Surface

1	2	3	4	5
μ_1	μ_2	μ_3	μ_4	μ_5

Figure 6.1

One-dimensional illustration of the surface array set up

The surface is assumed to lie in array element 2, element 1 is used for the no flux boundary condition and μ is the chemical potential at each point. The flux between each element is given by,

$$J_i = \frac{\mu_{i+1} - \mu_i}{\Delta x},$$ (6.1.1)

The flux between element 1 and element 2 (J_1) should be equal to zero such that,

$$\mu_1 = \mu_2$$ (6.1.2)

and therefore the boundary condition needed to implement the no flux condition is,

$$\frac{\partial \phi_i}{\partial x} = 0 \stackrel{hence}{\Rightarrow} \phi_1 = \phi_2,$$ (6.1.3)

The change in ϕ with each time step at the surface is given by,

$$\frac{\partial \phi_i}{\partial \tau} = \frac{J_i - J_{i-1}}{\Delta x} = \frac{\mu_{i+1} + \mu_{i-1} - 2\mu_i}{\Delta x^2},$$ (6.1.4)

so that at the surface,

$$\frac{\partial \phi_2}{\partial \tau} = \frac{\mu_3 + \mu_1 - 2\mu_2}{\Delta x^2} = \frac{\mu_3 - \mu_2}{\Delta x^2},$$ (6.1.5)

as $\mu_1 = \mu_2$. The same method is used to set the flux through the surface at the other side of the array to zero, i.e. so that $\Delta J\big|_{x=x'} = 0$. In order to check that no flux passes through the two surfaces at $x = 0$ and $x = x'$ and in order to test the periodic boundary conditions of the $y = 0$ and $y = y'$ surfaces test simulations were undertaken on a 128^2 array with $\Delta\tau = 0.0025$ and $\Delta x = 0.5$ for a 50:50 blend where $N_A = N_B = 200$, an example of which is shown in figure 6.2.

Figure 6.2

Example morphology formed when no flux condition is applied on two opposing
sides of the simulation ($x = 0$ and $x = 128$) and periodic boundary conditions are used
on the remaining sides of the array ($y = 0$ and $y = 128$)

It can be seen in figure 6.2 that in the horizontal direction the array is not
periodic unlike in the vertical direction.

To implement the additional term to account for the surface attraction in the
system, i.e. for a mixture in which the surface causes an excess surface free energy,
we need to find the total free energy given by $F = F_B + F_S$[113]. By combining
equations 1.3.7 and 2.7.3 we arrive at two free energy equations, one for F_B and one
for F_S.

$$F_B = \int_0^\infty \left[\frac{\phi}{N} \ln \phi + \frac{1-\phi}{N} \ln(1-\phi) + \chi\phi(1-\phi) \right] + \frac{1}{36\phi(1-\phi)} (\nabla\phi)^2 \, dx,$$

(6.1.6)

$$F_S = \int_{-\infty}^\infty \left(-h_1\phi_1 - \frac{1}{2} g\phi_1^2 \right) d\mathbf{R},$$

(6.1.7)

144

Here the first two surface terms in the free energy are related to parameters in the FH lattice model by equations 2.7.11 and 2.7.12. This leads to an equation to describe the evolution of the surface term,

$$\frac{\partial \phi(\mathbf{x}, \tau)}{\partial \tau} = \left(-h_1 - g\phi + \gamma \frac{\partial \phi}{\partial \mathbf{x}}\bigg|_{\mathbf{x}=0} \right) \delta(\mathbf{x}) \qquad (6.1.8)$$

which is used with equation 1.3.10 to describe the evolution of the polymer phase separation at or near a surface. Here $\delta(\mathbf{x})$ is the Dirac-delta function which ensures that the surface free energy only affects the $\mathbf{x} = 0$ boundary. For consistency with previous models also included is a third term, dependent on γ, in the surface free energy which accounts for the energy cost of gradients in composition at the surface, and was derived on the basis of the Kawasaki spin-exchange model.

6.2 Morphological Development at and near to a Surface

The development of the morphology at a surface and in the bulk at small τ can be seen in more detail below when $\Delta\tau = 0.0025$, $\Delta\mathbf{x} = 0.5$ on a 128^2 array with h_1 = 1.5, $g = 0.1$ and $\gamma = 0.1$ with a noise value of $\pm$ 0.00001 added every 100 computational time steps.

6.2.1   The Initial Phase Separation at a Surface
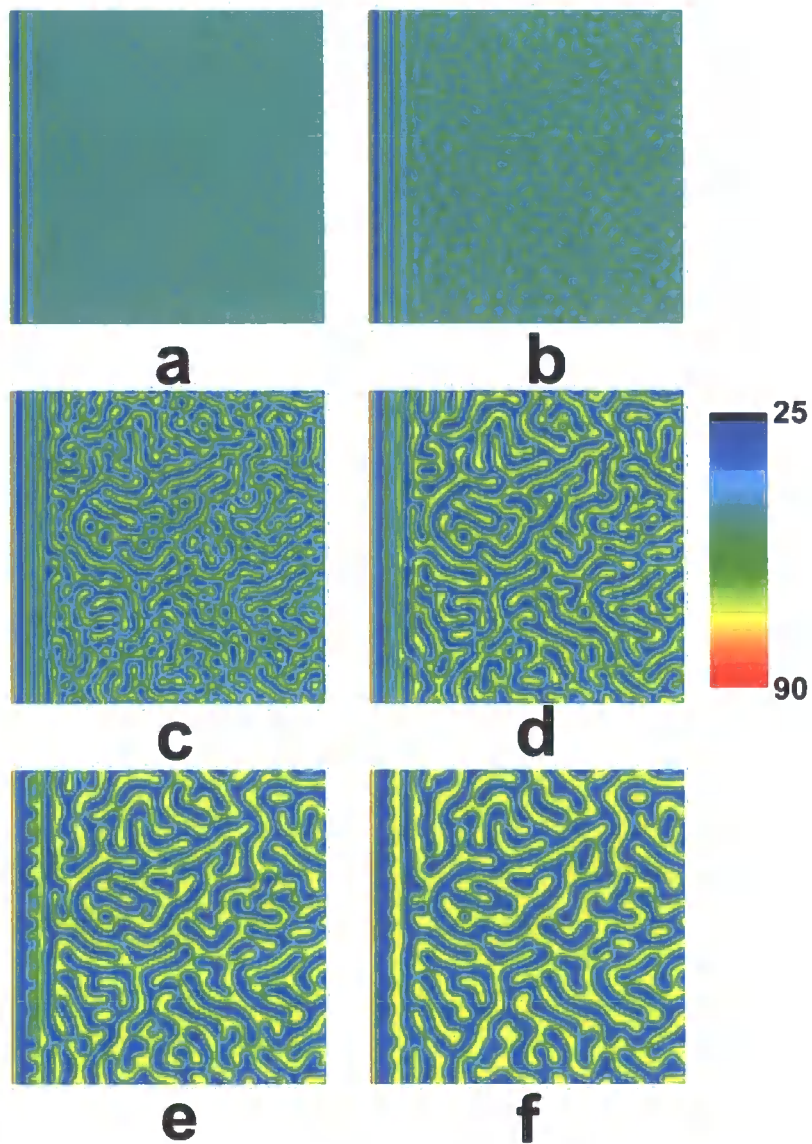
Figure 6.3

Development of the morphology at (a) $\tau = 1.25$, (b) $\tau = 2.5$, (c) $\tau = 5$, (d) $\tau = 7.5$, (e) $\tau = 10$ and (f) $\tau = 12.5$

It can be seen in figure 6.3 that in the early stages of phase separation an oscillating morphology is seen to form perpendicular to the surface outwards, this is because a depletion layer forms next to the surface layer which then leads to another layer of high volume fraction. Spinodal decomposition then occurs in the bulk and the oscillating surface morphology is seen to broaden to create fewer layers. This

process can be followed using depth profiling as undertaken experimentally using ion beam analysis[100,103,104].

Figure 6.4

Depth profile of morphology at various times corresponding to the time intervals seen in figure 6.3

The depth profile presented in figure 6.4 shows the growth of the morphology with time, the profile has been curtailed at **x** = 32 to improve clarity. The oscillating morphology near the surface can be seen to broaden and the phase separated morphology away from the surface can also be seen to grow with time.
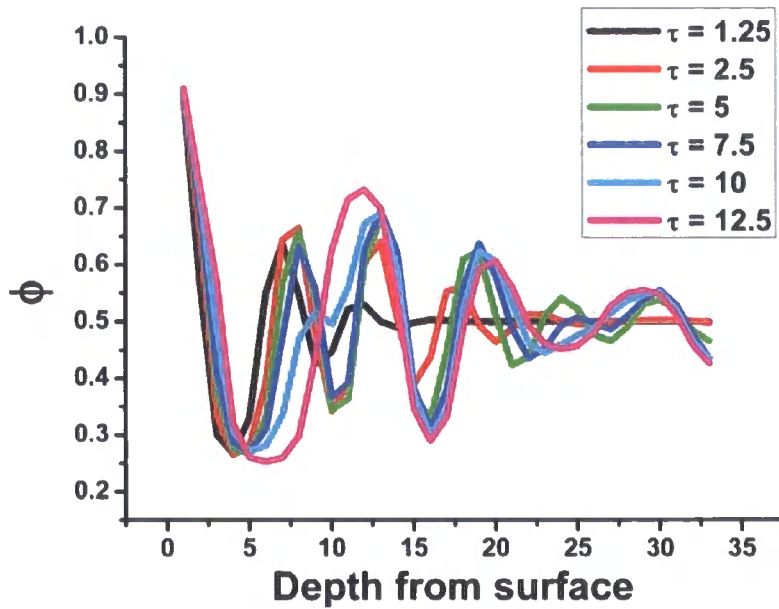
6.2.2 Phase Separation at Greater τ

Figure 6.5

Development of the morphology at (a) τ = 25, (b) τ = 125, (c) τ = 250, (d) τ = 500, (e) τ = 1250 and (f) τ = 2500

Figure 6.5 again shows the development of the polymer morphology, in this case for larger τ. Here we see a distinct broadening of the random co-continuous morphology in the bulk and a layered structure forming from the surface outwards. Here again the dynamics of the blend can be followed by depth profiling in figure 6.6.

Figure 6.6

Depth profile of morphology at various times corresponding to the time intervals seen in figure 6.5

Figure 6.6 shows a limited increase in the surface but a large broadening in the layered structure, as seen in figure 6.5.

6.2.3 The Effect of Altering the Surface Attraction

For comparison the morphologies formed when $h_1 = 0.6$, $g = 0.1$ and $\gamma = 0.1$ are shown in figure 6.7, here the attraction to the surface has been significantly decreased.
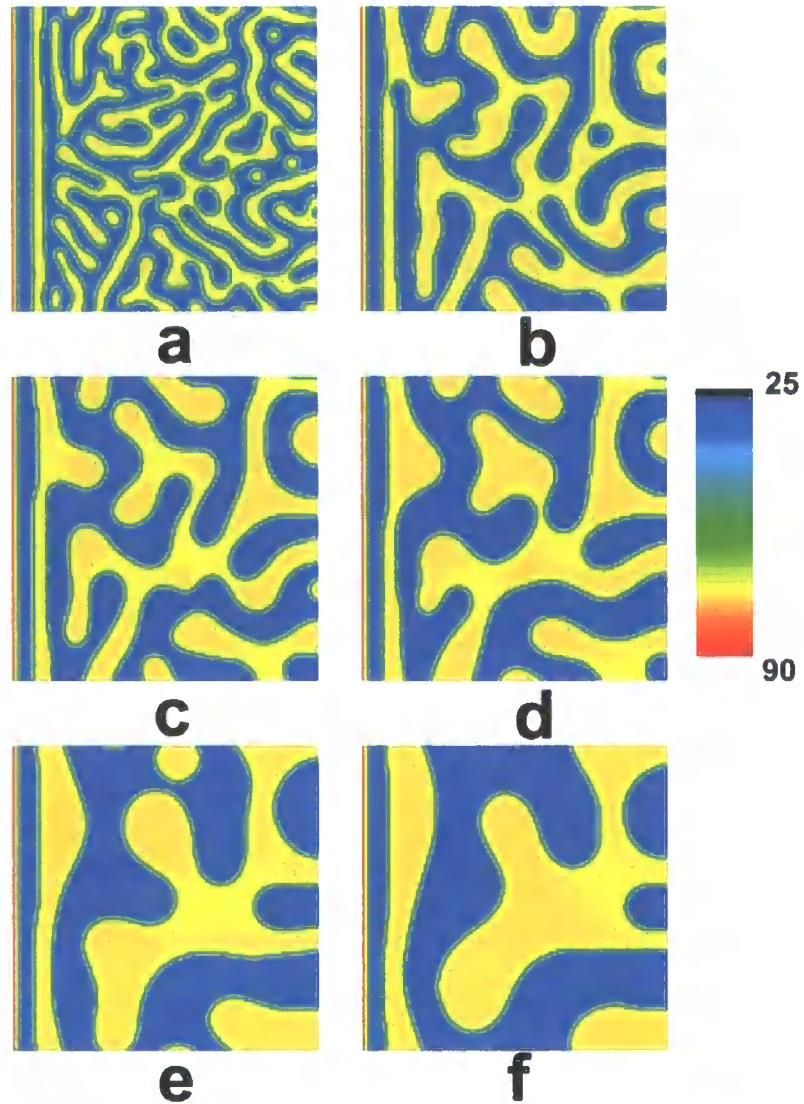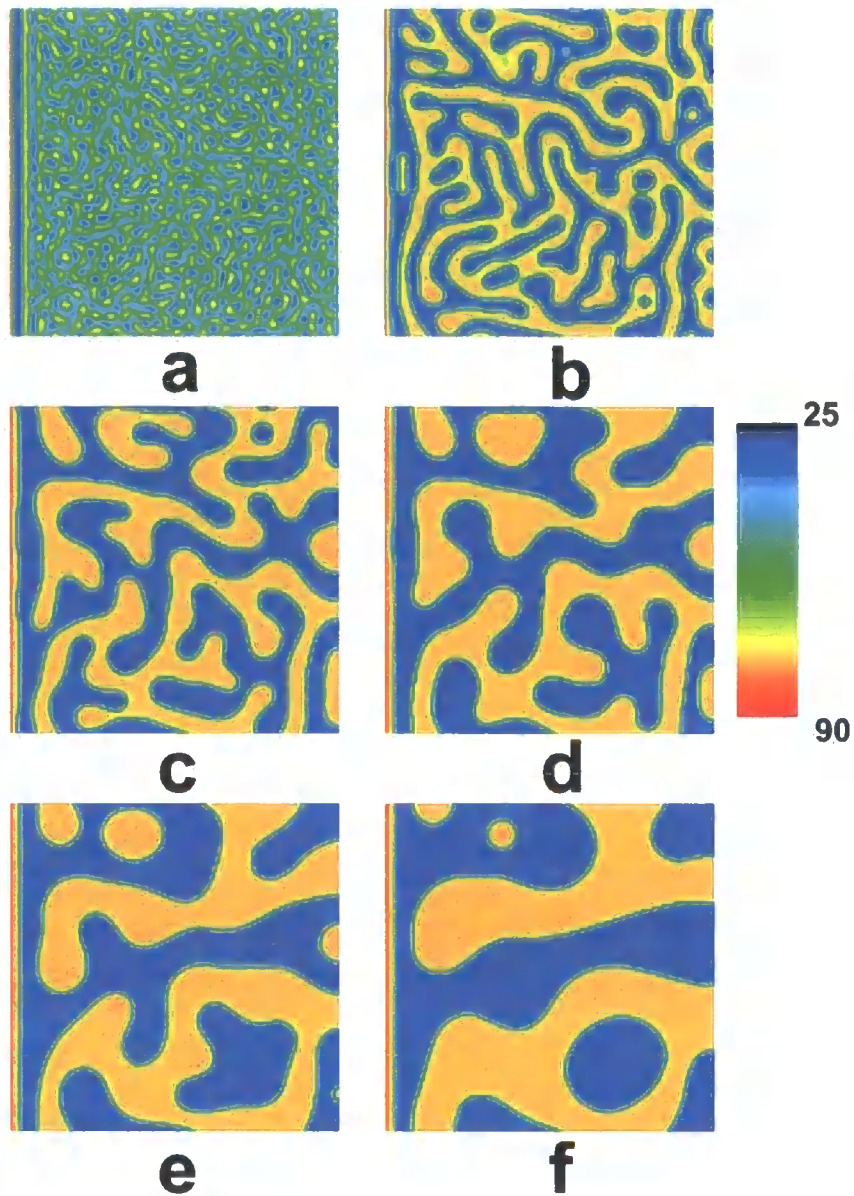
Figure 6.7

Development of the morphology at (a) $\tau = 2.5$, (b) $\tau = 25$, (c) $\tau = 125$, (d) $\tau = 250$, (e) $\tau = 1250$ and (f) $\tau = 2500$

In figure 6.7 we again see an oscillating morphology form near the surface in the early stages but as the surface attraction is reduced, in this case the phase separation process becomes more dominant than before and this oscillating morphology is lost. It is replaced by the random co-continuous morphology known from spinodal decomposition. We do however still see the surface layer followed by

a depletion layer and this growth is once again followed using depth profiling in figure 6.8.

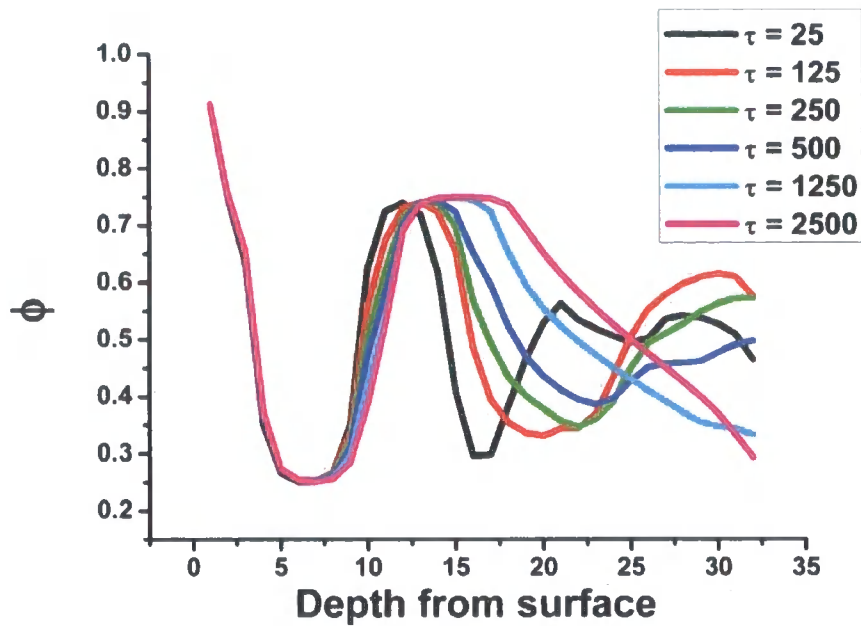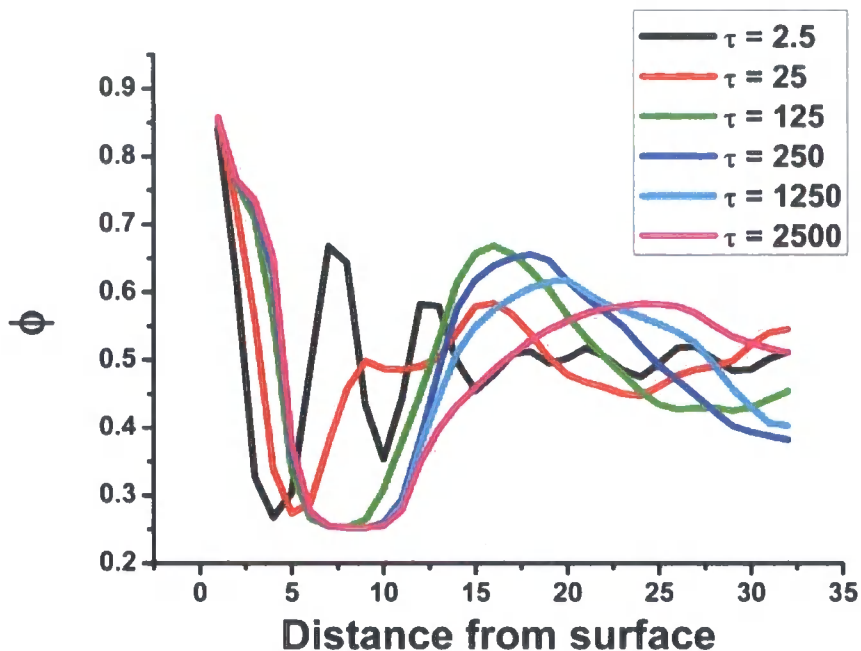*Figure 6.8*

Depth profile of morphology at various times corresponding to the time intervals seen in figure 6.7

In this case the surface attraction is weaker but we see a marked difference in the broadening of the surface when compared to figure 6.6. In figure 6.6 the surface undergoes rapid growth in the early stages, i.e. before $\tau = 25$, and then this growth rate distinctly decreases at later times, as seen in figures 6.4 and 6.6. In figure 6.8 however we see that the surface takes longer to undertake this initial broadening and the slow broadening only starts to occur at around $\tau = 1250$. It is also noted that the surface layer seems smaller in the case of a strongly attractive surface; this is expected because the increased attraction means the attracted component is more likely to want to reside at the surface.

6.3 Overcoming Inconsistencies in the Cahn-Hilliard Model

Equation 6.1.7 has been used by Diehl and Janssen[149] but here it is shown that it leads to inconsistencies when different spatial discretisations are used to numerically solve the equations of motion. To overcome these inconsistencies an

151

alternative approach is proposed which involves substituting the full free energy, equations 6.1.6 and 6.1.7, into the dynamic equation of motion, i.e.,

$$\frac{\partial \phi(\mathbf{x},\tau)}{\partial \tau} = \frac{1}{2}\nabla^2 \left[\frac{\chi_c}{2(\chi - \chi_s)} \ln \frac{\phi}{1-\phi} - \frac{2\chi}{\chi - \chi_s}\phi + \frac{2\phi - 1}{36\phi^2(1-\phi)^2}(\nabla \phi)^2 - \frac{1}{18\phi(1-\phi)}\nabla^2 \phi \right.$$
$$\left. + \left(-h_1 - g\phi + \gamma \frac{\partial \phi}{\partial \mathbf{x}} \bigg|_{\mathbf{x}=0} \right)\delta(\mathbf{x}) \right],$$

$$(6.1.9)$$

Equation 6.1.9 is solved using the finite difference approach seen in the previous chapters with the additional implementation of the Dirac-delta function only at the surface, therefore contributing to the free energy in the lattice sites at the surface layer only. At all other lattice sites, including at the neutral surface layer ($\mathbf{x}$ = $\mathbf{x}'$), only the bulk free energy terms are evaluated. In the following work we compare the evolution of structure due to equation 6.1.9 supplemented by the second boundary, which we denote model A, with that due to equation 1.3.9 supplemented by equation 6.1.8 which we denote model B.

As discussed in detail below we also believe that, due to discretisation, the values of h_1, g and γ should be divided by Δx, the finite difference spatial step. In order to verify our theoretical argument, we compare results when h_1, g and γ are (1) divided by Δx and, (2) are not divided by Δx for both model A and model B. Hence we compare 4 different types of simulation which we will refer to as, A(1), A(2), B(1) and B(2).

In each of the following sections h_1 = -1.5, g = 0.1, γ = 0.1 and N = 200, the blend is a 50:50 mixture and all results are averaged over 10 runs. This choice of variables is, of course, arbitrary but these values are typical of those used in surface-directed spinodal decomposition studies. In each case an average of ϕ is taken parallel to the surface for each value of $\mathbf{x}$.

6.3.1 Estimating the Surface Concentration

In order to gain an insight into the importance of the length-scales chosen for the numerical simulations, the surface concentration for a system undergoing equilibration without phase separation can be estimated using equation 6.1.9 if we assume that the composition perpendicular to the surface varies according to,

152

$$\phi = \phi_1 \exp\{-\xi Z\} + \phi_2 \qquad\qquad (6.1.10)$$

where ϕ_1 is the surface concentration and ϕ_2 is the bulk concentration. Here we have two unknowns, ϕ_1 and ξ, the correlation length. By minimising the free energy with respect to both ϕ_1 and ξ, we can determine the equilibration profile, as shown in figure 6.9. As we shall see equation 6.1.10 is an oversimplification since there must be some depletion layer between the surface enriched layer and the bulk in order to conserve material.
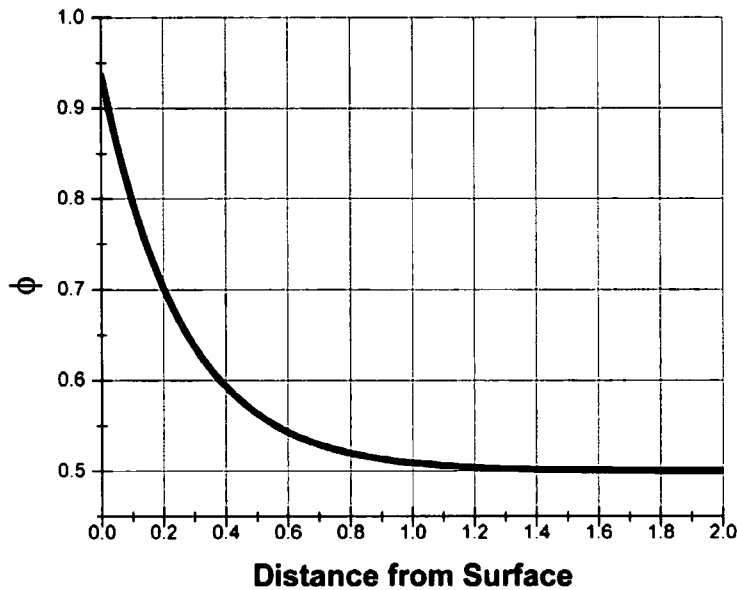
Figure 6.9

Variation of composition with distance from surface according to equation 6.1.10 with $\phi_1 = 0.436$ and $\xi = -3.862$. We have used $\phi_0 = 0.5$, $\chi = 0.00958$ and $N = 200$.

During simulations of phase separation generally[117] $\Delta x = 1$ however from figure 6.9 it is clear that in order to capture the full surface behaviour much smaller values of Δx are required. The value used for Δx will affect the surface behaviour as a consequence of discretising simultaneously a 1D effect and a 2D effect (the bulk free energy). The key point here is that the surface free energy only arises from cut-bonds at the molecular scale layer in contact with the surface.

Figure 6.10

Overlay of a Flory-Huggins lattice and a Cahn-Hilliard lattice.

However during Cahn-Hilliard discretisation the area represented by a lattice site is much greater than just the surface layer. This is illustrate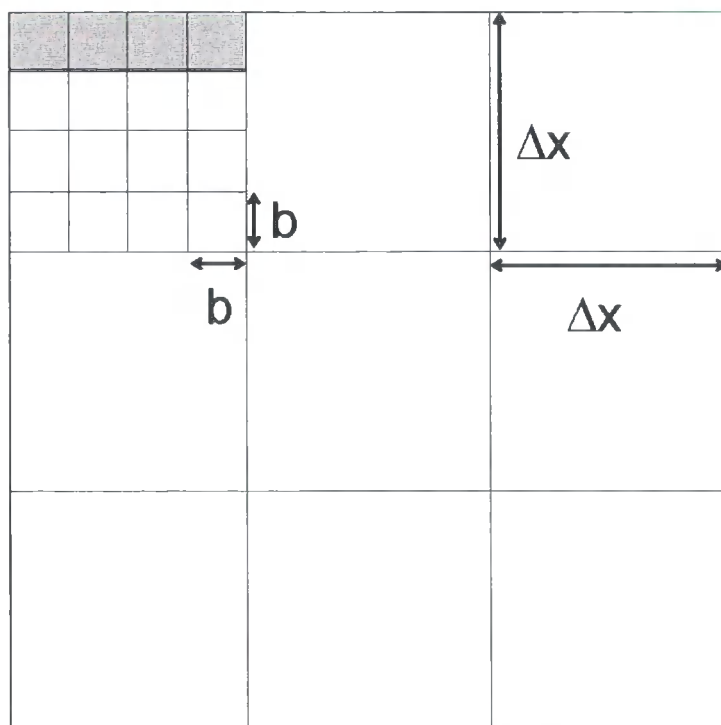d in figure 6.10; a Cahn-Hilliard lattice is shown where all the lattice sites are of size $(\Delta x)^2$ and a Flory-Huggins lattice site is overlaid where all the lattice sites are of size b^2, where b is approximately the monomer length. The effect of the surface free energy physically only contributes within the Flory-Huggins lattice sites at the surface; however the discretisation ensures that its effect is felt throughout a Cahn-Hilliard lattice site. Hence it is necessary to account for, and to remove, this discretisation effect. As noted already the total free energy, F, of a mixture is determined simply by summing the bulk, F_b, and surface, F_s, free energies[113], which for a discretised system becomes

$$F = \sum_{FHsites} F_b^{FHsite} + \sum_{FHsurface} F_s^{FHsite} , \text{ where } F_b \text{ and } F_s \text{ are assumed to be independent.}$$

However, in the simulations the composition is by definition constant within each Cahn-Hilliard lattice site, and some care is required. Within each Cahn-Hilliard lattice site there are $(\Delta x/b)^2$ bulk Flory-Huggins lattice sites and at the surface there are $(\Delta x/b)$ surface lattice sites, so we can write,

$$F_{Tot} = \sum_{CHsites} \left(\frac{\Delta x}{b}\right)^2 F_b{}^{FHsite} + \sum_{CHSurface} \left(\frac{\Delta x}{b}\right) F_s{}^{FHsite} \qquad (6.1.11)$$

Hence the ratio of bulk to surface FH sites at a surface CH site is $(\Delta x/b)^2/(\Delta x/b) = \Delta x/b$. Therefore if we decrease Δx, then within a CH site the relative number of surface sites increases, increasing the effect the surface has on the overall free energy of the system. In order to account for this effect it is necessary to scale the surface terms h_1, g, and γ by Δx according to

$$h_1 \rightarrow h_1/\Delta x$$
$$g \rightarrow g/\Delta x$$
$$\gamma \rightarrow \gamma/\Delta x$$

hence as Δx decreases the surface terms become more significant but within a smaller volume, as is required from the argument above. The effect of this method is to create a surface which has a consistent free energy value for any value of Δx. Note that the same arguments and outcomes apply for a 2D surface and a 3D bulk system.

6.4   Equilibration

In this section the results of equilibration for all 4 models are shown with $\chi = 0.00958$ and $\Delta\tau = 1 \times 10^{-4}$. Since for this mixture, $\chi_s = \chi_c = 0.01$, we are in the miscible region of the phase diagram where no phase separation occurs. During equilibration the system is allowed to evolve in the one-phase region, as the surface attracts one component of the blend a layer of this component forms along the surface. We allow this layer to evolve until a stable state is formed at which point the system is said to have equilibrated. We illustrate the influence of Δx by allowing the system to reach an equilibrium state for various values of Δx. The time scale for each simulation is not consistent in each case, the equilibrium position is identified and then the simulation is allowed to run to at least twice this period of time. A 1D simulation is used as it is numerically more efficient and we are not interested in the competition between the surface driving force and phase separation. Noise was added continuously during the equilibration step as it was found that this decreased

the required time to reach equilibrium. Noise of magnitude $\pm 1 \times 10^{-3}$ was added every 100 steps to mimic thermal fluctuations found in the blend. The results are shown in figure 6.11 for different Δx and are rescaled to the smallest Δx for comparison.
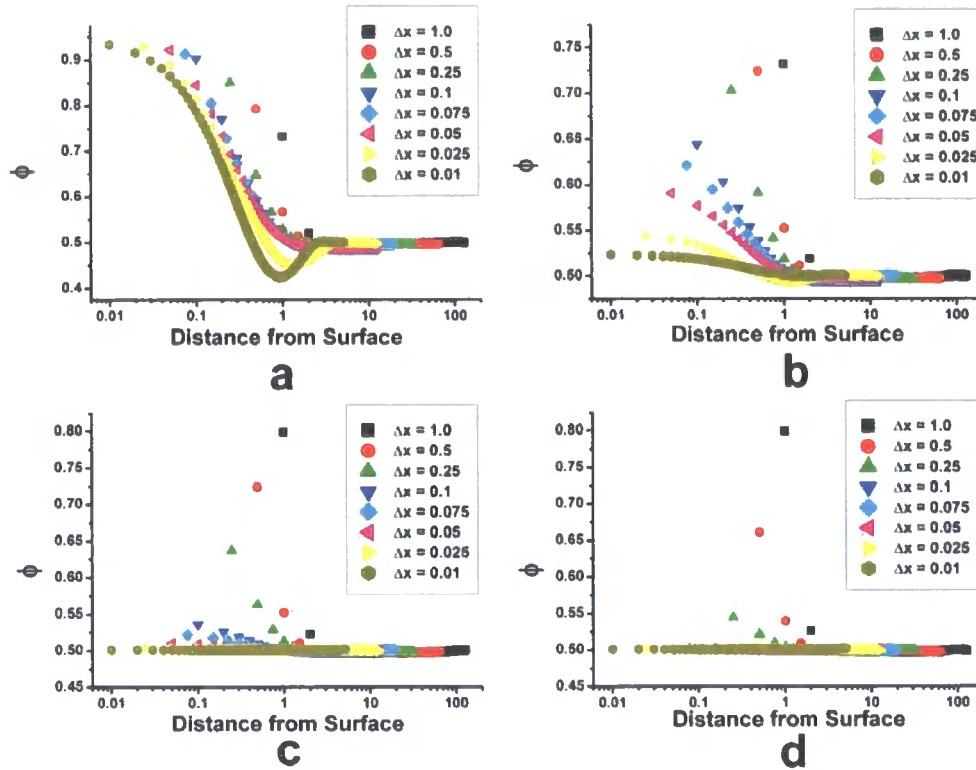

Figure 6.11

Comparison of equilibration for various Δx for (a) model A(1), (b) model A(2), (c) model B(1) and (d) model B(2).

It is clear that in all four models Δx has a dramatic effect on surface composition. The variation of the surface composition with distance only converges as Δx is reduced for model A1. A depletion layer appears as Δx is lowered, this layer appears to be partially absorbed into the bulk over time; however for the lowest Δx values the time scale of this absorption is computationally too demanding to be established. Figure 6.11(b) shows how the omission of the $1/\Delta x$ factor in the surface term affects the surface composition. It is clear that without this term there is no convergence of the behaviour as Δx is decreased. As expected from our earlier discussion, this is due to the relative magnitude of the surface term decreasing as Δx decreases, which is reflected in the reduced effect it has on the surface composition.

This result shows that the factor used to spatially discretise the surface term is important in creating an accurate simulation. Figures 6.11(c) and 6.11(d) for models B(1) and B(2) respectively also show significant behaviour. In both cases, the surface effect becomes negligible as Δx is decreased, although obviously for B(1) the effect is less dramatic than for B(2). This highlights the problems associated with using equation 1.3.9 supplemented by equation 6.1.8 to model surfaces consistently which is necessary if results are to be quantitatively compared with experiment.

6.5 Phase Separation

In this section we study the Δx dependence of the surface effects of a polymer blend which undergoes phase separation without equilibration. The blend is quenched to $\chi = 0.0104$ so that the mixed phase is now unstable for both $\Delta x = 0.5$ and $\Delta x = 0.25$. These simulations are undertaken with a time step of $\Delta \tau = 1 \times 10^{-4}$ in each case. Noise is only added once at the start of the quench and has a magnitude of $\pm 1 \times 10^{-3}$. All the simulations are undertaken to $\tau = 100$ and averaged over 10 runs. To ensure consistency, when $\Delta x = 0.5$, the simulation is performed on a 64^2 array and when $\Delta x = 0.25$ the simulation is undertaken on a 128^2 array.
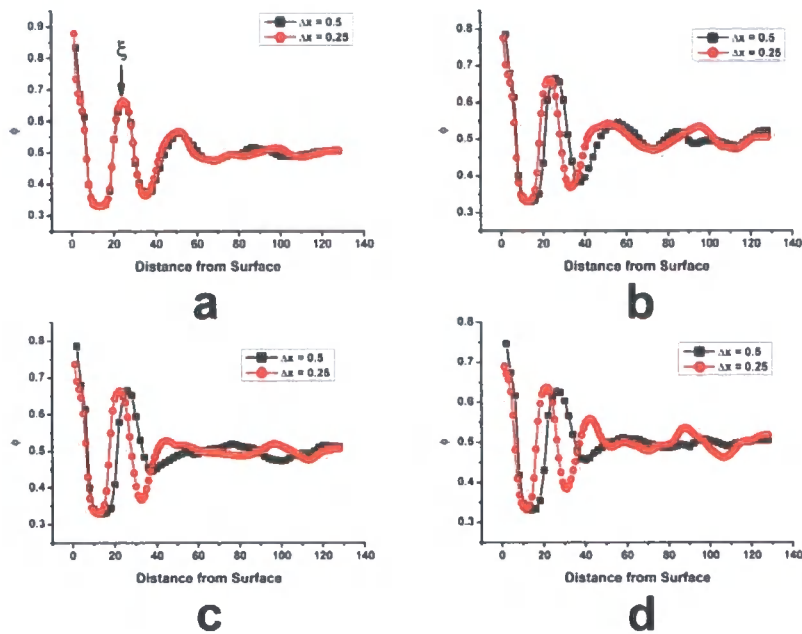
Figure 6.12

Comparison of phase separation for $\Delta x = 0.5$ and $\Delta x = 0.25$ for (a) model A(1), (b) model A(2), (c) model B(1) and (d) model B(2) at $\tau = 100$.

Figure 6.12(a) shows the expected result with the composition of the morphology being almost the same for both Δx values until well into the bulk region, thus validating our theoretical discussion. From figure 6.12(b) it can be seen that omitting the $1/\Delta x$ factor from the surface variables introduces differences between the results for the two different values of Δx. Figures 6.12(c) and 6.12(d) also show that model B does not show consistent convergent behaviour between different values of Δx. Such differences are, of course, unphysical, and are due to the use of equation 2.7.1 as a boundary condition. We also note that an additional problem arises with equation 2.7.1, in that it does not conserve total composition without additional constraints; i.e. a small amount of material is artificially generated since equation 2.7.1 is not a conservation equation. Whilst, of course, the surface composition is not a conserved quantity, the overall composition must be conserved.

To further support our argument in figure 6.13 we also illustrate the kinetics of the process by following the position of the first peak, labelled ξ in figure 6.12(a).
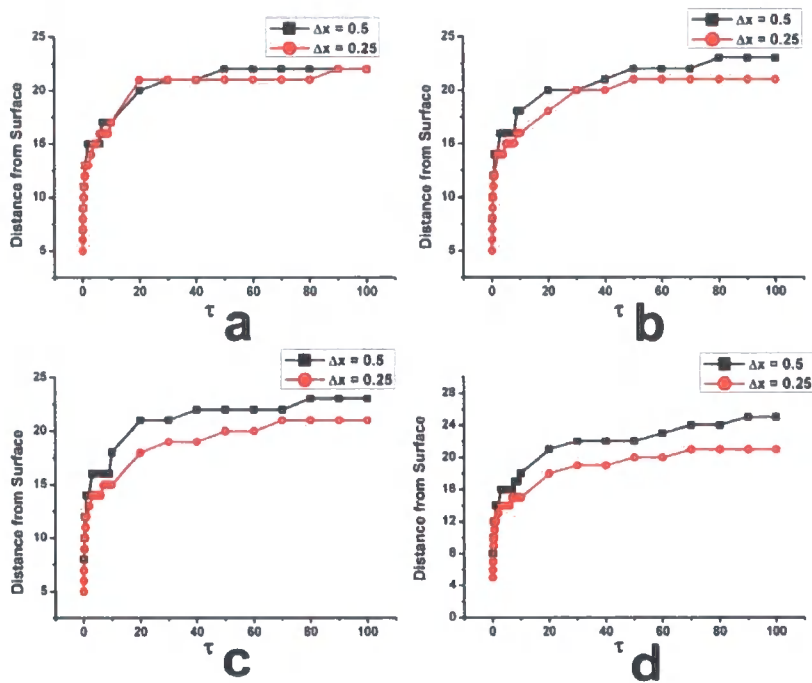
Figure 6.13

The position of ξ vs. time for (a) model A(1), (b) model A(2), (c) model B(1) and (d) model B(2).

Figure 6.13(a) shows that in the case of model A(1) the position of this peak remains consistent when differing Δx are used, however we see that when models A(2), B(1) and B(2) are used the position of the peak diverges for different values of Δx.

6.6   Equilibration and Phase Separation

The system is first allowed to equilibrate and is then quenched into the two phase region such that phase separation, for the two values of Δx used in section 6.5, occurs. The time step $\Delta \tau = 1 \times 10^{-4}$ is again used in all 4 models, with $\chi = 0.0096$ for the equilibration and $\chi = 0.0104$ for the phase separation. Here noise is added both continuously in the equilibration step, as in section 6.4, and at the start of the phase separation step, as in section 6.5 with a magnitude of $\pm 1 \times 10^{-3}$.

The results are compared for differing Δx in each of the four models and a comparison with a polymer blend which undergoes only phase separation and no equilibration (as in Section 6.5), is made. As in the previous section, to ensure consistency, when $\Delta x = 0.5$ the simulation is undertaken on a 64^2 array and when $\Delta x = 0.25$ the simulation is undertaken on a 128^2 array.

159

The equilibration is undertaken to $\tau = 500$ and the phase separation to $\tau = 100$. It is expected that the equilibration step will have an effect on the development of the morphology of the structure when compared to a blend which has not undergone an equilibration process as we are not starting from a uniform phase mixed morphology, however this effect should be minimised with decreasing Δx.
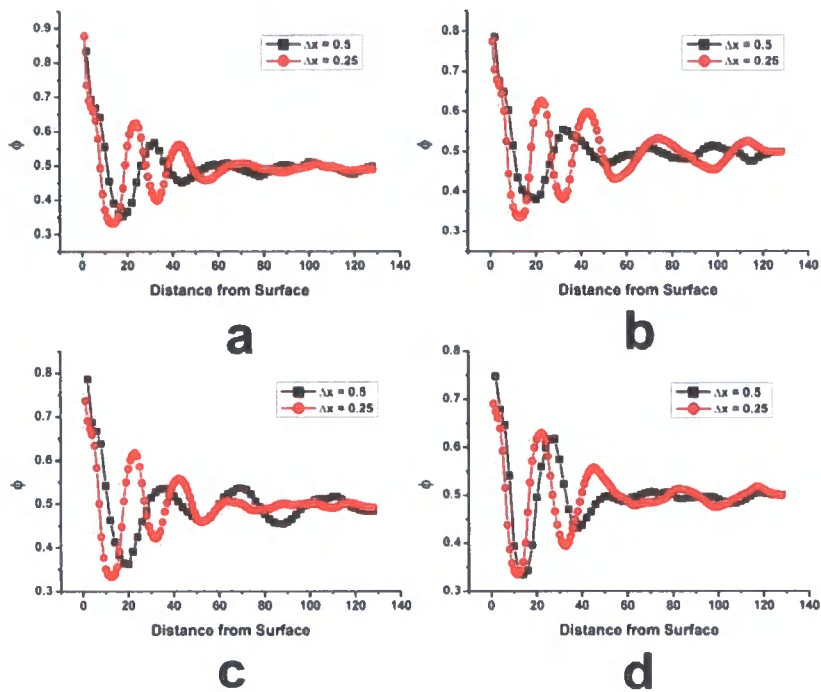

Figure 6.14

Comparison of phase separation for $\Delta x = 0.5$ and $\Delta x = 0.25$ for (a) model A(1), (b) model A(2), (c) model B(1) and (d) model B(2) after an equilibration of $\tau = 500$ and a phase separation of $\tau = 100$.

It is clear from figure 6.14 that the same trend as found in figure 6.12 is not presenting this case, this shows that the equilibration step has an effect on the morphology of the phase separating structure. Indeed in contrast to the previous section, it appears that figure 6.14(d) shows the best consistency between the results for different Δx. However, this is because the equilibration in this case has very little effect on the surface ϕ value. In other words, during the phase separation step, the two simulations are starting from a morphology which is more alike than is the case for the other models. This hypothesis is further corroborated by comparing figures 6.12(d) and 6.14(d) which are very similar.

In figures 6.15 and 6.16 a comparison of the results with those from section 6.5 are shown for $\Delta x = 0.5$ and $\Delta x = 0.25$ respectively.

Figure 6.15

Comparison of a phase separated blend morphology vs. an equilibrated and phase separated blend morphology for $\Delta x = 0.5$. For equilibration $\tau = 500$, for phase separation $\tau = 100$ for (a) model A(1), (b) model A(2), (c) model B(1) and (d) model B(2).
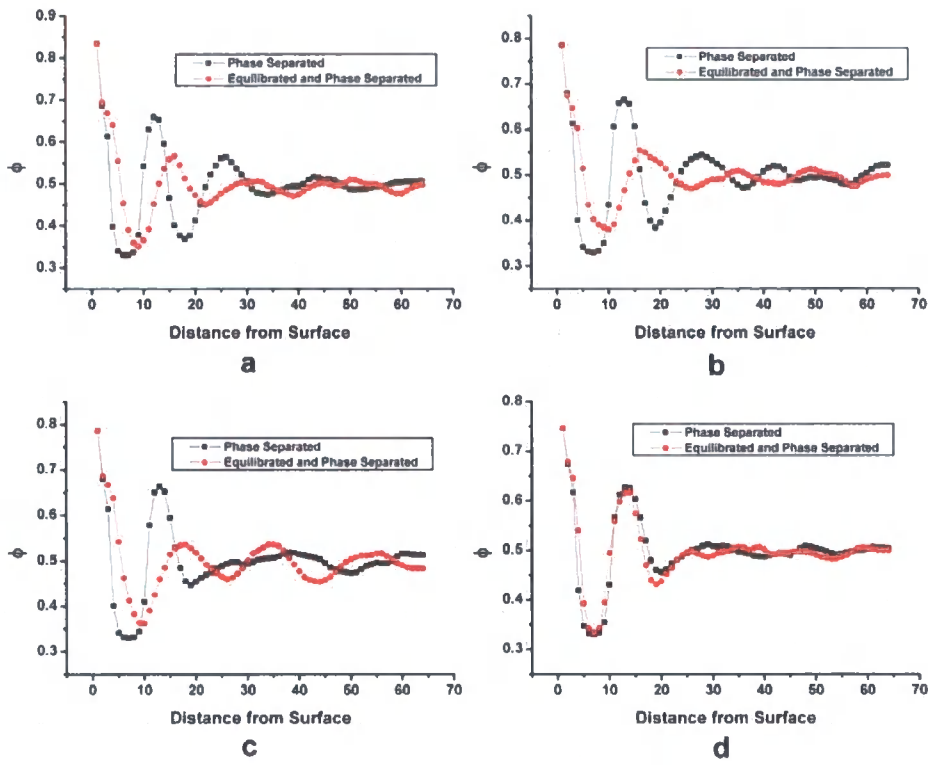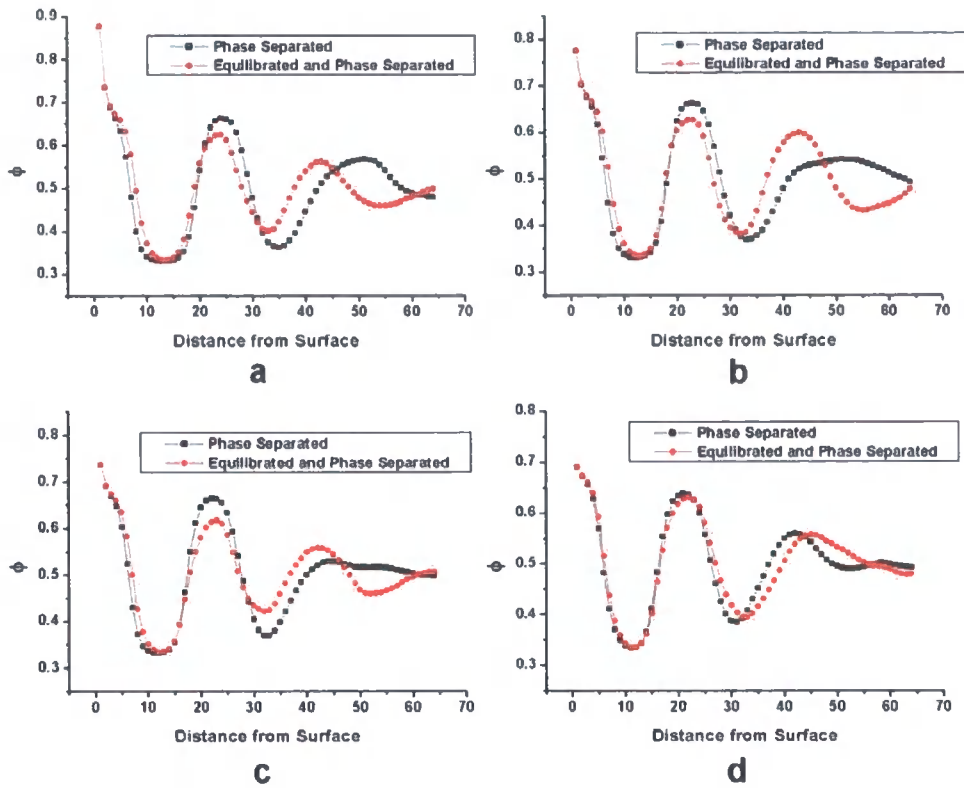
Figure 6.16

Comparison of a phase separated blend morphology vs. an equilibrated and phase separated blend morphology for $\Delta x = 0.25$. For equilibration $\tau = 500$, for phase separation $\tau = 100$ for (a) model A(1), (b) model A(2), (c) model B(1) and (d) model B(2).

It can be seen from figure 6.16 that the morphology in the bulk is of greater uniformity for models A1, A2 and B1 when $\Delta x = 0.25$ compared to when $\Delta x = 0.5$, which suggests that for small enough Δx equilibration has no effect on subsequent phase separation. It is expected that if the simulations were undertaken with much smaller Δx, around 0.01, then the two results in figures 6.15 and 6.16 would be identical. However results for $\Delta x = 0.01$ would mean that $\Delta \tau$ would need to be decreased significantly by at least one order of magnitude to create a numerically stable system.

Figures 6.15 and 6.16 show that the surface composition is equal for the simulations which have undergone only phase separation and those which have undergone both equilibration and phase separation. This shows that the equilibrium surface value of the composition is not affected by the equilibration step and that only the morphology of the developing blend is affected. This is, of course,

physically reasonable. However our work highlights the problem that in order to simulate surface-directed spinodal decomposition, finer length scales than it is desirable, or possible, to utilise are important if favourable wetting of one compound takes place prior to phase separation (as it almost certainly must). In other words the details of the wetting layer influence the subsequent phase separation.

The difference in the development of the morphology, in a system undergoing both equilibration and phase separation when compared to a blend which has undergone only phase separation, is due to the fact that the equilibration step induces a surface which is therefore already apparent at the start of the quench into the two-phase region and which seems to promote earlier phase separation in the bulk. Hence, the smaller the value of Δx the more accurate the surface composition profile. This does raise the question however of how small the Δx value can be made as this decrease requires an increase in the array dimensions, a decrease in the time step used in the simulation to ensure numerical stability, and a subsequent increase in the number of time steps, all of which are computationally expensive.

A comparison of the development of the morphology for two blends is shown in figure 6.17, one of the polymer blends has undergone only phase separation and the other has undergone both equilibration and phase separation.
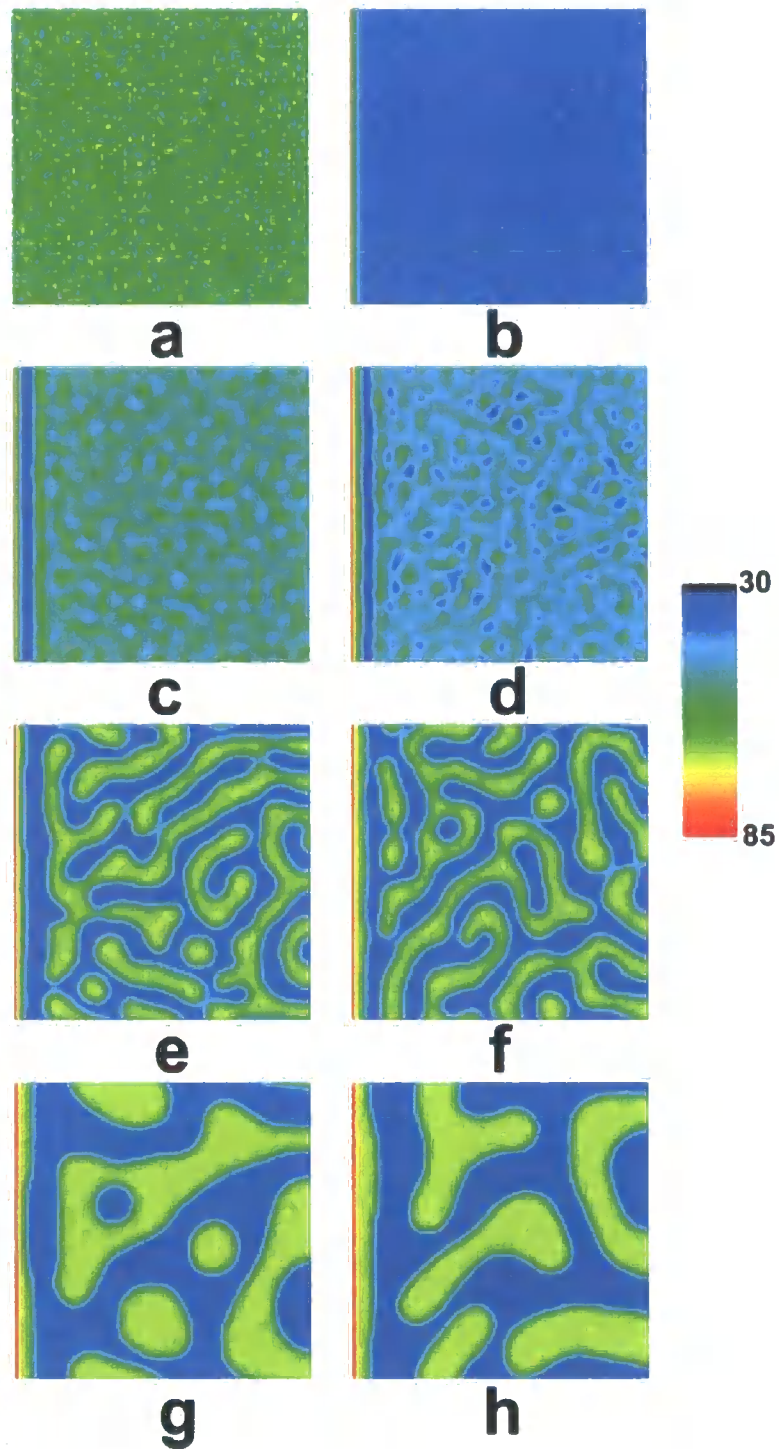
Figure 6.17

Development of the polymer morphology on a 64 x 64 array with $\Delta x = 0.5$ for model A(1) following a quench into the two-phase region for (a) $\tau = 0$, (b) $\tau = 1$, (c) $\tau = 10$ and (d) $\tau = 100$. Results are also shown for an equilibration of $\tau = 500$ followed by a phase separation of (e) $\tau = 0$, (f) $\tau = 1$, (g) $\tau = 10$ and (h) $\tau = 100$.

It can be seen from figures 6.17(b) and 6.17(f) that, by carrying out equilibration prior to phase separation, a surface is created earlier in the process. This surface appears to promote phase separation at smaller τ.   After the equilibration step a surface has been created in figure 6.17(e), which is not present in figure 6.17(a).   During the phase separation process the surface grows in each simulation, however the surface layer in the simulation which has undergone prior equilibration appears to be broader throughout the simulation.

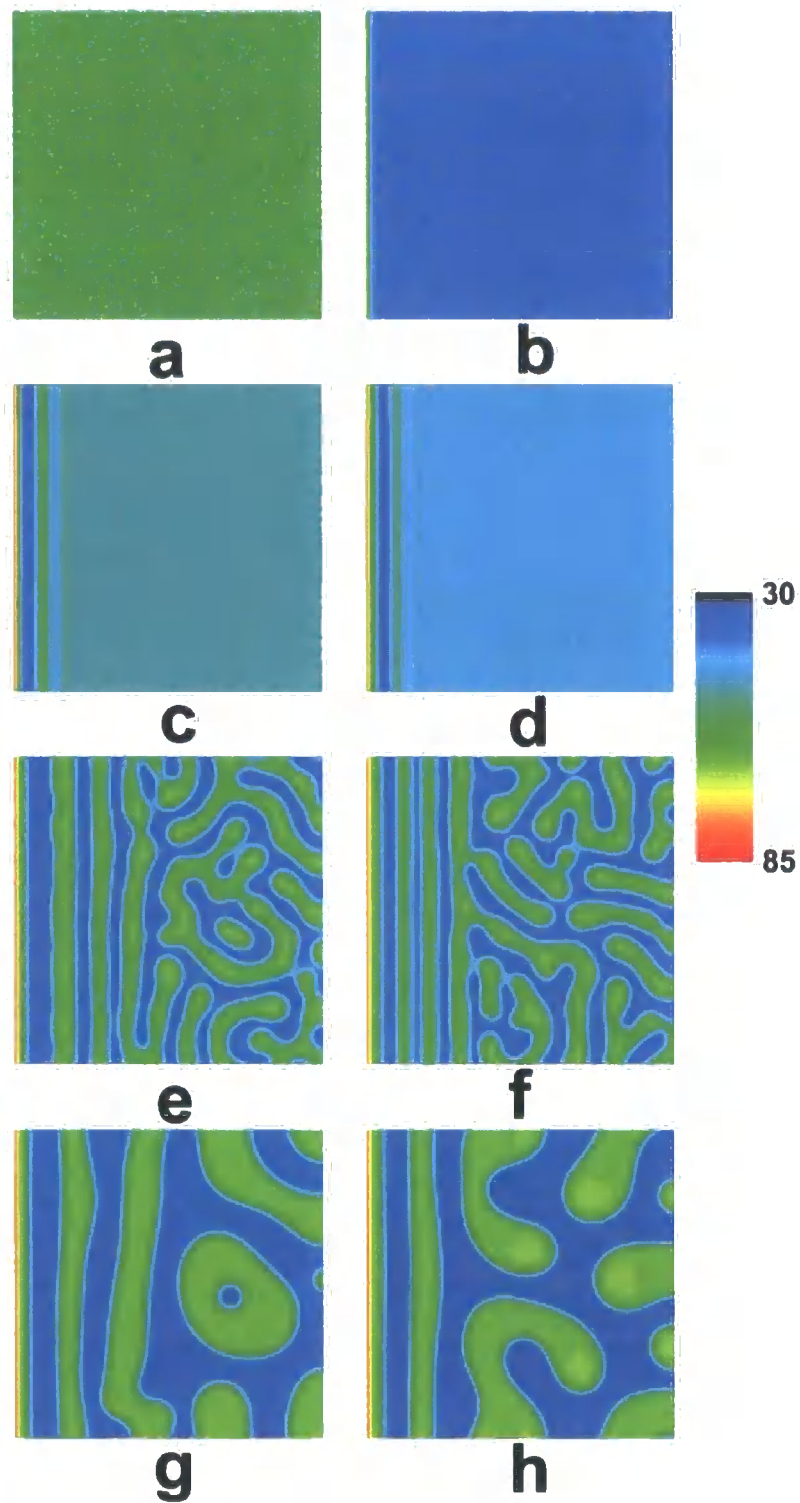*Figure 6.18*

Development of the polymer morphology on a 128^2 array with $\Delta \mathbf{x} = 0.25$ for model A(1) following a quench into the two-phase region for (a) $\tau = 0$, (b) $\tau = 1$, (c) $\tau = 10$ and (d) $\tau = 100$. Results are also shown for an equilibration of $\tau = 500$ followed by a phase separation of (e) $\tau = 0$, (f) $\tau = 1$, (g) $\tau = 10$ and (h) $\tau = 100$.

Figure 6.18 shows that any difference in morphology during the growth following both equilibration and phase separation and just following phase separation is minimised by reducing Δx. It can be seen that the difference in the surface morphology is greatly reduced when compared to figure 6.17. The reason for the greater layering shown in this case is discussed later.

6.7   Noise

Marko[114] undertook a study into the effect noise has upon the morphology produced in a simulation where surface terms are included. Here we recreate and extend that work in order to stress how imperative this term is to the simulations and to highlight the need to use the correct magnitude and frequency of noise within the simulations.

To study the effect of noise upon the system both the magnitude of the noise term was changed, when the frequency was constant, and the frequency of the noise was changed, with the magnitude kept constant.

6.7.1   The Effect of Altering the Noise Magnitude

Firstly we describe the morphologies formed when the noise magnitude is changed, here the noise is added continuously every 100 computational time steps and its magnitude is varied from $\pm 1 \times 10^{-3}$ to $\pm 1 \times 10^{-8}$. Here $\Delta \tau = 0.0025$, $\Delta x = 0.5$, $h_1 = 1.0$, $g = 0.1$, $\gamma = 0.1$ and the simulations are carried out on a 128^2 array.
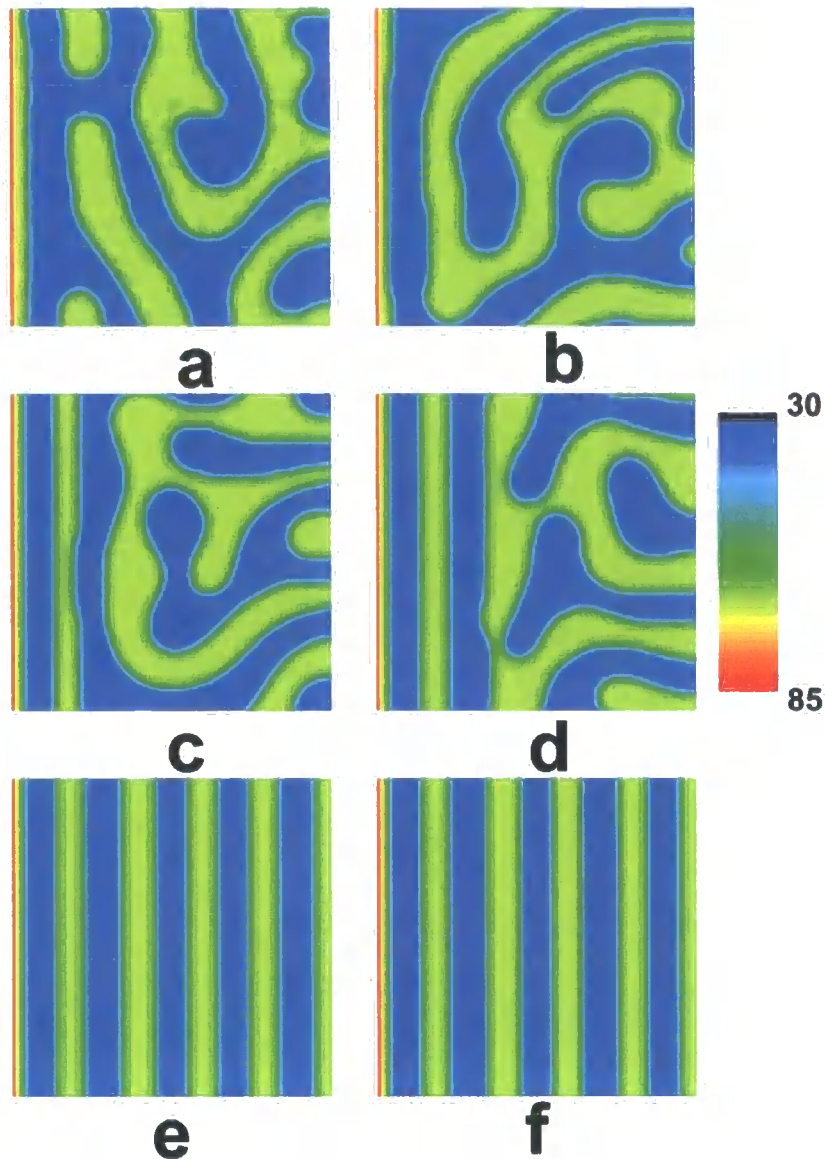
Figure 6.19

Examples of different morphologies at $\tau = 1000$ formed when noise magnitude is (a) $\pm 1\times10^{-3}$, (b) $\pm 1\times10^{-4}$, (c) $\pm 1\times10^{-5}$, (d) $\pm 1\times10^{-6}$, (e) $\pm 1\times10^{-7}$ and (f) $\pm 1\times10^{-8}$, when noise is added continuously every 100 time steps.

By comparing figures 6.19(a) and 6.19(f) it is clear to see that changing the magnitude of the noise, when all else is constant, has a great effect on the resultant morphology. In figure 6.19(f) a random morphology is not seen to occur as a gradient large enough to destabilise the blend in the bulk is not present, this means that the oscillating morphology formed due to the surface propagates throughout the system. As the noise magnitude is increased spinodal decomposition can be seen to occur away from the surface leading to an oscillating morphology followed by a

random co-continuous morphology, as seen in figure 6.19(d). As the magnitude of the noise is increased further the process of phase separation becomes dominating throughout the system and the oscillating morphology is lost with only a surface and depletion layer being formed before the random co-continuous morphology, as seen in figure 6.19(a).

6.7.2   The Effect of Altering the Noise Frequency
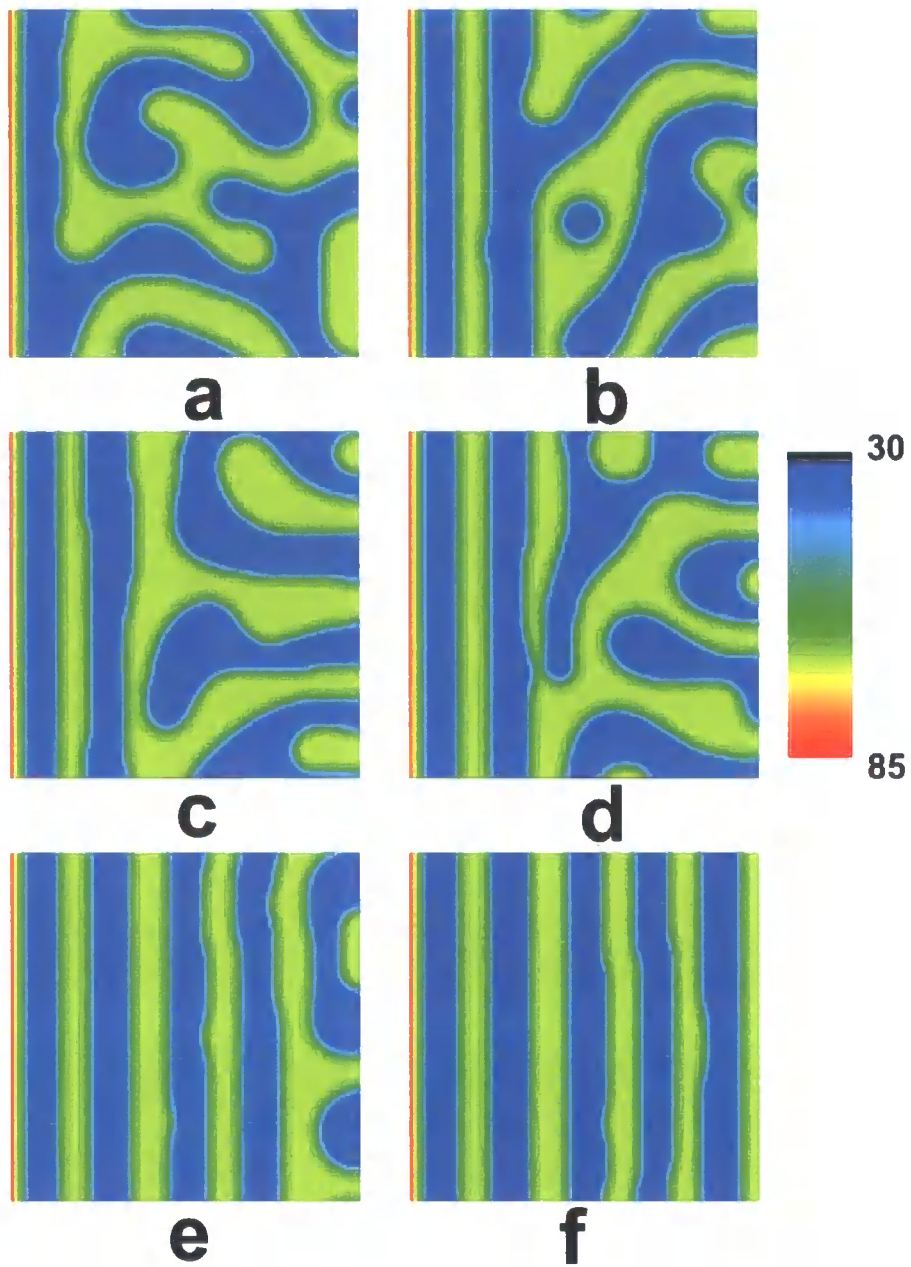
Figure 6.20

Examples of different morphologies at $\tau = 1000$ formed when noise of magnitude $\pm 1 \times 10^{-5}$ is added every (a) 1 computational step, (b) 100 computational steps, (c) 500 computational steps, (d) 1000 computational steps, (e) 10000 computational steps and (f) 50000 computational steps.

Again the effect of noise is clear in this case, when noise is added infrequently, as in figure 6.20(f), the surface force dominants the morphology of the blend and an oscillating structure is seen. As the frequency with which noise is

added increases we see that the spinodal decomposition process becomes dominating and surface and depletion layers are followed by a co-continuous structure in figure 6.20(a).

Figures 6.19 and 6.20 highlight the inconsistencies present when the noise term is altered, it is clear to see that if theoretical results are to be quantitatively compared to experimental results then this inconsistency needs to be overcome. Presently no physical or numerical solution to this problem presents itself so comparison of theoretical results with experimental results would seem to be the only way of deciding the levels of noise needed to give accurate simulation results. Clearly the competition between phase separation and the surface forces, i.e. the influence each has on the overall free energy, can be affected by the change in χ used to initiate the phase separation process. By increasing the quench depth the system phase separates to greater volume fractions of each component, the penalty for the creation of interface between the two components therefore increases as the gradients become larger and the system moves to reduce the overall free energy by broadening the domains to a greater extent. This process means that the bulk free energy component of the overall free energy has a greater effect than if a smaller quench was used and therefore the phase separation process will become more dominant, an example of this is seen in the following chapter.

6.8   Conclusions

We have explored the dynamics of phase separating polymer blends at and near a surface, using a finite difference scheme for a spatially and temporally discretised version of the Cahn-Hilliard equation. We have shown how the method developed by Binder can be used to model the dynamics of phase separation in a polymer blend at and near a surface and how depth profiling, comparable with He^3 ion beam analysis, can be used to follow the phase separation of the blend. Here we see an oscillating morphology growing perpendicular to the surface whilst random phase separation occurs in the bulk. We find that by controlling the attraction which the surface has for one component of the blend we can control the effect this oscillating morphology has on the system.

We have then highlighted the difficulty of using the Cahn-Hilliard equation, with boundary conditions designed to represent the surface effect, to model surfaces

consistently which is necessary if the results are to be quantitatively as well as qualitatively compared with experiment.

We find that anomalies are present when varying length scales are used within the simulation which affects the growth kinetics of the phase separated morphology. We therefore propose a minimal model to physically remove these anomalies. The method involves the scaling of the surface free energy parameters by the finite difference spatial step, which is needed to ensure that the balance of the magnitude of the surface and bulk free energy terms is unaffected by the choice of lattice size. The issue arises because the effect of the surface contribution to the free energy is felt throughout the discretised surface lattice sites, and our method therefore facilities the removal of the spatial anomalies. We show that (in the absence of an equilibration step to create a surface enriched layer prior to phase separation) our method leads to consistent results irrespective of the choice of lattice size; thus showing that artefacts can be removed by the careful choice of physical input.

We also show results from blends which have also undergone both surface equilibration, in the one phase region, and then phase separation. We see a difference in the development of the morphology in these two cases as the equilibration step results in a surface being present at the start of the phase separation step and which therefore promotes earlier phase separation in the bulk. In this instance we show that there are further problems due to the discretisation arising from the mismatch of lengthscales associated with the equilibration and the phase separation.

We also show that the level of noise added to the simulations has a great effect on the final morphology and if results are to be quantitatively compared with experimental results then care needs to be taken with this variable. Here we find that by changing either the magnitude of noise or the frequency with which it is added has a marked effect on the final morphology. This is because in these systems the final morphology is a compromise between the need for the system to phase separate via spinodal decomposition, to form a random co-continuous morphology, and for the surface forces to affect the morphology. Noise is clearly therefore not as important if no surface forces are present as the spinodal decomposition process is the only, and therefore dominating, process.

Chapter 7

Targeting Morphologies via Surface Patterning

The investigation presented in the previous chapter is extended to account for systems with patterned surfaces, both at a hard wall, as in the previous chapter, and when viewing, for example, a thin film on a wafer from above. Firstly the effect that altering the pattern size has on the system is investigated at a hard wall surface using the model proposed in chapter 6. The model is then extended to investigate a surface patterned using the printing methods described in chapter 2.7.3. Use is made of the interface counting method, first described in chapter 5, to follow the phase separation.

7.1 The Patterned Wall Model

The model is extended such that two different h_1 values can be implemented in the simulation; this means that different areas of the wall can be set to be attractive to different components of the blend. The simulations shown below are undertaken on a 64x128 array, this mimics a thin film blend and increases computational efficiency as our main interest is with occurrences at the surface and not in the bulk.

7.1.1 Morphology Growth at a Patterned Surface

Initially we investigate the growth of the morphology at the surface when the surface has been patterned such that each component is alternatively attracted to the surface in areas of 32 array units along the y axis. Here $h_1 = 0.75$ and -0.75 alternatively and $g = 0.1$, $\gamma = 0.1$, $\Delta \tau = 0.0025$ and $\Delta x = 0.5$, initially $\chi = 0.01$, the system is quench to $\chi = 0.0119$ and the simulations are allowed to evolve to $\tau = 2500$.
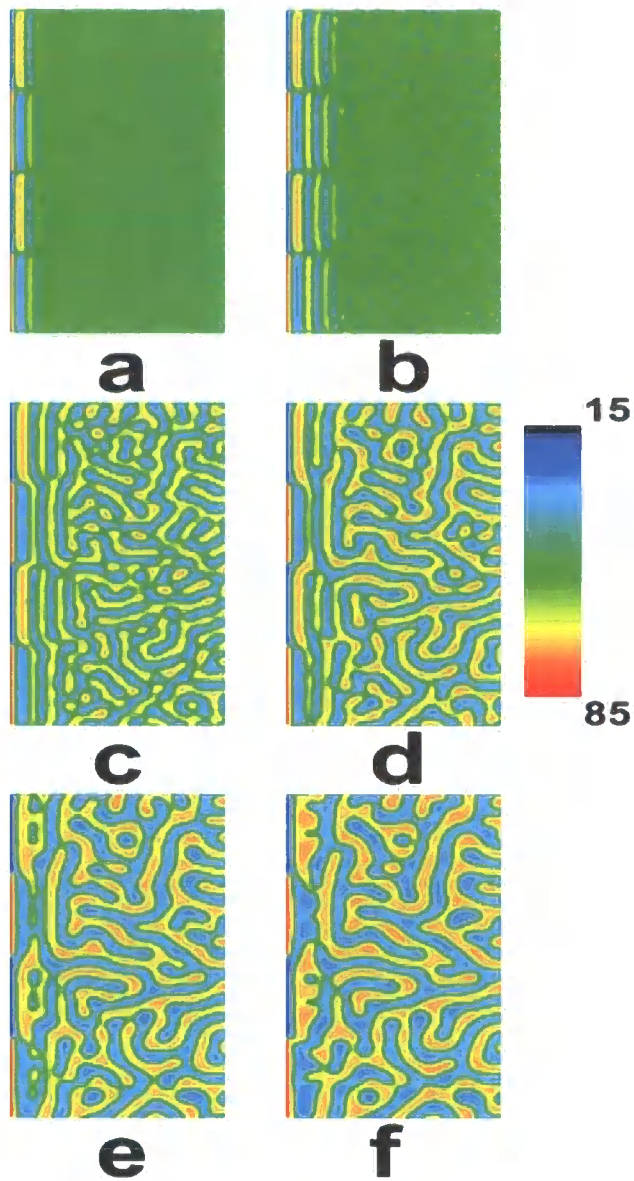
Figure 7.1

Growth of the morphology at and near a patterned surface at (a) $\tau = 1.25$, (b) $\tau = 2.5$, (c) $\tau = 5$, (d) $\tau = 7.5$, (e) $\tau = 10$ and (f) $\tau = 12.5$.

The morphology at low τ is shown in figure 7.1; the oscillating structure present in the previous chapter is again present here. The patterning of the surface is clear but we also note that the pattern at the surface propagates, via the depletion layer, into the bulk.

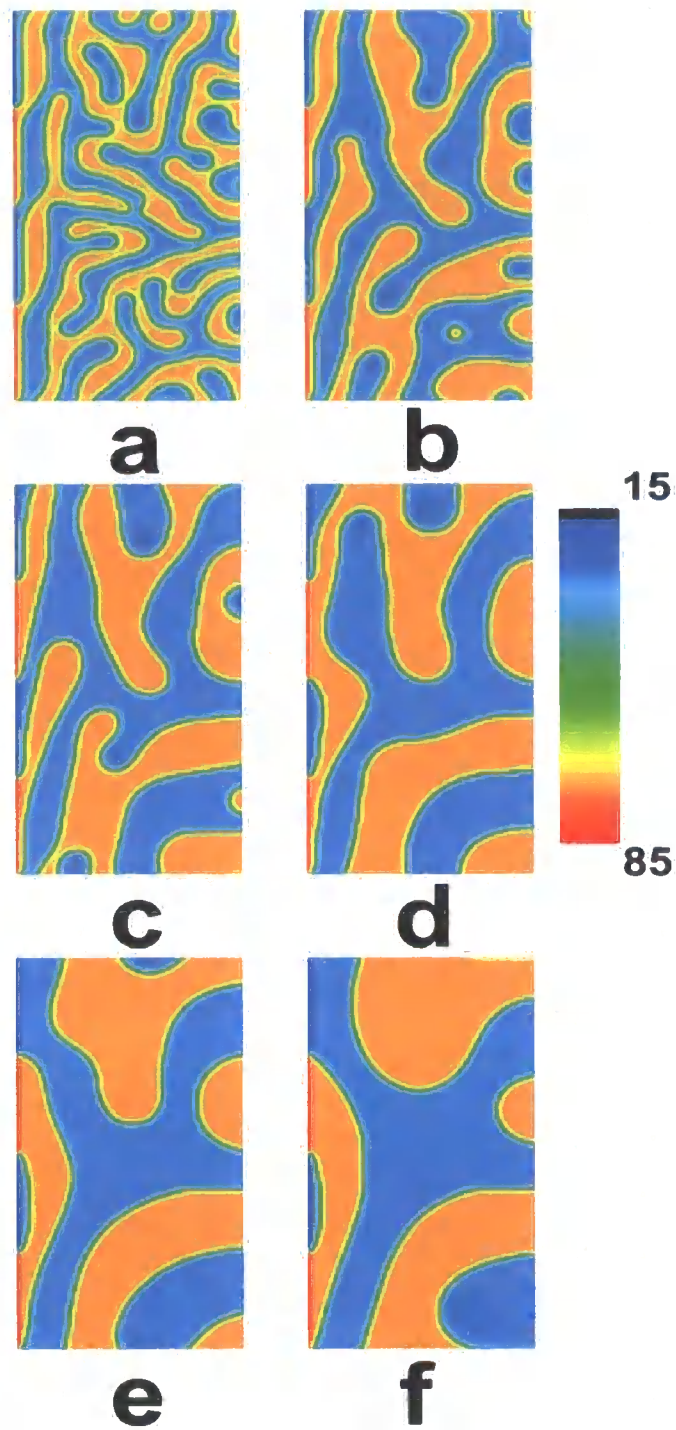*Figure 7.2*

Development of the morphology at (a) $\tau = 25$, (b) $\tau = 125$, (c) $\tau = 250$, (d) $\tau = 500$, (e) $\tau = 1250$ and (f) $\tau = 2500$.

Figure 7.2 shows how the morphology develops at later times, in each part of figure 7.2 a surface layer followed by a depletion layer is still seen, however, the propagation of the surface pattern into the bulk is lost to a great extent as the bulk free energy component of the overall free energy becomes dominant.

7.1.2   Effect of Altering the Pattern Size and Surface Magnitude

The size of the pattern can also be altered as shown in figure 7.3.
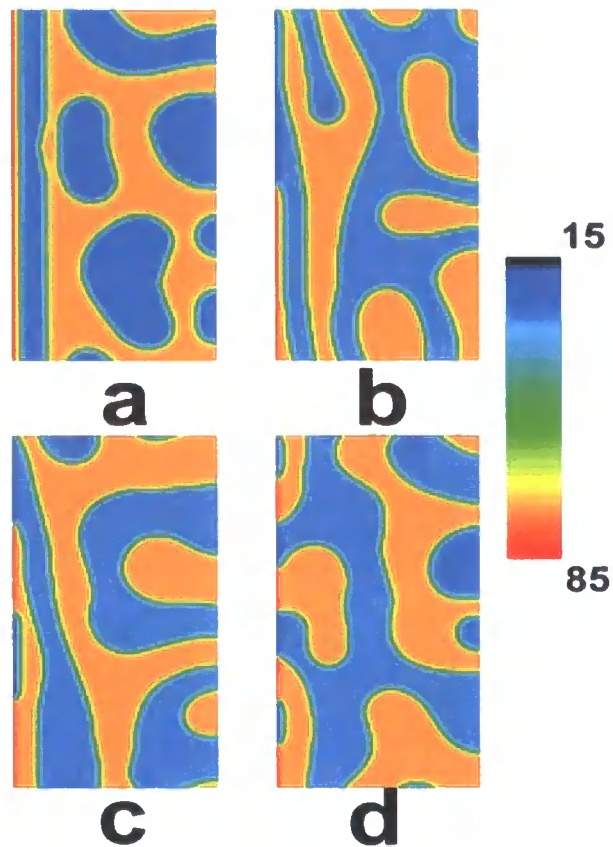
Figure 7.3

Comparison of different pattern sizes at $\tau = 500$ where the pattern is set at $\mathbf{x} = 0$ on a 64x128 array, the pattern size is (a) 128 array units, (b) 64 array units, (c) 32 array units and (d) 16 array units.

By reducing the pattern size it can be seen that the order produced by the surface in the bulk is somewhat reduced. This is because as the pattern size is reduced more interface between components is present leading to a higher energy

system, therefore the system moves to reduce the free energy by reducing the effect of the pattern in the bulk. Figure 7.3(c) shows that, at the surface, a small well defined pattern can exist and if the film is thin enough it is possible to see that this pattern may propagate throughout the film.

In the above examples the surfaces are set to be equal and opposite, i.e. with h_1 values of 0.75 and -0.75, however it is also possible to set the surface to be attractive to the same component, but by differing amounts, e.g. $h_1 = 1.5$ and 0.75, or attractive to different components but by varying amounts, e.g. $h_1 = 1.5$ and -0.75, examples of these situations are shown bin figure 7.4.
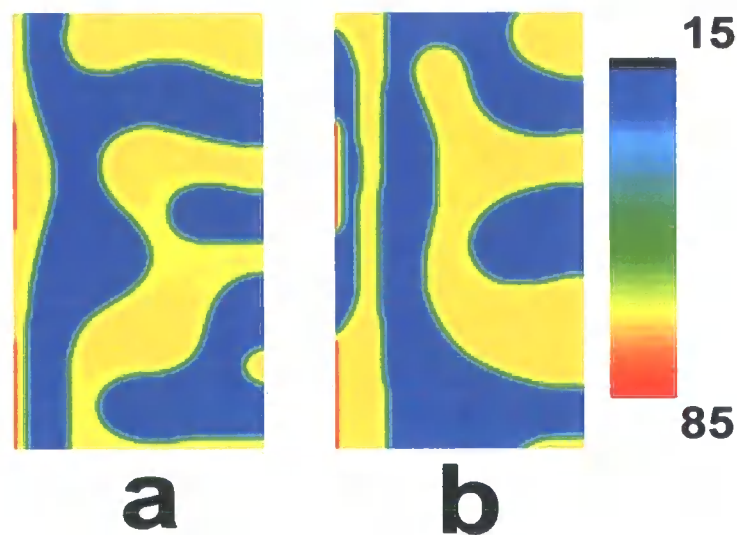
Figure 7.4

Example morphologies formed when (a) $h_1 = 1.5$ and 0.75 and (b) $h_1 = 1.5$ and -0.75 at $\tau = 500$ on a 64x128 array with a pattern of 32 array units.

The difference in colour at the surface in figure 7.4(a) clearly shows how the surface is patterned, with greater phase separation at the more attractive surfaces and a more defined depletion layer in the bulk. In figure 7.4(b) we see encroachment of one phase, where $h_1 = 1.5$, onto the area of reduced attraction for the second phase, where $h_1 = -0.75$.

7.2 Phase Separation on a Chemically Patterned Surface

As patterned surfaces at hard walls have been studied in detail in the literature the model is further developed to explore interesting morphologies formed on chemically patterned substrates, as described in chapter 2.7.3. As above, the patterning is expected to direct the spinodal decomposition process to form morphologies similar to those of the patterning on the surface. The system is again set up with a two-dimensional model thus neglecting effects that may occur in the direction normal to the substrate, such as surface directed spinodal decomposition and film height variations. For this reason the γ term introduced in equation 2.7.1 can be ignored as the model cannot take account of the correlation length normal to the surface, hence equation 6.1.9 becomes,

$$\frac{\partial \phi(\mathbf{x},\tau)}{\partial \tau} = \frac{1}{2}\nabla^2 \left[\begin{array}{l} \dfrac{\chi_c}{2(\chi-\chi_s)}\ln\dfrac{\phi}{1-\phi} - \dfrac{2\chi}{\chi-\chi_s}\phi + \dfrac{2\phi-1}{36\phi^2(1-\phi)^2}\left(\nabla\phi\right)^2 - \dfrac{1}{18\phi(1-\phi)}\nabla^2\phi \\ +\left(-h_1 - g\phi\right) \end{array} \right],$$

(7.2.1)

where h_1 and g are dependent on $\mathbf{x}$.

7.2.1 Regular Circular Pattern

The surface is regularly patterned with circles of equal diameter and spacing, as shown in figure 7.5, and phase separation is allowed to occur via the temperature jump method. In this case $N_A = 1105$ and $N_B = 913$ to model a 116K MW poly(vinylpyridine) (PVP) 949K MW polystyrene (PS) blend, as used by the group of Wilhelm Huck to experimentally undertake such work. The blend is quenched from $\chi = 0.002$ on the spinodal to $\chi = 0.00204$ in the two phase region,
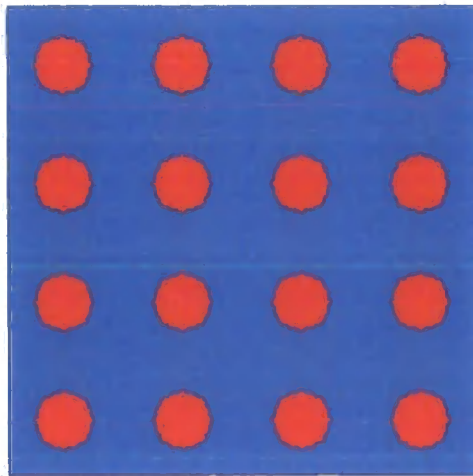
Figure 7.5

Circle pattern over which phase separation occurs.

Phase separation is undertaken over this pattern and the evolution of the morphology is followed with time. The patterned areas above (circles) are set to attract one component of the blend, with $h_1 = 0.5$, $g = 0.1$ and the non-patterned area is set to be neutral, attracting neither component. The simulations are undertaken on a 128^2 array with $\Delta\tau = 0.0025$ and $\Delta x = 0.5$ with a 50:50 blend,

Figure 7.6

Development of the morphology following a quench into the two phase region at (a) $\tau = 1$, (b) $\tau = 12.5$, (c) $\tau = 25$, (d) $\tau = 125$, (e) $\tau = 500$ and (f) $\tau = 2500$.

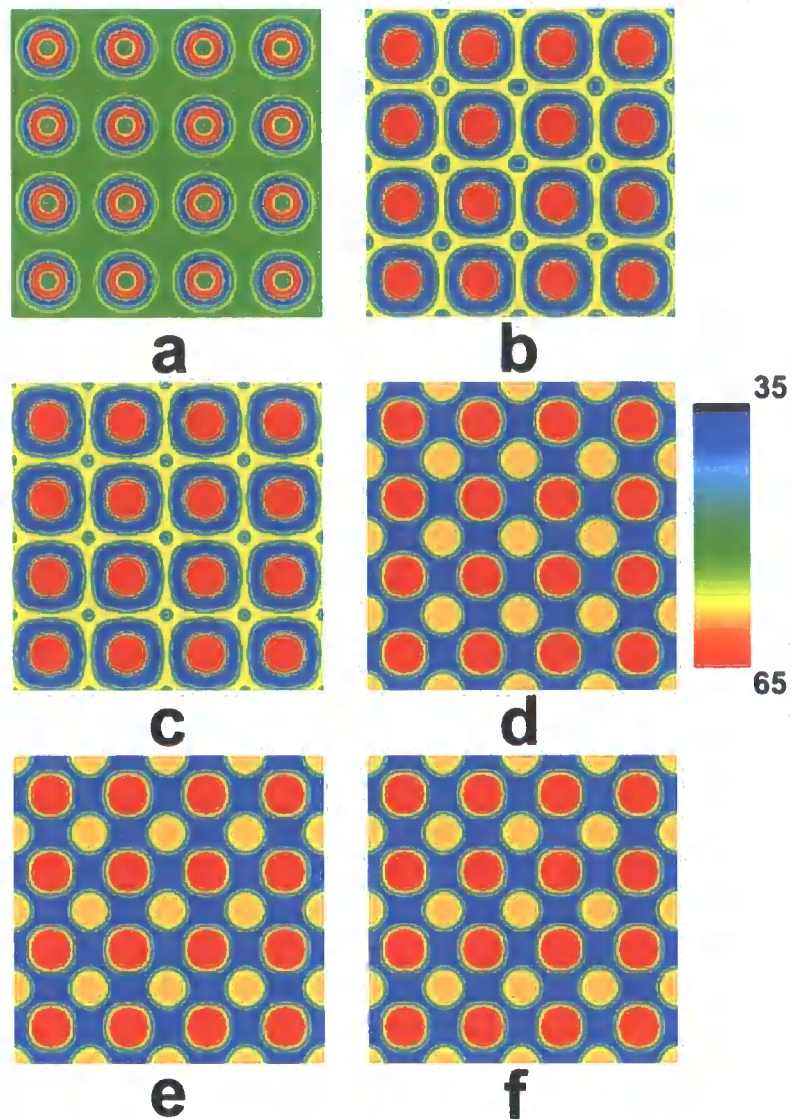Initially, in figure 7.6(a) phase separation occurs most prevalently at the pattern areas, followed by the corresponding depletion layer. Transient structures are then seen in the matrix around the pattern which are clearly a consequence of the pattern and the wavelength selection process associated with spinodal decomposition. As stated previously, during spinodal decomposition the blend phase separates to form a sinusoidal structure, and this is clearly seen in figures 7.6(b)-(f). The circles of polymer seen in the matrix are relatively stable with time and very little degradation is seen between figures 7.6(d) and 7.6(f). This is because sinusoidal structures are seen throughout the system, both horizontally, vertically and

diagonally and the system resides in a local free energy state. The cost of diffusion from the matrix to the patterned area is therefore high, making the structure seen in figure 7.6(f) locally stable. If we use a higher value of h_1 on the circles, as shown in figure 7.7, or without changing h_1 on the pattern, we make the matrix attractive to the second blend component, as shown in figure 7.8, then we find that these trapped structures do not persist.
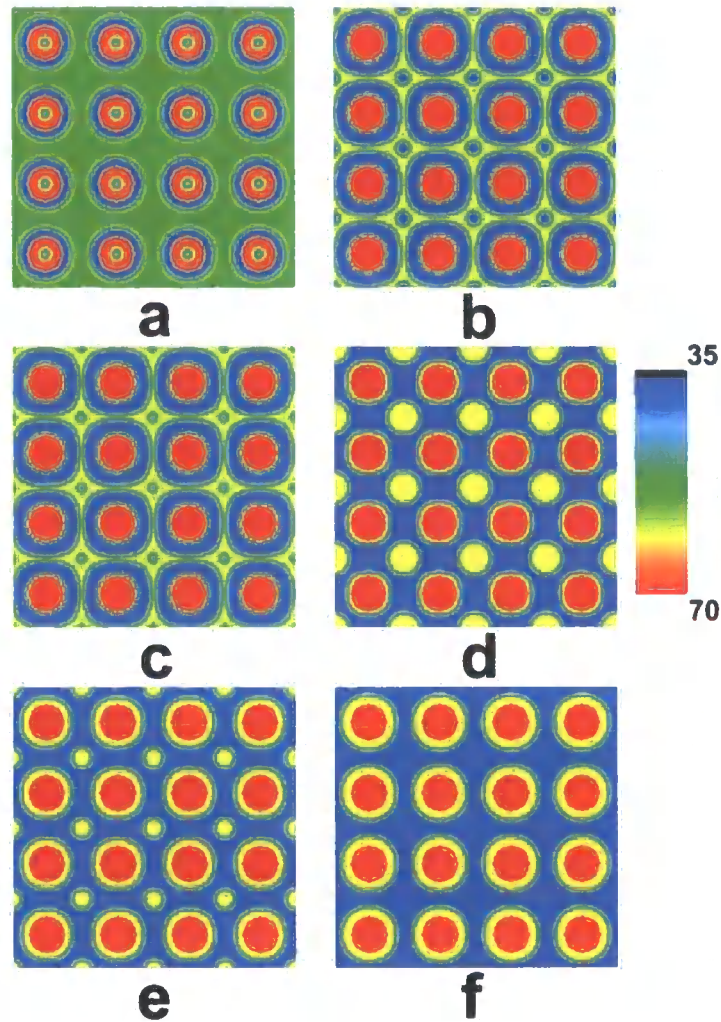

Figure 7.7

Development of the morphology when $h_1 = 1.5$ on the patterned areas and the matrix remains neutral at (a) $\tau = 1$, (b) $\tau = 12.5$, (c) $\tau = 25$, (d) $\tau = 125$, (e) $\tau = 500$ and (f) $\tau = 2500$.
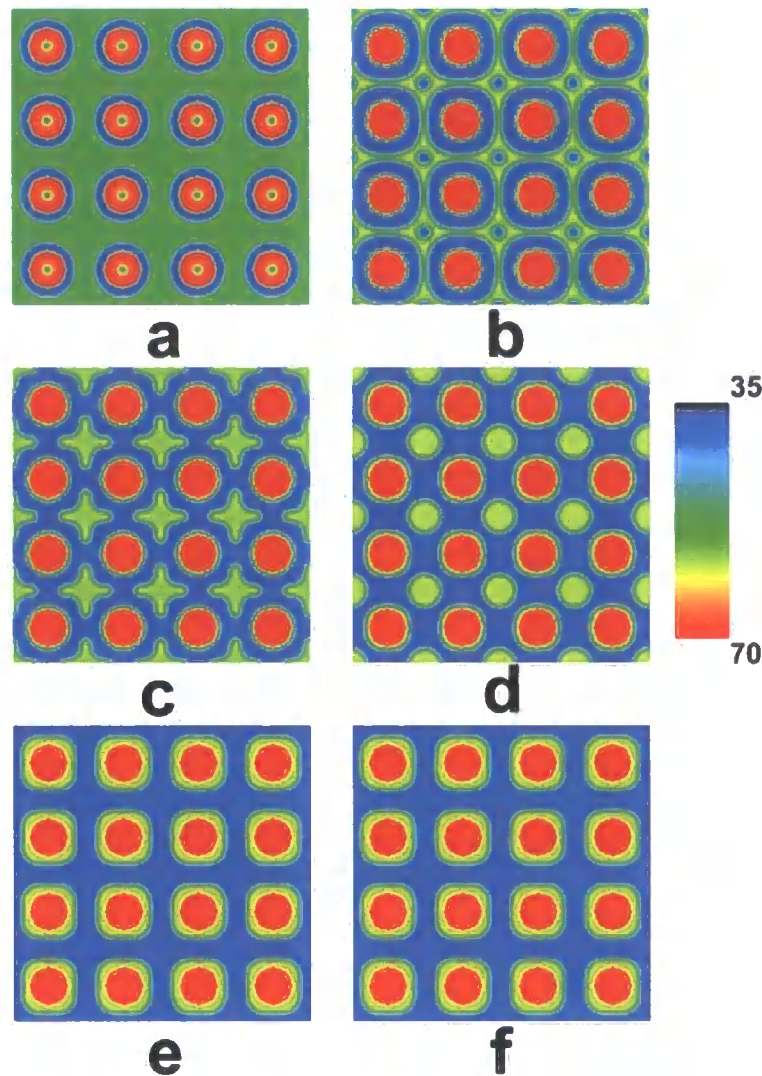
Figure 7.8

Development of the morphology when $h_1 = 0.5$ on the patterned areas and $h_1 = -0.5$ on the matrix at (a) $\tau = 1$, (b) $\tau = 12.5$, (c) $\tau = 25$, (d) $\tau = 125$, (e) $\tau = 500$ and (f) $\tau = 2500$.

By altering the surface properties, in figures 7.7 and 7.8, it has been possible to destabilise the morphology seen in figure 7.6(f), essentially we have increased the rate of the phase separation process, and we now find that, following the transient structures, the morphology is directed by and mimics the pattern. As a 50:50 blend is used the area of the pattern is not large enough to allow the entirety of the favoured component to form above it, however because the minimum interfacial area is required between components we find the system allows the formation of the favoured component around the patterned area, even when the matrix is favourable to the second component.

Experimentally if a structure such as that seen in figure 7.6(f) were present it may be difficult to change the favourability of the patterned area and the matrix, the easiest way to then remove these structures would be to alter the blend composition, as seen in figure 7.9 a small alteration in the blend composition can have a great effect on the outcome of the phase separation process.

Figure 7.9

Development of the morphology following a quench into the two phase region when $h_1 = 0.5$ on the patterned areas and the matrix is neutral at (a) $\tau = 1$, (b) $\tau = 12.5$, (c) $\tau = 25$, (d) $\tau = 125$, (e) $\tau = 500$ and (f) $\tau = 2500$ for a 47.5:52.5 blend.

The structure seen in figure 7.6(f) becomes unstable and decays to mimic the pattern, clearly by reducing the volume of the component which is favourable to the pattern we have reduced the stability of the sinusoidal structure seen in figure 7.6(f)

allowing the system to reach its overall lowest free energy value. For completeness, in figure 7.10, we show the effect of altering the blend composition to 52.5:47.5.
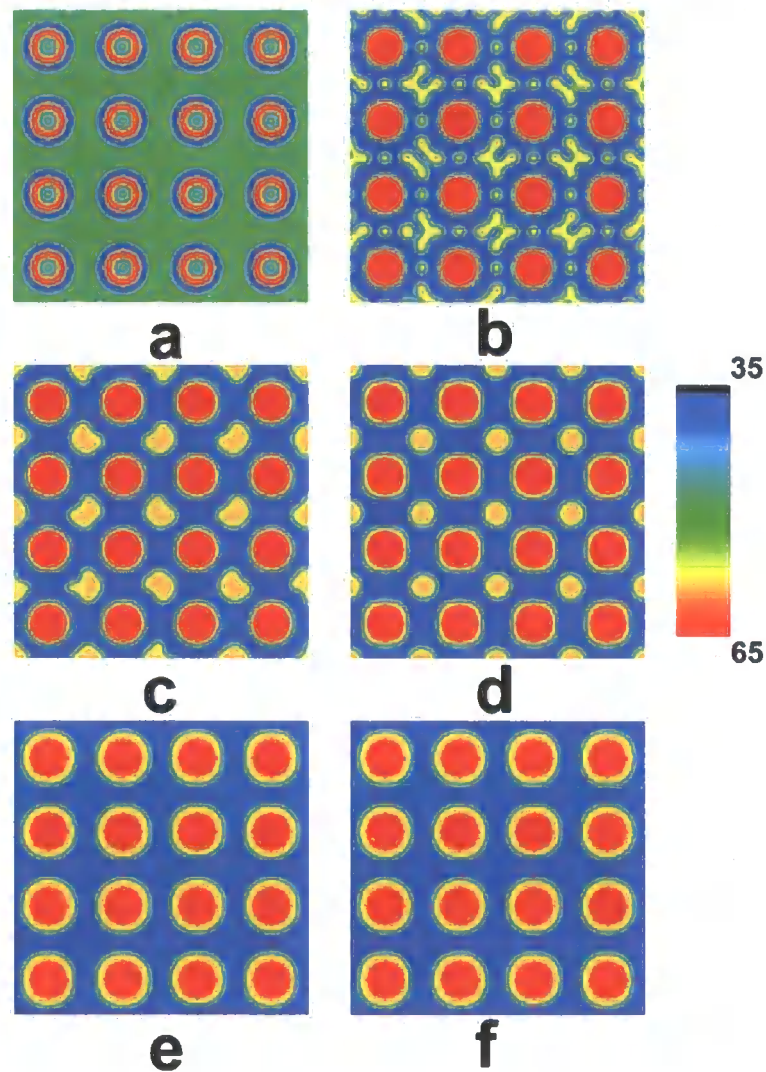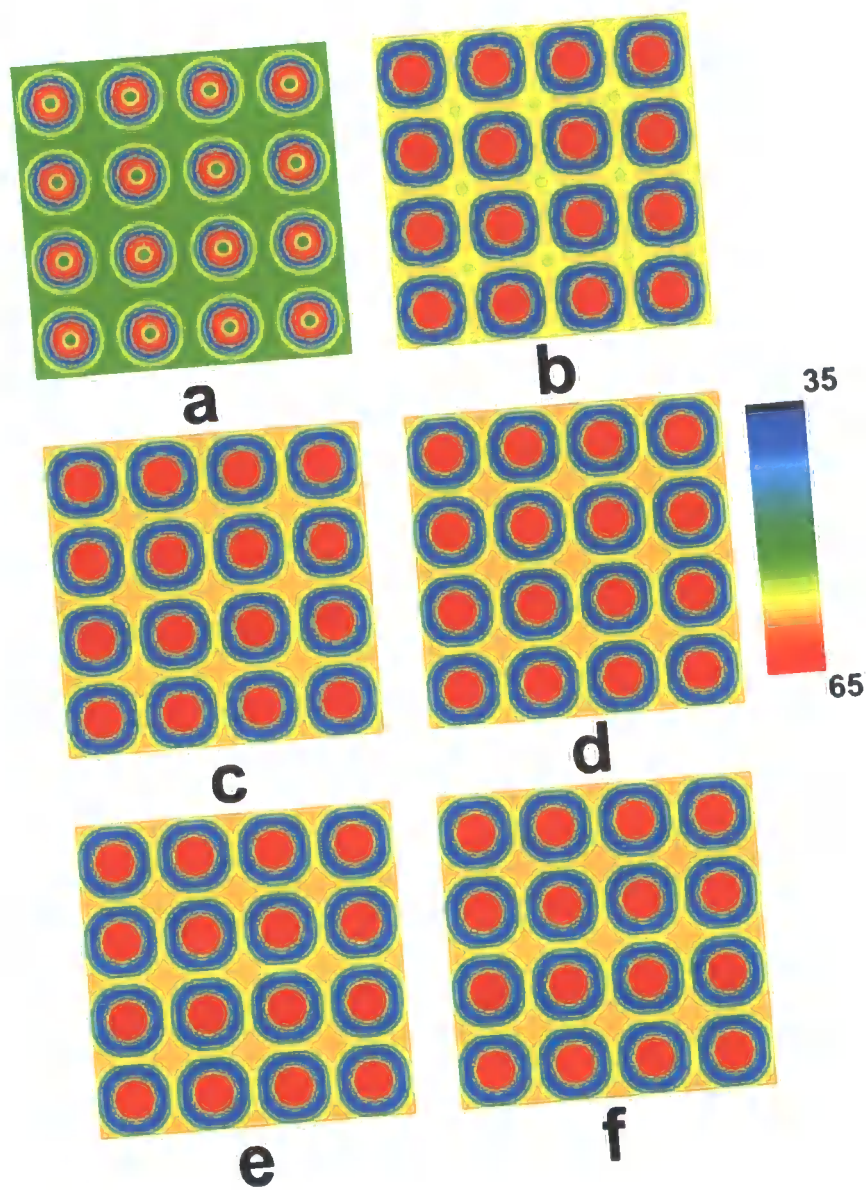

Figure 7.10

Development of the morphology following a quench into the two phase region when $h_1 = 0.5$ on the patterned areas and the matrix is neutral at (a) $\tau = 1$, (b) $\tau = 12.5$, (c) $\tau = 25$, (d) $\tau = 125$, (e) $\tau = 500$ and (f) $\tau = 2500$ for a 52.5:47.5 blend.

In this case the neutral matrix holds the excess of the component favoured by the pattern, which is phase separated to a reduced extent, as shown by the difference in colour contrast. Around the patterned area a depletion layer is visible as is expected from phase separation near a surface.

If the system used in figure 7.6 now undergoes a deeper quench, to χ = 0.00272, it is expected that the surface will have less of an affect on the final morphology due to the increased gradient in the interface between components. The results of this hypothesis are shown in figure 7.11.

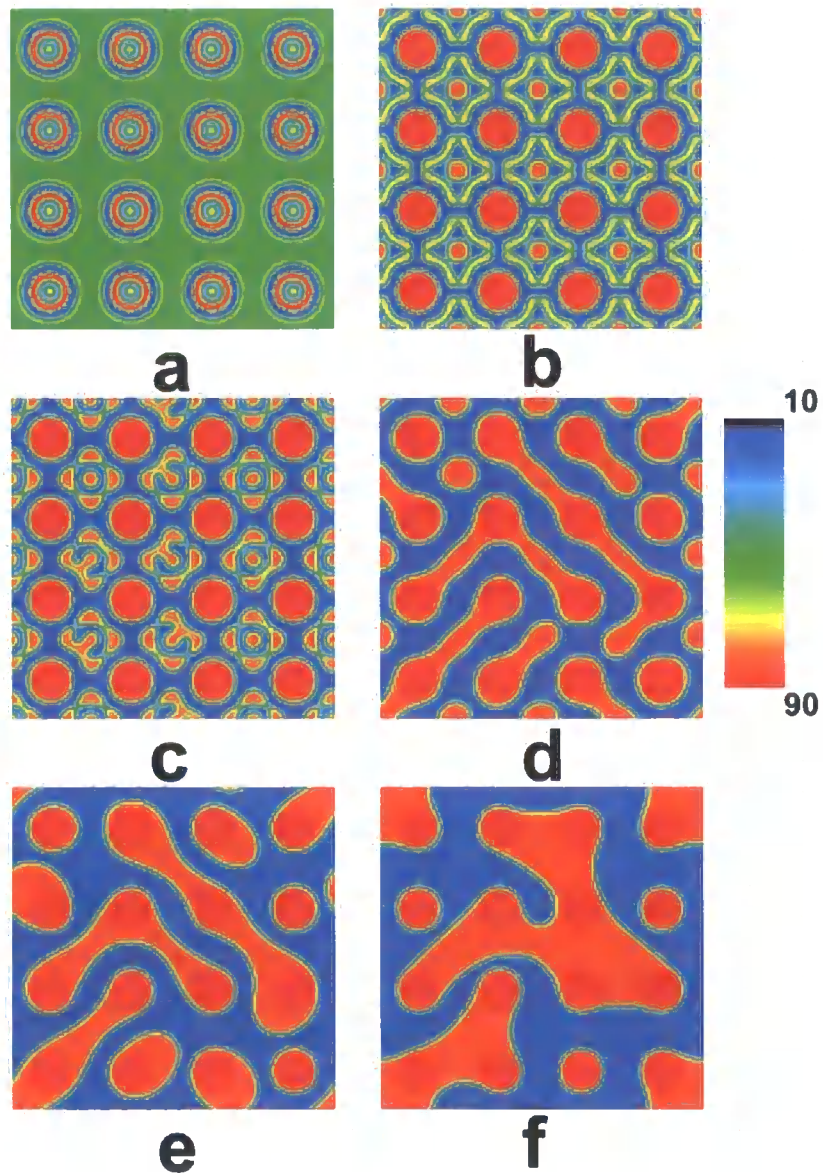*Figure 7.11*

Development of the morphology following a quench into the two phase region at (a) τ = 1, (b) τ = 12.5, (c) τ = 25, (d) τ = 125, (e) τ = 500 and (f) τ = 2500 when χ = 0.00272.

As suggested, when the quench depth is increased the surface attraction has a reduced influence on the final morphology, again interesting and elegant transient

structures are seen which are clearly influenced by the presence of the patterned surface. At later times however the greater extent of phase separation, and therefore greater difference in volume fraction between phases, forces the system to reduce the free energy of the bulk, with obvious costs to the surface free energy. This result re-enforces previous conclusions that the system is controlled by a balance between surface and bulk free energy. It is also clear from the above results that the morphology is definitely "tuneable" using this method, although a number of factors need to be considered when attempting to target specific morphologies.

The interface counting method is used to compare the amount of interface present with time for the examples shown in figures 7.6 and 7.7.
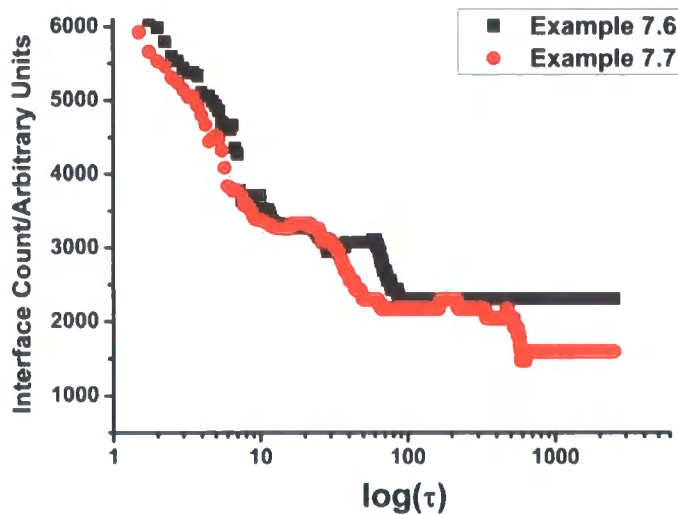
Figure 7.12

Time dependence of the total interfacial area corresponding to the phase separation kinetics shown in figures 7.6 and 7.7.

Figure 7.12 shows that by use of this method it is clear to see that the final morphologies of the examples shown in figures 7.6 and 7.7 are very different. At $\tau = 500$ we see a reduction in the amount of interface present in example 7.7 when compared to example 7.6, corresponding to the time at which the circles in the matrix diffuse to the patterned areas. However we see little reduction in the interface count for figure 7.6 after $\tau \approx 100$ indicating the pattern seen is indeed locally stable over time.

7.2.2 Forming Controlled Structures on a Regular Patterned Surface

If the circles in the above pattern were placed close enough together we propose that it should be possible for the excess polymer around the pattern to form a single structure throughout the system, for this reason we now change the spacing between the patterned areas. Initially a 160x128 array is used such that the distance between the centres of the patterned circles is 24 array units in the **x** direction, secondly a 128^2 array is used such that the distance between patterned circles is 16 array units in the **x** direction; the radius of the pattern is 4 array units and the distance between the centre of each patterned circle is 32 array units in the **y** direction in each case. The interface counting method is used and a contour plot is taken whenever a significant change is seen within the interface count. Here $h_1 = 0.5$ in the patterned areas and the matrix is set to be neutral, $g = 0.1$, $N_A = N_B = 500$ with $\Delta\tau = 0.0025$, $\Delta x = 0.5$ and a 40:60 blend composition is used.

Figure 7.13

(a) Interface count vs. time for a 160x128 system with points of interest shown corresponding to (b) τ = 15, (c) τ = 26, (d) τ = 44 and (e) τ = 75.

By making use of the interface count plot we are able to choose the most appropriate time points to create contour plots to help understand the occurrences during phase separation. Figure 7.13 shows the phase separation process occurring in a similar fashion to that in figure 7.9, however in this case the distance between the pattern in the **y** direction is greater than that in the **x** direction. Again interesting, and potentially useful, transient structures are seen between the patterned areas

which then give way to a system in which the morphology is directed by the surface patterning. Unfortunately however the phase separated morphology above the patterned areas do not join together to form a single structure as hoped so the distance between patterned areas is reduced in the next example to 16 array units and the simulation occurs on a 128^2 array with all other variables remaining constant.
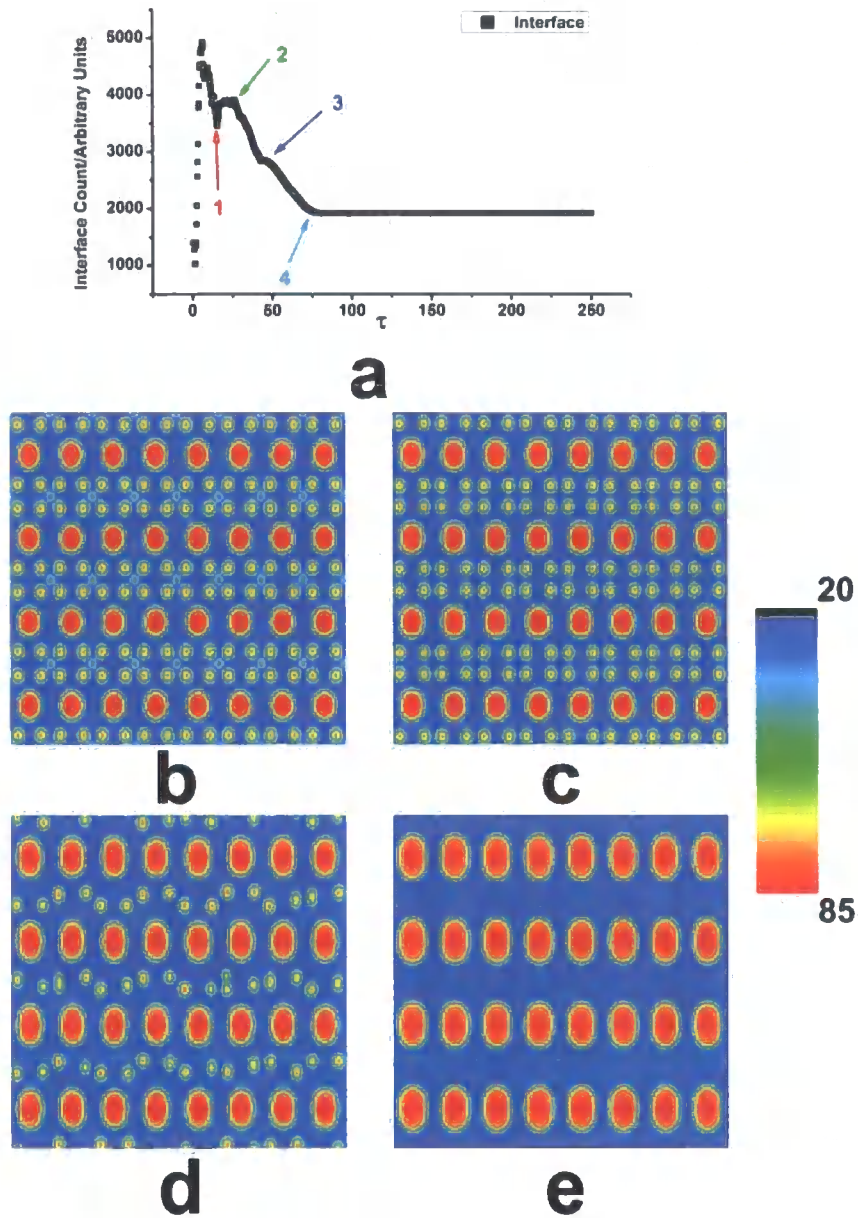

Figure 7.14

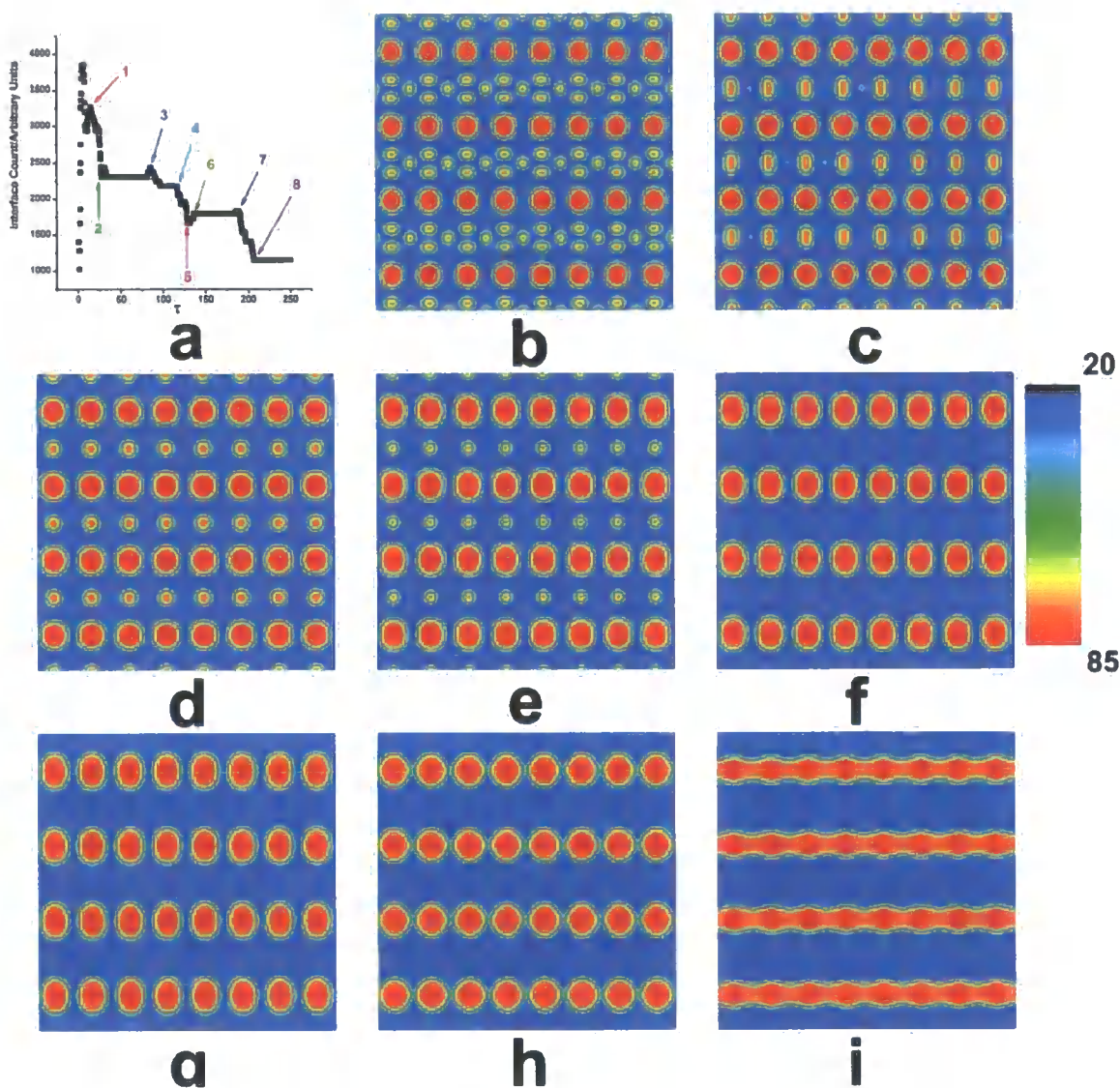(a) Interface count vs. time for a 128^2 system with points of interest shown corresponding to (b) $\tau = 15$, (c) $\tau = 25$, (d) $\tau = 85$, (e) $\tau = 118$, (f) $\tau = 126$, (g) $\tau = 138$, (h) $\tau = 190$ and (i) $\tau = 206$.

Figure 7.14 again shows an interface count and examples of the morphology at a number of interesting points. Here the pattern is close enough to allow single

structures to be formed along the x direction in figure 7.14(i); this transition can be seen to be favourable from figure 7.14(a) as the amount of interface significantly reduces between points h and i. Between points f and g the amount of interface is seen to increase, as is the case at points d and h. We believe this occurs by creating transient structures to either allow the system to reduce the overall interface, and therefore free energy, as in points d and h, or when the system has reduced its free energy significantly and an equilibrium state is being resolved, as in point f.

7.2.3 Patterning to Control Phase Separated Structure

Using this method we believe that it is now possible to target a vast number of different phase separated morphologies. By setting the patterned points close enough together it is possible to repeatedly form the above structure and therefore give a targeted morphology. Experimentally the use of inkjet printing is being developed to create such patterns and therefore to give the possibility of forming the pattern in a repeatable manner and with little error. The uses of such systems can at this time only be imagined but if, for example, one polymer, the red polymer in our case, was conductive and the second polymer were insulating then conductive lines of polymer can be laid near to each other with a high degree of accuracy but on a nano-meter length scale. This could lead to the development of Phase Separated Circuit Boards (PSCB's) for use in a large array of different products. To show control is possible over the final structures in these systems a different pattern has been used to that shown above, it is shown in figure 7.15.

Figure 7.15

Circle pattern over which phase separation occurs.

The above pattern is produced on a 138^2 array and phase separation for two blend compositions is carried out, these are a 35:65 blend and a 30:70 blend with h_1 = 0.5 in the patterned areas and the matrix is set to be neutral, $g = 0.1$, $N_A = N_B =$ 500, $\Delta\tau = 0.0025$ and $\Delta x = 0.5$.

Figure 7.16

Growth of morphology for a 35:65 blend at (a) $\tau = 2.5$, (b) $\tau = 125$, (c) $\tau = 250$, (d) $\tau = 1250$, (e) $\tau = 2500$ and (f) $\tau = 12500$.

Initially in figure 7.16 the phase separated morphology can be seen to mimic the patterned background, however with time the system broadens the structure, to reduce the overall free energy, and the pattern is seen to become lost by figure 7.16(f). A number of solutions to this problem present themselves from the above

investigation, including altering the attraction of each component to the surface, however the simplest is to alter the blend to a 30:70 composition; the results of such a change are shown in figure 7.17.
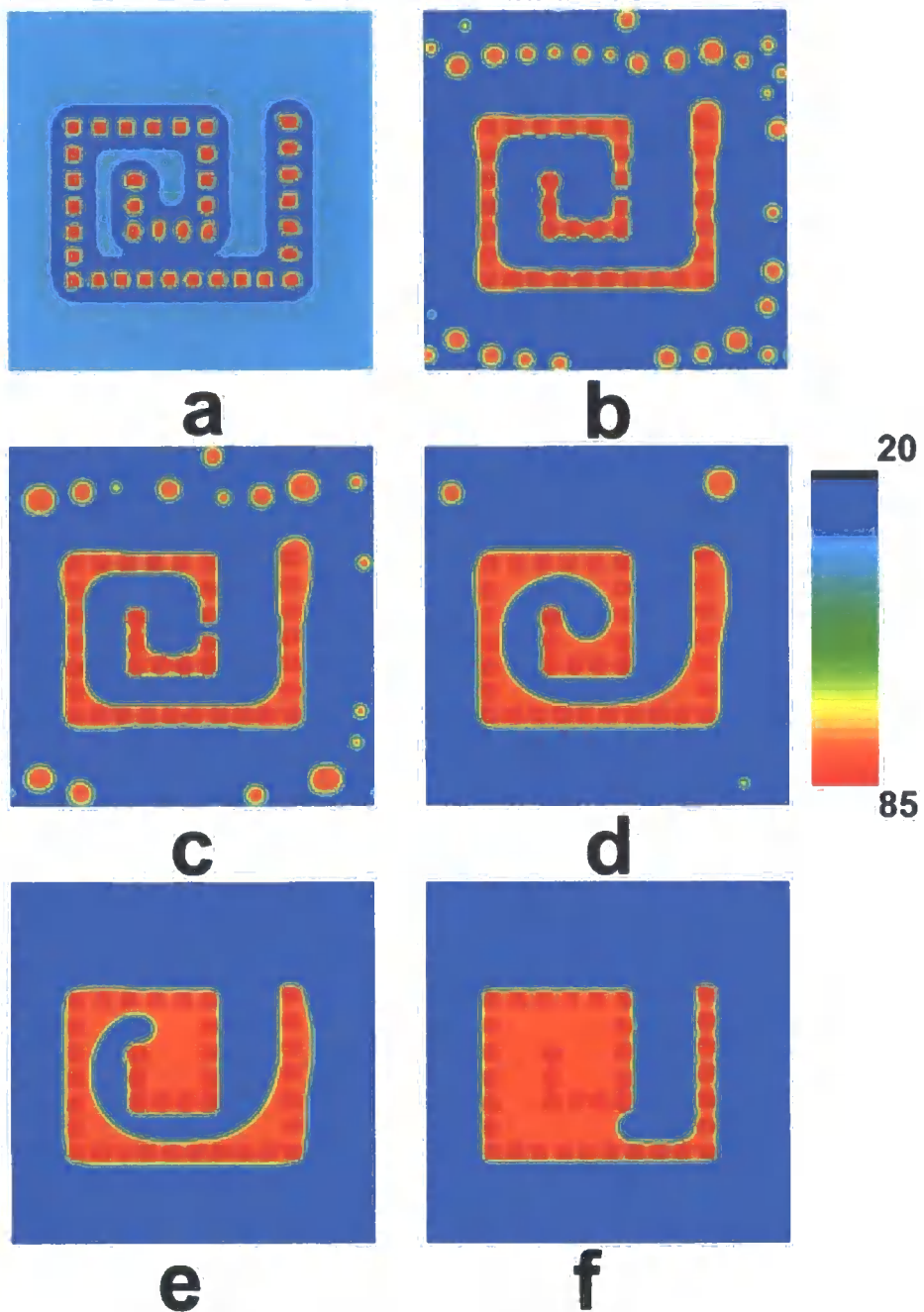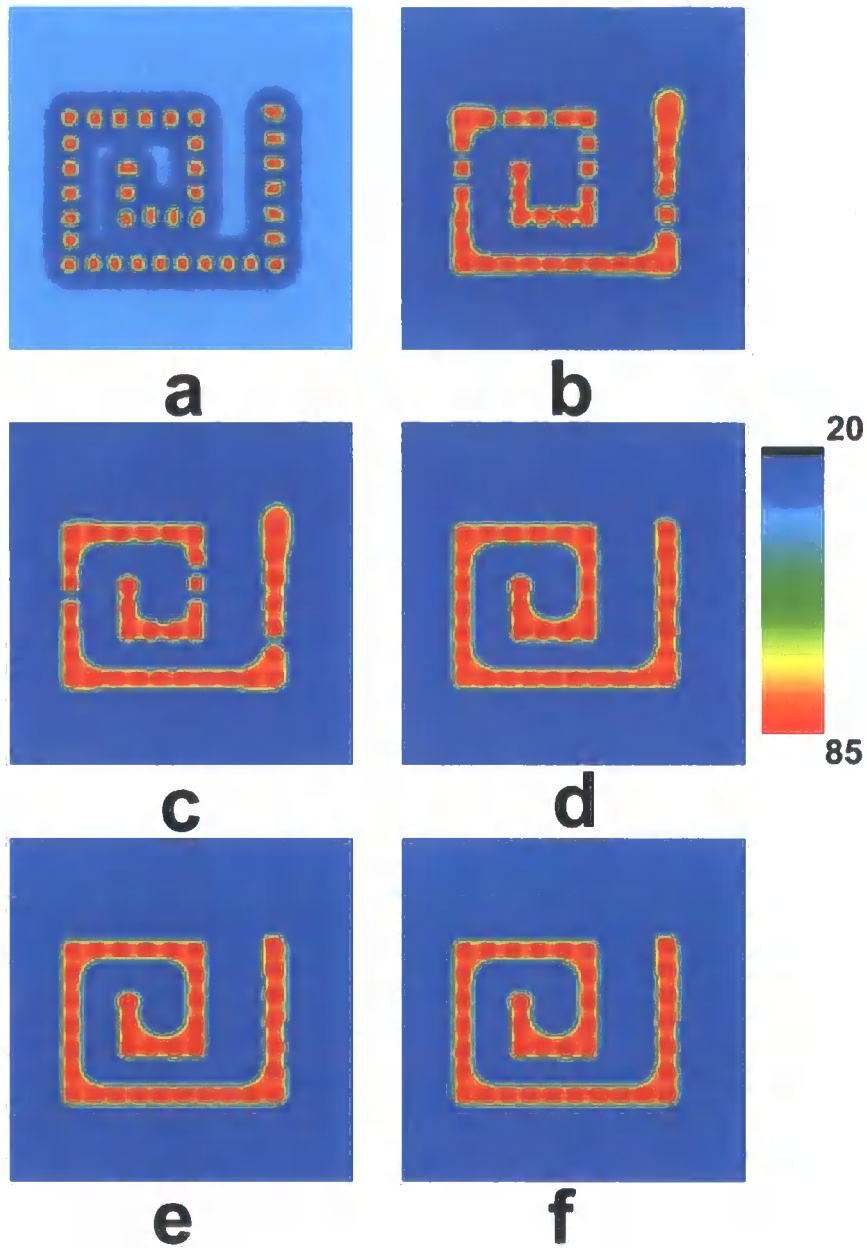

Figure 7.17

Growth of morphology for a 30:60 blend at (a) $\tau = 2.5$, (b) $\tau = 125$, (c) $\tau = 250$, (d) $\tau = 1250$, (e) $\tau = 2500$ and (f) $\tau = 12500$.

We see in figure 7.17 that the morphology mimics the pattern throughout the simulation and no more broadening can occur as only a limited amount of component

A, the red component, is present. We see no domain broadening occurring between figures 7.17(d) and 7.17(f) which shows a great contrast to the amount of domain broadening seen in 7.16(d) to 7.16(f). This comparison highlights the importance of controlling the system variables as very different final morphologies are seen in each case which from a technological point of view could have very different properties.

We therefore believe that this is an exciting way to target morphologies for many technological applications. The above examples show however that careful control is needed over the conditions, i.e. quench depth and blend composition, used when phase separation occurs in these systems. We note that although the above systems are limited to patterns made up from circles it is possible to pattern any shape onto the surface in our model and should be possible for most patterns experimentally.

7.3   Conclusions

In the current chapter the model developed in chapter 6 for polymer phase separation at and near a surface has been used to investigate phase separation both adjacent to and above a patterned surface. Initially a hard wall surface is patterned to be attractive to two components of a blend in an alternating fashion. We find that interesting alternating structures propagate throughout the system due to the interaction with the surface, as in the previous chapter. However the structures no longer alternate solely in a direction perpendicular to the wall but also parallel to the wall due to the patterning present there.

We also study the process of phase separation above a patterned surface; here we consider a system where a surface has been altered in specific areas to change the surface properties. We investigate patterns made from a series of circles and find transient structures develop that do not mimic the pattern but are a consequence of the wavelength selection process and the intrinsically dynamic nature of phase separation. In other words, although the final state may be a phase separated film whose morphology mimics that of the pattern, unusual transient structures develop. Such non-equilibrium structures may be undesirable, or may even be exploitable; in either case, an understanding of the underlying physical mechanisms is essential if control is to be gained. By changing the surface properties, quench depth and blend composition we believe it is possible to control these systems and show that we can either stabilise or remove these transient structures. By changing the distance

between the circle patterns we find that we can also form controllable lines of polymer between our patterned area and feel that such a system could have vast technological uses, for not only does it lead to target morphologies but also with the use of sophisticated conducting polymers it could lead to applications in organic semi-conducting technologies.

Chapter 8

Surface Directed Spinodal Decomposition in Ternary Blends

The methods used in chapters 5 and 6 are now further extended to model a three component (A, B and C) polymer blend undergoing phase separation at and near to a hard wall surface. Firstly the equations used in chapter 6 are developed to account for the third component of the blend and the ternary phase diagram is then found by calculating the spinodal. Phase separation of this three component blend is studied by altering the interaction parameters between the A and B components of the blend and by changing the attraction of each component to the surface to propose a number of different surface morphologies. These morphologies are then studied via parallel and perpendicular correlation functions, where it is found that layers of each polymer can be formed perpendicular to the surface or by surface competition, alternating morphologies can be seen parallel to the surface.

8.1 Modelling Surface Directed Spinodal Decomposition in a Three Component Polymer Blend

We initially develop the theory shown previously for three component polymer blends. Firstly we follow the method of Huang et al.[97] to construct the free energy functional for each component of the polymer blend from the Flory-Huggins free energy per lattice site for a three component polymer blend,

$$\frac{f_{FH}(\phi)}{k_B T} = \frac{\phi_A}{N_A}\ln\phi_A + \frac{\phi_B}{N_B}\ln\phi_B + \frac{\phi_C}{N_C}\ln\phi_C + \chi_{AB}\phi_A\phi_B + \chi_{AC}\phi_A\phi_C + \chi_{BC}\phi_B\phi_C,$$

$$(8.1.1)$$

where N_i is the degree of polymerisation of component i, when i = A, B or C and ϕ_i is the local composition volume fraction of component i.

Equation 5.1.1 has been developed to describe the morphological evolution of a two component polydisperse polymer blend, here we consider an incompressible system where $\phi_C = 1 - \phi_A - \phi_B$ so by combining equations 5.1.1 and 8.1.1 we are able to produce equations for components A and B to describe the morphological

evolution of a three component polymer blend in the bulk when Λ_{ij} is now determined by

$$\Lambda_{ij} = \left(\delta_{ij} - \phi_i \right) - \phi_j + 2\phi_i\phi_j, \qquad (8.1.2)$$

and for simplicity we use for the degree of polymerisation $N_A = N_B = N_C = N$. In equation 5.1.1 x and τ are rescaled spatial and temporal variables respectively, now given by $x = r/N^{1/2}b$ and $\tau = \lambda t/N^2 b^2$, where b is the Kuhn length of species i and λ is its mobility component. It is noted that equation 8.1.2 varies from equation 2.4.11 as $\lambda_A = \lambda_B = \lambda_C = \lambda$ since the degree of polymerisation for each component is the same; this is now incorporated into the rescaled temporal variable.

We define the equations needed to model the effects of a surface added into the system in a three component polymer blend. We start by composing an equation for the "bare" surface free energy[7],

$$f_s^b(\phi) = \frac{z'}{2kT} \left[\phi_A^2 \varepsilon_{AA} + \phi_B^2 \varepsilon_{BB} + \phi_C^2 \varepsilon_{CC} + 2\phi_A\phi_B\varepsilon_{AB} + 2\phi_A\phi_C\varepsilon_{AC} + 2\phi_B\phi_C\varepsilon_{BC} \right],$$

$$(8.1.3)$$

where z' bonds are cut when a new surface is made. It is useful to rewrite the above equation in the form,

$$f_s^b(\phi) = -h_A\phi_A - \tfrac{1}{2} g_A\phi_A^2 - h_B\phi_B - \tfrac{1}{2} g_B\phi_B^2 - \tfrac{1}{2} g_{AB}\phi_A\phi_B, \qquad (8.1.4)$$

The competition between the surface field and the energy cost associated with a gradient in the order parameter creates an equilibrium value of the order parameter at the surface and the above boundary condition is used to pin the surface value to this equilibrium value. The first boundary condition used in chapter 6, $\Delta J|_{x=0} = 0$, where J is the polymer flux, is used to ensure that the flux of the polymer components though the surface boundary is zero; this enforces conservation of the order parameter, where $J \propto \nabla \delta F / \delta \phi$.

As before a second boundary condition, from equation 8.1.4, is applied to one surface, at x = 0, and the first boundary condition is applied to two parallel surfaces

at $\mathbf{x} = 0$ and $\mathbf{x} = \mathbf{x}'$. For two dimensional simulations, periodic boundary conditions will be applied at the $\mathbf{y} = 0$ and $\mathbf{y} = \mathbf{y}'$ surfaces. The equations used to evolve the phase separation process in such are blend are now given by,

$$
\begin{aligned}
\frac{\partial \phi_A(\mathbf{x},\tau)}{\partial \tau} = & \Lambda_{AA} \nabla^2{}_{AA} \Big[\big(\ln \phi_A - \ln(1-\phi_A-\phi_B) + N\chi_{AC}(1-2\phi_A-\phi_B) + N\phi_B(\chi_{AB}-\chi_{BC}) \big) \\
& + \frac{1}{36}\left(\left(\frac{1}{(1-\phi_A-\phi_B)^2} - \frac{1}{\phi_A^2} \right)(\nabla\phi_A)^2 + \frac{1}{(1-\phi_A-\phi_B)^2}(\nabla\phi_B)^2 \right) \\
& - \left(\frac{1}{18}\left(\frac{1}{(1-\phi_A-\phi_B)} + \frac{1}{\phi_A} \right)\nabla^2\phi_A + \frac{1}{(1-\phi_A-\phi_B)}\nabla^2\phi_B \right) \Big] \\
& + \Lambda_{AB} \nabla^2{}_{AB} \Big[\big(\ln \phi_B - \ln(1-\phi_A-\phi_B) + N\chi_{BC}(1-\phi_A-2\phi_B) + N\phi_A(\chi_{AB}-\chi_{AC}) \big) \\
& + \frac{1}{36}\left(\left(\frac{1}{(1-\phi_A-\phi_B)^2} - \frac{1}{\phi_B^2} \right)(\nabla\phi_B)^2 + \frac{1}{(1-\phi_A-\phi_B)^2}(\nabla\phi_A)^2 \right) \\
& - \frac{1}{18}\left(\left(\frac{1}{(1-\phi_A-\phi_B)} + \frac{1}{\phi_B} \right)\nabla^2\phi_B + \frac{1}{(1-\phi_A-\phi_B)}\nabla^2\phi_A \right) \Big] \\
& + \left(-h_A - g_A\phi_A(\mathbf{R},0,\tau) - \frac{1}{2}g_{AB} + \gamma \frac{\partial\phi_A(\mathbf{R},\mathbf{x},\tau)}{\partial\mathbf{x}}\Big|_{\mathbf{x}=0} \right)\delta(\mathbf{x}) \Big],
\end{aligned}
$$

$$\text{(8.1.5)}$$

and,

$$
\begin{aligned}
\frac{\partial \phi_B(\mathbf{x},\tau)}{\partial \tau} = & \Lambda_{BA} \nabla^2{}_{BA} \Big[\big(\ln \phi_A - \ln(1-\phi_A-\phi_B) + N\chi_{AC}(1-2\phi_A-\phi_B) + N\phi_B(\chi_{AB}-\chi_{BC}) \big) \\
& + \frac{1}{36}\left(\left(\frac{1}{(1-\phi_A-\phi_B)^2} - \frac{1}{\phi_A^2} \right)(\nabla\phi_A)^2 + \frac{1}{(1-\phi_A-\phi_B)^2}(\nabla\phi_B)^2 \right) \\
& - \left(\frac{1}{18}\left(\frac{1}{(1-\phi_A-\phi_B)} + \frac{1}{\phi_A} \right)\nabla^2\phi_A + \frac{1}{(1-\phi_A-\phi_B)}\nabla^2\phi_B \right) \Big] \\
& + \Lambda_{BB} \nabla^2{}_{BB} \Big[\big(\ln \phi_B - \ln(1-\phi_A-\phi_B) + N\chi_{BC}(1-\phi_A-2\phi_B) + N\phi_A(\chi_{AB}-\chi_{AC}) \big) \\
& + \frac{1}{36}\left(\left(\frac{1}{(1-\phi_A-\phi_B)^2} - \frac{1}{\phi_B^2} \right)(\nabla\phi_B)^2 + \frac{1}{(1-\phi_A-\phi_B)^2}(\nabla\phi_A)^2 \right) \\
& - \frac{1}{18}\left(\left(\frac{1}{(1-\phi_A-\phi_B)} + \frac{1}{\phi_B} \right)\nabla^2\phi_B + \frac{1}{(1-\phi_A-\phi_B)}\nabla^2\phi_A \right) \Big] \\
& + \left(-h_A - g_A\phi_A(\mathbf{R},0,\tau) - \frac{1}{2}g_{AB} + \gamma \frac{\partial\phi_A(\mathbf{R},\mathbf{x},\tau)}{\partial\mathbf{x}}\Big|_{\mathbf{x}=0} \right)\delta(\mathbf{x}) \Big],
\end{aligned}
$$

$$\text{(8.1.6)}$$

where δ(x) is the Dirac-delta function, ensuring that the surface free energy only affects $x = 0$. For consistency with previous models we also include a third term, dependant on γ, in the surface free energy which accounts for the energy cost of gradients in composition at the surface, and was derived on the basis of the Kawasaki spin-exchange model. The surface term is added into the dynamic equation of motion. In the simulations we again scale the surface terms by $1/\Delta x$ to ensure consistency when discretising the equations of motion. We relate h_a, h_b, g_a, g_b and g_{ab} to real systems using the following which has been determined from the "bare" surface free energy[7] following the methodology see previously,

$$h_a = \frac{z' \chi_{AC}}{2z} - \frac{\Delta \gamma_{AC} b^2}{kT},$$ (8.1.7)

$$h_b = \frac{z' \chi_{BC}}{2z} - \frac{\Delta \gamma_{BC} b^2}{kT},$$ (8.1.8)

$$g_a = \frac{z' \chi_{AC}}{z},$$ (8.1.9)

$$g_b = \frac{z' \chi_{BC}}{z},$$ (8.1.10)

$$g_{AB} = z' \left(\frac{\chi_{AC} + \chi_{BC} - \chi_{AB}}{z} \right),$$ (8.1.11)

where z is the coordination number of the lattice, z' bonds are cut when a new surface is made and $\Delta \gamma_{ij}$ is the difference in surface tension between components i and j.

8.1.1 Phase Separation in a Three Component Blend

In the following we investigate two regions of the phase diagram by altering the various χ parameters. To do this we first show phase diagrams for a number of different variables in figure 8.1, where the spinodal curve is given by the determinant[97] of equation 2.6.2.
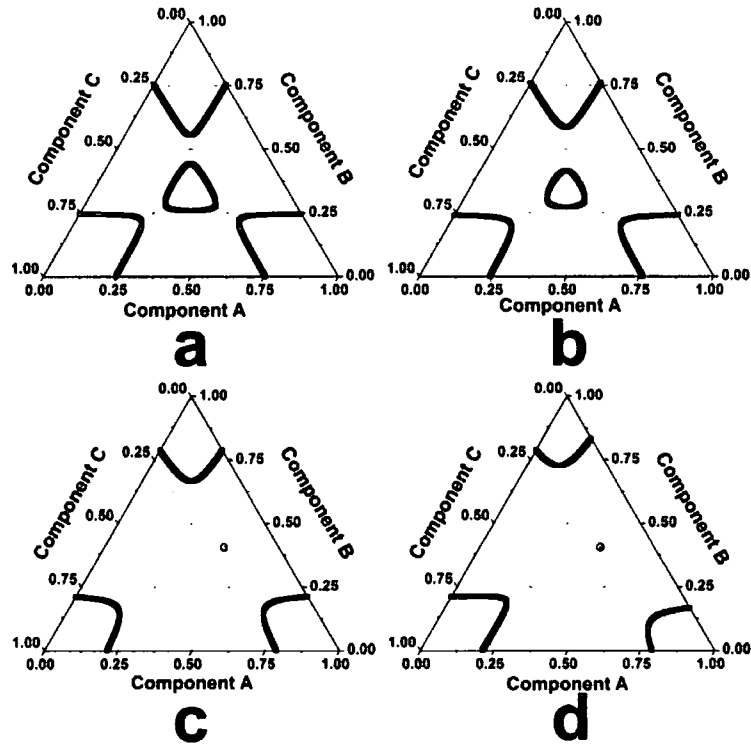
Figure 8.1

The phase diagrams, spinodal curve, of symmetric ternary systems where N = 200

for (a) $\chi_{AB} = \chi_{AC} = \chi_{BC} = 0.0135$, (b) $\chi_{AB} = \chi_{AC} = \chi_{BC} = 0.0137$, (c) $\chi_{AB} = \chi_{AC} = \chi_{BC}$

$= 0.015$ and (d) $\chi_{AB} = 0.018$, $\chi_{AC} = \chi_{BC} = 0.015$.

We use blend parameters corresponding to figures 8.1(c) and 8.1(d) during our simulations with surface variables and will undertake the work with a blend composition of $\phi_A = 0.4$, $\phi_B = 0.4$ and $\phi_C = 0.2$, represented by ● on the above phase diagrams, this allows us to probe a similar area of the phase diagram to Huang[97] et al. Figures 8.2 and 8.3 show example morphologies of the systems when no surface is present.

200
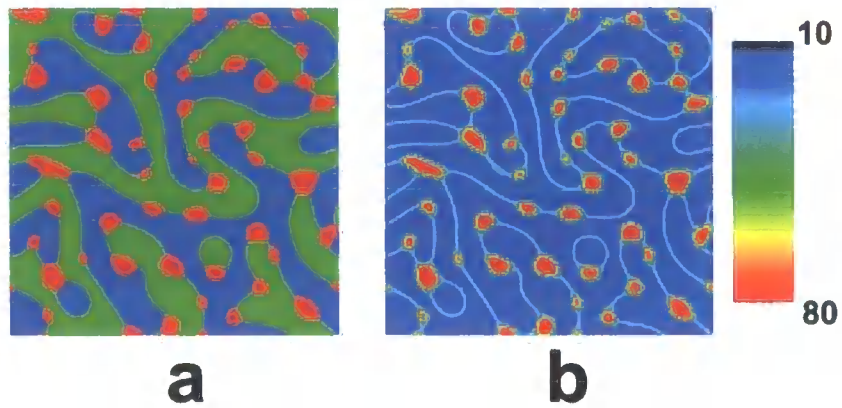
Figure 8.2

Example morphologies when $\chi_{AB} = \chi_{AC} = \chi_{BC} = 0.015$ at $\tau = 2500$ for (a) the three component system where ■ represents component A, ■ represents component B and ■ represents component C, and (b) the morphology of component C with phase separation described by the legend.

Figure 8.3

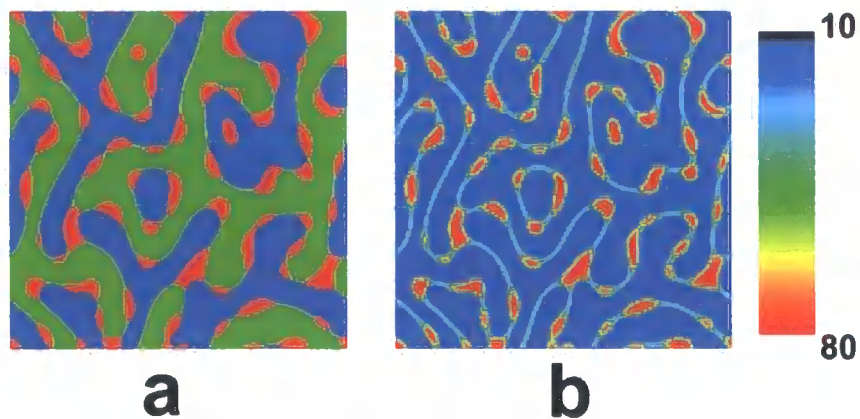Example morphologies when $\chi_{AB} = 0.018$, $\chi_{AC} = \chi_{BC} = 0.015$ at $\tau = 2500$ for (a) the three component system where ■ represents component A, ■ represents component B and ■ represents component C, and (b) the morphology of component C.

A comparison of figures 8.2(b) and 8.3(b) shows that when χ_{AB} is increased the volume fraction of component C, at the interface between components A and B,

increases and the formation of droplets of component C is reduced, this is due to the increased "dislike" of each other components A and B experience when χ_{AB} is increased.

8.1.2   Phase Separation at a Surface

In the following investigation a matrix of size 128 x 256 is used, where the surface resides along the longer dimension, with $\Delta\tau = 0.001$, $\Delta x = 0.5$ and an initial random noise of ±0.001. Four different surface attraction conditions are investigated with $h_a = \pm0.5$ and $h_b = \pm0.5$ so that we probe the morphology when $h_a = h_b > h_c$, $h_a > h_c > h_b$, $h_b > h_c > h_a$ and $h_c > h_a = h_b$. In each case component C is neither attracted nor repelled by the surface and is said to be in a neutral state. Following the methodology of Puri and Binder[115] we probe $\overline{\phi}_i$, the average value of the volume fraction for each component of the blend perpendicular to the surface, and the point at which the morphology first intersects $\overline{\phi}_i$ when moving perpendicular to the surface. We also define both a perpendicular and parallel correlation function, respectively using,

$$G_{\perp} = \left\langle \left(\phi(Z=0) - \overline{\phi}_{ij} \right) \left(\phi(Z=Z) - \overline{\phi}_{ij} \right) \right\rangle, \qquad (8.1.12)$$

$$G_{\parallel} = \left\langle \phi(x)\phi(x+1) \right\rangle - \left\langle \phi(x) \right\rangle^2, \qquad (8.1.13)$$

and a characteristic length in each case, defined as $l_{\perp} = \frac{1}{2}G_{\perp}(Z=0)$ and $l_{\parallel} = \frac{1}{2}G_{\parallel}(x=0)$, where x is the distance parallel to the surface and Z is the distance perpendicular to the surface.

We define four different surface parameter cases for each set of χ parameters, i.e. in case 1 $h_a = 0.5$ and $h_b = 0.5$, in case 2 $h_a = 0.5$ and $h_b = -0.5$, in case 3 $h_a = -0.5$ and $h_b = 0.5$ and finally in case 4 $h_a = -0.5$ and $h_b = -0.5$, the resultant surface segregation is shown in figure 8.4 for each case.
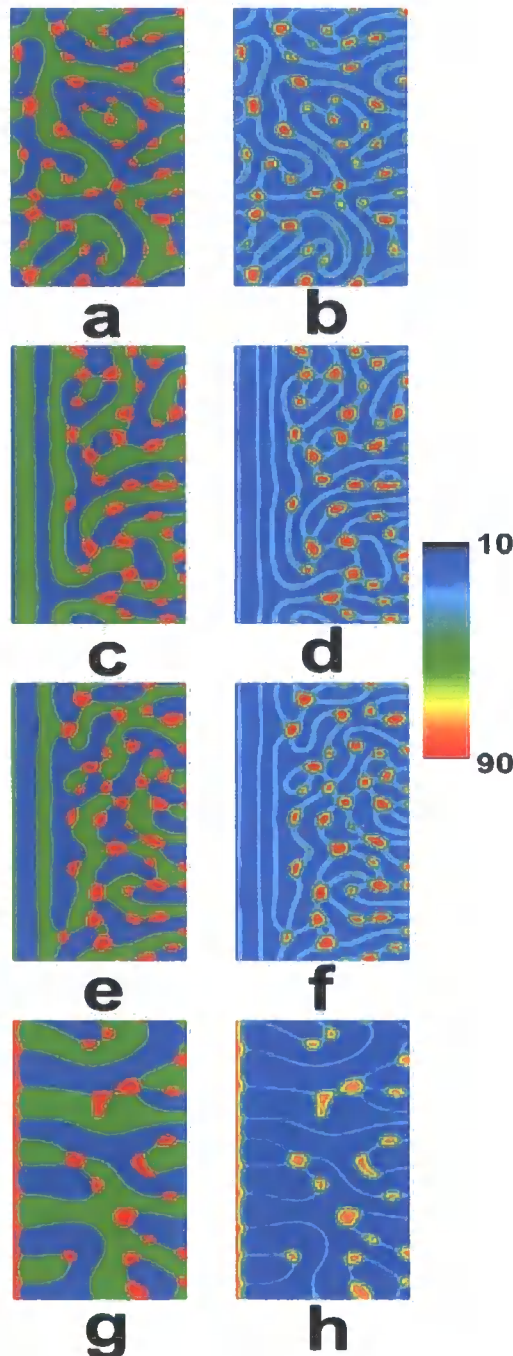
Figure 8.4

Morphologies when $\chi_{AB} = \chi_{AC} = \chi_{BC} = 0.015$ at $\tau = 1000$ where ■ represents component A, ■ represents component B and ■ represents component C in (a), (c), (e) and (g) and the morphology of component C is shown in (b), (d), (f) and (h). In (a) and (b) $h_a = 0.5$ and $h_b = 0.5$, in (c) and (d) $h_a = 0.5$ and $h_b = -0.5$, in (e) and (f) $h_a = -0.5$ and $h_b = 0.5$ and in (g) and (h) $h_a = -0.5$ and $h_b = -0.5$.

By setting the value of h_i to be positive we see that component i becomes attracted to the surface, such that in figure 8.4(a) both components A and B are

equally compelled to form at the surface on the left hand side of the diagram and a pseudo random morphology is formed. Upon setting component A to form at the surface and component B to be repelled by the surface (corresponding to h_a = 0.5 and h_b = -0.5) we see A-C-B layers forming in figure 8.4(c), as component C is the minor phase its layer is thin, residing between the layers of components A and B. The opposite is seen in figure 4(e) where a B-C-A layer is formed by reversing the signs of the h values for components A and B. Finally in figure 8.4(g) we see that because both components A and B have negative h values component C forms at the surface and is also present at the interface between components A and B, only at a reduced volume fraction. Figures 8.4(a) – 8.4(f) show results consistent to those seen in previous studies for binary blends where layers are formed perpendicular to the surface, in figure 8.4(g) we model a situation which is dissimilar to any system possible with a binary blend and which could have important technological uses.

8.2   Simulation Results

The following simulations were undertaken to τ = 3000 on a 128 x 256 array where the surface is placed along the longer axis of the system. A non square array was used so as to increase the computational efficiency of the system as our main interest is with the processes occurring at the surface and not in the bulk. All simulations were undertaken with $\Delta\tau$ = 0.001, Δx = 0.5 and were averaged over 5 runs with different initial random noise each time. The simulations were carried out with a blend composition of ϕ_A =0.4, ϕ_B =0.4 and ϕ_C =0.2.

8.2.1   Variation of ϕ with Depth from the Surface

Firstly we show plots of $\bar{\phi}_i$, the average of phi, for each component vs. depth into the system perpendicular to the surface, **r**. The plot is only taken to 50 units from the surface as a random morphology is formed at larger depths, as seen in figures 8.3 and 8.4, and as stated above our main interest is in the interactions each component undergoes due to the surface and the other blend components. We present results for χ_{AB} = χ_{AC} = χ_{BC} = 0.015 for each case as defined above and for each component of the blend. We also follow $\bar{\phi}_i$ for each component with time and then find the depth, r, at which ϕ_i first intersects $\bar{\phi}_i$, where i = A, B or C.

Figure 8.5

$\overline{\phi}_i$ vs. **r** for times shown in the legend when $\chi_{AB} = \chi_{AC} = \chi_{BC} = 0.015$ and $h_a = h_b = 0.5$ for (a) component A, (b) component B, (c) component C and (d) the value of **r'** at which ϕ_i first intersects $\overline{\phi}_i$, where i = A, B or C.

Figure 8.6

$\overline{\phi}_i$ vs. **r** for times shown in the legend when $\chi_{AB} = \chi_{AC} = \chi_{BC} = 0.015$ and $h_a = 0.5$, $h_b = -0.5$ for (a) component A, (b)component B, (c) component C and (d) the value of **r'** at which ϕ_i first intersects $\overline{\phi}_i$, where i = A, B or C.

Figure 8.7

$\overline{\phi}_i$ vs. **r** for times shown in the legend when $\chi_{AB} = \chi_{AC} = \chi_{BC} = 0.015$ and $h_a = -0.5$,

$h_b = 0.5$ for (a) component A, (b) component B, (c) component C and (d) the value of

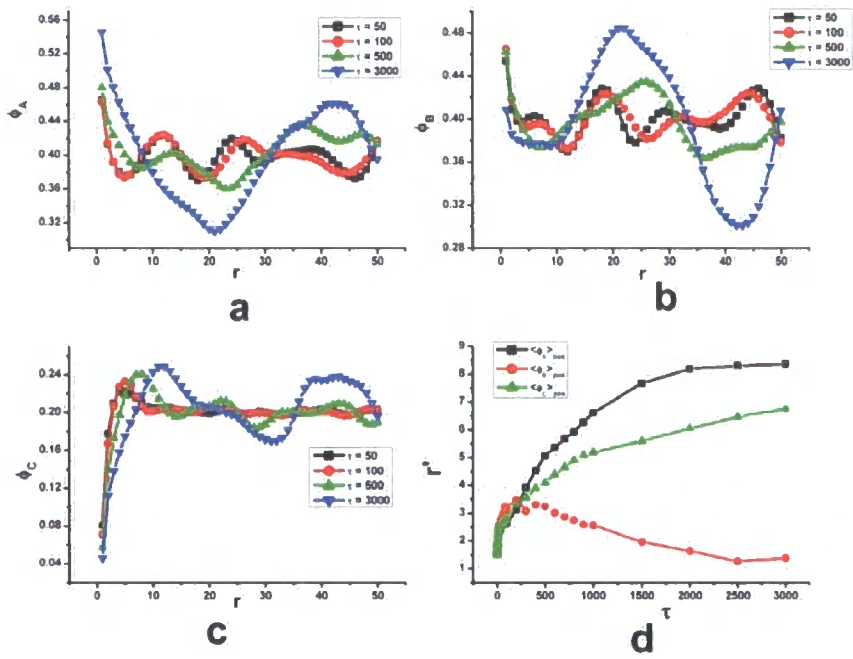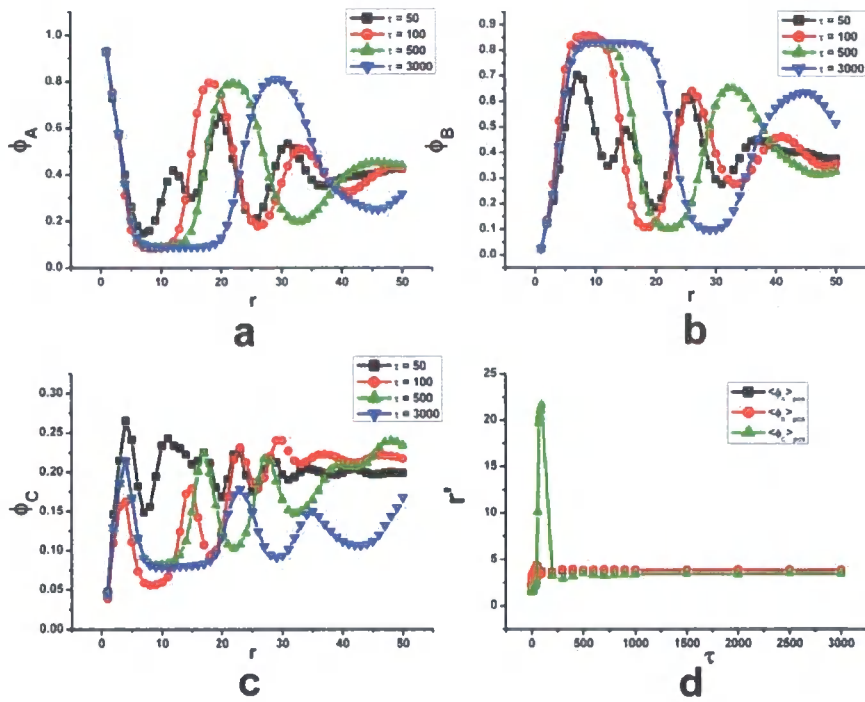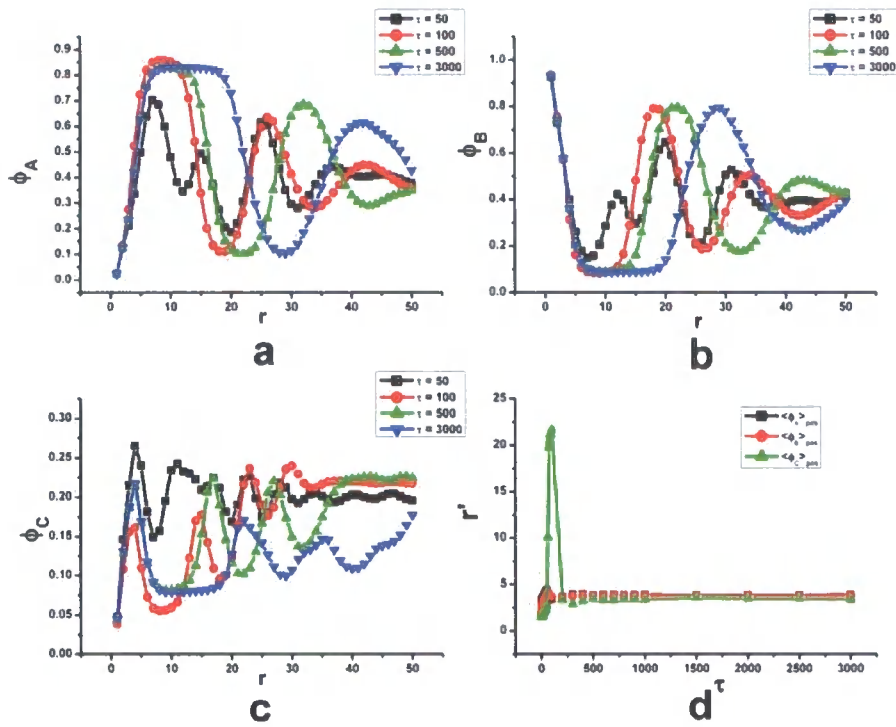**r'** at which ϕ_i first intersects $\overline{\phi}_i$, where i = A, B or C.
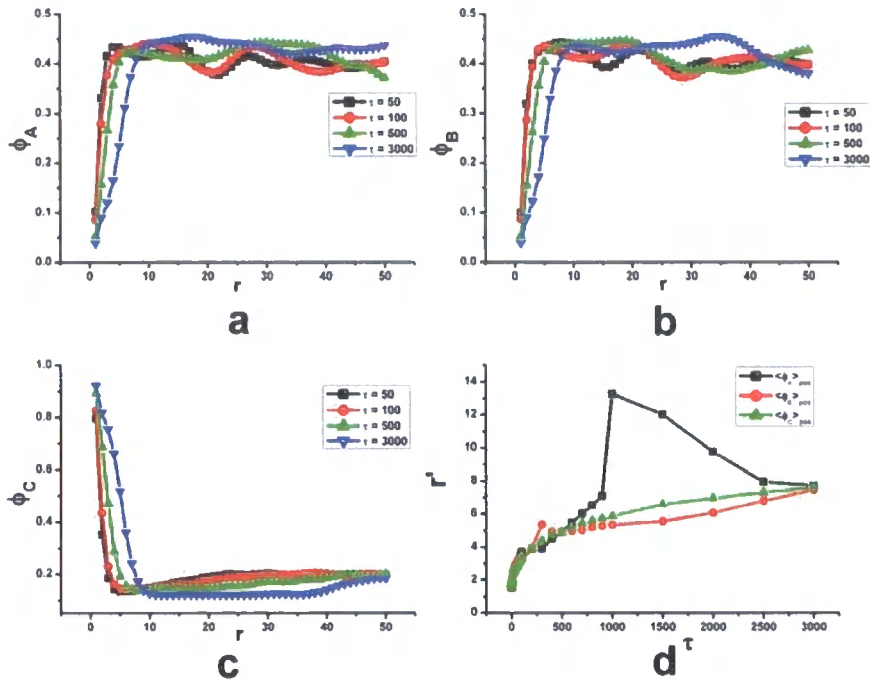
Figure 8.8

$\bar{\phi}_i$ vs. **r** for times shown in the legend when $\chi_{AB} = \chi_{AC} = \chi_{BC} = 0.015$ and $h_a = h_b = -0.5$ for (a) component A, (b)component B, (c) component C and (d) the value of **r'** at which ϕ_i first intersects $\bar{\phi}_i$, where i = A, B or C.

Figures 8.5 – 8.8 show a number of notable features of the simulations. In figures 8.5(a), 8.5(b) and 8.5(c) we clearly see the growth of the surface into the bulk with time, we also see the formation of a sinusoidal structure perpendicular to the surface, consistent with the spinodal decomposition process, forming in each case and then broadening with time. We note that in figure 8.5 the value of **r'**, the value of **r** at which ϕ_i first intersects $\bar{\phi}_i$, increases for both components A and C as the surface broadens with time, however for component B the position increases to a maximum at around $\tau = 500$, then starts to reduce again. It can be seen from figure 8.5(b) that the magnitude of ϕ_B at the surface reduces with time, therefore reducing the position at which ϕ_i first intersects $\bar{\phi}_i$. In this system the component which dominates at the surface is dictated by the random noise at the start of the simulation only as all other variables are the same and we therefore believe this result to be due to the random formation of the surface segregation. The surface in figure 8.6 has been set to be attractive to component A but repulsive to component B, this can be

208

seen by analysing figures 8.6(a) and 8.6(b). In figure 8.6(a) we see that at the surface $\phi_A \approx 0.95$ whereas $\phi_B \approx 0.00$ and $\phi_C \approx 0.05$. In this system a small amount of surface broadening occurs, however we see a large broadening of the depletion layer with time and the propagation of a sinusoidal structure into the bulk. We note that, for components A and B, the value at which ϕ_i first intersects $\overline{\phi}_i$ increases rapidly as τ increases (in each case) before becoming almost constant with little positional change. Component C however has a large increase in r for a short time before reducing to a position consistent with the other components present; this is due to the phase separated structure of this component not intersecting $\overline{\phi}_i$ in the first depletion layer, as shown in figure 8.9.
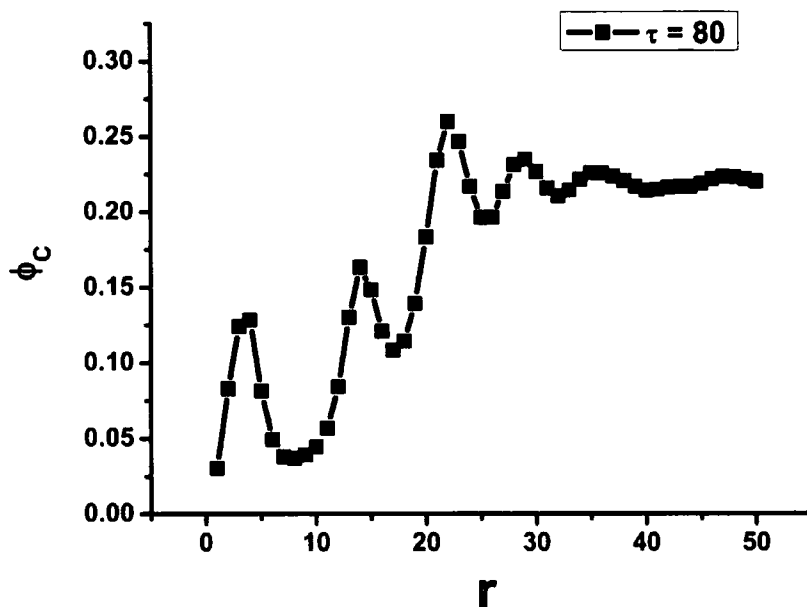
Figure 8.9

ϕ_C vs. r when $\chi_{AB} = \chi_{AC} = \chi_{BC} = 0.015$ and $h_a = h_b = -0.5$

We see that ϕ_C does not intersect $\overline{\phi}_C$ (0.2 in this case) until $r \approx 23$, as the first depletion layer is damped to a maximum value of $\phi_C = 0.14$, leading to the corresponding increase seen in figure 8.6(d). Here the reduction in the magnitude of the initial depletion peak is only temporary as the system attempts to reach equilibrium.

The trends for components A and B seen in figure 8.7 are the reverse of those seen in figure 8.6, corresponding to the exchange of the values of h_a and h_b. The results for component C in this case are concordant with those seen in figure 8.6 as the system is undergoing the same interactions. Figure 8.8 corresponds to the situation where component C forms at the surface; here we see a growth in the surface layer in all three components. Again the position, **r',** at which ϕ_i first intersects $\overline{\phi}_i$ for component A appears to "jump" to a higher value and then return to a similar area to the other components, this is again due to the process seen in figure 8.9.

Figure 8.10

$\overline{\phi}_i$ vs. **r** when $\chi_{AB} = 0.018$, $\chi_{AC} = \chi_{BC} = 0.015$ and $h_a = 0.5$, $h_b = -0.5$ for (a) component A, (b) component B, (c) component C and (d) the value of **r'** at which ϕ_i first reaches $\overline{\phi}_i$, where i = A, B or C.

Figure 8.10 shows the results of a simulation in which identical surface parameters to figure 8.6 are used but when $\chi_{AB} = 0.018$, $\chi_{AC} = \chi_{BC} = 0.015$, corresponding to an increase in χ_{AB}. A comparison of figures 8.6 and 8.10 shows similar trends occurring, but in the latter case greater phase separation in components A and B is present, corresponding to the increase in χ_{AB}. We also note the phase

separated sinusoidal structure appears to have developed further in figure 8.10, again due to the increase in χ_{AB}. In figure 8.11 χ_{AB} is again increased but for the case when $h_a = h_b = -0.5$.
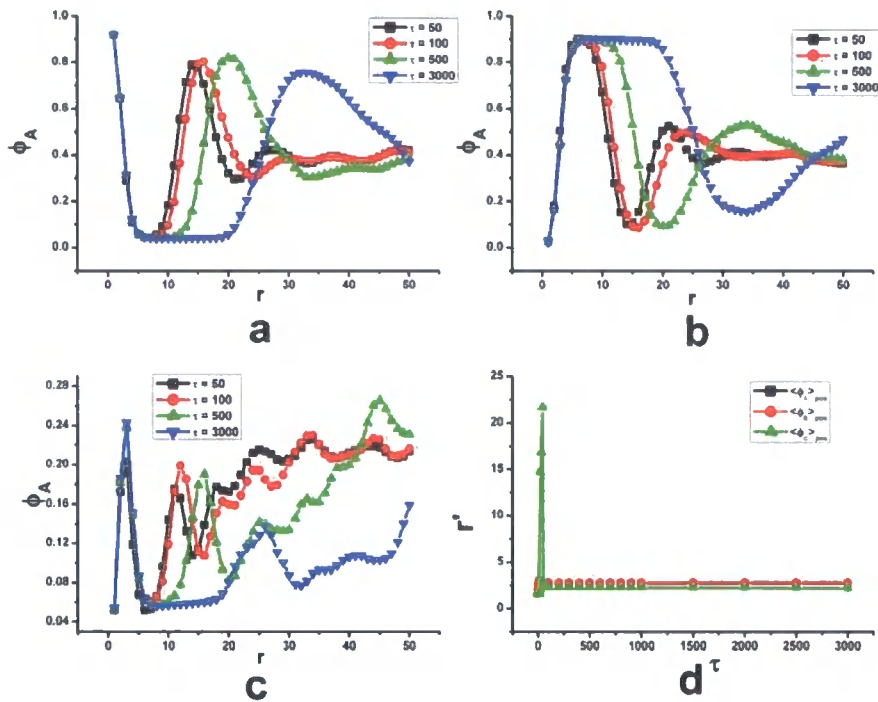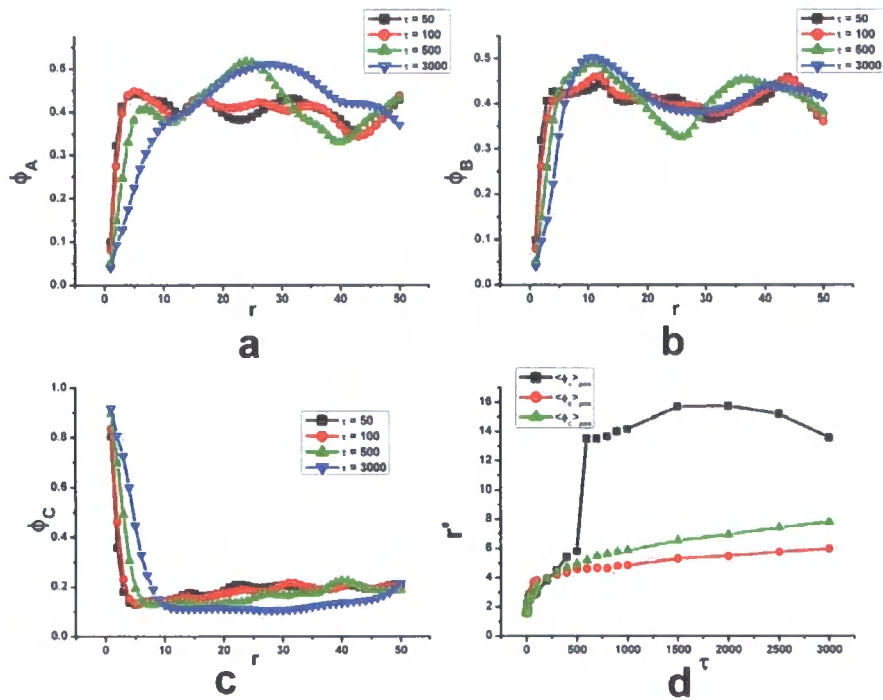

Figure 8.11

$\bar{\phi}_i$ vs. **r** when $\chi_{AB} = 0.018$, $\chi_{AC} = \chi_{BC} = 0.015$ and $h_a = -0.5$, $h_b = -0.5$ for (a) component A, (b) component B, (c) component C and (d) the value of **r** at which ϕ_i first reaches $\bar{\phi}_i$, where i = A, B or C.

A comparison of figures 8.11 and 8.8 again shows a more developed structure perpendicular to the surface due to the increase in χ_{AB}. We see a large increase in figure 8.11(d) when ϕ_A first reaches $\bar{\phi}_i$ at around $\tau = 500$ corresponding to a result similar to that shown in figure 8.9 for component A. This is an artefact of the domain broadening process as domain broadening involves diffusion of polymeric material from one position to another, therefore one peak in the above diagram will broaden whilst another is annihilated, this is seen in figure 8.12.
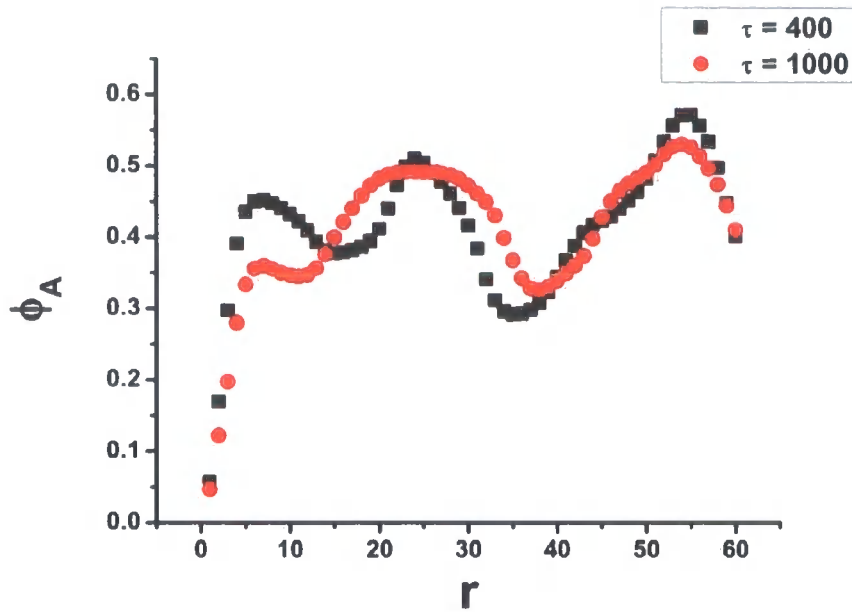
Figure 8.12

ϕ_A vs. **r** when $\chi_{AB} = 0.018$, $\chi_{AC} = \chi_{BC} = 0.015$ and $h_a = h_b = -0.5$ at two different times, as shown in the legend.

As shown in equation 8.1.12 and 8.1.13 we also follow the perpendicular and parallel correlation functions for each set of variables, firstly we discuss the results from the perpendicular correlation function.

8.2.2 The Perpendicular Correlation Function

We show results from $\chi_{AB} = \chi_{AC} = \chi_{BC} = 0.015$ and $h_a = h_b = 0.5$ for components A, B and C at three different times with a plot of the correlation function vs. distance into the surface and we also show the position at which $G_\perp$ reaches $\frac{1}{2}G_{\perp max}$. The results are created following the method of Puri and Binder[115] where Z is defined as the distance from the surface at which correlation begins and for component A are shown in figure 8.13.

Figure 8.13

$G_{-|}$ vs. **r** when $\chi_{AB} = \chi_{AC} = \chi_{BC} = 0.015$ and $h_a = h_b = 0.5$ for component A when (a) τ = 100, (b) τ = 500, (c) τ = 3000 and (d) the position at which $G_{-|}$ reaches $\frac{1}{2}G_{-|max}$.

As expected the results for component B are commensurate to those shown for component A in figure 8.13 and will therefore not be shown here. The perpendicular correlation indicates greater phase accumulation at the surface followed by a random morphology, as seen in figure 8.4, and a growth in the surface layer with time. The expected sinusoidal wave growing perpendicular to the surface can however clearly be seen with the surface composition being followed by a depletion layer, as seen frequently in two component blends. At $Z \neq 0$, i.e. when the correlation is performed from a distance other than the surface, the initial correlation value is seen to be decreased, as we no longer reside at the attractive surface and the volume fraction of component A (B) is reduced. The results for component C are also shown in figure 8.14.
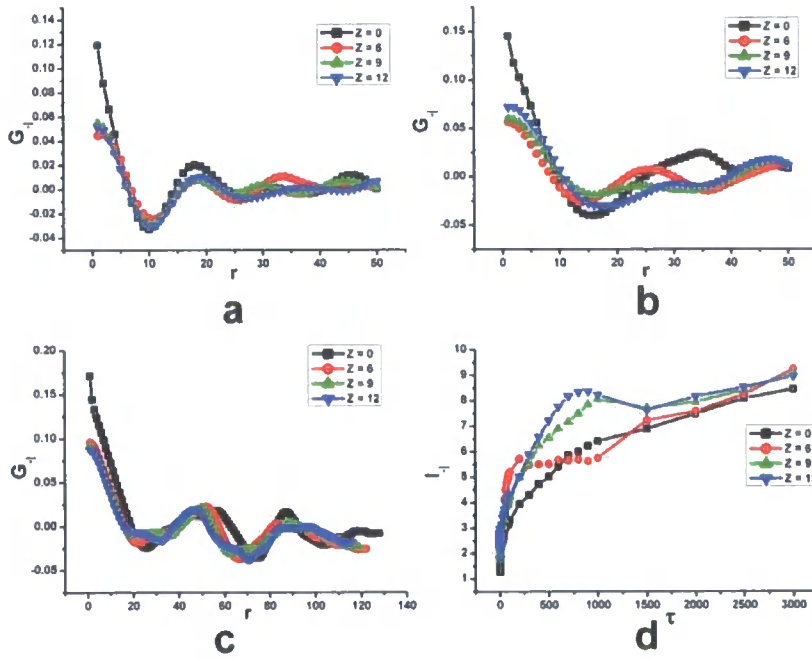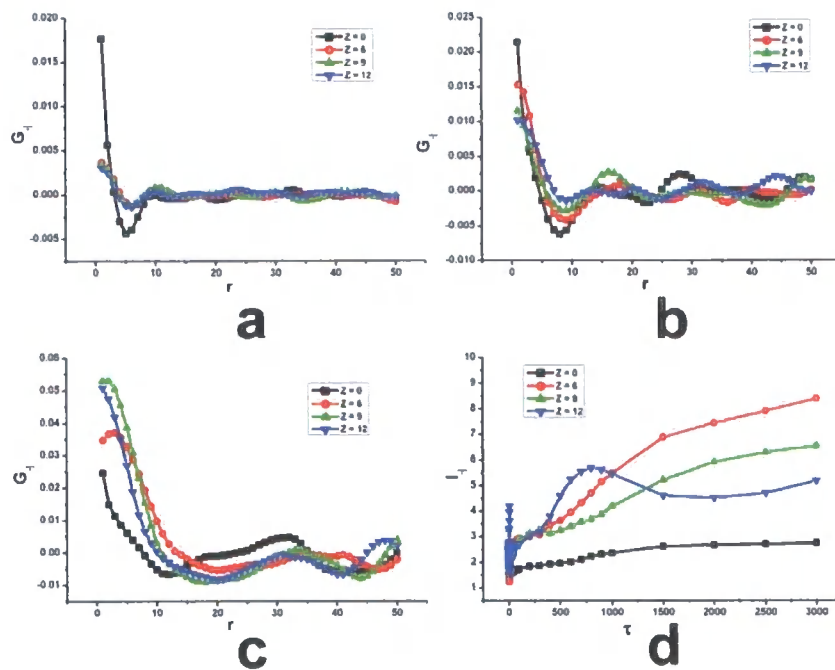
213

Figure 8.14

$G_{-|}$ vs. **r** when $\chi_{AB} = \chi_{AC} = \chi_{BC} = 0.015$ and $h_a = h_b = 0.5$ for component C when (a) $\tau = 100$, (b) $\tau = 500$, (c) $\tau = 3000$ and (d) the position at which $G_{-|}$ intersects $\frac{1}{2}G_{-|max}$.

If we note the scale of $G_{-|}$ in figure 8.14 and compare this to the scale in figure 8.13 we see that the correlation magnitude in this case in significantly smaller, this is because very little of component C is resident at the surface and also because the volume fraction of component C in the blend is reduced when compared to components A and B. Initially $G_{-|}$ for $Z = 0$ has the greatest magnitude as at small τ little phase separation in the bulk has occurred but components A and B have been attracted to the surface. The formation of components A and B at the surface means that component C is also forced to form here as it resides in the interface between components A and B. As τ increases in figure 8.14(c) we see that the correlation at $Z = 12$ becomes dominant, this is to be expected as the greatest volume fraction of component C lies in the bulk morphology, although the correlation is still small when compared to that for components A and B.
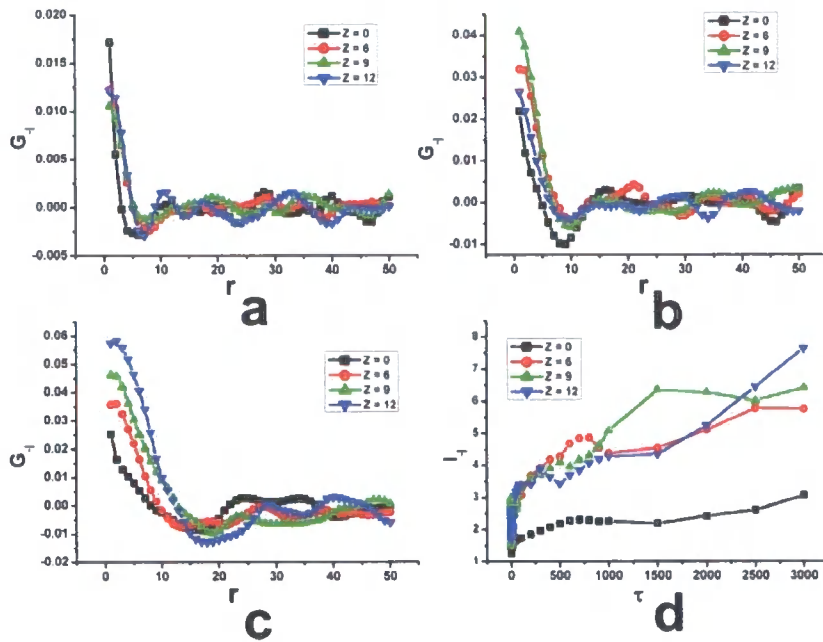
Figure 8.15

$G_{-|}$ vs. **r** when $\chi_{AB} = 0.018$ $\chi_{AC} = \chi_{BC} = 0.015$ and $h_a = h_b = 0.5$ for component C

when (a) $\tau = 100$, (b) $\tau = 500$, (c) $\tau = 3000$ and (d) the position at which $G_{-|}$ reaches

$\frac{1}{2}G_{-|max}$.

Figure 8.15 presents results from the situation where $\chi_{AB} = 0.018$ $\chi_{AC} = \chi_{BC} = 0.015$, here we see a slight increase in the values of $G_{-|}$ away from the surface, presumably because a greater volume fraction of component C is resident at the interface between components A and B. It is again worth noting the scale of $G_{-|}$ in figure 8.15 as it shows that very little correlation is present.

We now investigate the case where $h_a = 0.5$ and $h_b = -0.5$, here component A is attracted to the surface and component B is repulsed by the surface giving an A-C-B layered structure. We show results analogous to those in figures 8.13 and 8.14 for each component of the blend.

215

Figure 8.16

$G_{-|}$ vs. **r** when $\chi_{AB} = \chi_{AC} = \chi_{BC} = 0.015$, $h_a = 0.5$ and $h_b = -0.5$ for component A when (a) $\tau = 100$, (b) $\tau = 500$, (c) $\tau = 3000$ and (d) the position at which $G_{-|}$ reaches $\frac{1}{2}G_{-|max}$.

Figure 8.16 shows that the correlation is greatest at the surface when $Z = 0$, a large depletion layer is then seen for each value of Z and it can be seen that both the surface and depletion layer grow with time with a sinusoidal structure being formed perpendicular to the surface. In figure 8.16(c) we see that when $Z \neq 0$ the correlation at small distances from the surface is seen to be equivalent in each case, this is because in this case we initially reside in the depletion layer and the magnitude of component A is similar for each value of Z. We see a great increase in $l_{|}$ in the cases where $Z \neq 0$, this is because, as above, in these cases the correlations start in an area where very little of component A is present, i.e. in a layer of component B or C and therefore do not reach $l_{|}$ until they are a great distance into the bulk morphology, this also explains why $l_{|}$ for $Z = 12$ is lower than that of $Z = 6$ or $Z = 9$, as the distance to the bulk is smaller.
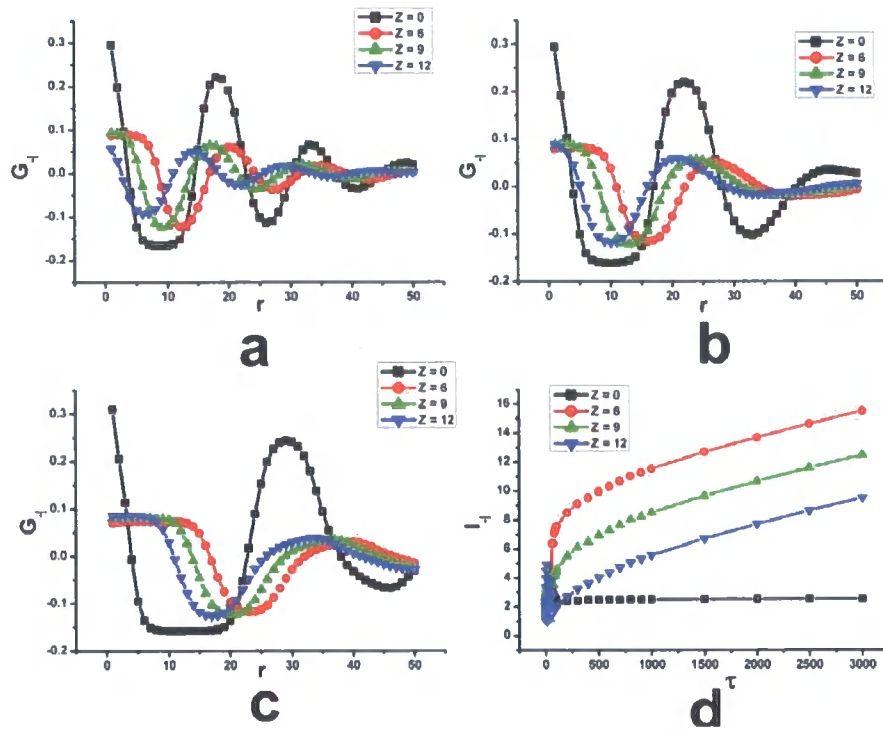
216

Figure 8.17

$G_{-|}$ vs. **r** when $\chi_{AB} = \chi_{AC} = \chi_{BC} = 0.015$, $h_a = 0.5$ and $h_b = -0.5$ for component B when (a) $\tau = 100$, (b) $\tau = 500$, (c) $\tau = 3000$ and (d) the position at which $G_{-|}$ reaches $\frac{1}{2}G_{-|max}$.

Figure 8.17 shows the perpendicular structure factor for component B. In figure 8.17(a) we see no trend in the magnitude of $G_{-|}$ at small **r**, this we believe is due to the layered formation of the phase separated system near to the surface leading to varying amounts of component B being present at any distance from the surface. At larger **r** however we see a sinusoidal structure is present which alternates around $G_{-|} = 0$, as expected from spinodal decomposition. At $\tau = 3000$ the sinusoidal structure which alternates around $G_{-|} = 0$ is still present, indicating phase separation in the bulk. The volume fraction of component B at small **r** appears to be equal for all values of Z initially but a rapid decrease in $G_{-|}$ is seen when Z = 0, whereas when $Z \neq 0$ a different structure is seen. In the latter case Z is located in the layer of components A and B and therefore is constant until the bulk region is reached. This reasoning also explains the trend seen in figure 8.17(d).
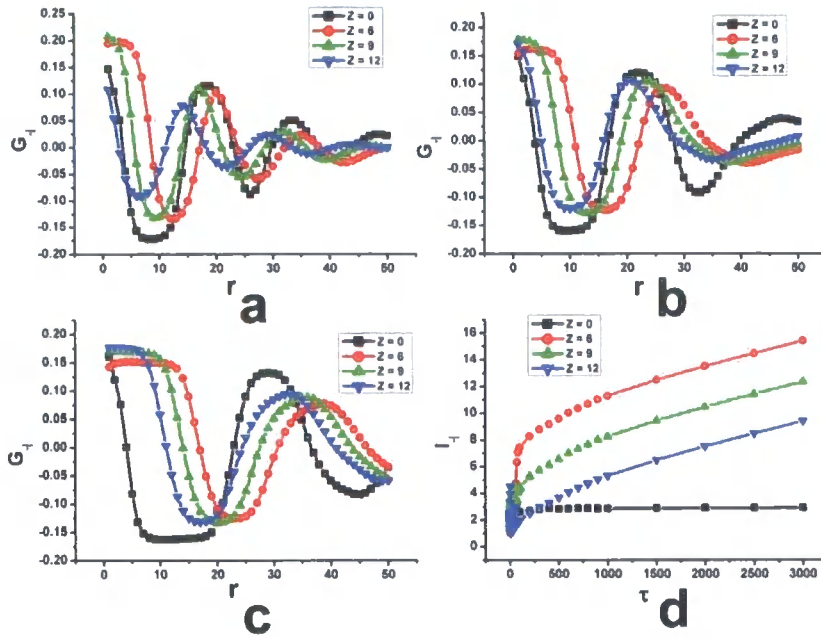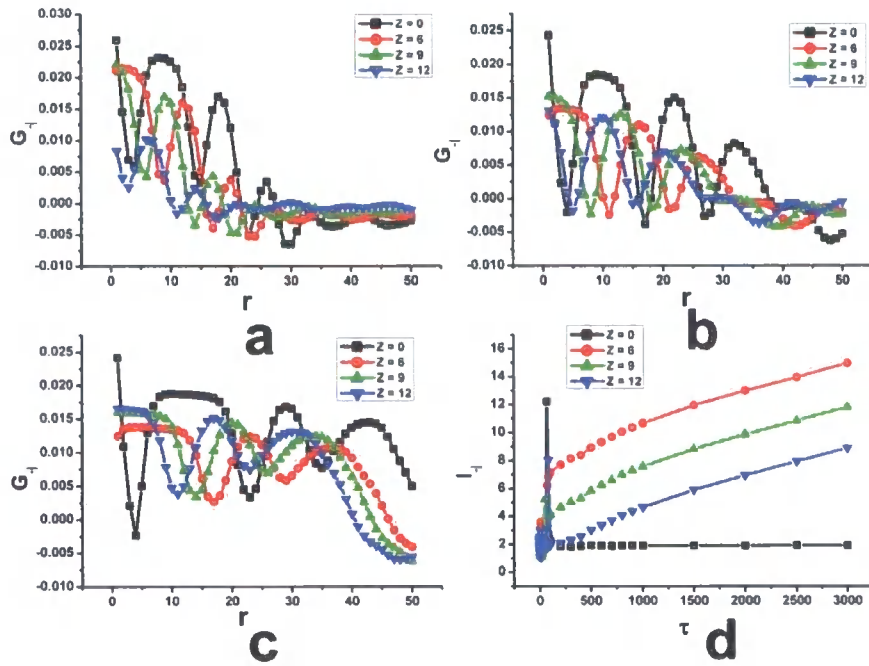
Figure 8.18

$G_{-|}$ vs. **r** when $\chi_{AB} = \chi_{AC} = \chi_{BC} = 0.015$, $h_a = 0.5$ and $h_b = -0.5$ for component C when (a) $\tau = 100$, (b) $\tau = 500$, (c) $\tau = 3000$ and (d) the position at which $G_{-|}$ reaches $\frac{1}{2}G_{-|max}$.

In figure 8.18 $G_{-|}$ is shown for component C, once again the magnitude of $G_{-|}$ is much smaller in component C than in either components A or B as there is a lower volume fraction of component C in the blend. As component C is now present between layers of A and B we see much greater structure in each part of figure 8.18 than that seen in figure 8.14, here we see a layer of component C occurring around **r** = 10, the depletion layer in figures 8.16 and 8.17. Again a damped sinusoidal structure develops from the surface outwards but in this case the period is much smaller due to the position of component C in the A-B interface. Initially, in figures 8.18(a) and 8.18(b) this structure is greatly damped and reduces to almost zero due to the very small volume fraction of component C present in the bulk morphology and because at very early times most of the phase separated volume of component C will reside in the surface depletion layer.

When $\chi_{AB} = 0.018$ and $\chi_{AC} = \chi_{BC} = 0.015$ the results for components A and B and C are very similar to those seen in figures 8.16-8.18; but with greater broadening due to the greater driving force for phase separation produced by increasing χ.

218

When $h_a = -0.5$ and $h_b = 0.5$ component B becomes attracted to the surface and a layer is formed, followed by a layer of component C and finally a layer of component A, the results from this simulation are analogous to that shown above with the results for components A and B interchanged.

We finally note the more interesting, and novel, results produced when $h_a = h_b = -0.5$, see figure 8.4(g) and 8.4(h), here a situation which is not possible in a binary blend at a surface is found with a layer of component C at the surface followed by equal areas of components A and B becoming a random morphology in the bulk, $G_{-|}$ is shown for components A, B and C in figures 8.19-8.21 respectively.

Figure 8.19

$G_{-|}$ vs. **r** when $\chi_{AB} = \chi_{AC} = \chi_{BC} = 0.015$, $h_a = h_b = -0.5$ for component A when (a) $\tau = 100$, (b) $\tau = 500$, (c) $\tau = 3000$ and (d) the position at which $G_{-|}$ reaches $\frac{1}{2}G_{-|max}$.

219
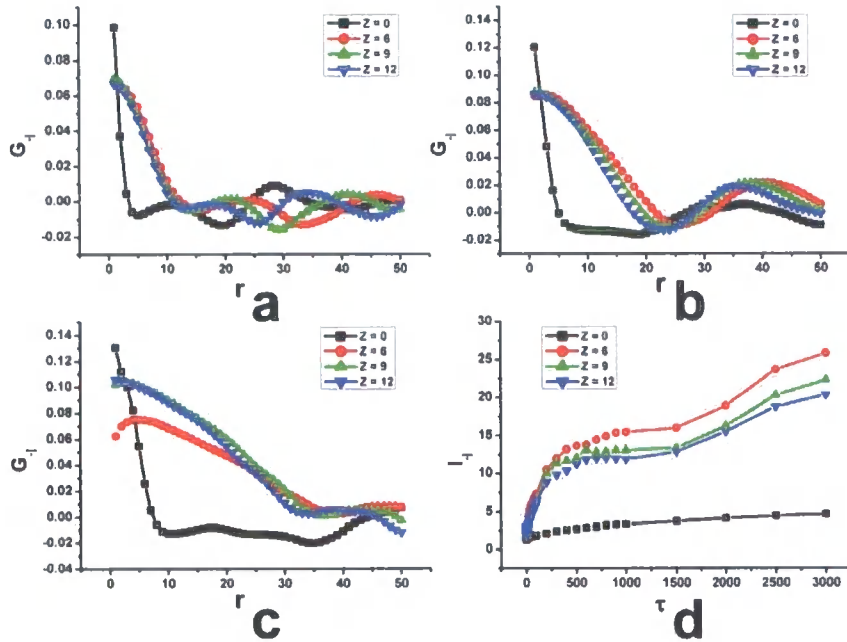
Figure 8.20

$G_{-|}$ vs. **r** when $\chi_{AB} = \chi_{AC} = \chi_{BC} = 0.015$, $h_a = h_b = -0.5$ for component B when (a) $\tau =$ 100, (b) $\tau = 500$, (c) $\tau = 3000$ and (d) the position at which $G_{-|}$ reaches $\frac{1}{2}G_{-|max}$.

For components A and B we find that $G_{-|}$ tends to the formation of equivalent curves when Z = 9 and Z = 12, this is because at these points we move out of the initial layer of component C and into the area where components A and B alternate with equal volume fractions. At Z = 0 however, $G_{-|}$ starts from a high value and becomes almost zero with increasing **r**, due to the low volume fraction of each component at the surface when compared to the bulk. We also see that $l_{-|}$ is almost equivalent for the cases when Z ≠ 0 indicating that after the initial layer of component C equal volume fractions of components A and B are present at each distance perpendicular to the surface. Again in each case $G_{-|}$ reduces and alternates around $G_{-|} = 0$ indicating a randomly phase separated system.
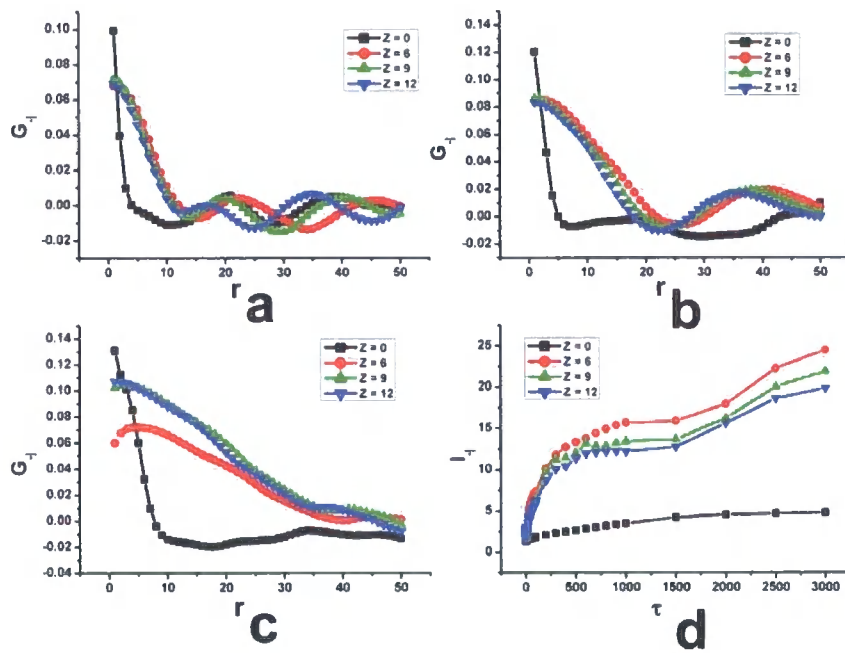
Figure 8.21

$G_{-|}$ vs. **r** when $\chi_{AB} = \chi_{AC} = \chi_{BC} = 0.015$, $h_a = h_b = -0.5$ for component C when (a) $\tau =$ 100, (b) $\tau = 500$, (c) $\tau = 3000$ and (d) the position at which $G_{-|}$ reaches $\frac{1}{2}G_{-|max}$.

A comparison of figures 8.21 and 8.18 indicates dissimilar results, in the case of figure 8.21 we have a very large surface enrichment in component C so therefore when Z = 0, $G_{-|}$ is large. However as component C is the minor component in the blend low volume fractions of component C are present in the bulk so low values of $G_{-|}$ are seen at greater **r**. When Z ≠ 0 little correlation is seen; again this is due to the limited volume fraction of component C residing in the bulk. In figure 8.21(d), when Z = 0, $l_{-|}$ increases with time as the surface layer broadens, however when Z = 6 we see a rapid reduction in $l_{-|}$ at around $\tau = 1000$. This corresponds to the time that the surface layer broadens to Z = 6, which therefore brings a rapid increase in the initial value of $G_{-|}$, as seen in figure 8.21(c), and therefore a reduction in $l_{-|}$.

A comparison of the morphologies formed when $\chi_{AB} = 0.015$ and 0.018 is made in figure 8.22.
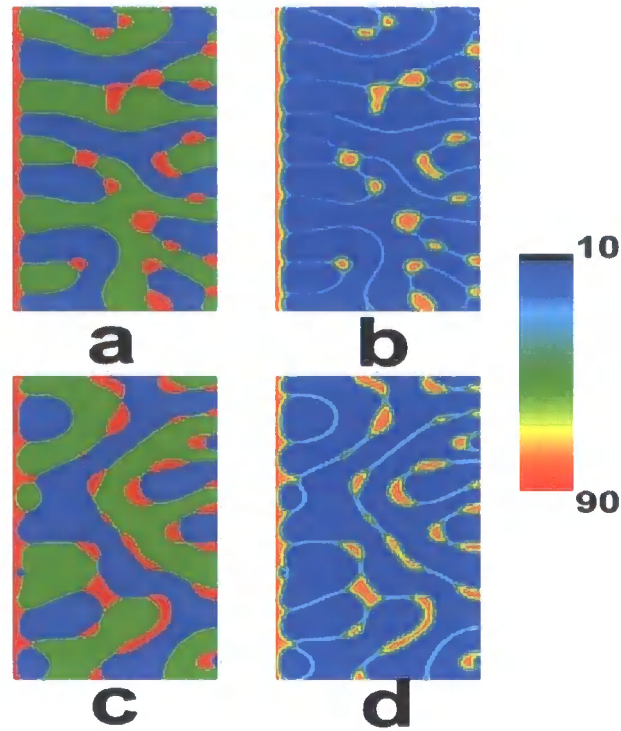
Figure 8.22

Morphologies where ▪ represents component A, ▪ represents component B and ▪ represents component C in (a) and (c) and the morphology of component C is shown in (b) and (d). In each case $h_a = h_b = -0.5$ and in (a) and (b) $\chi_{AB} = \chi_{AC} = \chi_{BC} = 0.015$ but in (c) and (d) $\chi_{AB} = 0.018$ and $\chi_{AC} = \chi_{BC} = 0.015$.

Figure 8.22 shows larger A and B domains present when $\chi_{AB} = 0.018$ but a greater volume fraction of component C in the interface between components A and B, this means a smaller amount of component C is able to form at the surface and components A and B penetrate further into the component C resident at the surface, this can be seen by comparing $l_{\parallel}$ in figures 8.21 and 8.23.
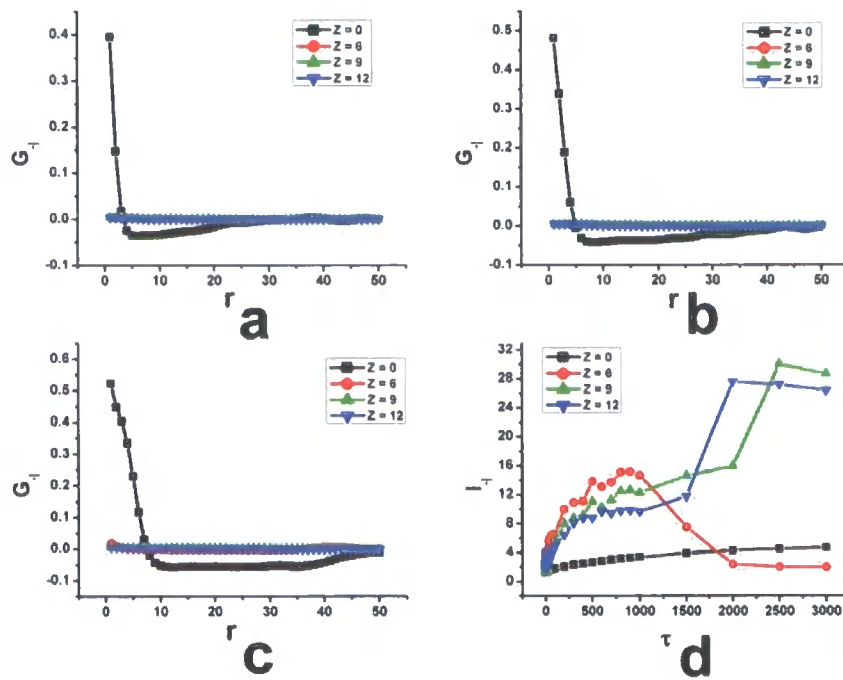
Figure 8.23

$G_{-|}$ vs. **r** when $\chi_{AB} = 0.018$, $\chi_{AC} = \chi_{BC} = 0.015$, $h_a = h_b = -0.5$ for component C when (a) $\tau = 100$, (b) $\tau = 500$, (c) $\tau = 3000$ and (d) the position at which $G_{-|}$ reaches $\frac{1}{2}G_{-|max}$.

In figure 8.23 we see not only a large reduction in the magnitude of $l_{-|}$ but the values of $l_{-|}$ when Z = 6 and 12 start to reduce at large τ, this would be not only indicative of the fact that a greater amount of component C is present in the bulk morphology but also that, as seen in figure 8.22, components A and B penetrate further into component C at the surface forcing component C further into the bulk region. This reasoning can be used to explain the large increase in the initial values of Z = 6 in figure 8.23(c) as a greater volume of component C is found at this distance when compared to figure 8.21(c).

Finally $G_{-|}$ for components A and B are shown in figures 8.24 and 8.25.

223

Figure 8.24

$G_{-|}$ vs. **r** when χ_{AB} = 0.018, χ_{AC} = χ_{BC} = 0.015, h_a = h_b = -0.5 for component A when
(a) τ = 100, (b) τ = 500, (c) τ = 3000 and (d) the position at which $G_{-|}$ reaches
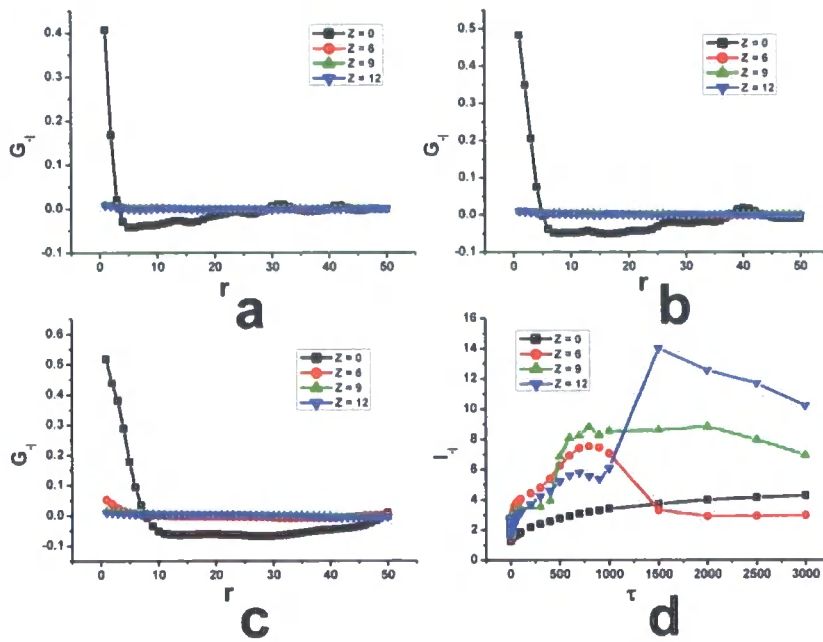$\frac{1}{2}G_{-|max}$.
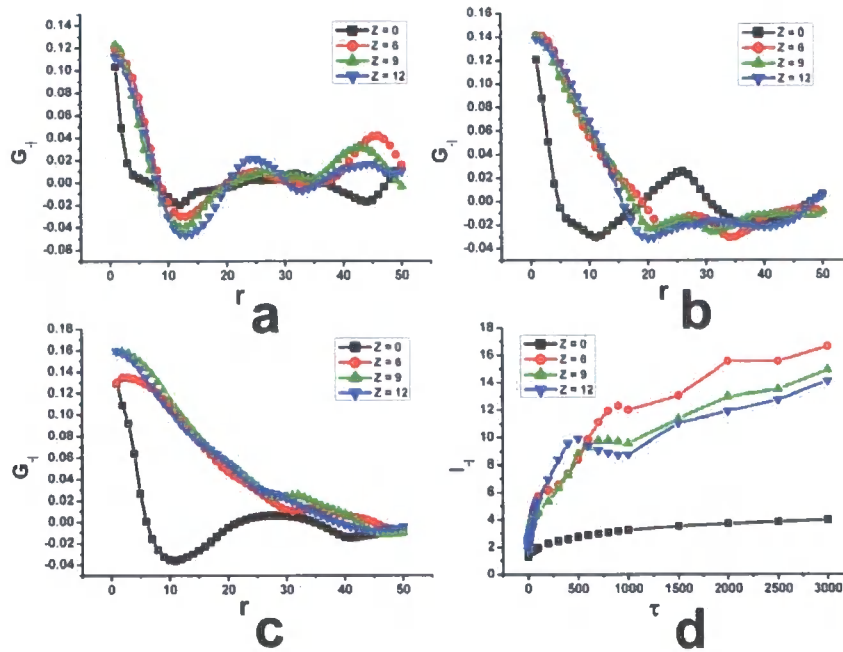
Figure 8.25

$G_{-|}$ vs. **r** when $\chi_{AB} = 0.018$, $\chi_{AC} = \chi_{BC} = 0.015$, $h_a = h_b = -0.5$ for component B when
(a) $\tau = 100$, (b) $\tau = 500$, (c) $\tau = 3000$ and (d) the position at which $G_{-|}$ reaches
$\frac{1}{2}G_{-|max}$.

A comparison of figures 8.24 and 8.25 with figures 8.19 and 8.20 respectively shows an increase in the initial values of $G_{-|}$ when $Z \neq 0$ indicating an increase in the volume fraction of each component at these points, this can be explained by the greater degree of domain broadening, due to the increase in χ, resulting in less interface being present at each point perpendicular to the surface.

8.2.3 The Parallel Correlation Function

Next we provide results for $G_{||}$, the parallel correlation function. For the case where $h_a = h_b = 0.5$ we show $G_{||}$ for components A and C in figures 8.26 and 8.27 respectively.

225

Figure 8.26

$G_\parallel$ vs. **x** when $\chi_{AB} = \chi_{AC} = \chi_{BC} = 0.015$, $h_a = h_b = 0.5$ for component A when (a) $\tau = 100$, (b) $\tau = 500$, (c) $\tau = 3000$ and (d) the position at which $G_\parallel$ reaches $\frac{1}{2}G_{\parallel max}$.

From figure 8.26 we see that at early times a greater magnitude of $G_\parallel$ is present at the surface, $Z = 0$, than is present further into the bulk region. As τ increases the magnitude of $G_\parallel$ for $Z \neq 0$ increases as the surface effects are felt at greater distances. We also see a broadening in the sinusoidal pattern as τ increases, this is due to the broadening of the A and B domains with time, also the values of $l_\parallel$ increase similarly in each case as the domains broaden with time. The results for component B in this case are again very similar and therefore are not displayed here.
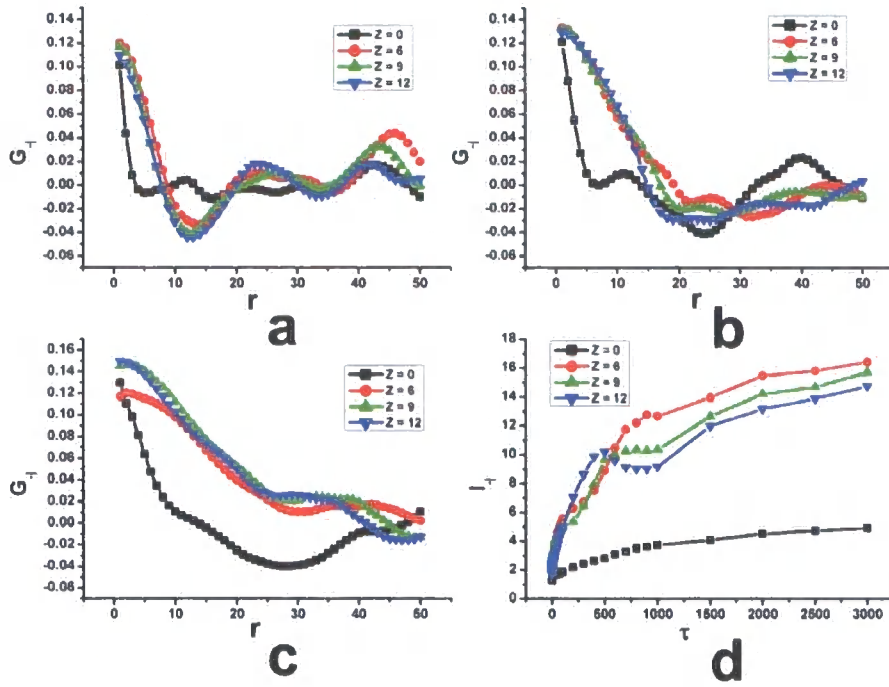
226

Figure 8.27

$G_{\parallel}$ vs. **x** when $\chi_{AB} = \chi_{AC} = \chi_{BC} = 0.015$, $h_a = h_b = 0.5$ for component C when (a) $\tau = 100$, (b) $\tau = 500$, (c) $\tau = 3000$ and (d) the position at which $G_{\parallel}$ reaches $\frac{1}{2}G_{\parallel max}$.

The magnitude of $G_{\parallel}$ for component C is once again vastly reduced when figures 8.26 and 8.27 are compared indicating the reduction in volume fraction of component C. We see that $G_{\parallel}$ at $Z = 0$ is almost zero for the entire period of the simulation; this is expected as in this case very little of component C is resident at the surface. Upon moving further into the bulk, at greater distances from the surface, we see the magnitude of the correlation increasing, as the further from the surface the greater the amount of component C present. When $Z \neq 0$ we see that $l_{\parallel}$, and indeed the trend in $G_{\parallel}$, becomes almost equivalent in each case indicating that away from the surface the situation becomes similar in each case. Initially at small **x** for the cases when $Z \neq 0$ the magnitude of $G_{\parallel}$ is equivalent in each case, however with increased τ the magnitude at small **x** for $Z = 6$ is seen to decrease. The reasoning for this is due to the broadening of the surface layer, as this layer broadens the volume fraction of component C at $Z = 6$ decreases leading to the corresponding decrease in the magnitude of $G_{\parallel}$ at this point. The broadening of the structures in the bulk regions of figure 8.27 again indicates that the domains are broadening with time to try and reduce the presence of the high energy interface.
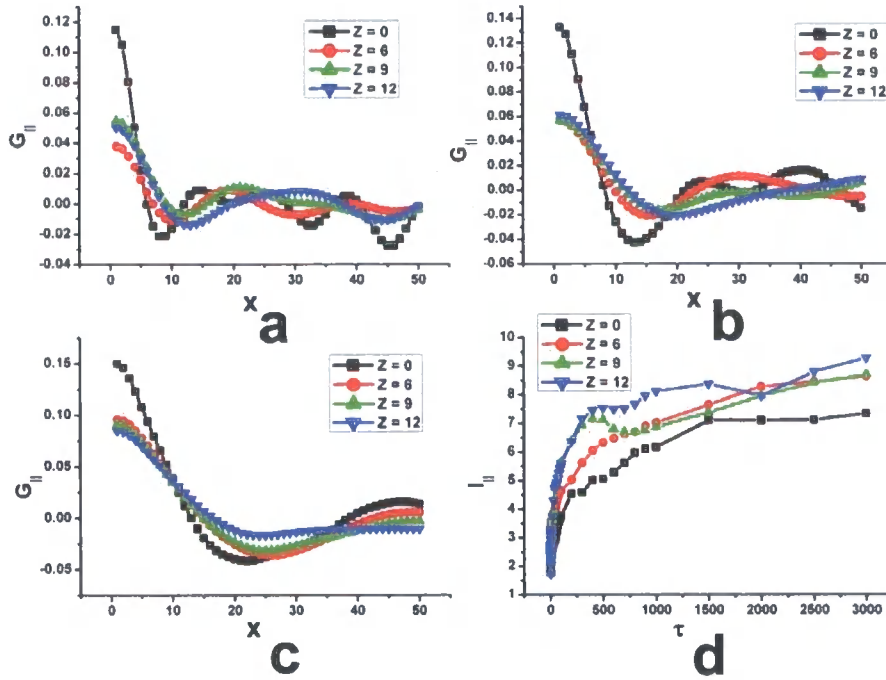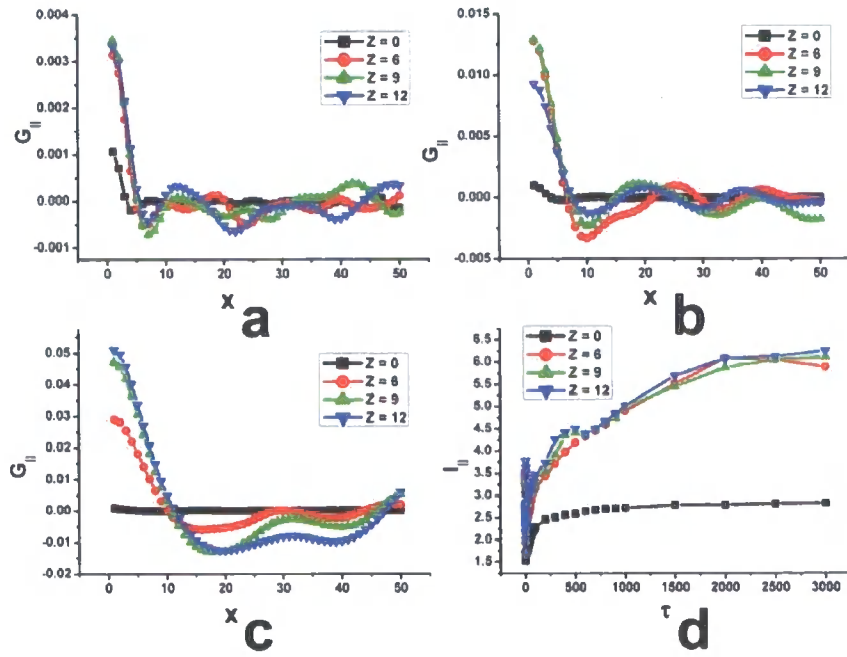
227

Figure 8.28

$G_\parallel$ vs. **x** when $\chi_{AB} = \chi_{AC} = \chi_{BC} = 0.015$, $h_a = 0.5$, $h_b = -0.5$ for component A when (a) $\tau = 100$, (b) $\tau = 500$, (c) $\tau = 3000$ and (d) the position at which $G_\parallel$ reaches $\frac{1}{2}G_{\parallel max}$.

Figure 8.28(a) only shows correlation when Z = 12 as a layer of component A has formed parallel to the surface which has constant volume fraction along its length, therefore in this layer a $G_\parallel$ of around zero is seen. Initially, as in figure 8.28(a) this layer has not broadened to Z = 12, however we see that by $\tau = 500$ the magnitude of $G_\parallel$ in the Z = 12 layer has decreased to a point which is equivalent to the magnitude of the other layers, indicating that the surface has broadened to this point. In figure 8.28(c) no correlation is seen for any value of Z, note the scale of $G_\parallel$ in figure 8.28(c). The values of $l_\parallel$ are higher than in previous examples but the trend is also of a more random nature; obviously as the values of $G_\parallel$ are infinitesimal the value of $l_\parallel$ is more susceptible to random fluctuations throughout the morphology. For components A and B the results are clearly very similar, as is the case when χ_{AB} = 0.018 since in each case a layered structure is also seen. When $h_a = -0.5$ and $h_b = 0.5$ we find a layered B-C-A structure and find that $G_\parallel$ for each component follows the trend seen in figure 8.28.

When $h_a = h_b = -0.5$ and a situation where component C forms at the surface followed by both components A and B we find $G_\parallel$ varies as in figure 8.29 for component A, and similarly for component B.
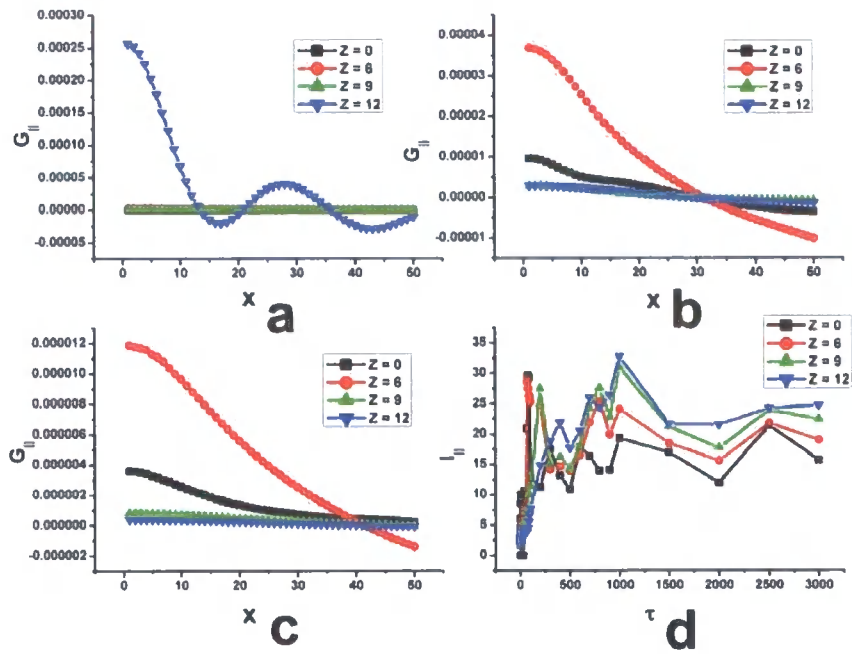

Figure 8.29

$G_\parallel$ vs. **x** when $\chi_{AB} = \chi_{AC} = \chi_{BC} = 0.015$, $h_a = h_b = -0.5$ for component A when (a) $\tau = 100$, (b) $\tau = 500$, (c) $\tau = 3000$ and (d) the position at which $G_\parallel$ reaches $\frac{1}{2}G_{\parallel max}$.

In figure 8.28 we see little correlation at $Z = 0$, as a layer of component C has formed, however as the value of Z increases a greater magnitude of $G_\parallel$ is observed indicating an increase in the amount of component A, or B, present. In figures 8.29(a) and 8.29(b) when $Z \neq 0$ the structure is similar in each case indicating that after the initial layer of component C the structure does not vary much with **r** and is therefore equivalent for each value of Z. Here the growth of the surface layer can be followed as in figure 8.29(c) the magnitude to $G_\parallel$ at $Z = 6$ decreases as a homogeneous layer is forming. The structure seen in figure 8.29 can be seen to broaden with time as expected due to domain broadening within the system.

Figure 8.30

Correlation function vs. **r** when $\chi_{AB} = \chi_{AC} = \chi_{BC} = 0.015$, $h_a = h_b = -0.5$ for component C when (a) $\tau = 100$, (b) $\tau = 500$, (c) $\tau = 3000$ and (d) the position at which $G_{\parallel}$ reaches $\frac{1}{2}G_{\parallel max}$.

When examining component C, in figure 8.30, we see complete correlation since $\phi(\mathbf{x})$ is constant for all $\mathbf{x}$ due to the layered structure. As τ increases, $G_{\parallel}$ increases in magnitude only for the situation where Z = 6, however a smaller increase is see for larger Z. We believe that the surface layer of component C extends out to around Z = 6 in figure 8.30(c), and then the A-B structure is initiated giving an increase in $G_{\parallel}$ for component C as we now have large concentration fluctuations. At larger Z however only small volume fractions of component C are present meaning that much smaller concentration fluctuations are present giving a smaller increase in $G_{\parallel}$. The value of $l_{\parallel}$ is greatest for the case when Z = 0, we believe this is due to the value being so small that a situation similar to the one shown in figure 8.28 is observed.
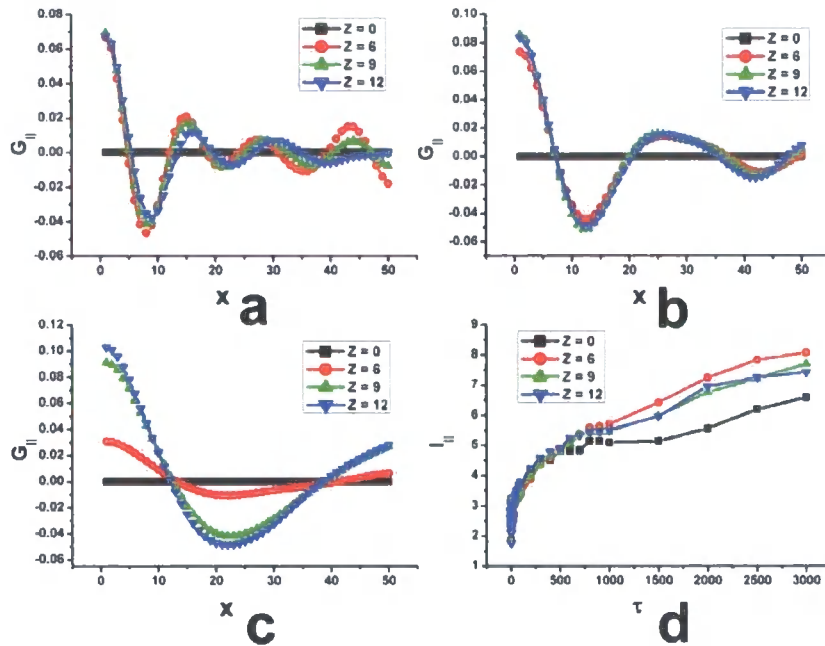
230
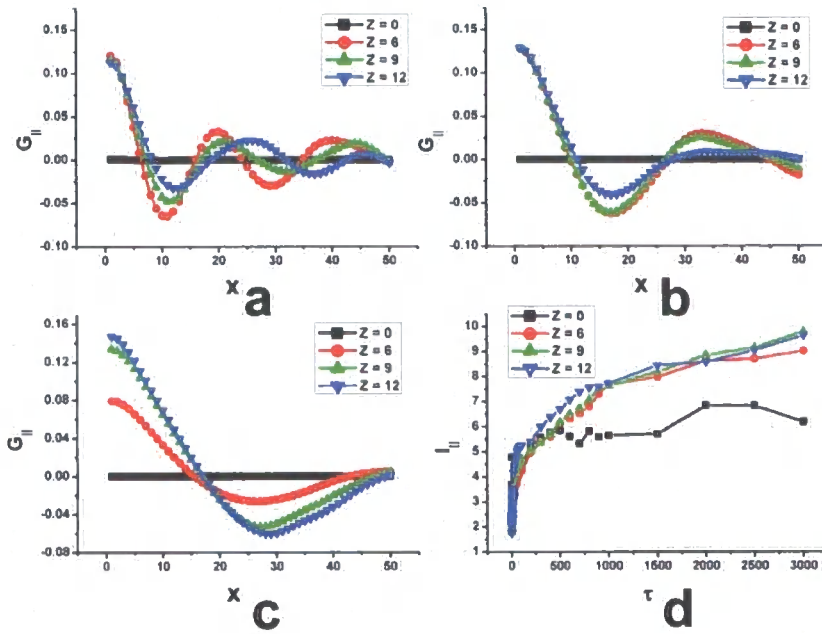
Figure 8.31

Correlation function vs. **r** when $\chi_{AB} = 0.018$, $\chi_{AC} = \chi_{BC} = 0.015$, $h_a = h_b = -0.5$ for component A when (a) $\tau = 100$, (b) $\tau = 500$, (c) $\tau = 3000$ and (d) the position at which $G_{\parallel}$ reaches $\frac{1}{2}G_{\parallel max}$.
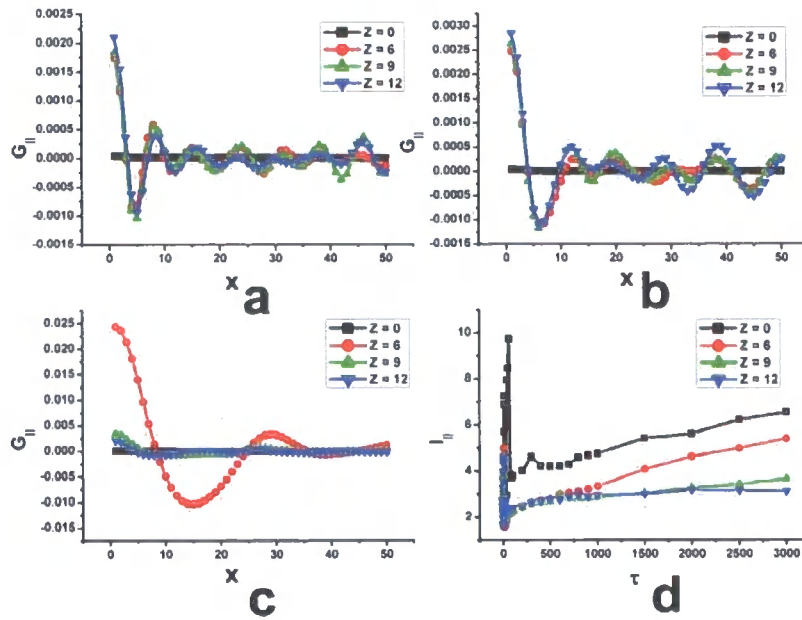
231
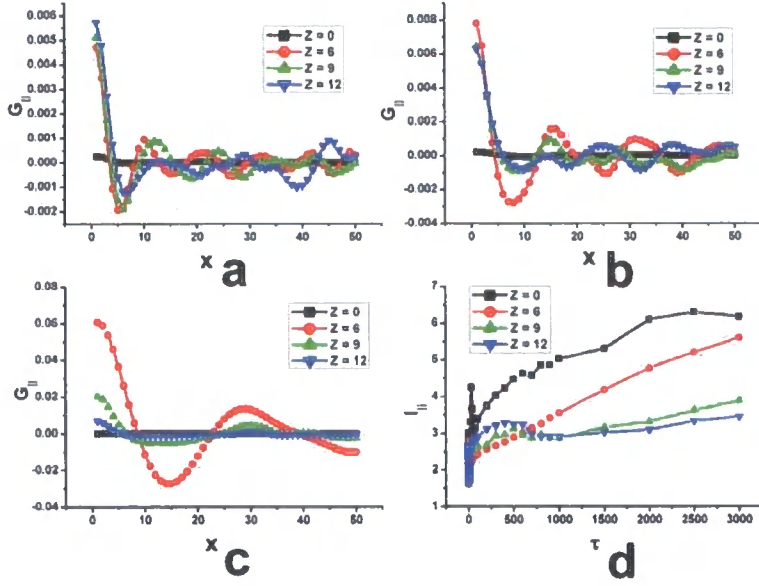
Figure 8.32

Correlation function vs. **r** when $\chi_{AB} = 0.018$, $\chi_{AC} = \chi_{BC} = 0.015$, $h_a = h_b = -0.5$ for component C when (a) $\tau = 100$, (b) $\tau = 500$, (c) $\tau = 3000$ and (d) the position at which $G_{\parallel}$ reaches $\frac{1}{2}G_{\parallel max}$.

A comparison of figures 8.31 and 8.29 with 8.32 and 8.30 respectively shows similar trends appearing, however with greater line broadening and a larger magnitude of $G_{\parallel}$ as a consequence of the increase in χ_{AB}.

8.3   Conclusions

We have derived a model to simulate the effect on morphology of a surface in a three component ABC polymer blend using Cahn-Hilliard theory. We use our methodology to model four different situations, namely the case when both components A and B are attracted to the surface, the case where component A is attracted to the surface and component B is repulsed, the opposite case where component B is attracted to the surface and component A is repulsed and finally the case where components A and B are both repulsed by the surface. We also simulate two situations where χ, the Flory interaction parameter, is varied i.e. in the first case $\chi_{AB} = \chi_{AC} = \chi_{BC} = 0.015$ and in the second $\chi_{AB} = 0.018$, $\chi_{AC} = \chi_{BC} = 0.015$. The simulations are followed by observing the average volume fraction at point's

perpendicular to the surface and also by defining correlation functions both parallel and perpendicular to the surface.

The blend used during the simulations is a 40:40:20 blend and therefore component C, the minority phase, forms at the interface between components A and B. We find that when χ_{AB} is increased from 0.015 to 0.018 a greater volume fraction of component C is resident in the interface between components A and B and also that the A and B domains broaden to a greater extent to further minimise the high energy interface. In the case where components A and B are equally attracted to the surface we see an alternating A-B morphology form at the surface with very little component C present, and a random tri-continuous morphology is formed in the bulk. However when component A is preferentially attracted to the surface, and component B is repulsed by the surface we see that a three layered A-C-B structure is formed with a damped periodic sinusoidal structure forming perpendicular to the surface, as seen in the binary case. Upon the reversal of the surface parameters a B-C-A layered structure is formed and in both cases a random tri-continuous morphology is again seen in the bulk region. Finally we modelled the novel situation where components A and B are repulsed by the surface. We find that in this case a layer of component C forms at the surface followed by an alternating A-B morphology in the depletion layer. When moving further into the bulk region, when the surface effect has been damped to such an extent that the phase separation process becomes dominant, we see the tri-continuous random morphology once again appear. The effect of increasing χ_{AB} in this case is an interesting one as the volume fraction of component C at the surface is reduced so that a greater amount of component C can be resident in the A-B interface, we also see that the domains of components A and B in the surface depletion layer penetrate further into the surface layer of component C. In each of the four above cases component C was neither attracted nor repulsed by the surface.

Chapter 9

Conclusions and Future Work

In this section a brief overview of the work described above is shown with the main conclusions of the study, this is followed by suggestions for future work.

9.1   Conclusions

The above study helps to further our understanding in the area of phase separation in polymer blends via spinodal decomposition. Initially the reasons for and process of phase separation were described with the method used to model a phase separating system to aid with the understanding of the physics involved in the work.

Studies were then undertaken into phase separation in the two component (binary) blend undergoing initially phase separation after a rapid temperature quench and then phase separation after a controlled two-quench process. Here a primary structure was observed after the first quench which was allowed to coarsen with time. A second quench was then undertaken further into the two phase region where secondary domains were observed in the larger primary structure, these domains then aggregate together before being annihilated due to interfacial tension. The time dependence of the growth of this secondary structure was found to share features in common with that expected from Cahn's linearised theory. This model was then extended to form a system that is continuously quenched, i.e. the quench depth changes continuously in a controlled manner throughout the simulation. The morphologies formed via this method were then compared to the morphologies formed via a simple one-step temperature quench and little difference is seen in the size of the final morphology however the morphologies formed in the early stages appear restricted.

This simple continuous quench system was then extended to model Reaction Induced Phase Separation (RIPS) systems in which the phase separation is induced when a reaction, in this case polymerisation, occurs within the system. Initially a ternary system was studied with different reaction rates and although the rate of reaction was found to effect point of phase separation it was not found to affect the degree of phase separation. A quaternary system was then studied where the state of

polymerisation of one of the components is altered to try to understand the effect on the final extent of phase separation. It was found that the greater the degree of polymerisation of the final system the more rapidly phase separation occurred due to the increase in the driving force for the phase separation process. A network was then included in the system, it grew during the polymerisation process and had a substantial effect on the final morphology formed. In this case the network resists the high-energy deformation of the phase separation process and an equilibrium is created to balance the two forces. In this case the final degree of polymerisation of the polymerising component did not affect the final morphology as the network resists the phase separation process equally in each case.

A surface was then added into the binary blend and the system was set up such that one component of the blend was preferentially attracted to this surface over the other component. Here we find alternating structures form perpendicular to the surface into the bulk region. The difficulty with using Cahn-Hilliard theory to model surfaces consistently was highlighted and a minimum method to physically overcome length scale anomalies is presented. The effect of surface equilibration prior to phase separation is also shown to highlight the difference in morphological development during spinodal decomposition and the importance of incorporating this step in order to create more realistic simulations. Here the importance of the addition of noise to simulations that include a surface is highlighted. In this case both the magnitude and frequency of the noise are altered in a controlled manner and it is found that the level of noise has an effect on the equilibrium between the phase separation process and the surface attraction forces, and therefore the final morphology. It should possible to compare these systems by experiment and by using trial and error it could then be possible to understand the level of noise needed for each simulation, this however may be a long and difficult process. It may therefore be possible to calculate the thermal fluctuations occurring in each blend at any given temperature so that this information can be input into the model and used to improve accuracy.

Phase separation in a binary blend on a patterned surface was then investigated. Initially a hard wall surface has an alternating pattern set and we see interesting alternating patterns form into the bulk region not only perpendicular to the surface but also parallel to it. The phase separation process above a patterned surface, e.g. a silicone wafer that has been altered to give differing surface properties,

is also shown. An investigation into different surface patterns is shown where interesting transient structures, which are stable under certain conditions, appear. By changing factors such as surface attraction, quench depth and blend composition we have shown that it should be possible to control the morphologies of these structures to give targeted morphologies.

Finally an investigation into phase separation at a hard wall surface in a three component, ABC, blend was undertaken. In this case the surface attraction was altered to create four systems in which each component was resident at the surface. Two different blend interaction values were used to further change the phase separation properties and correlation function perpendicular and parallel to the surface were used to follow the spinodal decomposition. We find when one component is the minority phase it resides at the interface between the other components, however when it is the major component it becomes a matrix within which are the other two components. In each case we find it is possible to tune the properties of the system to create a number of novel, interesting and possibly technologically useful structures which could not be easily formed by another method.

9.2   Future Work

This study has elucidated a number of interesting features and methods to attempt to control and target the final morphology of a polymer blend that is undergoing phase separation via spinodal decomposition. Further studies are however clearly possible and the work described here could be extended in a great number of ways, a few examples of which are given here. The first method to develop the work could be to include viscoelastic properties into the simulation, here the system acts neither as a perfectly elastic solid or a viscous fluid but maintains some properties of both systems. The inclusion of these properties would lead to a system that may phase separate to create very different structures, if these structures could be controlled in some way this could lead to systems with very interesting properties. The interaction between a system which forms a network component, is trying to phase separate but is constrained by a wall could be easily developed using the theories above but would have three systems competing to dominate the equilibrium composition. If the conditions were therefore changed correctly a number of different morphologies may be accessible. An investigation into the uses

of block copolymers in systems such as those shown above would also create an interesting study at both a surface but also in the bulk, if for example two-step phase separation were attempted. At a surface however great ordering could be created, as block copolymers tend to form a lower range of morphologies.

Bibliography

(1)   Flory, P. J. *J. Chem. Phys.* **1942**, *10*, 51.

(2)   Huggins, M. L. *Ann. NY. Acad. Sci.* **1942**, *42*, 1.

(3)   Flory, P. J. *Principles of Polymer Chemistry*; Cornell U. P.: Ithaca, N.Y., 1978.

(4)   deGennes, P. G. *Scaling Concepts in Polymer Physics*: Ithaca, New York, 1979.

(5)   Cowie, J. M. G. *Polymers: Chemistry and Physics of Modern Materials*; Blakie, 1991.

(6)   Clarke, N. *Department of Physics*; University of Sheffield: Sheffield, 1994.

(7)   Jones, R. A. L.; Richards, R. W. *Polymers at Surfaces and Interfaces*; Cambridge University Press: Cambridge, 1999.

(8)   Vilgis, T. A.; Benmouna, M.; Benoit, H. *Macromolecules* **1991**, *24*, 4481-4488.

(9)   Doi, M.; Edwards, S. F. *The Theory of Polymer Dynamics*; oxford Science Publications, 1986.

(10)   Binder, K. *J. Chem. Phys.* **1983**, *79*, 6387-6408.

(11)   Cahn, J. W.; Hilliard, J. E. *J. Chem. Phys.* **1958**, *28*, 258-267.

(12)   deGennes, P. G. *J. Chem. Phys.* **1980**, *72*, 4756-4763.

(13)   Pincus, P. *J. Chem. Phys.* **1981**, *75*, 1996.

(14)   Binder, K. *J. Chem. Phys.* **1983**, *79*, 6387.

(15)   Glotzer, S. C. *Annual Reviews of Computational Physics* **1995**, *2*, 1.

(16)   Cook, H. E. *Acta Metall.* **1970**, *18*, 297-306.

(17)   Sanchez, I. C. *Ann. Rev. Mater. Sci.* **1983**, *13*, 387-412.

(18)   Chakrabarti, A.; Toral, R.; Grunton, J. D.; Muthukumar, M. *J. Chem. Phys.* **1990**, *92*, 6899-6909.

(19)   Chakrabarti, A.; Toral, R.; Gunton, J. D.; Muthukumar, M. *Phys. Rev. Lett.* **1989**, *63*, 2072.

(20)   Brown, G.; Chakrabarti, A. *J. Chem. Phys.* **1993**, *98*, 2451.

(21)   Cahn, J. W. *J. Chem. Phys.* **1965**, *42*, 93.

(22)   Mazenko, G. F.; Valls, O. T. *Phys. Rev. Lett.* **1987**, *59*, 680-683.

(23)   Langer, J. S.; Bar-on, M.; Miller, D. *Phys. Rev. A* **1975**, *11*, 1417.

(24)   Rogers, T. M.; Elder, K. R.; Desai, R. C. *Phys. Rev. B* **1988**, *37*, 9638-9649.

(25)   Chakrabarti, A.; Gunton, J. D. *Phys. Rev. B* **1988**, *37*, 3798.

(26)   Oono, Y.; Puri, S. *Phys. Rev. Lett.* **1987**, *58*, 836-839.

(27)   Langer, J. S. *Acta Metall.* **1973**, *21*, 1649.

(28)   Akcasu, A. Z.; Klein, R. *Macromolecules* **1993**, *26*, 1429.

(29)   Tanaka, H. *J. Phys.: Condens. Matter* **2000**, *12*, R207.

(30)   Kotnis, M. A.; Muthukumar, M. *Macromolecules* **1992**, *25*, 1716-1724.

(31)   Hashimoto, T.; Takenaka, M.; Izumitani, T. *J. Chem. Phys.* **1992**, *97*, 679-689.

(32)   Takenaka, M.; Izumitani, T.; Hashimoto, T. *J. Chem. Phys.* **1993**, *98*, 3528-3539.

(33)   Castellano, C.; Glotzer, S. C. *J. Chem. Phys.* **1995**, *103*, 9363-9369.

(34)   Aksimentiev, A.; Moorthi, K.; Holyst, R. *J. Chem. Phys.* **2000**, *112*, 6049-6062.

(35)   Fialkowski, M.; Holyst, R. *J. Chem. Phys.* **2004**, *120*, 5802-5808.

(36)   Garcia-Ojalvo, j.; Lacasta, A. M.; Sancho, J. M.; Toral, R. *Europhys. Lett.* **1998**, *42*, 125-130.

(37)   Ibanes, M.; Garcia-Ojalvo, J.; Toral, R.; Sancho, J. M. *Eur. Phys. J. B* **2000**, *18*, 663-673.

(38)   Abrams, C.; Lee, N.; Obukhov, S. *Europhys. Lett.* **2002**, *59*, 397.

(39)   Ahlrichs, P.; Everaers, R.; Dunweg, B. *Phys. Rev. E* **2001**, *64*, 040501.

(40)   Dunweg, B.; Reith, D.; Steinhauser, M.; Kramer, K. *J. Chem. Phys.* **2002**, *117*, 914.

(41)   Kwak, K. D.; Okada, M.; Chiba, T.; Nose, T. *Macromolecules* **1993**, *26*, 4047.

(42)   Hayashi, M.; Jinnai, H.; Hashimoto, T. *J. Chem. Phys.* **2000**, *113*, 3414.

(43)   Hashimoto, T.; Hayashi, M.; Jinnai, H. *J. Chem. Phys.* **2000**, *112*, 6886.

(44)   Hayashi, M.; Jinnai, H.; Hashimoto, T. *J. Chem. Phys.* **2000**, *112*, 6897.

(45)   Fialkowski, M.; Holyst, R. *J. Chem. Phys.* **2002**, *117*, 1886.

(46)   Graca, M.; Wieczorek, S. A.; Fialkowski, M.; Holyst, R. *Macromolecules* **2002**, *35*, 9117.

(47)   Clarke, N. *Phys. Rev. Lett.* **2002**, *89*, 215506.

(48)   Tanaka, H. *Phys. Rev. E* **1993**, *47*, 2946-2949.

(49)   Sigehuzi, T.; Tanaka, H. *Phys. Rev. E* **2004**, *70*, 051504.

(50)   Tanaka, H.; Araki, T. *Phys. Rev. Lett.* **1998**, *81*, 389-392.

(51)   Williams, R. J. J.; Rozenberg, B. A.; Pascault, J. P. *Advances in Polymer Science* **1997**, *128*, 95-156.

(52)   Manson, J. A.; Sperling, L. H. *Polymer Blends and Composites*; Plenum Press: New york, 1976.

(53)   Glotzer, S. C.; Marizo, E. A. D.; Muthukumar, M. *Phys. Rev. Lett.* **1995**, *74*, 2034-2037.

(54)   Chan, P. K.; Rey, A. D. *Macromolecules* **1996**, *29*, 8934-8941.

(55)   Chan, P. K.; Rey, A. D. *Macromolecules* **1997**, *30*, 2135-2143.

(56)   Ishii, Y.; Ryan, A. J.; Clarke, N. *Polymer* **2003**, *44*, 3641.

(57)   Clarke, N.; McLeish, T. C. B.; Jenkins, S. D. *Macromolecules* **1995**, *28*, 4650.

(58)   Kim, S.; An, J. H. *Journal of Applied Polymer Science* **1995**, *58*, 491-500.

(59)   Oh, J.; Rey, A. D. *Computational and Theoretical Polymer Science* **2000**, *11*, 205-217.

(60)   Clarke, N. *Eur. Phys. J. E* **2001**, *4*, 327.

(61)   Scott, R. l.; Magat, M. *J. Chem. Phys.* **1945**, *13*, 172-177.

(62)   Pagonabarraga, I.; Cates, M. E. *Macromolecules* **2003**, *36*, 934.

(63)   Takenaka, M.; Hashimoto, T. *Phys. Rev. E* **1993**, *48*, R647.

(64)   Sollich, P. *J. Phys.: Condens. Matter* **2002**, *14*, R79-R117.

(65)   Fredrickson, G. H.; Sides, S. W. *Macromolecules* **2003**, *36*, 5415-5423.

(66)   Schichtel, T. E.; Binder, K. *Macromolecules* **1987**, *20*, 1671-1687.

(67)   Takenaka, M.; Hashimoto, T. *Macromolecules* **1994**, *27*, 6117-6123.

(68)   Warren, P. B. *Phys. Rev. Lett.* **1997**, *80*, 1369-1372.

(69)   Warren, P. B. *Phys. Chem. Chem. Phys.* **1999**, *1*, 2197-2202.

(70)   Yashin, V. V.; Balazs, A. C. *J. Chem. Phys.* **2004**, *121*, 2833-2843.

(71)   Brochard, F.; Jouffrouy, J.; Levinson, P. *J. Phys. Lett.* **1983**, *44*, L-455.

(72)   Brochard, F. *Molecular conformations and dynamics of macromolecules in condensed systems*; Elsevier: New york, 1988.

(73)   Briber, R. M.; Bauer, B. J. *Macromolecules* **1988**, *21*, 3296-3303.

(74)   Bettachy, A.; Derouchie, A.; Benhamou, M.; Daoud, M. *Journal De Physique I* **1990**, *1*, 153-158.

(75)   Tran-Cong, Q.; Nagaki, T.; Yano, O.; Soen, T. *Macromolecules* **1991**, *24*, 1505-1510.

(76) Benmouna, F.; Maschke, U.; Coqueret, X.; Benmouna, M. *Macromolecular Theory and Simulation* **2001**, *10*, 63-70.

(77) Frisch, H. L. *British Polymer Journal* **1985**, *17*, 149-153.

(78) Binder, K.; Frisch, H. L. *J. Chem. Phys.* **1984**, *81*, 2126-2136.

(79) Kuhn, W.; Grun, F. *J. Poly. Sci.* **1946**, *1*, 183.

(80) Schulz, M.; Binder, K. *J. Chem. Phys.* **1993**, *98*, 655-659.

(81) Schulz, M.; Frisch, H. L. *J. Chem. Phys.* **1994**, *101*, 10008-10022.

(82) Schulz, M.; Frisch, H. L. *J. Chem. Phys.* **1997**, *107*, 2673-2682.

(83) Li, W.; Ryan, A. J.; Meier, I. K. *macromolecules* **2002**, *35*, 5034-5042.

(84) Inoue, T. *Prog. Polym. Sci.* **1995**, *20*, 119-153.

(85) Elicabe, G. E.; Larrondo, H. A.; Williams, R. J. J. *Macromolecules* **1997**, *30*, 6550-6555.

(86) Alig, I.; Rullmann, M.; Holst, M. *Macromolecular Symposia* **2003**, *198*, 245-257.

(87) Meynie, L.; Fenouillot, F.; Pascault, J.-P. *Polymer* **2004**, *45*, 1867-1877.

(88) Hashimoto, T.; Izumitani, T. *Macromolecules* **1993**, *26*, 3631-3638.

(89) Izumitani, T.; Hashimoto, T. *Macromolecules* **1994**, *27*, 1744-1750.

(90) Fisher, I.; Siegmann, A. *Polymer Composites* **2002**, *23*, 464-477.

(91) Takenaka, M.; Hashimoto, T. *Macromolecules* **1996**, *29*, 4134.

(92) Takenaka, M.; Hashimoto, T. *Phys. Rev. E* **1995**, *52*, 5142.

(93) Liang, H.; He, X.; Jiang, B. *Macromolecular Theory and Simulation* **1999**, *8*, 173.

(94) Russo, A. P.; Nauman, E. B. *J. Poly. Sci. Part B: Poly. Phys.* **2000**, *30*, 1301-1306.

(95) Yeung, C.; Desai, R. C.; Noolandi, J. *Macromolecules* **1994**, *27*, 55-62.

(96) Ma, Y.-q. *J. Chem. Phys.* **2001**, *114*, 3734.

(97) Huang, C.; Cruz, M. O. d. l.; Swift, B. W. *Macromolecules* **1995**, *28*, 7996.

(98) Takenaka, M.; Chu, B. *macromolecules* **1995**, *28*, 3240-3247.

(99) Aradian, A.; Saulnier, F.; Raphael, E.; Gennes, P. G. d. *Macromolecules* **2004**, *37*, 4664-4675.

(100) Geoghegan, M.; Jones, R. A. L.; Clough, A. S. *J. Chem. Phys.* **1995**, *103*, 2719-2724.

(101) Jones, R. A. L.; Norton, L. J.; Kramer, E. J.; Bates, F. S.; Wiltzius, P. *Phys. Rev. Lett.* **1991**, *66*, 1326-1329.

(102) Kim, E.; Krausch, G.; Kramer, E. J.; Osby, J. O. *Macromolecules* **1994**, *27*, 5927-5929.

(103) Geoghegan, M.; Ermer, H.; Jungst, G.; Krausch, G.; Brenn, R. *Phys. Rev. E* **2000**, *62*, 940-950.

(104) Rysz, J.; A.Bernasik; Ermer, H.; A.Budkowski; Brenn, R.; Hashimoto, T.; Jedlinski, J. *Europhys. Lett.* **1997**, *40*, 503.

(105) Jones, R. A. L.; Kramer, E. J.; Rafailovich, M. H.; Sokolov, J.; Schwarz, S. A. *Physical Review Letters* **1989**, *62*, 280.

(106) Binder, K.; Frisch, H. L. *Zeitschrift für Physik B Condensed Matter* **1991**, *84*, 403-418.

(107) Puri, S.; Frisch, H. L. *J. Phys.: Condens. Matter* **1997**, *9*, 2109-2133.

(108) Puri, S.; Binder, K. *Phys. Rev. A* **1992**, *46*, R4487-R4489.

(109) Brown, G.; Chakrabarti, A. *Phys. Rev. A* **1992**, *46*, 4829-4835.

(110) Chen, H.; Chakrabarti, A. *Phys. Rev. E* **1997**, *55*, 5680-5688.

(111) Bastea, S.; Puri, S.; Lebowitz, J. L. *Phys. Rev. E* **2001**, *63*, 041513.

(112) Puri, S.; Binder, K. *Journal of Statistical Physics* **1994**, *77*, 145-172.

(113) Genzer, J.; Composto, R. J. *Europhys. Lett.* **1997**, *38*, 171-176.

(114) Marko, J. F. *Phys. Rev. E* **1993**, *48*, 2861-2879.

(115) Puri, S.; Binder, K. *Phys. Rev. E* **1994**, *49*, 5359-5377.

(116) Binder, K.; Puri, S.; Frisch, H. L. *Faraday Discus.* **1999**, *112*, 103-117.

(117) Puri, S.; Binder, K. *Phys. Rev. Lett.* **2001**, *86*, 1797-1800.

(118) Puri, S.; Binder, K. *Phys. Rev. E* **2002**, *66*, 061602.

(119) Liu, A. J.; Durian, D. J.; Herbolzheimer, E.; Safran, S. A. *Phys. Rev. Lett.* **1990**, *65*, 1897-1900.

(120) Liu, A. J. *Phys. Rev. A* **1991**, *44*, 7894-7897.

(121) Monette, L.; Liu, A. J.; Grest, G. S. *Phys. Rev. A* **1992**, *46*, 7664-7678.

(122) Tanaka, H. *Phys. Rev. Lett.* **1993**, *70*, 2770-2773.

(123) Zhang, Z.; Chakrabarti, A. *Phys. Rev. E* **1994**, *50*, 4290-4293.

(124) Zhang, Z.; Chakrabarti, A. *Phys. Rev. E* **1995**, *52*, 2736-2741.

(125) He, X.; Song, M.; Liang, H.; Pan, C. *J. Chem. Phys.* **2001**, *114*, 10510-10513.

(126) Sevink, G. J. A.; Zvelindovsky, A. V.; Fraaije, J. G. E. M.; Huinink, H. P. *J. Chem. Phys.* **2001**, *115*, 8226-8230.

(127) Jones, D. M.; Smith, J. R.; Huck, W. T. S.; Alexander, C. *Adv. Mater.* **2002**, *14*, 1130.

(128) Fichet, G.; Stutzmann, N.; Muir, B. V. O.; Huck, W. T. S. *Advanced Materials* **2002**, *14*, 47.

(129) Li, H.-W.; Muir, B. V. O.; Fichet, G.; Huck, W. T. S. *Langmuir* **2003**, *19*, 1963.

(130) Li, H.-W.; Kang, D.-J.; Blamire, M. G.; Huck, W. T. S. *Nanotechnology* **2003**, *14*, 220.

(131) Hamelinck, P. J.; Huck, W. T. S. *J. Mater. Chem.* **2005**, *15*, 381-385.

(132) Fichet, G.; Corcoran, N.; Ho, P. K. H.; Arias, A. C.; MacKenzie, J. D.; Huck, W. T. S.; Friend, R. H. *Adv. Mater.* **2004**, *16*, 1908-1912.

(133) Karim, A.; Douglas, J. F.; Lee, B. P.; Glotzer, S. C.; Rogers, J. A.; Jackman, R. J.; Amis, E. J.; Whitesides, G. M. *Phys. Rev. E* **1998**, *57*, R6273.

(134) Kielhorn, L.; Muthukumar, M. *J. Chem. Phys.* **1999**, *111*, 2259.

(135) Chen, H.; Chakrabarti, A. *J. Chem. Phys.* **1998**, *108*, 6897-6905.

(136) Chakrabarti, A.; Chen, H. *J. Poly. Sci. Part B: Poly. Phys.* **1998**, *36*, 3127-3136.

(137) Balazs, A. C.; Ginzburg, V. V.; Qui, F.; Peng, G.; Jasnow, D. *J. Chem. Phys.* **2000**, *104*, 3411.

(138) Qiu, F.; Peng, G.; Ginzburg, V. V.; Balazs, A. C. *J. Chem. Phys.* **2001**, *115*, 3779-3784.

(139) Peng, G.; Qiu, F.; Ginzburg, V. V.; Jasnow, D.; Balazs, A. C. *Science* **2000**, *288*, 1802.

(140) Bates, F. S. *Science* **1991**, *251*, 898-905.

(141) Lin, B.; Morkved, T. L.; Meron, M.; Huang, Z.; Viccaro, P. J.; Jaeger, H. M.; Williams, S. M.; Schlossman, M. L. *J. App. Phys.* **1999**, *85*, 3180-3184.

(142) Hasegawa, N.; Okamoto, H.; Kawasumi, M.; Usuki, A. *J. App. Poly. Sci.* **1999**, *74*, 3359-3364.

(143) Huh, J.; Ginzburg, V. V.; Balazs, A. C. *Macromolecules* **2000**, *33*, 8085-8096.

(144) Thompson, R. B.; Ginzburg, V. V.; Matsen, M. W.; Balazs, A. C. *Macromolecules* **2002**, *35*, 1060-1071.

(145) Buxton, G. A.; Balazs, A. C. *Phys. Rev. E* **2003**, *67*, 031802/031801-031802/031812.

(146) Press, W. H.; Teukolsky, S. A.; Vetterling, W. T.; Flannery, B. P. *Numerical Recipes in Fortran 90 The Art of Parallel Scientific Computing*, 2 ed.; Cambridge University Press, 1999.

(147) Keestra, B. J. In *mechanical Engineering*; Eindhoven University of Technology: Eindhoven, 2004; p 145.

(148) Glotzer, S. C.; Gyure, M. F.; Sciortino, F.; Coniglio, A.; Stanley, H. E. *Phys. Rev. E* **1994**, *49*, 247-258.

(149) Diehl, H. W.; Janssen, H. K. *Phys. Rev. A* **1992**, *45*, 7145-7155.